VELOCITY MEASUREMENTS IN RESERVOIR ROCK SAMPLES FROM A LIMESTONE UNIT USING VARIOUS PORE FLUIDS, AND INTEGRATION WITH WELL LOGS AND SEISMIC DATA

by

Christopher C. Purcell

Bachelors in Physics, University of Pittsburgh, 2006

Submitted to the Graduate Faculty of

Geology and Planetary Sciences in partial fulfillment

of the requirements for the degree of

Doctor of Philosophy

University of Pittsburgh

2012

UNIVERSITY OF PITTSBURGH

Dietrich School of Arts and Sciences

Geology and Planetary Sciences

This dissertation was presented

by

Christopher C. Purcell

It was defended on

June 7th, 2012

and approved by

Brian Stewart, Associate Professor, Geology and Planetary Science

Thomas Anderson, Professor Emeritus, Geology and Planetary Science

Mark Abbott, Associate Professor, Geology and Planetary Science

Yee Soong, National Energy Technology Laboratory

Dissertation Advisor: William Harbert, Department Chair and Professor, Geology and Planetary Science

VELOCITY MEASUREMENTS IN RESERVOIR ROCK SAMPLES FROM A LIMESTONE UNIT USING VARIOUS PORE FLUIDS, AND INTEGRATION WITH WELL LOGS AND SEISMIC DATA

Chris Purcell, PhD

University of Pittsburgh, 2012

One of the most promising methods proposed to mitigate excess global CO_2 is carbon sequestration, a process in which CO_2 is pressurized and injected into geologic formations. A technical challenge surrounding the geologic sequestration of CO_2 is tracking the movement of the fluids pumped underground. Monitoring, verification and accounting activities related to CO_2 storage are important for assuring that sequestered CO_2 does not escape to the surface. Tracking this carbon dioxide can be considerably aided by reflection seismic-based detection methods. This thesis employs lab scale velocity measurements of core samples, under *in situ* reservoir pressure and temperature conditions, combined with multiple 3D reflection seismic surveys, to effectively track the movements of CO_2 after injection.

The National Energy Technology Laboratory (NETL) of the United States Department of Energy began to participate in research of an enhanced oil recovery project including the injection of CO_2 deep into a reservoir structure, repeat reflection seismic surveys, collection of well logs, and rock physics analysis of sample core material. Our study is concentrated on a small area of this field around the injection site. At this site, hydrocarbons were previously moved via water injection. We obtained ultrasonic elastic wave velocity measurements that were conducted under several different saturation scenarios, including CO_2 saturated samples, so a quantification of the conditions in different parts of the reservoir could be determined.

This approach can help to characterize what is taking place inside the reservoir. Core-scale velocity measurements under *in situ* conditions allow us to predict changes in future well log or seismic surveys. The large amounts of CO_2 accumulated over the past four decades in this reservoir give us a real world example of how an EOR site matures. Combining core scale, well log scale, and seismic scale measurements allows a better understanding of the various processes at work when CO_2 is sequestered in a limestone reservoir.

TABLE OF CONTENTS

LIST OF TABLES

LIST OF FIGURES

LIST OF EQUATIONS

PREFACE

A PhD, an undertaking of no small magnitude, cannot be completed in isolation. This is especially true in my own case, and there are a great many people who should be thanked, but I will limit it to a small number here. Obviously, my family, friends and colleagues have been a great help throughout this long process, and it could not have been done without their help and support. To my parents and my brother, who were a constant help in reminding me that, yes, at some point I would need to graduate and enter the "real world". To my roommates, Isaac, Matt, and Kristen, who helped me push through the last year of work by constantly indulging my increasing ridiculous and impulsive hobbies, pursuits, and activities with nothing but encouragement, fervour, and active participation. Listing but a small fraction of these would take much more space than I have here. To Fernando, my constant couch companion, who witnessed the creation of more of this thesis than any man or beast. To Cindy, for providing a dose of much needed art and culture into my scientific pursuits. To Michelle, for her constant moral, scientific, and coffee related support. To Kate, for helping to answer all manner of silly questions and for providing all manner of distractions throughout all of my work days over the last 5 years. To Jon and Josh, whose legal and mechanical advice and participation in my many pursuits was always helpful. To Adam and Lindsey, who made my summer in Texas more fun that I thought possible. To Hillary and Laura, who always allowed me the opportunity to let my hair down. Although I

may have talked to her more than anyone else about my work, I am confident I was still unable to explain it satisfactorily to her. I am thankful to have been stationed in my office with the best possible combination of students the department has to offer: Alan, Dave, Matt and Aubrey. A thanks should also be given to former students whose guidance was invaluable in my early days in grad school: Broxton, Nathan, Vlad and Byron. Dave was able to instill in me a passion for two new pursuits: farming and coring. May his thumbs always be green and his water-sediment interfaces always be clear. Matt, in addition to statistical assistance, was able to take my fledgling geologic T-Shirt dreams to more layers than I would have thought possible. Academically, I need to thank Serge Shapiro, whose immense knowledge and illuminating discussions assisted me greatly. I would also like to thank Mark Abbott for allowing me to assist his group in their quest for cores. And I want to save a special thanks for the two obvious people not mentioned above: Alan Mur and Bill Harbert. Alan, my partner in academic crime, was a constant source of support and help throughout this entire process. From beer fueled academic arguments to late night caffeine powered esoteric topics of conversation, his intellectual and social fervidness scope were a constant throughout my time in grad school. A large portion of this work was done in conjunction with him, and his input was taken into consideration for the entirety. Last but certainly not least, I would like to thank Bill Harbert, my advisor on this project. An advisor's role in a project is, no doubt, a large one, but Bill always took the extra step, not only with me, but with all of the students in the department. Bill, I am honored and humbled to have been your student, and I know that everything you have passed on to me will serve me well down the road.

1.0 INTRODUCTION

One of the most promising methods proposed to mitigate global CO_2 is Carbon Sequestration, a process in which CO_2 is pressurized and injected into geologic formations. A technical challenge surrounding the geologic sequestration of CO_2 is tracking the movement of the fluids pumped underground. Monitoring, verification and accounting activities related to CO_2 storage are important for assuring that any sequestered CO_2 does not escape to the surface, and these can be considerably aided by reflection seismic based detection methods. Through the use of lab scale velocity measurements, under *in situ* conditions, combined with multiple 3D reflection seismic surveys, we hope to be able to effectively track the movements of CO_2 after injection.

The area of study is a Limestone reservoir located in the Permian Basin in western Texas. This project included the injection of CO_2 at a depth of approximately 2040m into a reef structure, repeat reflection seismic surveys, and rock physics analysis of sample core material. Our study area is a small area of the field around the phase II injection site. At this site, hydrocarbons were previously flooded out using water, and were then flooded with CO_2 during the summer of 2008. In this paper we present new ultrasonic elastic wave velocity measurements that were conducted on core samples under several different saturation scenarios, including CO_2 saturated samples, so an approximate estimate of the conditions in different parts of the reservoir could be obtained.

This multi-scale approach can help to characterize what is occurring inside of the reservoir. Fine scale measurements of how CO_2 affects pore-space dissolution can help to inform us of any changes in overall reservoir storage capacity due to changing porosity. Core-scale velocity measurements under *in situ* conditions will allow us to predict changes in future well log or seismic surveys. The large amounts of CO_2 accumulated over the past four decades in areas surrounding our study site give us a real world example of how an EOR site matures. Combining microscale, mesoscale, and macroscale information should lead to a better understanding of the various processes at work when CO_2 is sequestered in a limestone reservoir.

1.1 CORE PREPARATION

Figure 1: Left: NER Autolab 1500 Center: Sonic velocity core holder assembly Right: Resistivity heads with Limestone core.

Two large core samples of the reservoir limestone were obtained. A 2" (5.08 cm) diameter sample was taken from each core. Core #1 comes from a depth of approximately 6500 ft (1981 m), while core #2 comes from a depth of 6180 ft (1884 m) below the surface. Core #1 has a bulk density of 2.200 g/cm^3 and a length of 2.85 in (72.35 mm), while core #2 has a Bulk Density of 2.550 g/cm^3 and a length of 2.69 in (68.28 mm). In addition, samples of Berea Sandstone were measured as a known reference material. The cores were tested in a Helium Porosimeter, which determines the porosity of a sample of known size. Core #1 had a porosity of 18.53%, while core #2 had a porosity of 6.39%.

We performed ultrasonic velocity measurements on Berea sandstone and Limestone samples. These were in the form of pre-cut cores approximately 77 mm in diameter. After visual inspection the cores were subsampled using a large water lubricated drill press in order to fit our core holders. The ends of core samples are cut using an automated wet saw and any rough edges were filed down. Samples were then placed in a desiccator jar and allowed to dry overnight. The sample was then weighed and measured with calipers. The porosity of sample was then measured using a Helium Porosimeter. The sample was then loaded into the AutoLab 1500 instrument for ultrasonic velocity analysis (Figure 1). The sample was then put inside a rubber sleeve and positioned in the AutoLab 1500. The rubber sleeve was then mated to the velocity heads, creating a seal and the entire assembly was placed inside the AutoLab, at which point ultrasonic velocity measurements were made.

1.2 ROCK PHYSICS MEASUREMENTS

The National Energy Technology Laboratory (NETL) Geological Sequestration Core Flow Laboratory the New England Research (NER) AutoLab 1500 PS2 ultrasonic transducer measured one compressional and two orthogonally polarized shear waves and associated waveforms. The sampling interval of the waveforms was 1.00E-08 seconds. For each step the first arrival of P, S_1 and S_2 were picked from waveforms. These picks then allowed the determination of V_p, V_{S1}, V_{S2}, Young's modulus and Poisson's ratio, using software from NER. These values were checked by independent calculations made using the measured density, sample dimensions, and appropriate travel times (in μsecs).

In our experimental procedure, we started with air filled samples (fluid 1), and measured $V_P^{(1)}$, $V_{SH}^{(1)}$, $V_{SV}^{(1)}$, and $\rho^{(1)}$. We also completed measurements using water and CO_2 as the pore-filling phase, (fluid 2). Measurements were completed using the PS^2 ultrasonic transducer, which measured one compressional and two orthogonally polarized shear waves and waveforms at various confining and pore pressures (Table 1: List of Velocity Measurements. Waveforms were quite consistent and first arrivals were relatively clear on all records analyzed.

We conducted several different types of tests on the Limestone Core #1 reservoir sample. We first ran experiments where the confining pressure was incrementally raised up to 50 MPa. A marked increase in P-Wave velocity was seen, indicating the closure of microcracks in the sample (Kaselow and Shapiro (2004)). We then flooded the cores with CO_2 under different temperature/pressure conditions, which included gaseous, liquid, and supercritical phases. In-situ

temperature conditions were replicated through the use of a heating element built into the AutoLab unit. We varied the pore pressure of the sample between 0 and 30 MPa while maintaining a constant confining pressure of 30, 40, and 50 MPa. Increasing pore pressure caused the velocity to decrease rapidly under all confining pressure regimes (Purcell 2010). This agrees well with other studies (Wang 1989).

We also completed hysteresis experiments on a CO_2 limestone sample. It showed little velocity change between pressurization and depressurization at the low effective pressures associated with our reservoir (Purcell 2010). We also completed a higher resolution hysteresis experiment where only confining pressure was changed, and no pore fluids were introduced into the sample. The pressure was varied between 3 and 50 MPa in increments of 1 MPa, and then depressurized in the same way. Between each confining pressure increase, the sample was allowed to equilibrate for 5 minutes before measurements were made. At high pressures, the velocities agreed well, but at low confining pressures, the velocities on the depressurization curve were found to be higher by ~5%.

Experiment #	Rock Type	Pore Filling Phase	CP (MPa)	PP (MPa)
1215721076	LIMESTONE #1	CO_2	30	0-24
1215722869	LIMESTONE #1	CO_2	40	0-24
1215723376	LIMESTONE #1	CO_2	50	0-27
1213901004	Berea #2	dry	0-48	N/A
1213888788	Berea #2	dry	0-48	N/A
1213295699	Berea #2	dry	0-60	N/A

1213300158	Berea #2	CO_2	40	0-13.6
1213904566	Berea #2	CO_2	30	0-13.6
1213902929	Berea #2	CO_2	40	0-13.6
1213905049	Berea #2	CO_2	50	0-13.6
1213991349	Berea #2	water	30	0-24
1213988733	Berea #2	water	40	0-24
1213990513	Berea #2	water	50	0-25
1215715928	LIMESTONE #1	dry	0-52	N/A
1213983392	Berea #2	water	0-60	N/A
1232123606	Berea #2	CO_2	0-50	0-35
1234988766	LIMESTONE #1	CO_2	40	0-30-0
1235589085	Shale	dry	0-50-0	N/A
1231962095	Berea #2	dry	0-60-0	N/A
1233770523	LIMESTONE #1	CO_2	40	0-33
1280256166	LIMESTONE #1	dry	0-50-0	0

Table 1: List of Velocity Measurements

1.2.1 Theoretical Rock Physics Calculations

In order to better understand the velocity changes associated with differing pressures, temperatures, and saturations, various theoretical rock physics were completed in order to study how closely theory matches our experiments.

1.2.1.1 Gassmann Equations

We used Gassmann (Gassmann 1951) and Biot (Biot 1956) theory to calculate the expected water and CO_2 results from the fluid 1 measurements. Expected CO_2 density at a temperature of 298°K (25°C) between 0.0 and 55.8 were calculated from the NIST on-line isothermal properties database (Lemmon 2005).

Gassmann (Gassmann 1951) and Biot (Biot 1956) based calculations of expected elastic wave velocities are useful in rock physics analysis of the expected reflectivity of CO_2 saturated units (McKenna 2003). Initially, we calculated the dynamic bulk and shear moduli from $V_P^{(1)}$, $V_{SH}^{(1)}$, and $\rho^{(1)}$ using the standard equations (Sheriff 1995). We then used the Gassmann-Biot equation (Gassmann 1951; Biot 1956) to transform the bulk modulus for a rock saturated with fluid 2 (CO_2 at the appropriate pressure and temperature conditions), which has associated quantities ($V_P^{(2)}$, $V_{SH}^{(2)}$, $V_{SV}^{(2)}$, and $\rho^{(2)}$).

$$\frac{K_{sat}}{(K_{mineral}-K_{sat})} = \frac{K_{dry}}{(K_{mineral}-K_{dry})} + \frac{K_{fluid}}{\varphi(K_{mineral}-K_{fluid})}$$

Equation 1: Gassmann's Equation

For low frequencies, the bulk and shear moduli can be calculated using the following equations (McKenna 2003):

$$V_p = \sqrt{\frac{K_{sat}-\frac{4}{3}\mu_{sat}}{\rho_{sat}}} \text{ or } K^{(1)} = \rho\left(V_p^{(1)^2} - \left(\frac{4}{3}(V_{SH}^{(1)})\right)^2\right)$$

Equation 2: Bulk Modulus from velocity

$$V_S = \sqrt{\frac{\mu_{sat}}{\rho_{sat}}} \text{ or } \mu^{(1)} = \rho(V_{SH}^{(1)})^2$$

Equation 3: Shear Modulus from velocity

$$K_{sat} = K_{dry} + \frac{\left(1 - \frac{K_{dry}}{K_{mineral}}\right)^2}{\frac{\varphi}{K_{fluid}} + \frac{1-\varphi}{K_{grain}} - \frac{K_{dry}}{K_{grain}^2}}$$

Equation 4: Saturated Bulk Modulus Equation

Note that from the Gassmann equation (Avseth 2007).

$\mu_{sat} \quad \mu_{dry}$

Equation 5: Saturated Shear Modulus Equation

We can also calculated the expected bulk and shear moduli for fluid saturated conditions using experiments involving a different pore-filling fluid, Here, we solved:

$$\frac{K_{sat}^{(2)}}{K_{mineral} - K_{sat}^{(2)}} - \frac{K_{fluid}^{(2)}}{\varphi\left(K_{mineral} - K_{fluid}^{(2)}\right)} = \frac{K_{sat}^{(1)}}{K_{mineral} - K_{sat}^{(1)}} - \frac{K_{fluid}^{(1)}}{\varphi\left(K_{mineral} - K_{fluid}^{(1)}\right)}$$

Equation 6: Gassmann Fluid Substitution

$$K_{sat}^{(2)} = \frac{K_{mineral}}{\left(1 + \frac{K_{sat}^{(1)}}{K_{mineral} - K_{sat}^{(1)}} - \frac{K_{fluid}^{(1)}}{\varphi\left(K_{mineral} - K_{fluid}^{(1)}\right)} - \frac{K_{fluid}^{(2)}}{\varphi\left(K_{mineral} - K_{fluid}^{(2)}\right)}\right)}$$

Equation 7: Solution for Saturated Bulk Modulus

With:

$$\mu_{sat}^{(2)} = \mu_{sat}^{(1)}$$

Equation 8: Saturated Shear Modulus

We adjusted the bulk density for the fluid change, where $\rho^{(2)}$ is the density of the material saturated with fluid (2) or CO_2.

$$\rho^{(2)} = \rho^{(1)} + \varphi(\rho_{fluid}^{(2)} - \rho_{fluid}^{(1)})$$

Equation 9: Saturated Density

We then recalculated the expected V_P and V_S elastic wave velocities for fluid 2 at the appropriate pressure and temperature conditions.

$$V_p^{(2)} = \sqrt{(K_{sat}^{(2)} + (4/3)\mu_{sat}^{(2)})/\rho^{(2)}}$$

Equation 10: V_P from Saturated Moduli

$$V_S^{(2)} = \sqrt{\mu_{sat}^{(2)}/\rho^{(2)}}$$

Equation 11: V_S from Saturated Moduli

1.2.1.2 Mavko-Jizba

Mavko and Jizba (Mavko 1991) present a modification of Gassmann-Biot that takes grain scale fluid flow velocity dispersion into account by using the high frequency unrelaxed shear and bulk frame moduli to predict the total dispersion. This method is independent of pore geometry or pore aspect ratio. Local fluid flow effects depend on the presence of compliant cracks and grain contacts. They show that the unrelaxed wet frame compressibility at a given pressure is approximately equal to the dry frame compressibility at very high pressure.

The presence of cracks and pores in a rock cause the elastic moduli to be lower than that of the minerals it is made of. Fluid saturation offsets this effect, but is frequency dependent. Gassmann's equation (Gassmann 1951) relates the saturated bulk modulus to the dry rock modulus, but is limited to low frequencies and does not assume idealized pore shapes. Biot's equation (Biot 1956) includes coupling of fluid and solid stresses, but details of pore shape are neglected.

Ultrasonic velocity measurements are often faster than predicted by either of these equations. This dispersion increases with frequency and fluid viscosity, and decreases with effective pressure due to grain scale flow effects. A passing wave creates differing areas of pore pressure and flow due to the effect of variations in pore shape, orientation and saturation. When a rock is saturated and then compressed, pressure is induced in the pore fluid. Stiffer sections of the pore space have a low induced pore pressure, but compliant cracks and pores transfer more stress to the fluid and therefore have a higher pore pressure. At low frequencies, this pressure gradient has

enough time to equilibrate, but at ultrasonic frequencies, the pressure does not have enough time to equilibrate. This isolates the compliant pores from the stiff pores and from one another, which gives higher elastic moduli values, which is known as squirt dispersion.

Mavko and Jizba (Mavko 1991) use the high frequency unrelaxed bulk and shear moduli to estimate the effects of grain scale flow on bulk and shear dispersion. It is relatively independent of specific crack geometries, but is similar to Gassmann because the unrelaxed saturated moduli are estimated from K_{dry}, K_0, and K_f . They derived an expression that shows that the unrelaxed frame compressibility is approximately equal to the high pressure dry rock compressibility plus a second order correction for porosity change.

$$\frac{1}{K_{uf}(\sigma)} \approx \left(\frac{1}{K_{dry}}\right)_{high\ \sigma} + \left(\frac{1}{K_f} - \frac{1}{K_0}\right)\varphi_{soft}(\sigma) - \left(\frac{1}{K_f} - \frac{1}{K_0}\right)^2 \sum_{soft\ porosity} \frac{\varphi_i^2}{\frac{d\varphi_i}{d\sigma}} + \cdots$$

Equation 12: Mavko and Jizba expression for unrelaxed frame compressibility

The equation above is the result that shows that to first order the unrelaxed bulk frame compressibility is approximately equal to the dry frame compressibility at a high confining pressure. The second term adds the compressibility from the soft porosity. The first two terms give the distribution of stiff and soft porosity, and if the soft porosity term is small, the second

term isn't needed. We ignore the higher terms because intermediate pore stiffness has a negligible effect on the compressibility.

$$\frac{1}{\mu_{dry}} - \frac{1}{\mu_{ut}} \approx \frac{4}{15}\left(\frac{1}{K_{dry}(\sigma)} - \frac{1}{K_{ut}(\sigma)}\right)$$

Equation 13: Mavko Jizba equation for shear frame dispersion

The equation above gives the shear frame dispersion, which is proportional to the bulk frame dispersion. The proportionality of shear dispersion and bulk dispersion occurs as a result of the different orientation of compressive stresses the crack-like soft porosity is subjected to.

1.2.1.3 Gurevich et al.

The Mavko-Jizba expressions are only valid for liquid pore-filling phases, they do not correctly predict the effect of gaseous pore-filling phases on the unrelaxed frame bulk and shear moduli. Gurevich (Gurevich, Makarynska et al. 2010) derived an expression that generalizes the Mavko-Jizba equations to gas-saturated rocks. These relations reduce to the Mavko-Jizba equations when the pore-filling phase is liquid.

Beginning with the Mavko-Jizba equations:

$$\frac{1}{K_{uf}(\sigma)} \approx \left(\frac{1}{K_{dry}}\right)_{high\ \sigma} + \left(\frac{1}{K_f} - \frac{1}{K_0}\right)\varphi_{soft}(\sigma)$$

Equation 14: Mavko Jizba expression for Frame compressibility

$$\frac{1}{\mu_{dry}} - \frac{1}{\mu_{uf}} \approx \frac{4}{15}\left(\frac{1}{K_{dry}(\sigma)} - \frac{1}{K_{uf}(\sigma)}\right)$$

Equation 15: Mavko Jizba expression for shear frame compressibility

Where K_{dry} and μ_{dry} are bulk and shear moduli of the rock at a given confining pressure, K_f and K_0 are the bulk moduli of the fluid and the grains, is the compliant porosity at a given pressure, and K_{uf} is the dry bulk modulus of a rock without compliant porosity.

These equations agree well with experimental data, including ours. However, for the first equation to be valid, the fluid bulk modulus K_f must be much larger than K_{uf}. This is the case for fluids, but is invalid for gasses or for dry rocks, where the expression goes to infinity. Gurevich corrects for this using this equation:

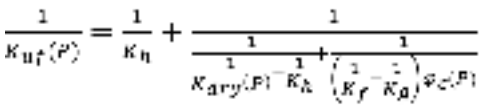

Equation 16: Gurevich expression for Unrelaxed Frame compressibility

Since the compliant porosity is usually very small, $(K_{dry}^{-1} - K_h^{-1})^{-1}$ is very small compared to $\Phi_c(K_f^{-1} - K_g^{-1})^{-1}$, and this equation reduces to the Mavko-Jizba equation. For a dry rock, $\Phi_c(K_f^{-1} - K_g^{-1})^{-1}$ becomes zero, and K_{uf} reduces to K_{dry} (Gurevich, Makarynska et al. 2010). This equation is particularly useful for our calculations because at low pore pressures, our samples contain gaseous CO_2.

1.2.1.4 Comparison of Theoretical to Experimental Results

We calculated the expected velocities for our samples using the standard Gassmann equations and the Mavko-Jizba equations (Gassmann 1951) (Mavko 1991). We then used the Generalized Mavko-Jizba equations given by Gurevich, which correct for gas saturated rocks (Gurevich, Makarynska et al. 2010). The calculated results were then compared with our experimental results of CO_2 saturated Limestone #1 material at 50°C, and found good agreement with both the Mavko-Jizba and Gurevich equations at high effective pressures (Purcell 2010).

The differences between the three methods for the Limestone #1 limestone are significant. The Gassmann equations give lower velocity predictions than the Mavko-Jizba equation except for low effective pressures corresponding to a gaseous phase (Figure 2). The Mavko-Jizba and Gurevich equations give the same results at higher effective pressures, but the Gurevich generalized version of the equation is more accurate at low effective pressures, due to the low bulk modulus of gaseous CO_2 (Gurevich, Makarynska et al. 2010).

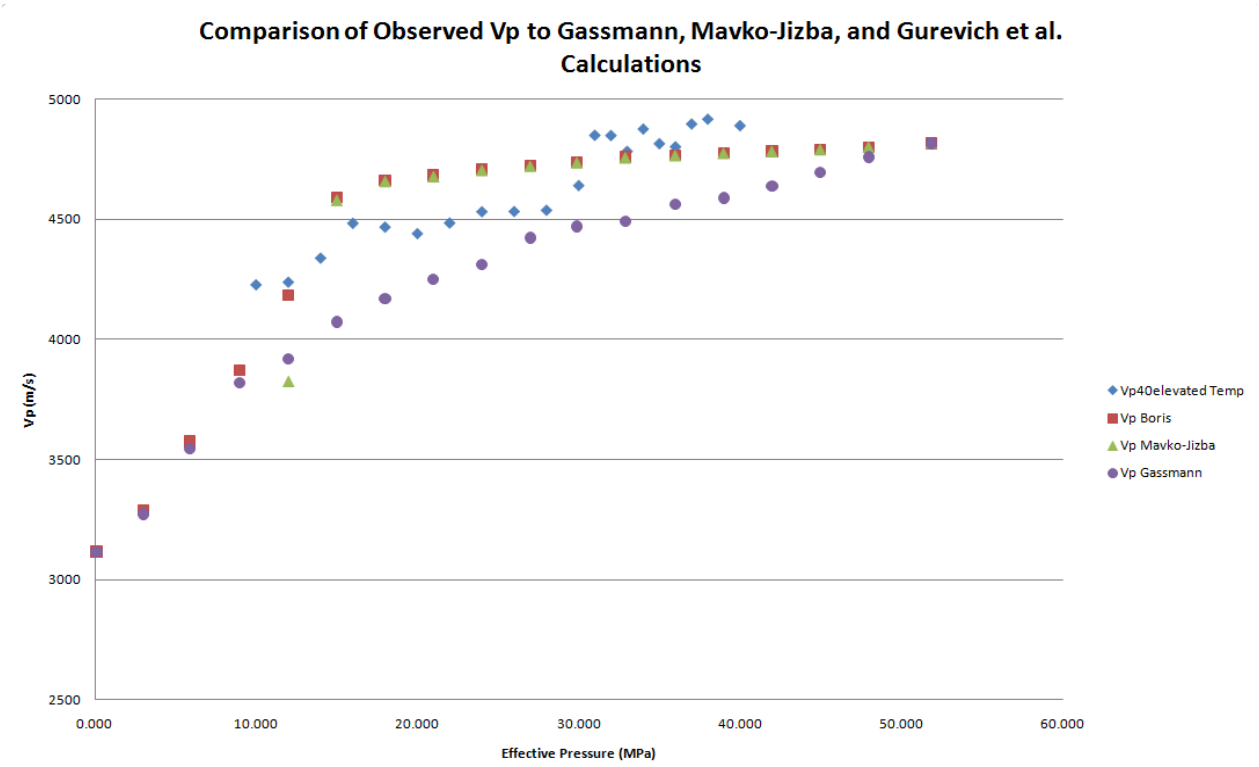

Figure 2: Comparison of Gassmann, Mavko-Jizba and Gurevich et al equations to CO_2 saturated Limestone #1 experimentally determined velocities.

1.2.2 Berea Sandstone Rock Physics Experiments

We first used samples of Berea Sandstone in order to familiarize ourselves with the core preparation process and the operation of the AutoLab 1500. Berea sandstone is a widely used reference material that has fairly uniform grain size along with high porosity and permeability, making any effect of saturation easier to see.

The first set of experiments performed were a test of the effect of increasing confining pressure on sonic velocity. After loading the core material into the AutoLab, confining pressure was increased in 3 MPa increments up to a maximum pressure of 48 MPa. At each step, time was given to allow the pressure to equilibrate, and sonic velocity measurements were collected. This same experiment was then repeated, and the results compared.

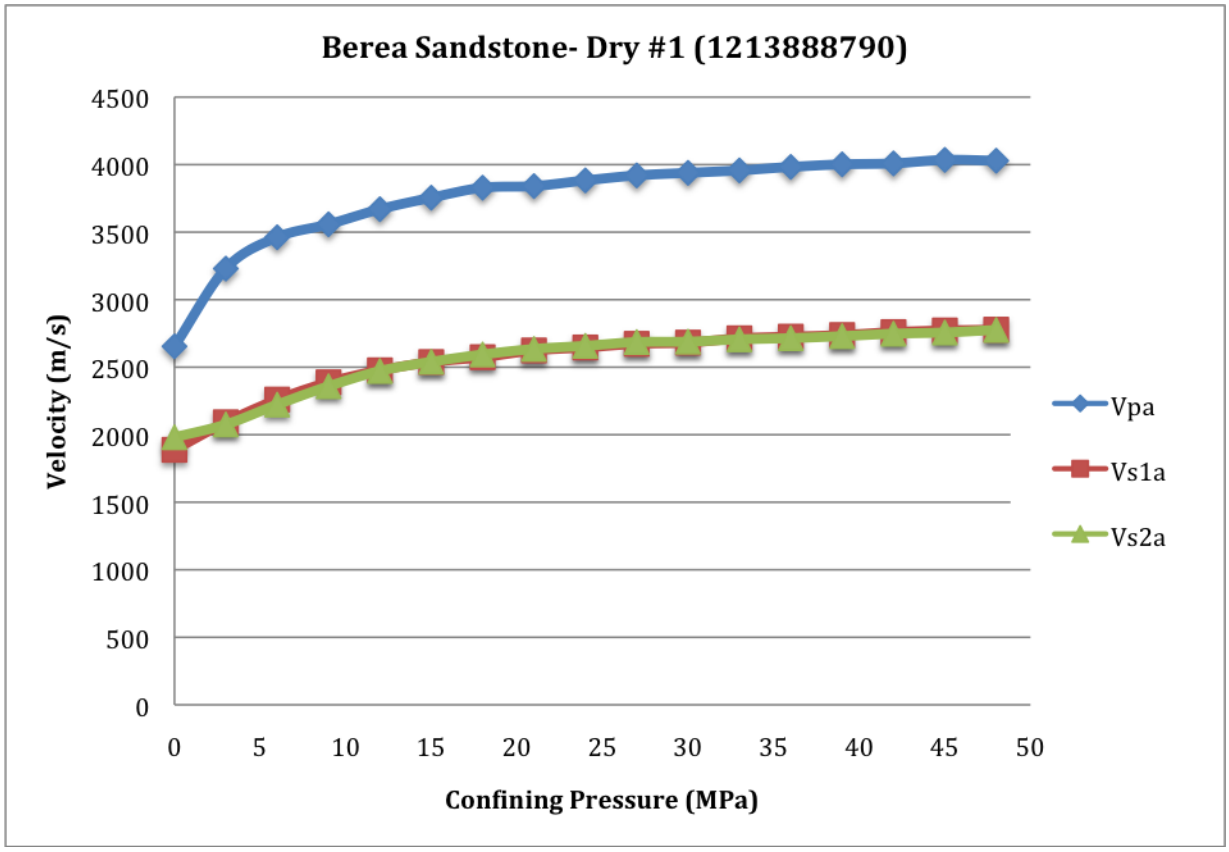

Figure 3: Berea Dry #1, Velocity vs. Confining Pressure

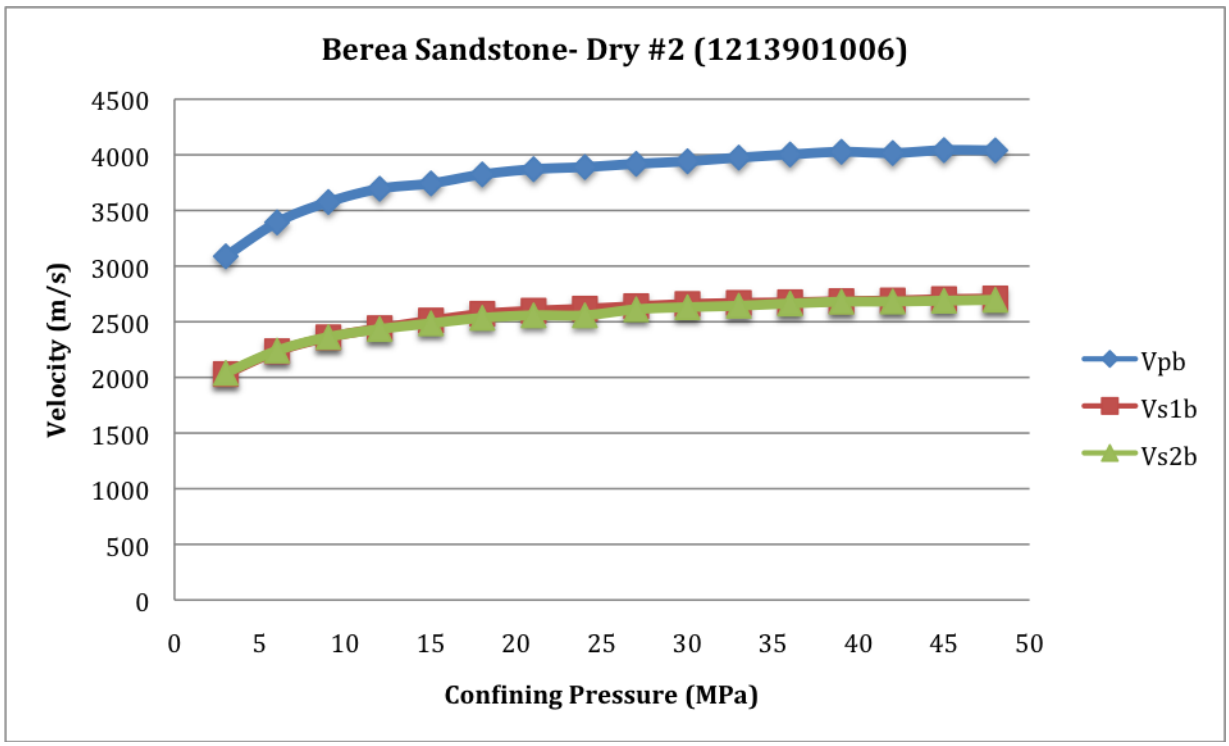

Figure 4: Berea Dry #2, Velocity vs. Confining Pressure

As can be seen in Figure 3 and Figure 4Figure 3: Berea Dry #1, Velocity vs. Confining Pressure, V_p, V_{S1} and V_{S2} all become larger with increasing confining pressure. When the confining pressure increased from 0-24 MPa, V_p increased from 2654 m/s to 3883 m/s, a change of ~46%. However, when the confining pressure was increased further from 24-48 MPa, V_p only increased from 3883 m/s to 4029 m/s, a change of ~4%.

For V_{S1}, when the confining pressure increased from 0-24 MPa, V_{S1} increased from 1888 m/s to 2646 m/s, a change of ~40%. However, when the confining pressure was increased further from 24-48 MPa, V_{S1} only increased from 2646 m/s to 2778 m/s, a change of ~5%. For V_{S2}, when the confining pressure increased from 0-24 MPa, V_{S2} increased from 1981 m/s to 2658 m/s, a change

of ~34%. However, when the confining pressure was increased further from 24-48 MPa, V_{S2} only increased from 2658 m/s to 2776 m/s, a change of ~4%.

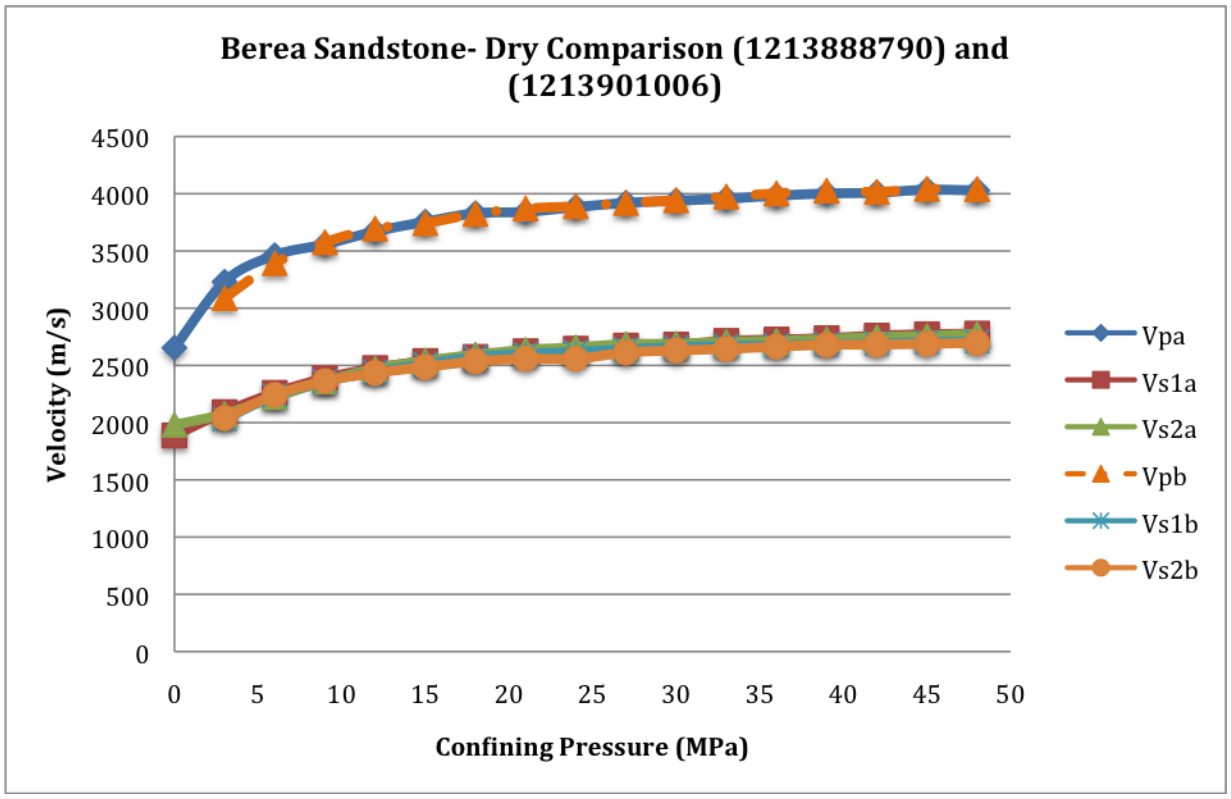

Figure 5 Berea Dry Comparison, Velocity vs. Confining Pressure

This large velocity change from 0-24 MPa with a much smaller velocity change over 24-48 MPa can be accounted for because of compliant porosity. As the pressure increases, the compliant porosity begins to close, stiffening the rock framework. By 24 MPa, most of this compliant porosity is already closed, hence the much smaller linear trend in velocity from 24-48 MPa.

If we compare the two repeat experiments, we can see that they match up very well to one another, with very little difference between in velocities, as can be seen in Figure 5. This confirms the accuracy of our experimental setup.

For the next set of experiments, we saturated the Berea Sandstone cores with tap water in order to gain insight into any velocity changes associated with adding pore fluid. Samples were dessicated, evacuated in a vacuum oven set to ambient temperature, and then dropped into a container of water placed underneath the sample in the vacuum to help ensure complete saturation. The saturated sample was weighed, and found to correspond to the weight of the sample plus the weight of the volume of water needed to completely fill the pore space. The sample was then jacketed, loaded into the AutoLab, and experiments began.

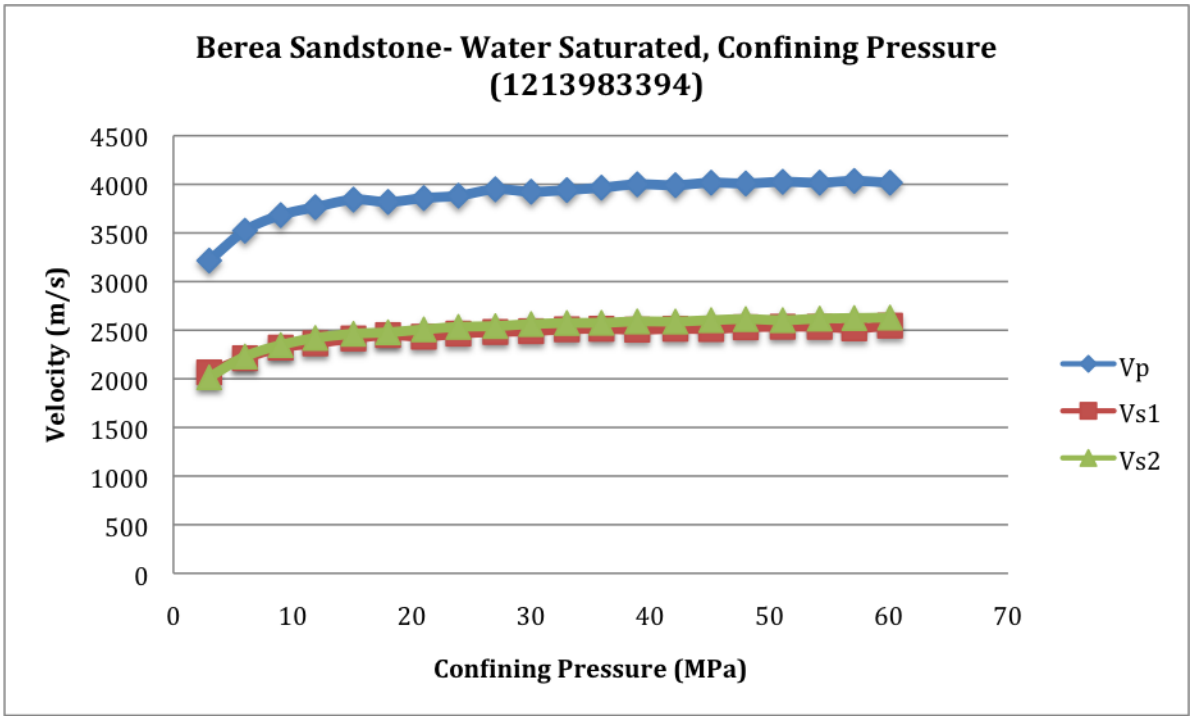

Figure 6 Berea Water Saturated Confining Pressure, Velocity vs. Confining Pressure

First, the water-saturated sample was subjected to increasing confining pressure from 3-60 MPa, in steps of 3 MPa. As we can see in Figure 6, it shows the same characteristic change in velocity that the dry samples did. When we compare the water saturated samples to the dry samples in Figure 7, we note two things: V_P for water saturated samples is consistently higher from 3-15 MPa, and then matches well with dry measurements for the rest of the run; and that at confining pressures above 15 MPa, V_{S1} and V_{S2} are lower than the dry measurements. According to theory, the water saturated V_P velocities should be higher, and there should be no change in V_{S1} and V_{S2} velocities. A likely explanation for this discrepancy is, however, easily found. The water-saturated sample was loaded in to the core holder with no fluid pore pressure. As the confining pressure increases, it is likely that some of the water is squeezed out of the sample and into the downstream pore pressure plumbing system. Although this volume is small (~1 cc), this could explain the drop in V_P above 15 MPa, and patchy saturation effects could explain the lower S-Wave velocities we see above 15 MPa.

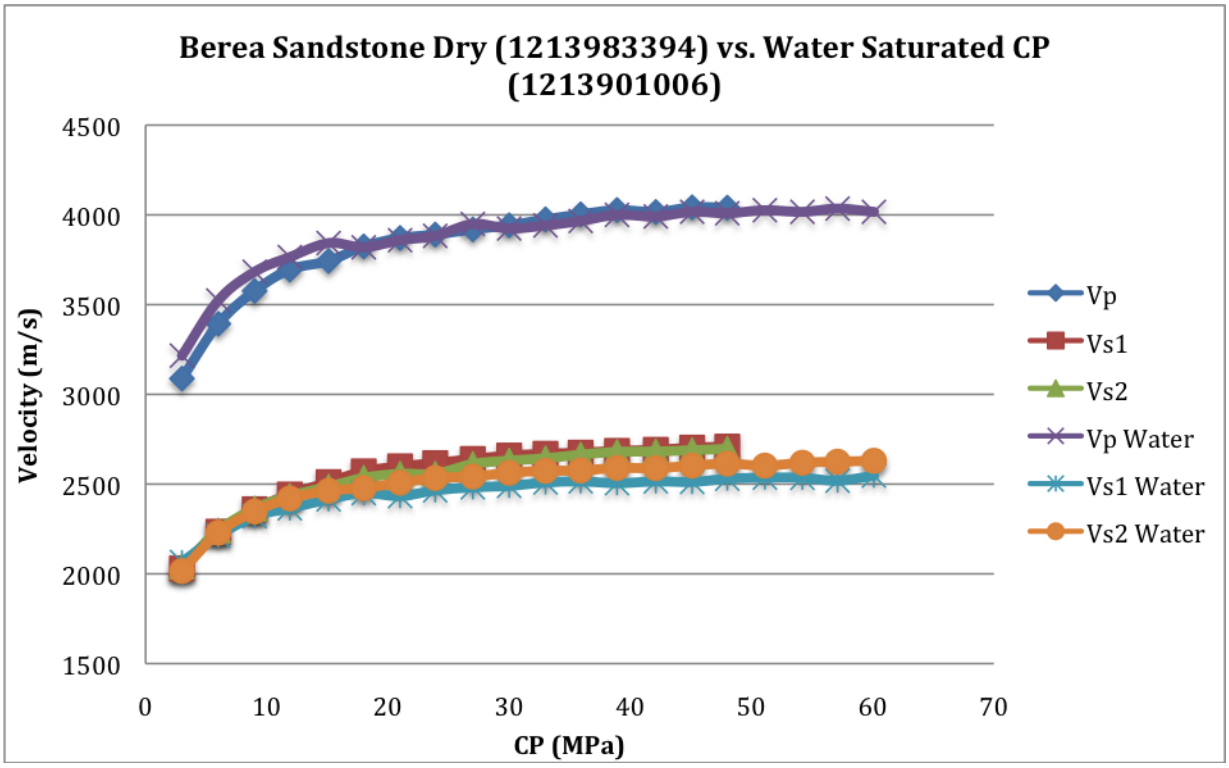

Figure 7 Berea Dry vs. Water Saturated, Velocity vs. Confining Pressure

In the next set of experiments, we wanted to see the effect that pore water would have on a sample when pressurized. This was accomplished by saturating the sample using the above method. In order to increase the pore pressure in these experiments, Argon gas was used to pressurize the water-saturated sample. A downstream plug was used to prevent the escape of water from the core.

For the first run, we raised the confining pressure to 30 MPa, and then raised the pore pressure in increments of 3 MPa, up to 24 MPa. We note a small but steady decrease in both V_P and V_S velocities seen in Figure 8.

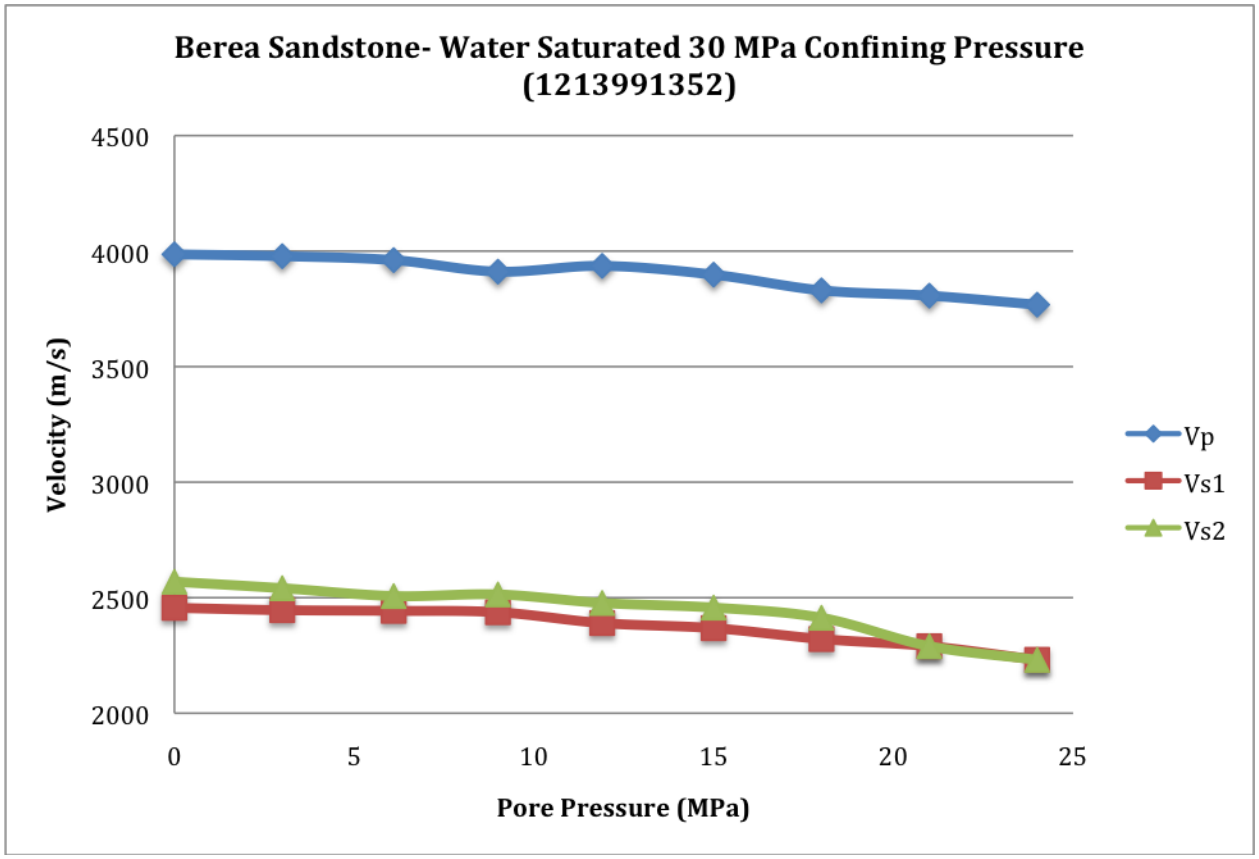

Figure 8 Berea Water Saturated 30 MPa Confining Pressure, Velocity vs. Pore Pressure

We then repeated the experiments at 40 MPa (Figure 9) and 50 MPa (Figure 10) confining pressure and found the same decreasing velocity trend with increasing pore pressure. The decrease in velocity in all three experiments is due to the decreasing Effective Pressure (Defined as: Effective Pressure = Confining Pressure – Pore Pressure). As the Pore Pressure increases, fluid pressure forces the compliant porosity to open back up, lowering the Bulk Modulus of the rock and decreasing the velocity.

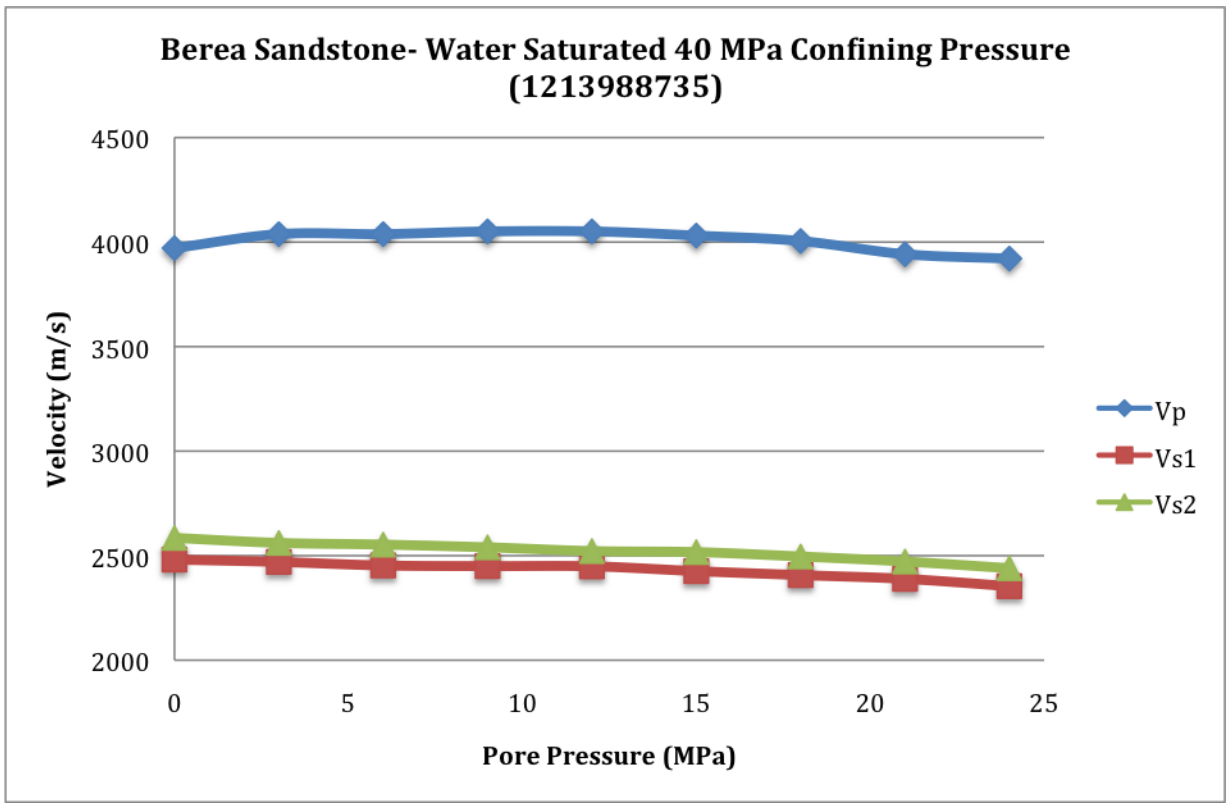

Figure 9 Berea Water Saturated 40 MPa Confining Pressure, Velocity vs. Pore Pressure

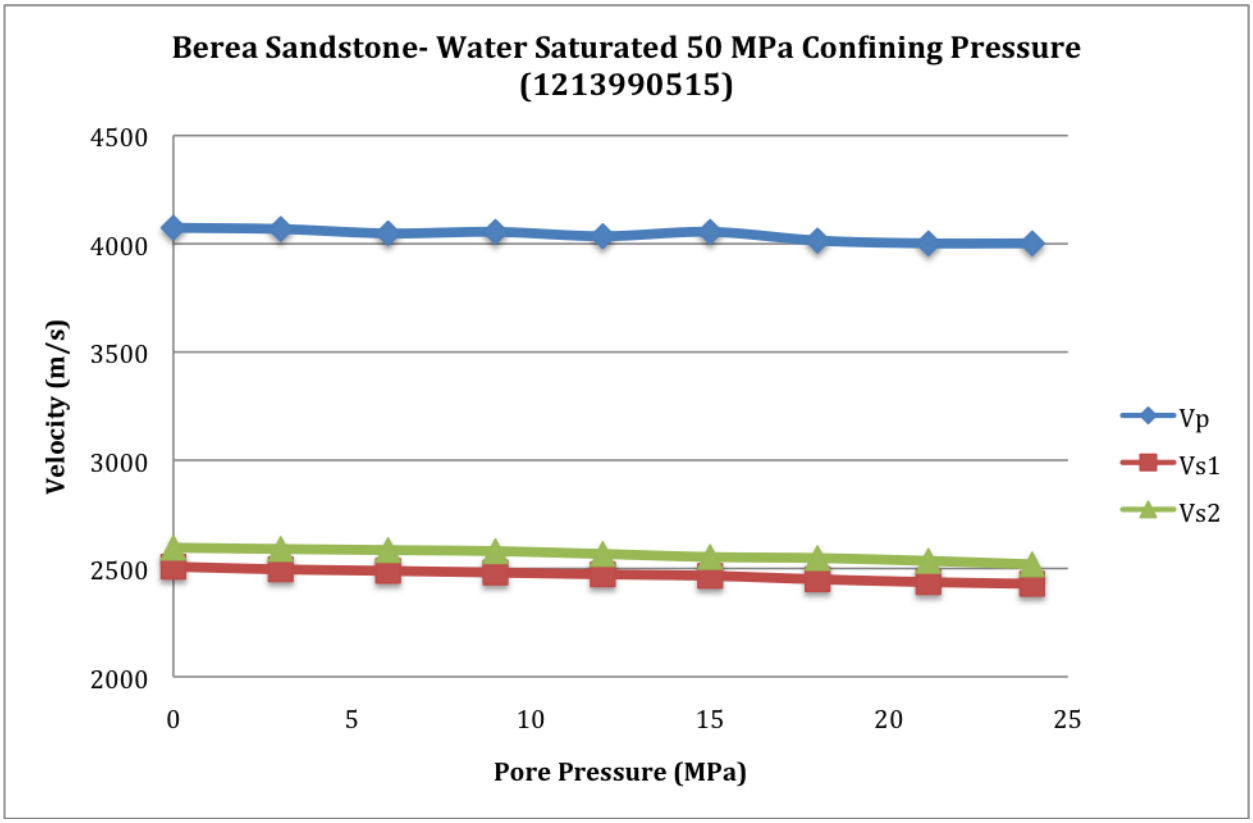

Figure 10 Berea Water Saturated 50 MPa Confining Pressure, Velocity vs. Pore Pressure

When we compare the velocities of all three runs, we can see in Figure 11 that for V_P, the velocity steadily increases with increasing effective pressure, as expected. The differences in confining pressure have little effect on the velocity, as can be seen where the curves overlap one another. This is because fluid pressure has a large effect on the Bulk Modulus of the rock.

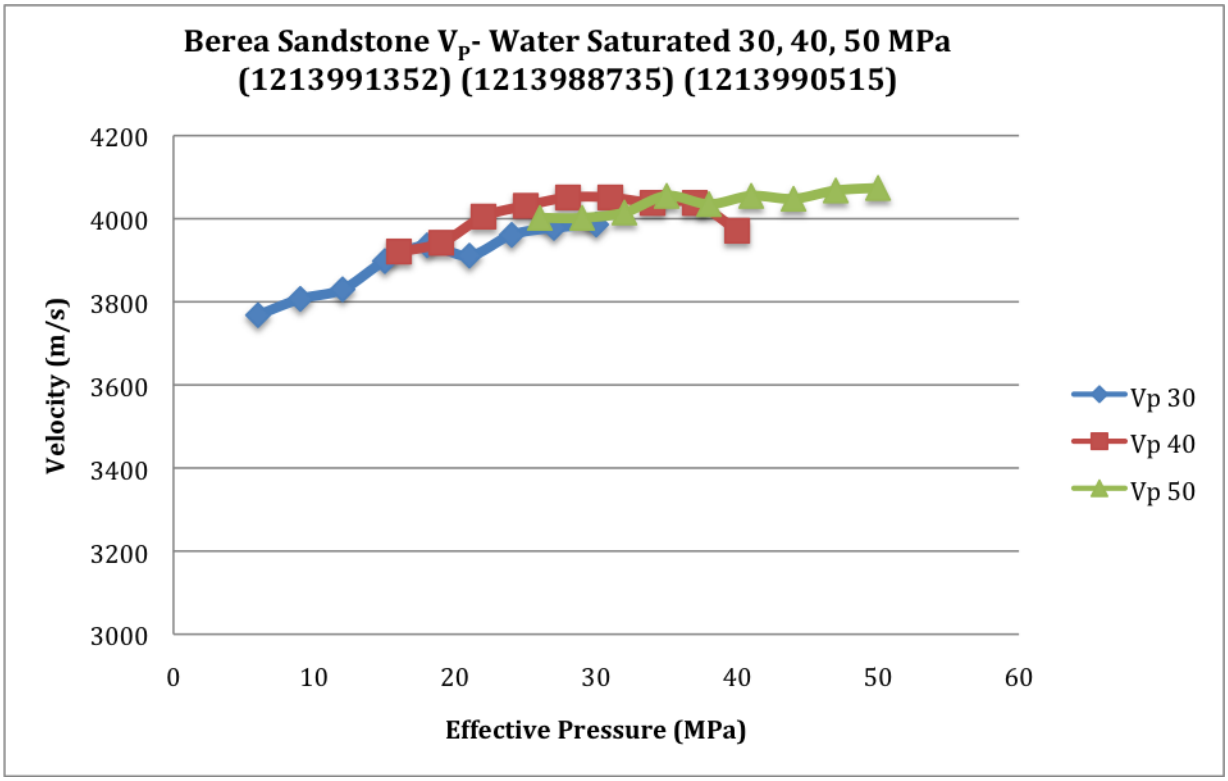

Figure 11 Berea Water Saturated V_P Comparison, V_P vs. Effective Pressure

When we compare V_{S1} and V_{S2} velocities for each of the three runs, we see a similar trend of gently increasing velocities with increasing effective pressure, due to the closure of compliant porosity (Figure 12). We see a distinct difference between V_{S1} and V_{S2} above ~10 MPa, possibly due to patchy saturation due to the high pressure Argon entering the sample and displacing some of the water. The patchy saturation of the Water/Argon is aligned with the V_{S2} transducer direction, causing a higher velocity to be recorded compared to the V_{S1} transducer.

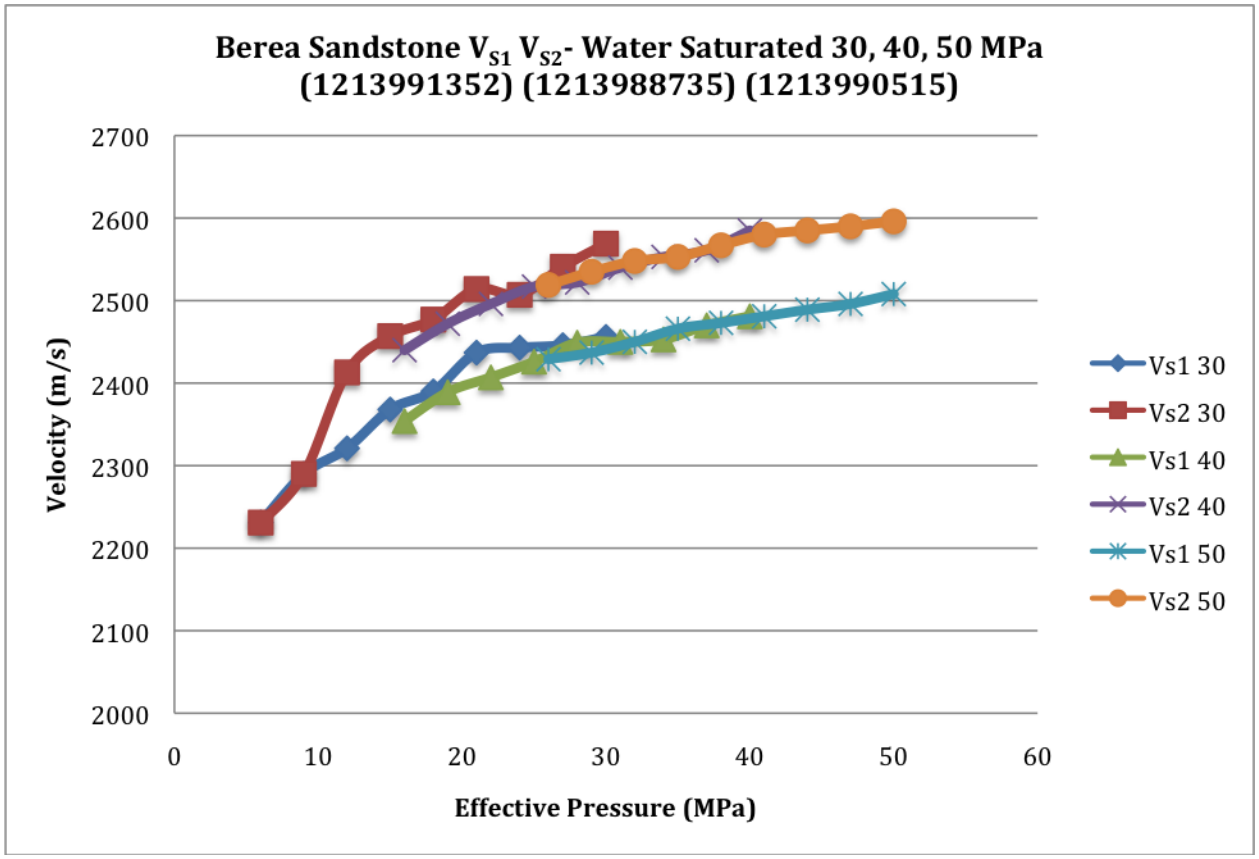

Figure 12 Berea Water Saturated V_S Comparison, Velocity vs. Effective Pressure

The next set of experiments conducted was to pressurize the pore space with CO_2 to see what effect it would have on the measured ultrasonic velocities. The samples were cut, dried, weighed, and then loaded into the core holder assembly. A given confining pressure was applied, and then the intensifier piston was pressurized with CO_2 and opened to the sample. In order to pressurize beyond the tank pressure, the sample was closed off, the intensifier re-pressurized, and then opened up to the sample. This process was repeated as many times as necessary to reach the required pore pressure.

The first experiment performed was done at a confining pressure of 30 MPa, and the pore pressure of the CO_2 was varied from 6-21 MPa. As can be seen, V_P decreases with increasing

pore pressure (Figure 13). The drop in V_P from 6 to 21 MPa is 7.7%. In addition, V_{S1} and V_{S2} also decrease with increasing pore pressure. V_{S1} decreases by 8.3%, and V_{S2} decreases by 7.7% over the range of 6 to 21 MPa.

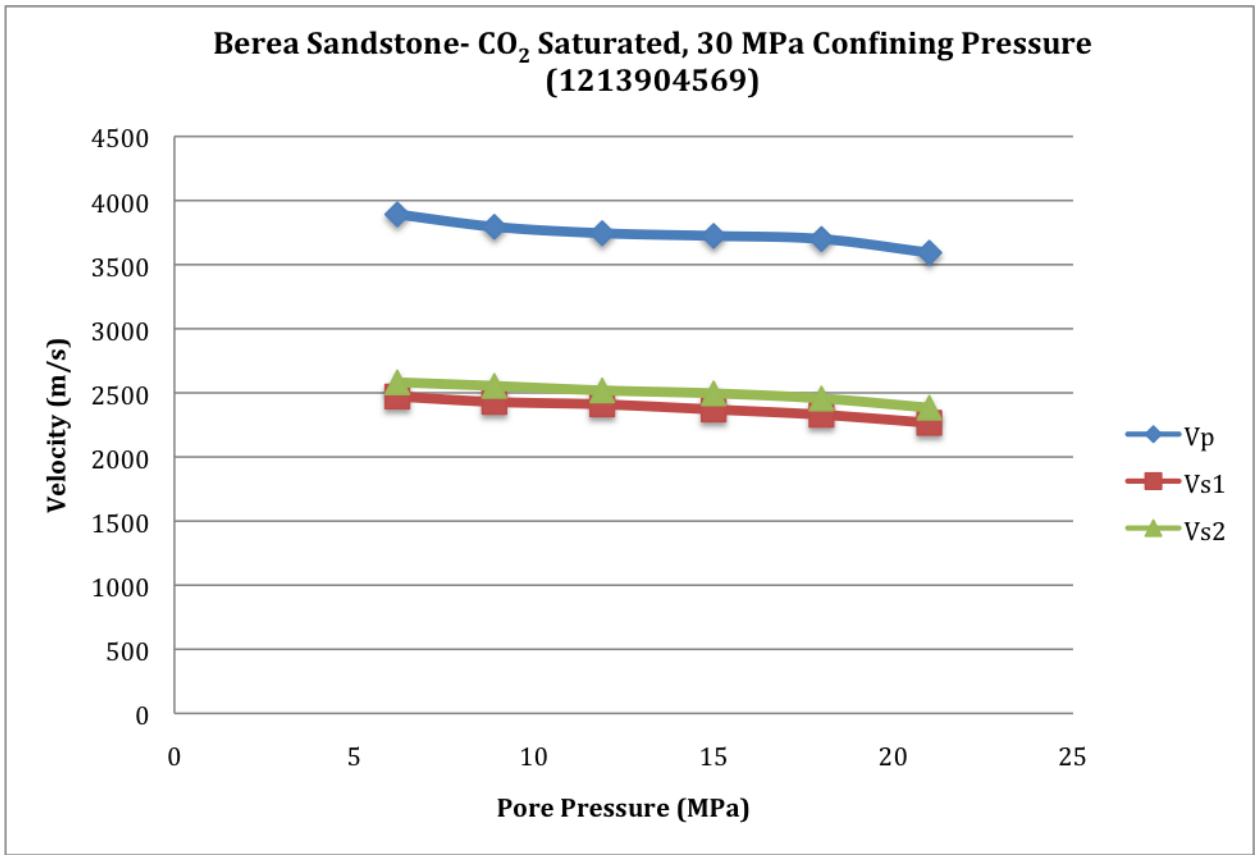

Figure 13 Berea CO_2 Saturated 30 MPa Confining Pressure, Velocity vs. Pore Pressure

The next experiment was to set the confining pressure at 40 MPa and then to vary the pore pressure. The pore pressure was varied from 3 to 30 MPa while the confining pressure was held constant. As in the experiment above, there was a constant decrease in V_P, V_{S1} and V_{S2} velocity with increasing pore pressure. V_P decreased by 6.8% from 3 to 30 MPa, V_{S1} decreased by 10.8%, and V_{S2} decreased by 9.5% over the same interval (Figure 14).

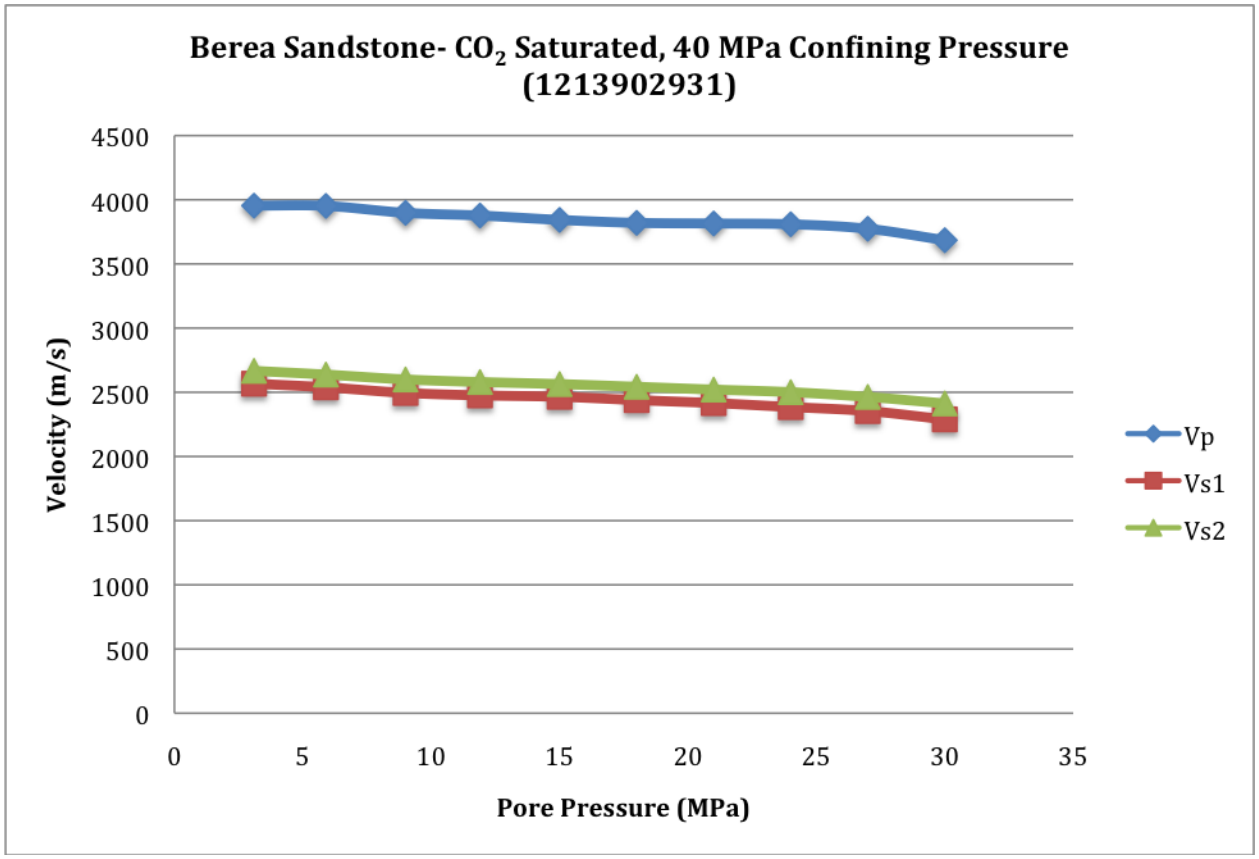

Figure 14 Berea CO_2 Saturated 40 MPa Confining Pressure, Velocity vs. Pore Pressure

Finally, we set the confining pressure at 50 MPa and varied the pore pressure of CO_2 from 6 to 36 MPa. As in the two earlier experiments, there was a constant decrease in V_P and V_S velocities. V_P dropped 5.4 % as the pressure was ramped up. V_{S1} decreased by 7.7% and V_{S2} decreased by 7.0% as the pressure was increased from 6 to 36 MPa (Figure 15).

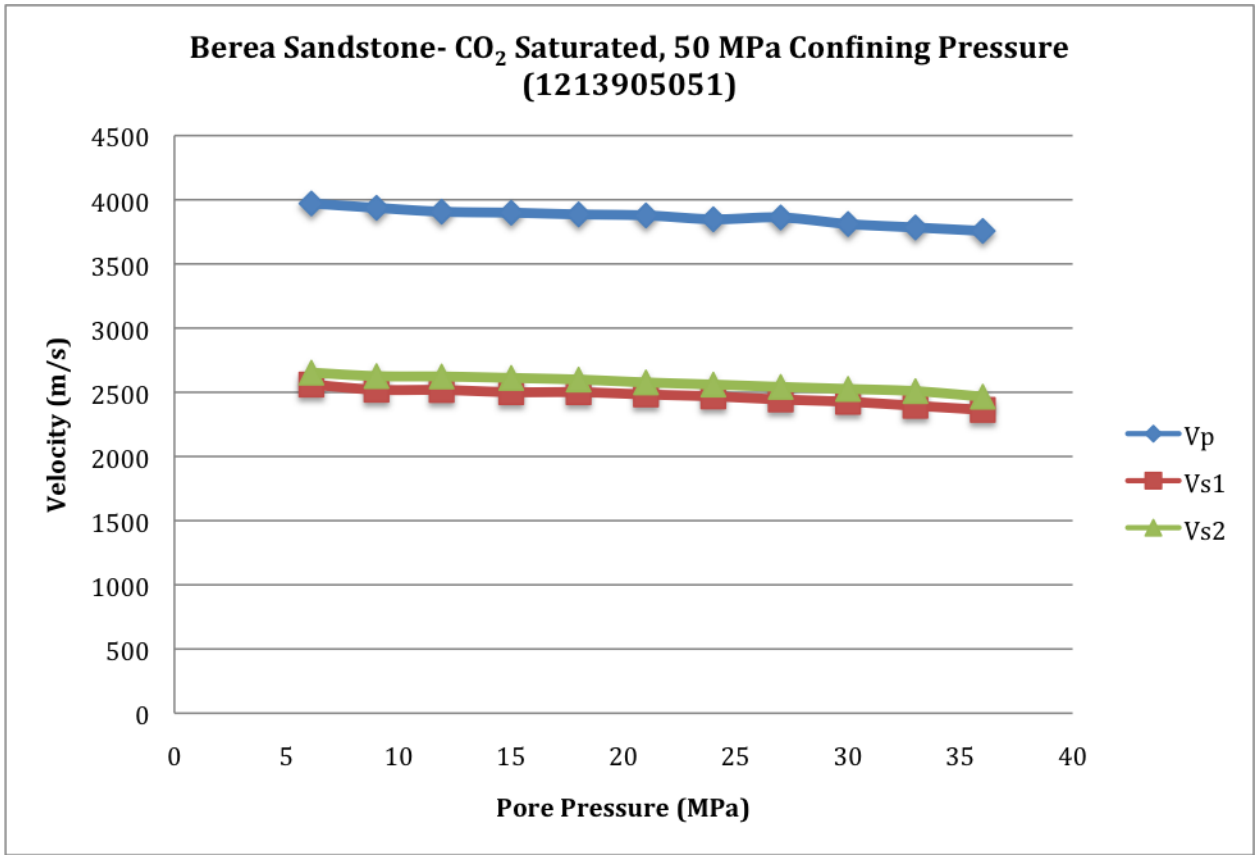

Figure 15 Berea CO_2 Saturated 50 MPa Confining Pressure, Velocity vs. Pore Pressure

If we compare the 30 MPa, 40 MPa and 50 MPa confining pressure experimental runs to one another, we notice some distinct patterns (Figure 16 and Figure 17). With increasing effective pressure (decreasing confining pressure), we can see a steady increase in the velocity of V_P, V_{S1} and V_{S2}. V_{S1} and V_{S2} follow the same general trend, but the V_{S2} velocity is ~4% higher over the whole pressure range (Figure 17). This is most likely due to the orientation of the shear wave transducers, which are placed 90° apart from one another. The discrepancy in shear velocities is likely due to fluid effects, since they are not seen in other experiments. Pore space heterogeneities would account for differing fluid dispersion effects on the shear wave velocities.

When the compressional P-wave velocities of our CO_2 and water saturated samples of Berea Sandstone are compared, for each saturating fluid we see the same general increasing trend in all three confining pressure states (Figure 16). Second, at a given effective pressure, for a given saturating pore phase, that the confining pressure seems to have little bearing on the velocity. At a given effective pressure for either water or CO_2, there is a spread of values of around 50 m/s for the different confining pressure states.

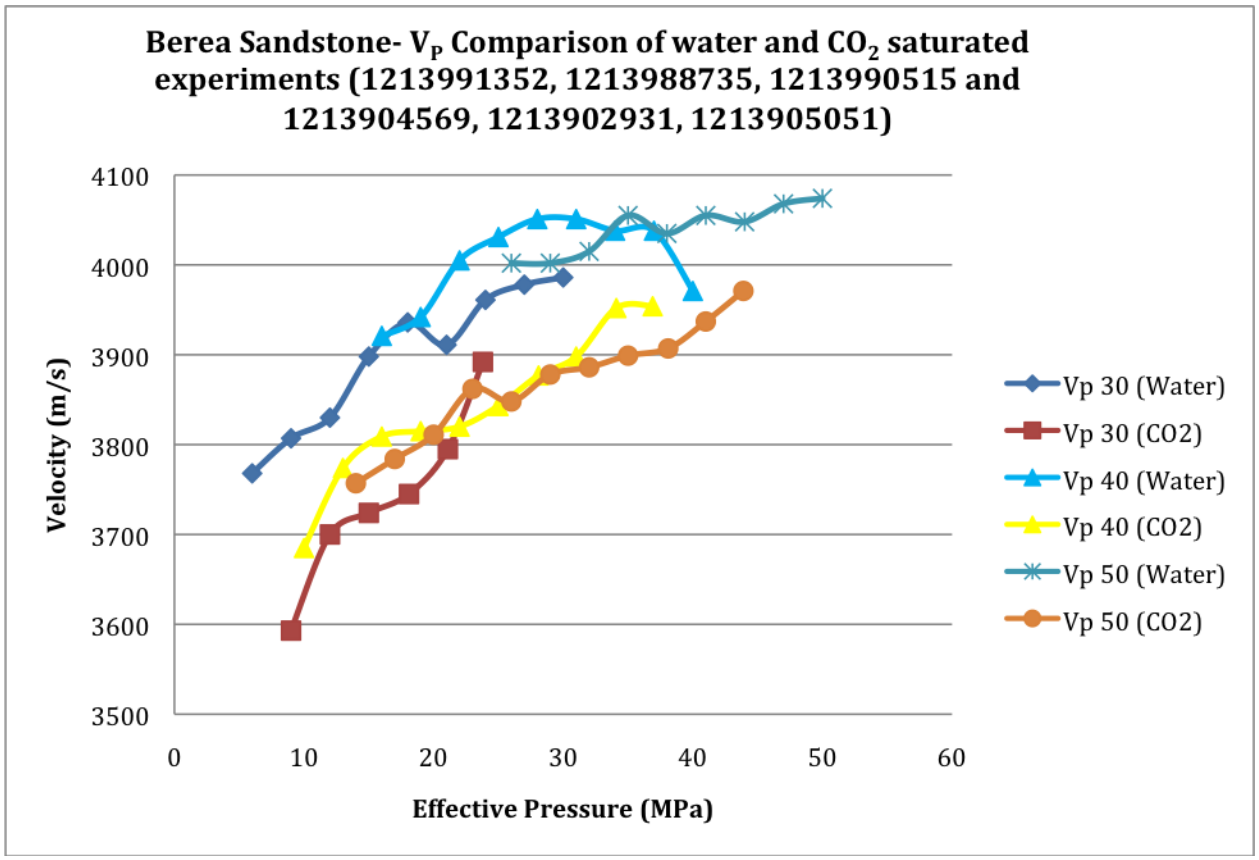

Figure 16 V_P Comparison of Water and CO_2 Saturated Berea, V_P vs. Effective Pressure

However, there is no clear pattern of which confining pressure state produces the highest velocity at a given effective pressure. The reason for this is unclear, but larger confining

pressures could have an effect of the closure of the microporosity, slightly changing the bulk modulus of the sample.

The main result of this comparison is that CO_2 produces lower velocities at a given effective pressure than tap water does. This difference is on the order of ~100 m/s, which corresponds to a 3-4% change in the P-Wave velocity. A change of this magnitude should be detectible in a 4D seismic reflection survey.

If we compare the shear wave velocities from the CO_2 and Water saturated experiments, we see a different situation. CO_2 saturated experiments show an increase in shear velocity over water saturated samples, which increases as the effective pressure becomes larger. At lower effective pressures, there is very little difference between CO_2 and water saturated velocities.

In addition, V_{S2} velocities are consistently higher than V_{S1} velocities, but follow the same pattern of increasing velocity. This is explained by a non-homogenous distribution of porespace in our sample, or possibly by a distribution of fractures or layers in the sample.

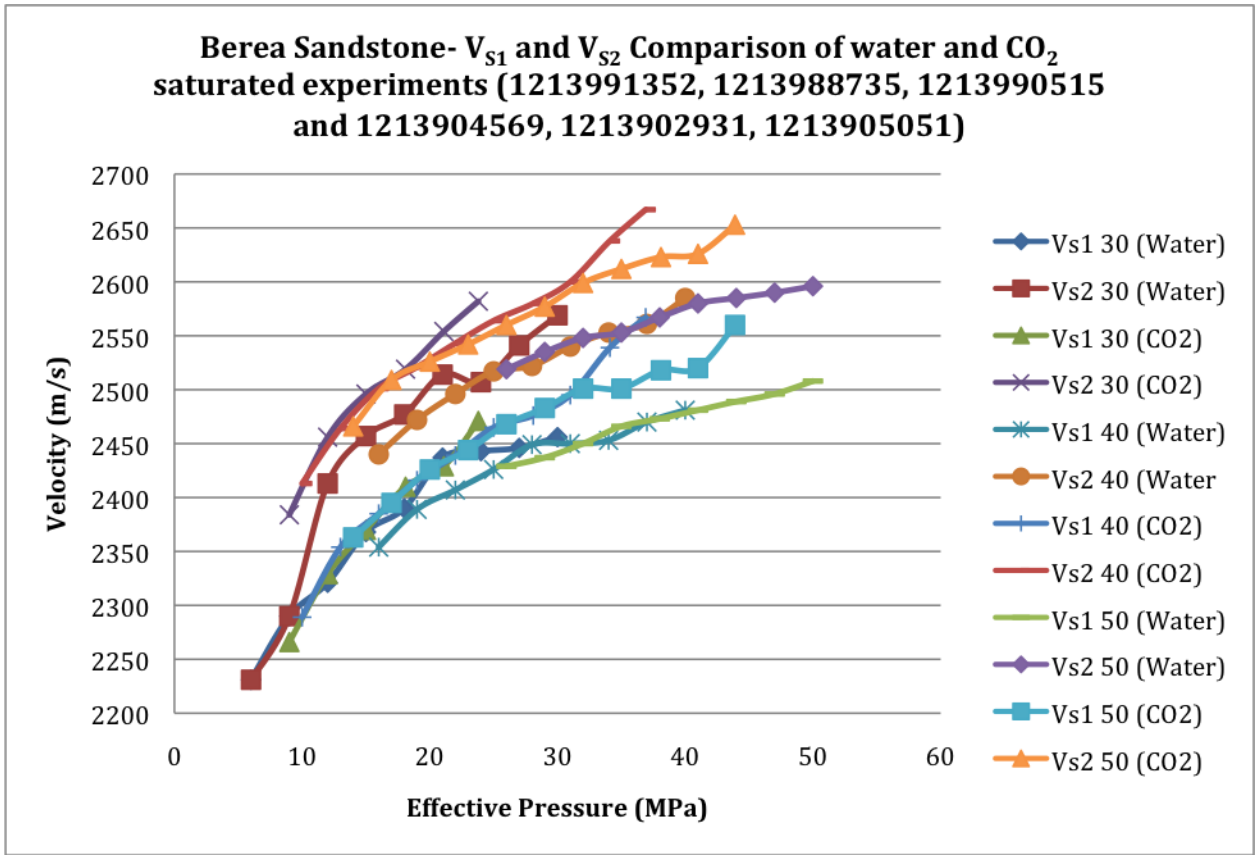

Figure 17 V_S Comparison of Water and CO_2 Saturated Berea, Shear Velocity vs. Effective Pressure

1.2.3 Limestone #1 Core Rock Physics Experiments

Next, we performed a set of experiments on core material obtained from the Limestone #1 unit. We took a 2 inch diameter core from a section of rock corresponding to a depth of ~6500 ft. The core was drilled, cut, and dried before being loaded into the AutoLab. The core, known as Limestone #1, had a diameter of 50.15 mm and a length of 72.35 mm. It had a measured bulk density of 2.20 g/cm^3 and a measured porosity of 18.5%.

The first experiment consisted of increasing the confining pressure with no pore-filling phase. We increased the confining pressure from 0.1 MPa to 51 MPa in increments of 3 MPa. As can be seen, V_P increased over the whole range of values, and V_{S1} and V_{S2} increased slowly up to about 30 MPa before leveling off. From 0.1 to 51 MPa, V_P increased by 2,566 m/s, an increase of 83.1%. V_{S1} increased by 1,045 m/s, or 56.6%, and V_{S2} increased by 946 m/s, or 49.2% (Figure 18).

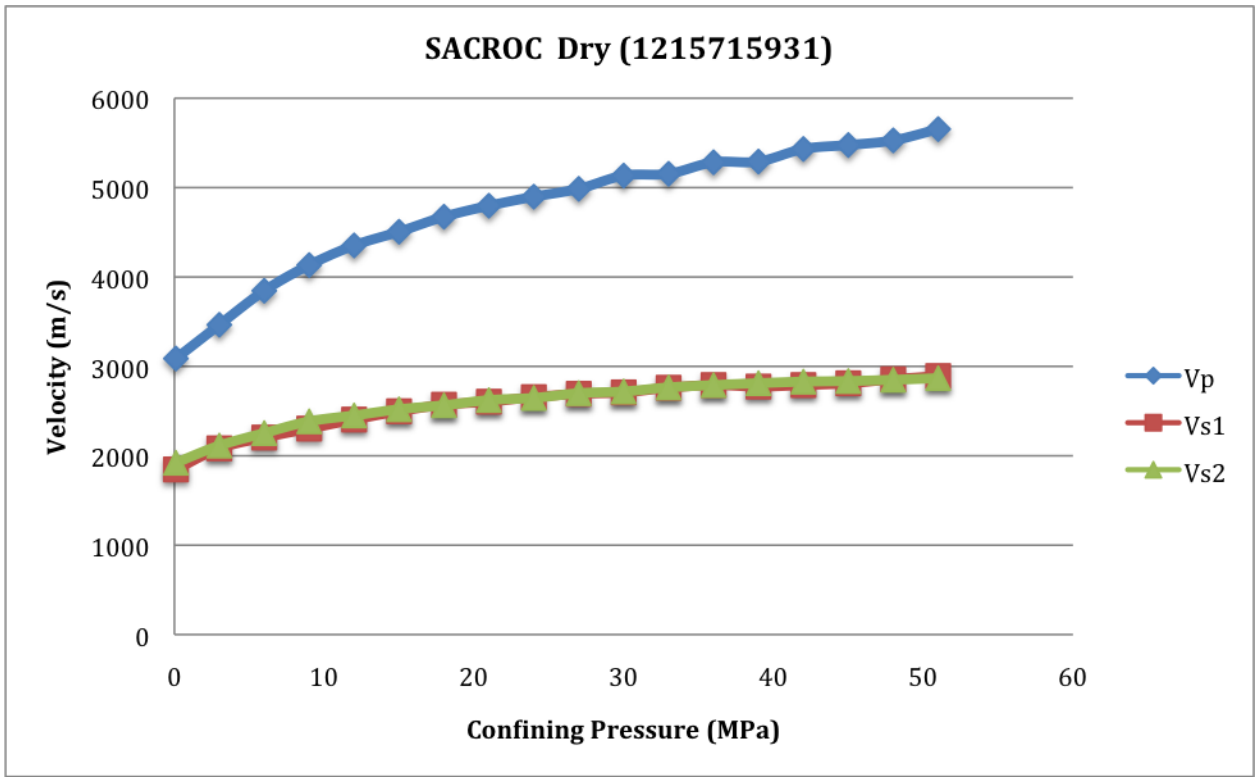

Figure 18 Limestone #1 Dry, Velocity vs. Confining Pressure

In the next set of experiments, the pore space was filled with CO_2 using the same procedure as with the Berea Sandstone. First, we held the confining pressure constant at 30 MPa and varied the pore pressure from 3-24 MPa, in increments of 3 MPa. The velocity decreases steadily with increasing pore pressure. V_P decreases by 18% as the pore pressure of CO_2 increases from 3 to

24 MPa. V_{S1} and V_{S2} decrease by 15.4% and 12.8% respectively over the same interval (Figure 19).

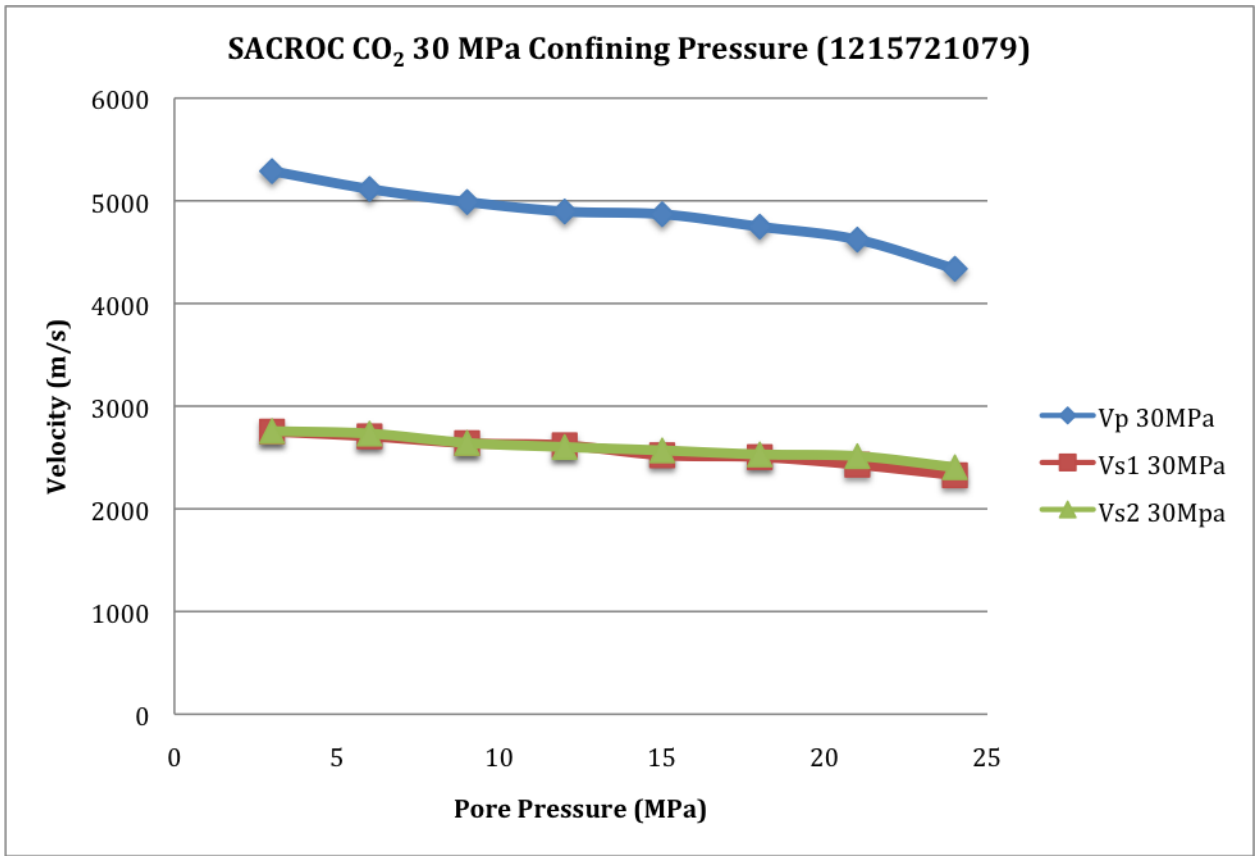

Figure 19 Limestone #1 CO_2 Saturated 30 MPa Confining Pressure, Velocity vs. Pore Pressure

Next, the confining pressure was held constant at 40 MPa while the pore pressure was varied from 6 to 30 MPa. Again, we see a constant decrease of V_P, V_{S1} and V_{S2} with increasing pore pressure. As the pore pressure was increased from 6 to 30 MPa, V_P decreased by 10.9%, V_{S1} decreased by 11.6%, and V_{S2} decreased by 8.5% (Figure 20).

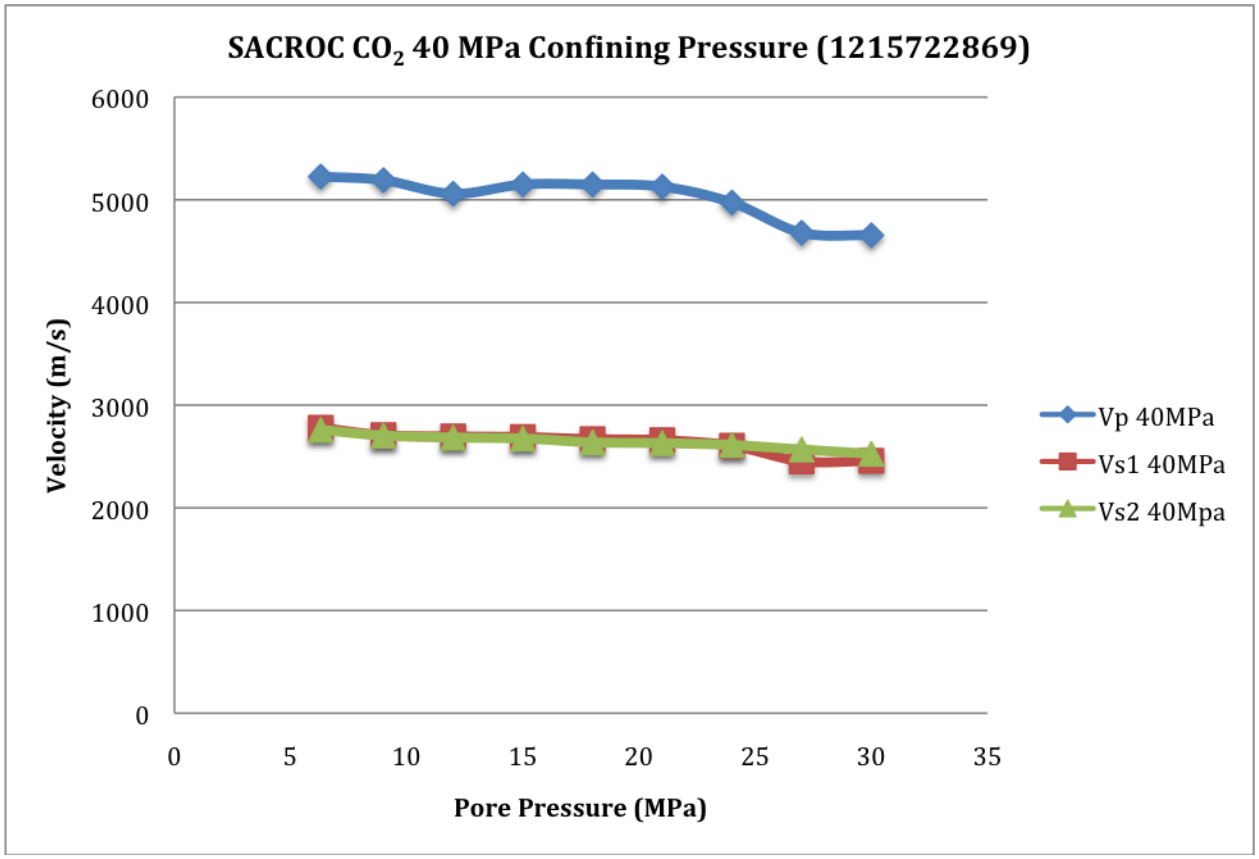

Figure 20 Limestone #1 CO_2 Saturated 40 MPa Confining Pressure, Velocity vs. Pore Pressure

Finally, the confining pressure was held at 50 MPa, and the pore pressure of CO_2 was varied from 6 to 30 MPa. As with the other two experiments, V_P, V_{S1} and V_{S2} all steadily decreased as the pore pressure was increased. V_P decreased by 5.7% as the pore pressure went from 6 to 30 MPa, V_{S1} decreased by 5.5%, and V_{S2} decreased by 4.1% (Figure 21).

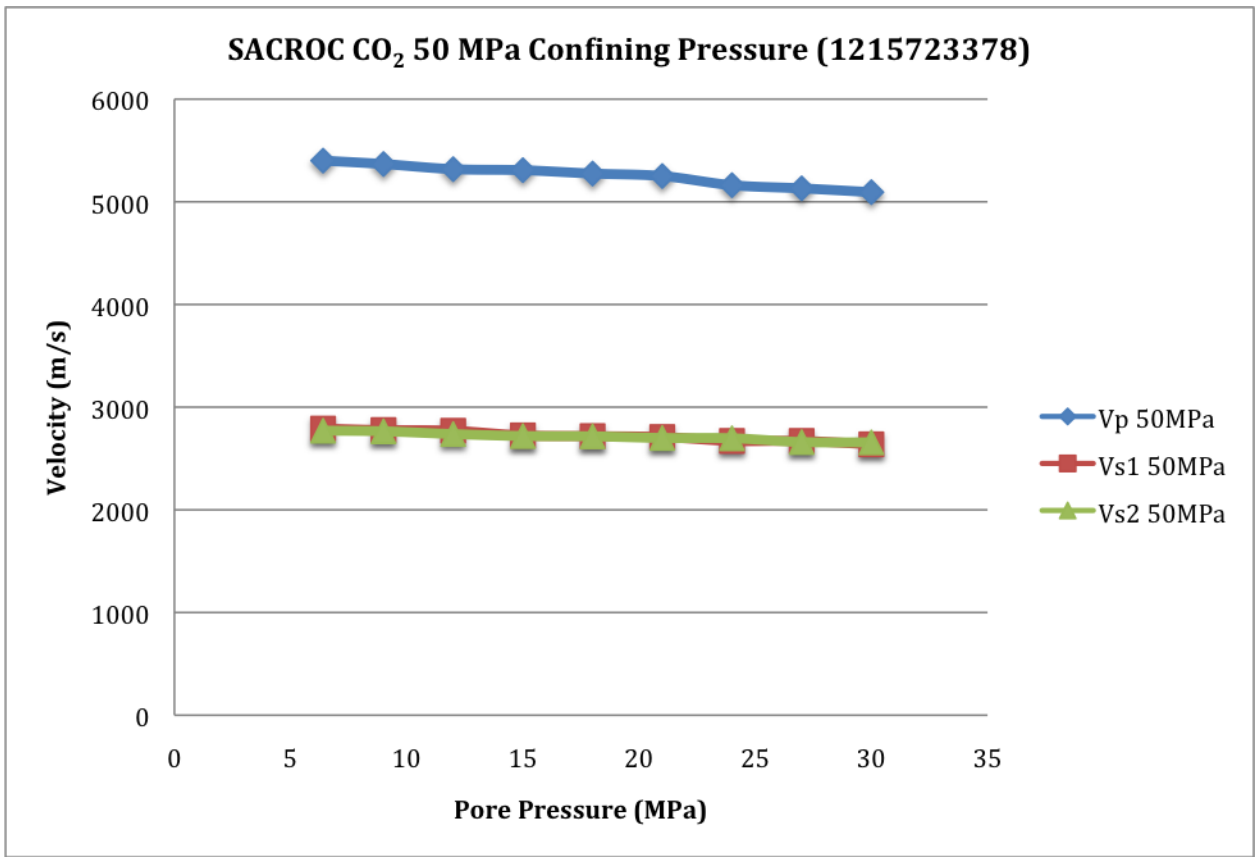

Figure 21 Limestone #1 CO_2 Saturated 50 MPa Confining Pressure, Velocity vs. Pore Pressure

We then compare V_P velocities from each of the three CO_2 saturated Limestone #1 experiments. When we compare the V_P velocities using Effective Pressure (Figure 22), we see that the three experimental runs overlap one another. The lowest velocities are found for the lowest effective pressure, and increasing the effective pressure increases the velocity. It is not a steady increase; from 3 to ~20 MPa it rises quickly, and above ~30 MPa the values begin to level off. The reason this occurs is due to the CO_2 propping the compliant porosity open at low effective pressure, which corresponds to a high pore pressure.

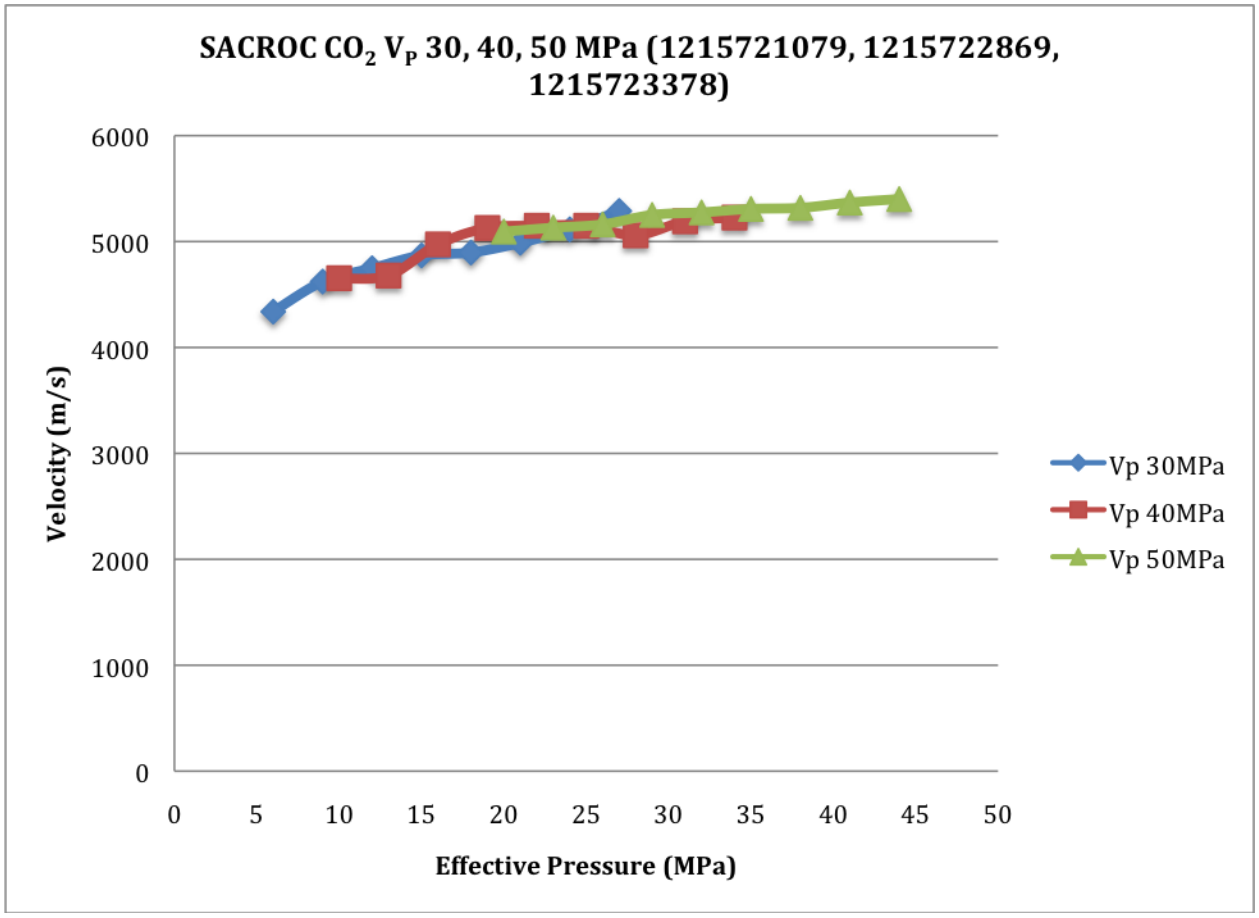

Figure 22 Limestone #1 CO_2 Saturated V_P Comparison, Velocity vs. Effective Pressure

When we compare V_{S1} and V_{S2} velocities from all three experiments, we see a similar rise in velocity with increasing Effective Pressure (Figure 23).

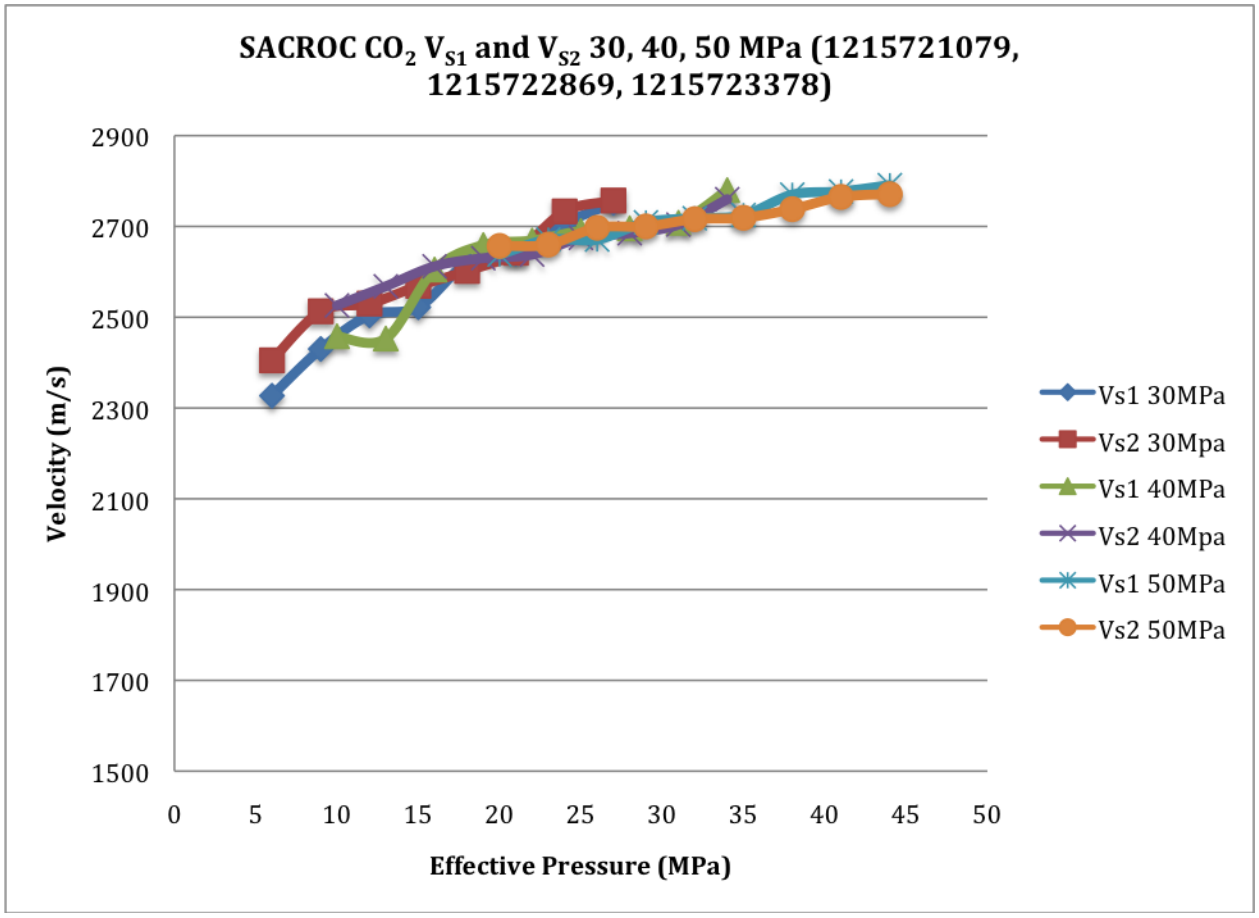

Figure 23 Limestone #1 CO_2 Saturated V_S Comparison, Velocity vs. Effective Pressure

1.2.4 Hysteresis Experiments

In order to discover whether the Limestone #1 shows any path dependent elastic hysteresis, various experiments were performed. The first hysteresis experiment was performed at room temperature with a dry sample of Limestone #1. The pressure was increased in 1 MPa increments from 3 to 50 MPa, and then from 50 to 4 MPa. We waited five minutes between each measurement for the sample to equilibrate with the pressure of the confining fluid.

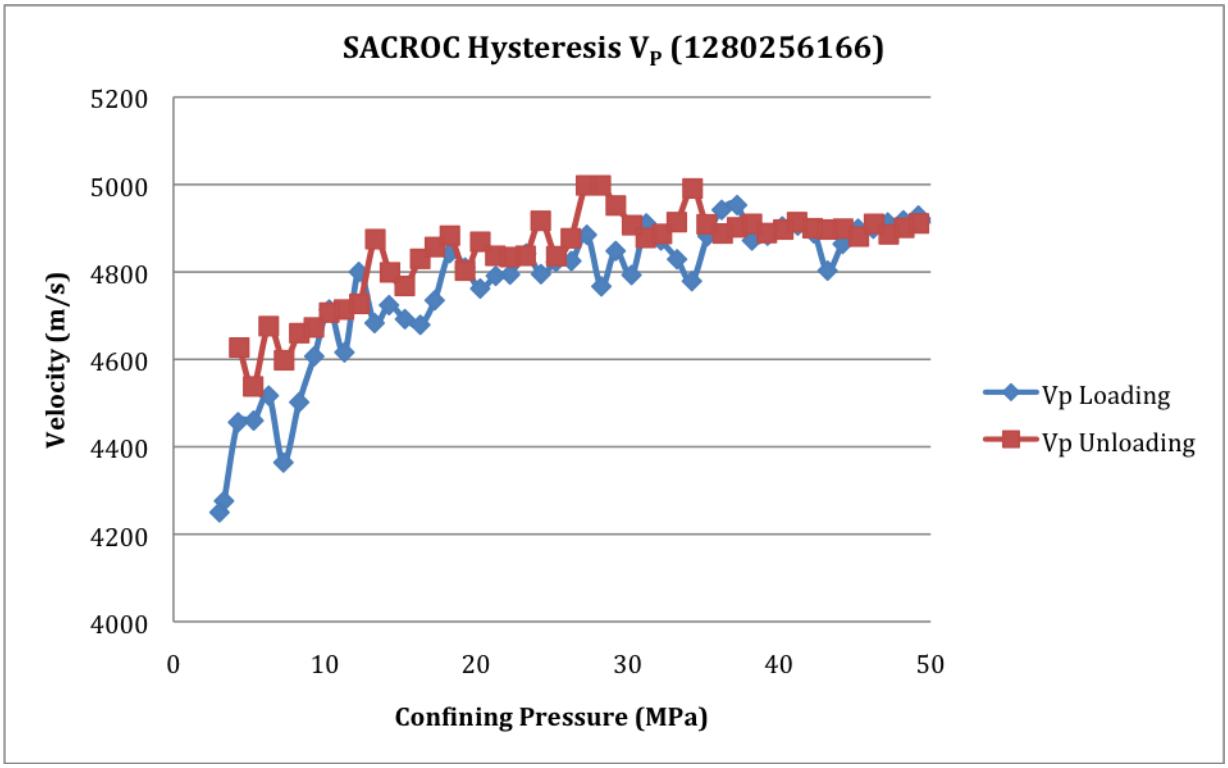

Figure 24 Limestone #1 Hysteresis V_P, Velocity vs. Confining Pressure

By comparing the loading and unloading paths of confining pressure versus velocity, we can see if the rock has sufficient time to relax back to its baseline stress state, or if there is a lingering effect of pressurization on the velocity. Looking at the V_P paths, we can see a difference between the loading and unloading curves (Figure 24). The unloading curve exhibits a higher velocity than the loading curve, especially below ~30 MPa confining pressure. While there are some pressures where the loading path velocity is higher than the unloading path velocity, this is most likely due to experimental error in picking the first arrivals of the waveform.

For V_{S1} and V_{S2}, the unloading curve velocities are also higher than the loading velocities, and the differences are larger below ~30 MPa. For V_P, V_{S1} and V_{S2}, we see the characteristic closure of microcracks that lead to an increase of velocity (Figure 25 and Figure 26).

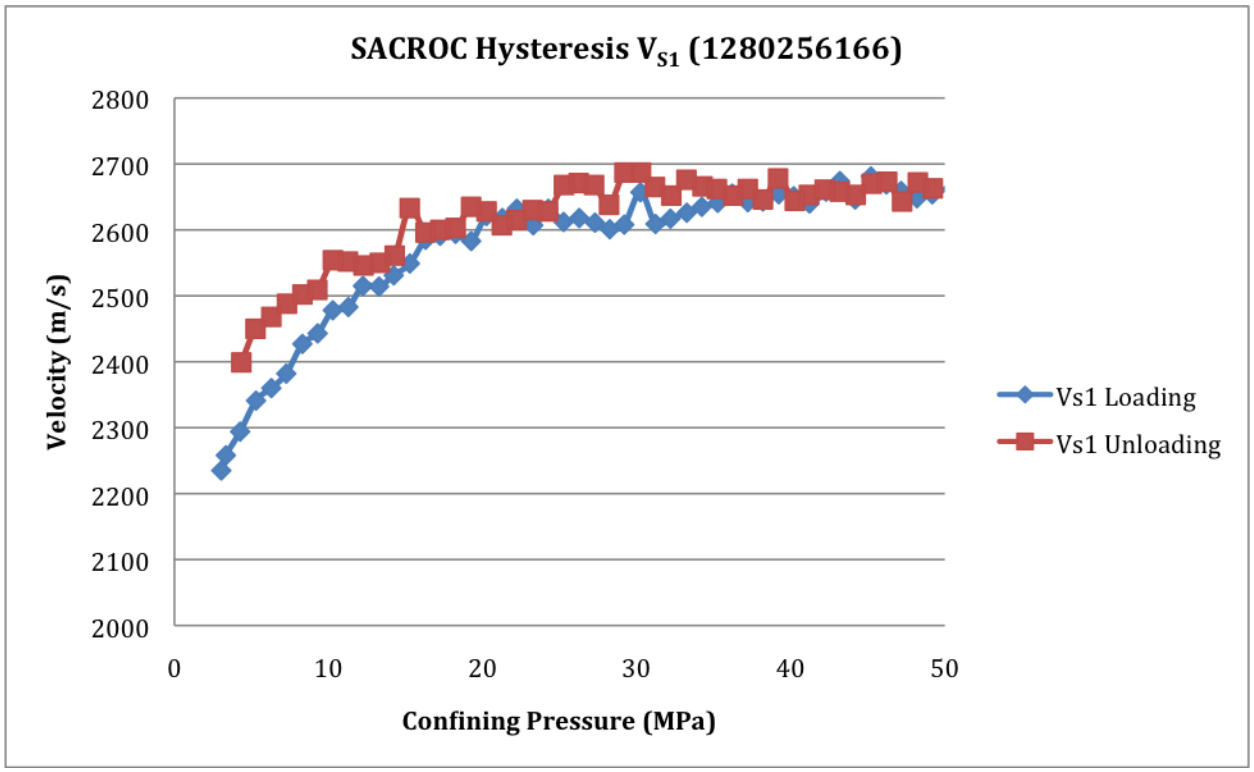

Figure 25 Limestone #1 Hysteresis V_{S1}, Velocity vs. Confining Pressure

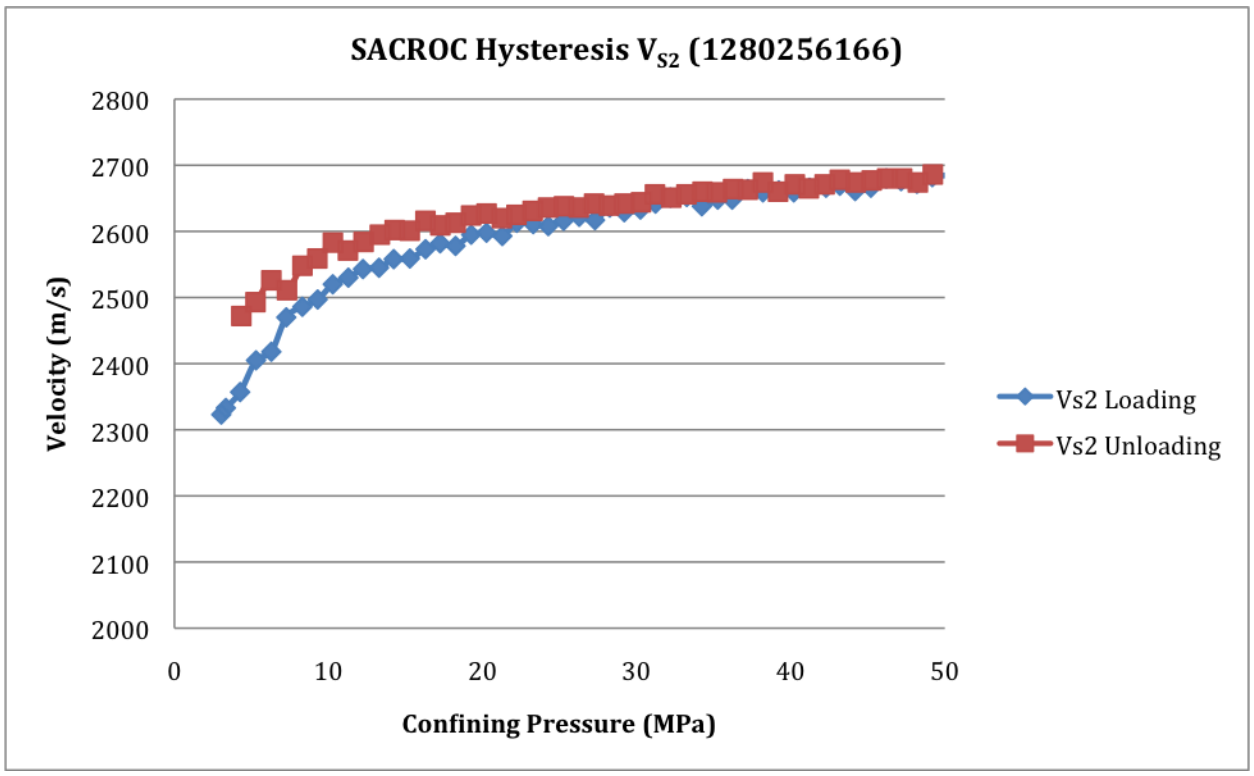

Figure 26 Limestone #1 Hysteresis V_{S2}, Velocity vs. Confining Pressure

We can quantify the difference between the loading and unloading curves by subtracting the loading velocities from the unloading velocities, to get the difference in m/s. The velocity difference at low confining pressures is ~100 m/s for V_{S1} and V_{S2}, and ~150 m/s for V_P (Figure 27). As the pressure increases, the difference decreases, reaching zero by ~25 MPa . There is a large spread in the V_P differences, most likely due to the larger errors in picking arrival times.

If we plot the difference as a percentage of the loading velocity, we can see that the unloading velocities are ~4-5% higher at low pressures for V_P, V_{S1} and V_{S2} (Figure 28). The differences quickly decrease with increasing confining pressure and drop below 1% only past ~20 MPa.

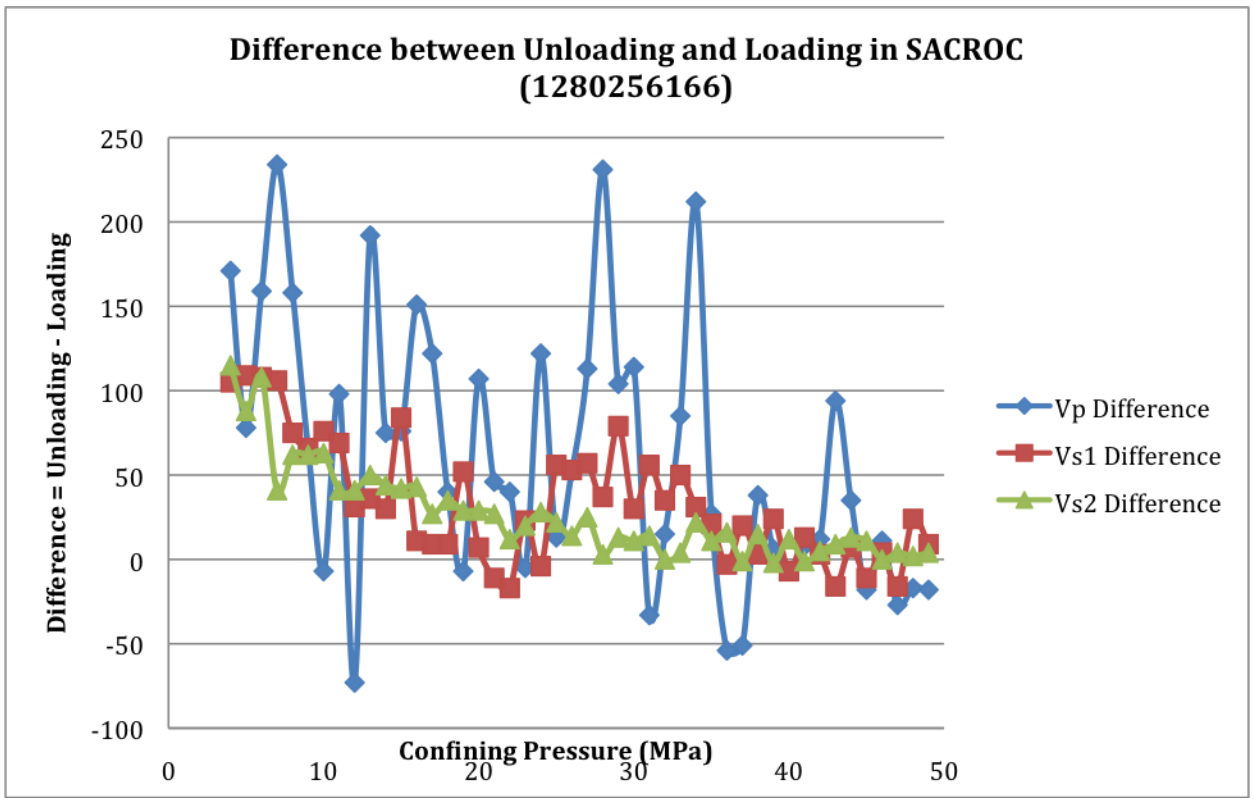

Figure 27 Limestone #1 Unloading-Loading, Difference vs. Confining Pressure

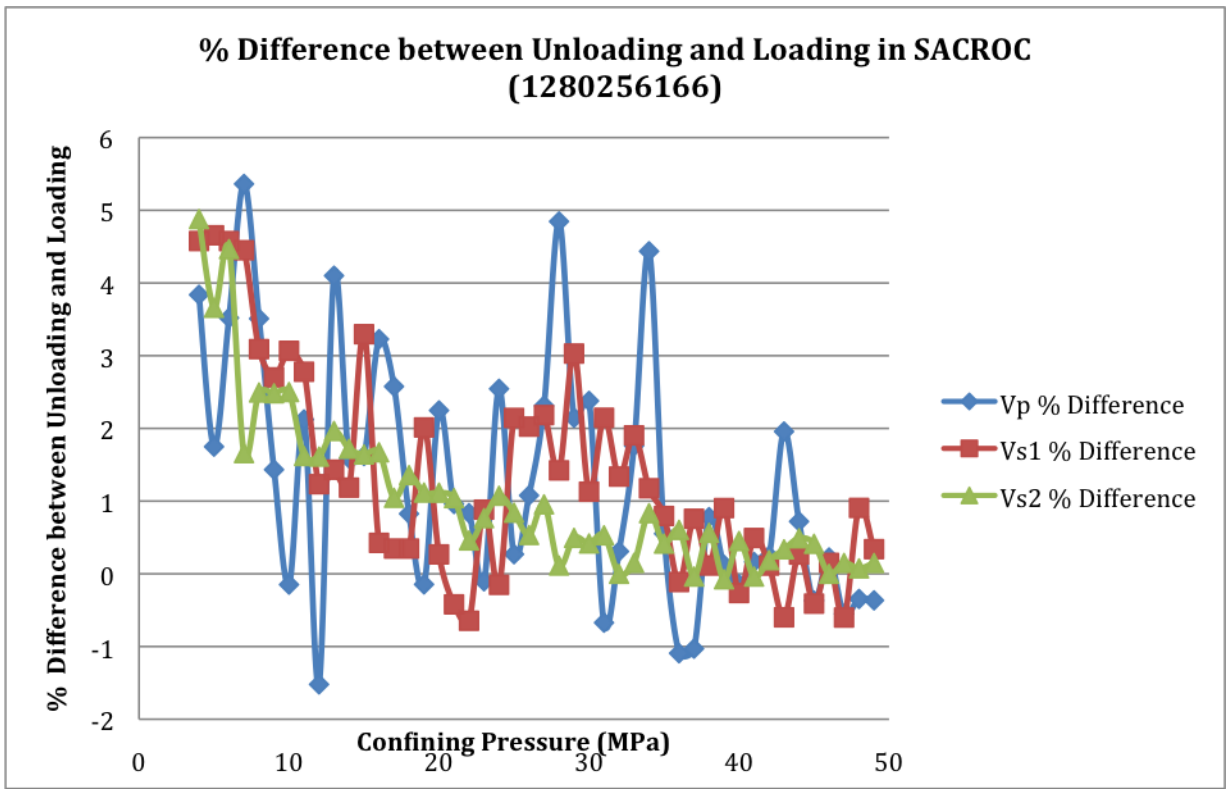

Figure 28 Limestone #1 Unloading-Loading % Difference, % vs. Confining Pressure

The reason for these differences between the loading and unloading path velocities is due to the closure of microcracks within the limestone. As the pressure increases, microcracks are closed, and expressed as an increase in the velocity of the sample. When the confining pressure is unloaded from the sample, the cracks begin to open, however, this is not an instantaneous process. Even with 5 minutes between measurements, we still saw velocity differences of up to 5% between the loading and unloading paths. The rate at which these cracks close is not known, although future experiments are planned to investigate this phenomenon.

1.2.5 Anisotropy Experiments

Seismic anisotropy is the variation of velocity with direction, and is an indicator of alignment of features that are smaller than the seismic wavelength, such as cracks, pores, or layers, leading to a directional variation in seismic velocity. Anisotropy experiments were performed on two limestone cores of widely differing porosity (6.6% vs. 18.5%). The experiments were performed by rotating the core 45° after each set of experiments. Four sets of measurements were completed at 0°, 45°, 90° and 135°, and confining pressure was varied from 5-60 MPa for each run, with no saturating fluid. Core #1, which has a porosity of 18.5%, is from a depth of 6500 ft, and Core #2, which has a porosity of 6.6%, was from a depth of 6180 ft (Figure 29).

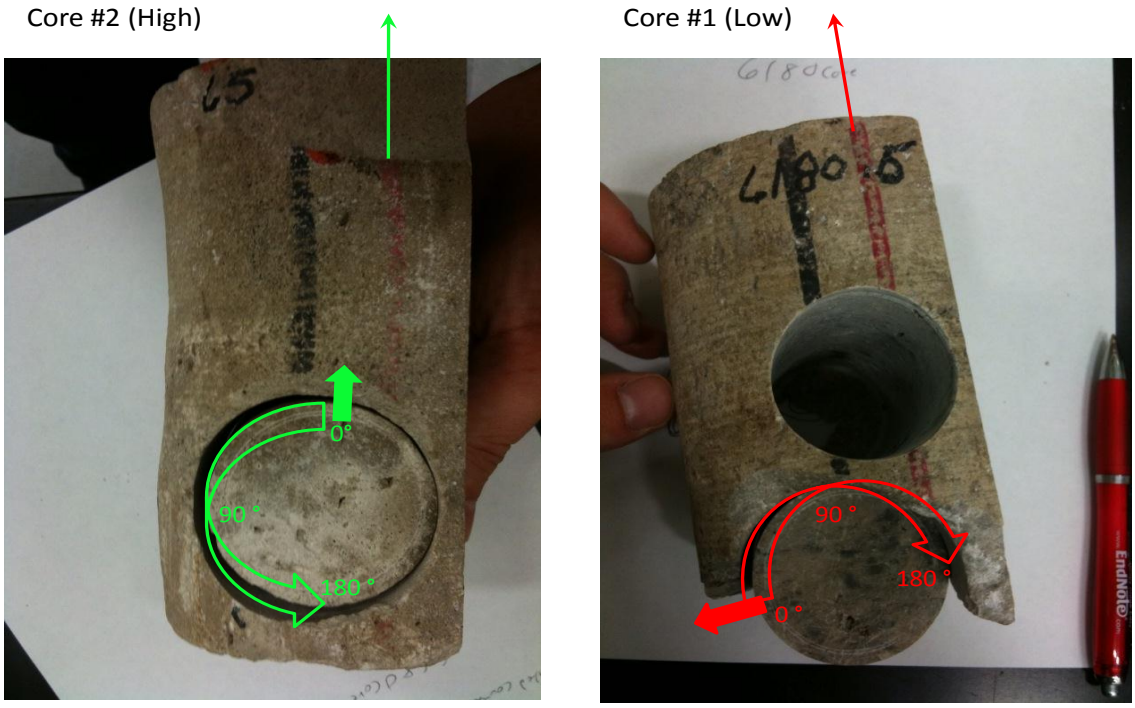

Figure 29 Core Orientation and Rotation: High Porosity Core (#2) on left, Low Porosity Core (#1) on right. Large arrows point up, small arrows show first measurement and subsequent rotation.

First, the 0°, 45°, 90° and 135° runs were plotted against one another to see if the variation was greater than experimental error. When we plot V_P vs. Confining Pressure for the low porosity core, we see that at 35, 45, and 55 MPa, there are large differences in the velocity depending on the rotation of the core (**Error! Reference source not found.**). When we look at the high porosity core, we see a smaller range of variation consistently over the pressure range (Figure 31).

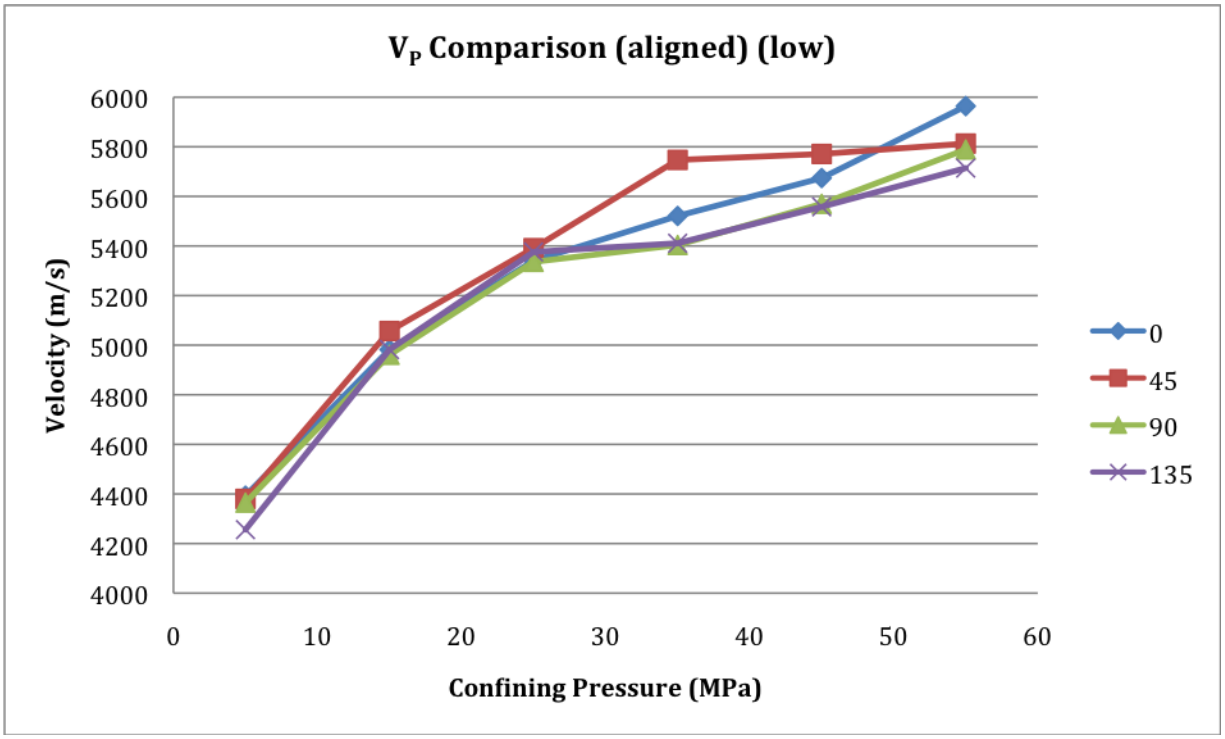

Figure 30 V_P Anisotropy Comparison (Low), Velocity vs. Confining Pressure

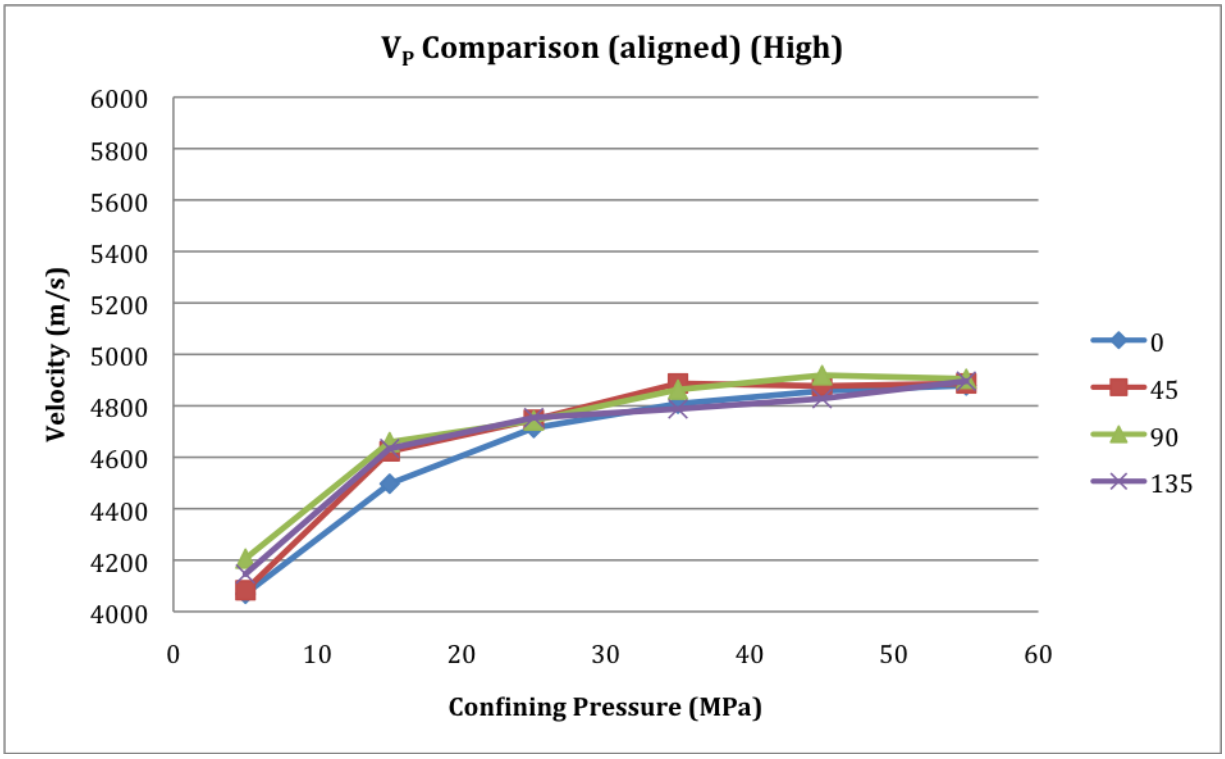

Figure 31 V_P Anisotropy Comparison (High), Velocity vs. Confining Pressure

When the V_{S1} velocities are compared, we see a similar variation to V_P: the low porosity core exhibits higher spreads of velocities at higher pressures, and the high porosity core shows a fairly consistent spread of velocities over the whole pressure range (Figure 32 and Figure 33).

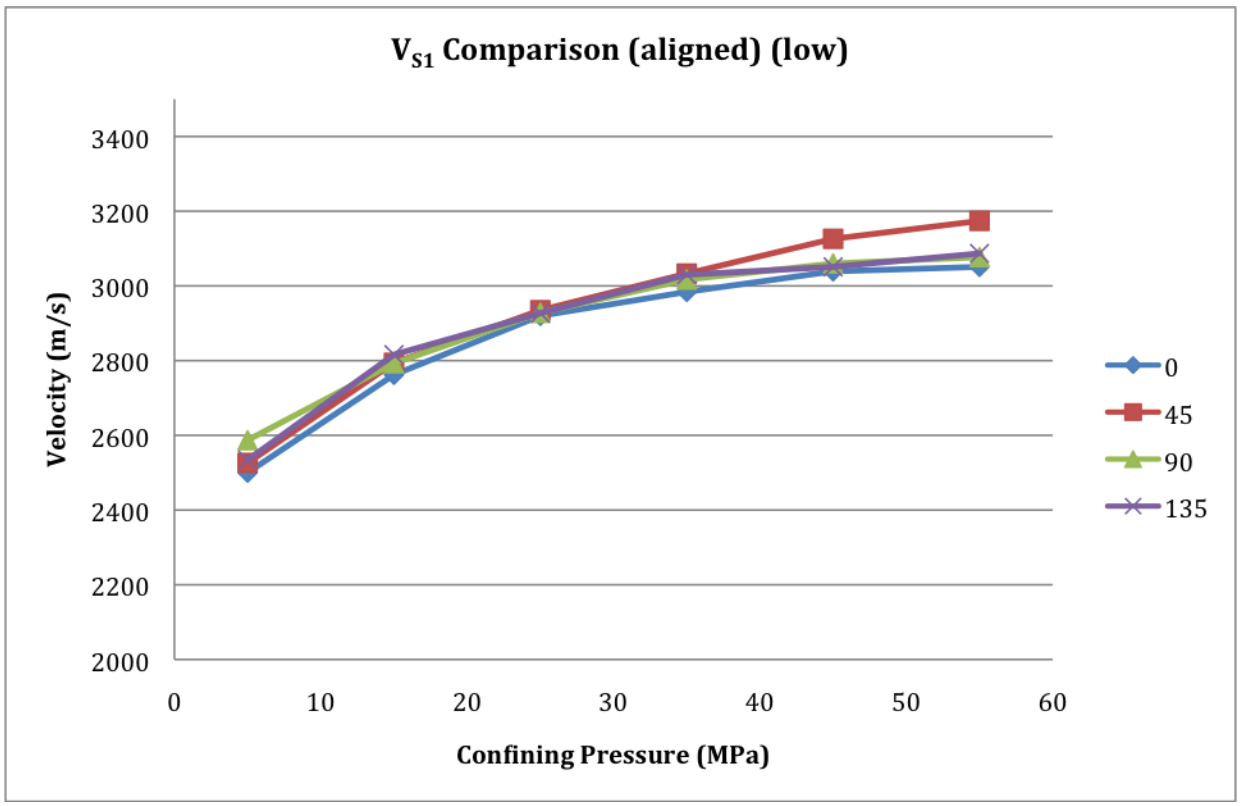

Figure 32 V_{S1} Anisotropy Comparison (Low), Velocity vs. Confining Pressure

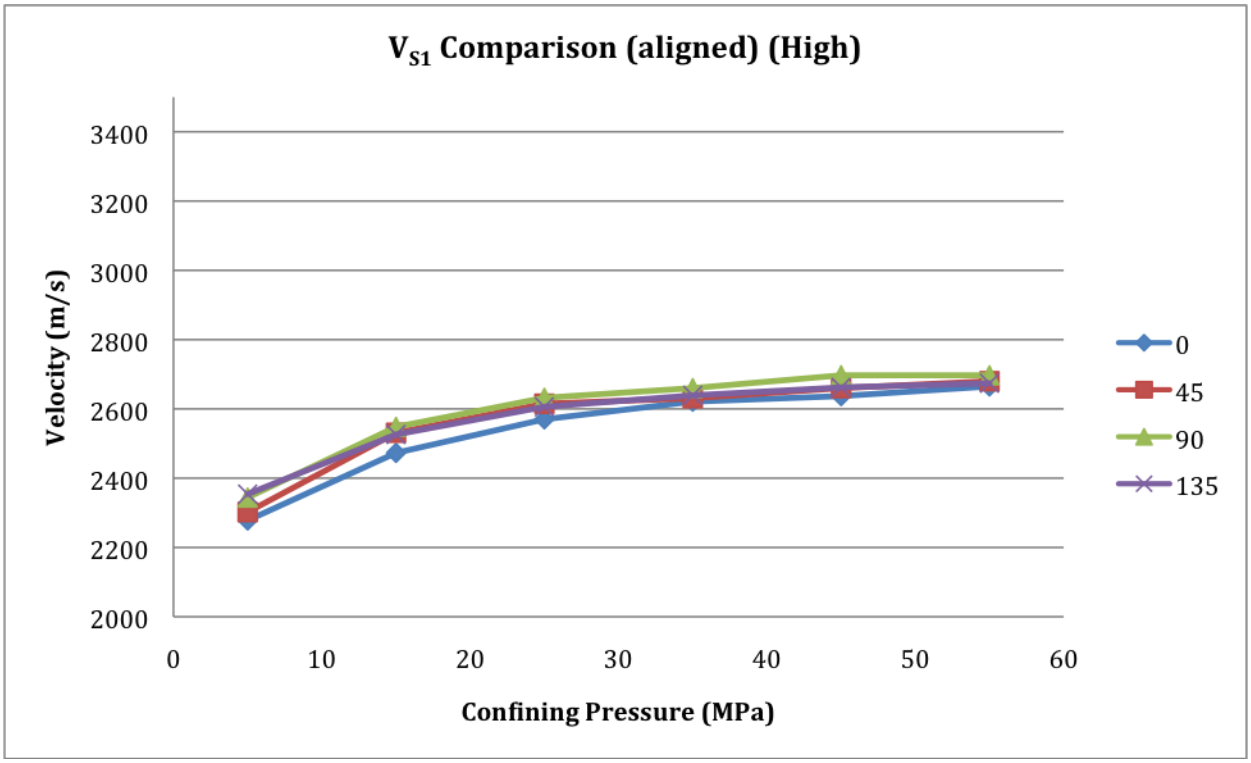

Figure 33 V_{S1} Anisotropy Comparison (High), Velocity vs. Confining Pressure

When the V_{S2} velocities are compared, differences from V_P and V_{S1} velocities are seen. Over the whole pressure range, V_{S2} shows a velocity spread of greater than 200 m/s for the low porosity core (Figure 34). For the high porosity core, the results are very similar to V_{S1}, a small spread of velocities over the whole pressure range (Figure 35).

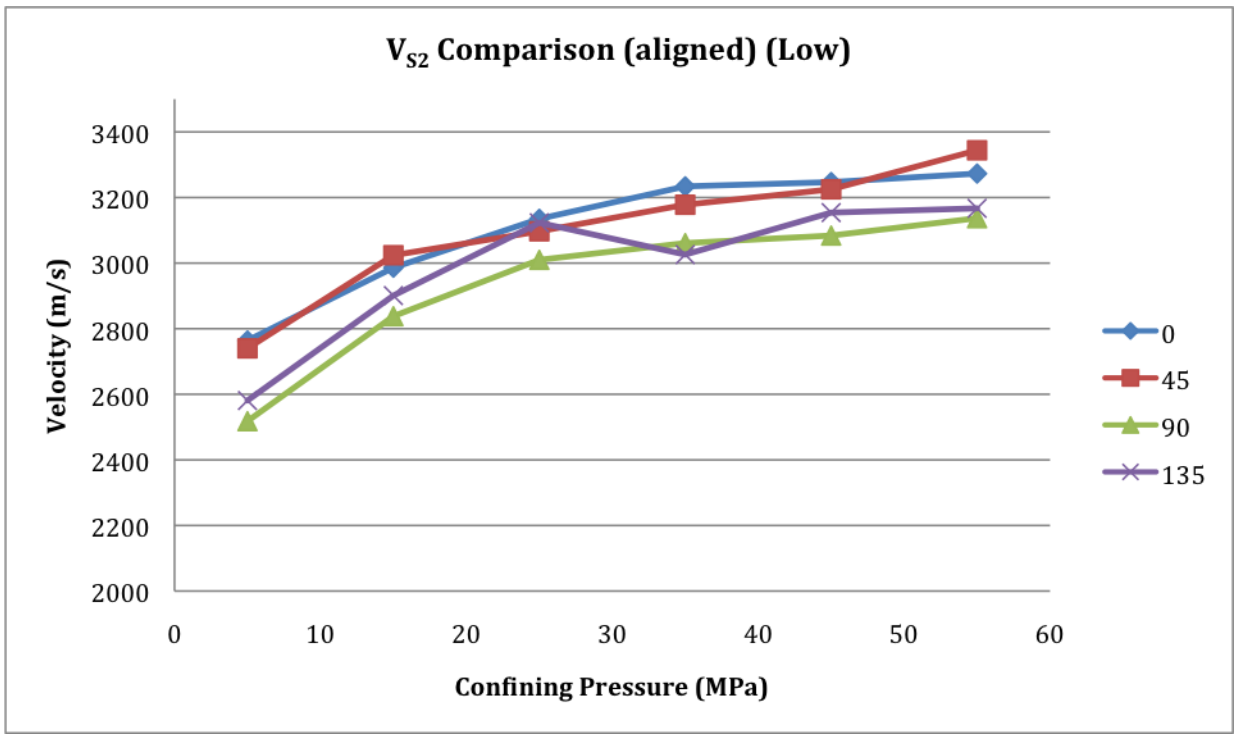

Figure 34 V_{S2} Anisotropy Comparison (Low), Velocity vs. Confining Pressure

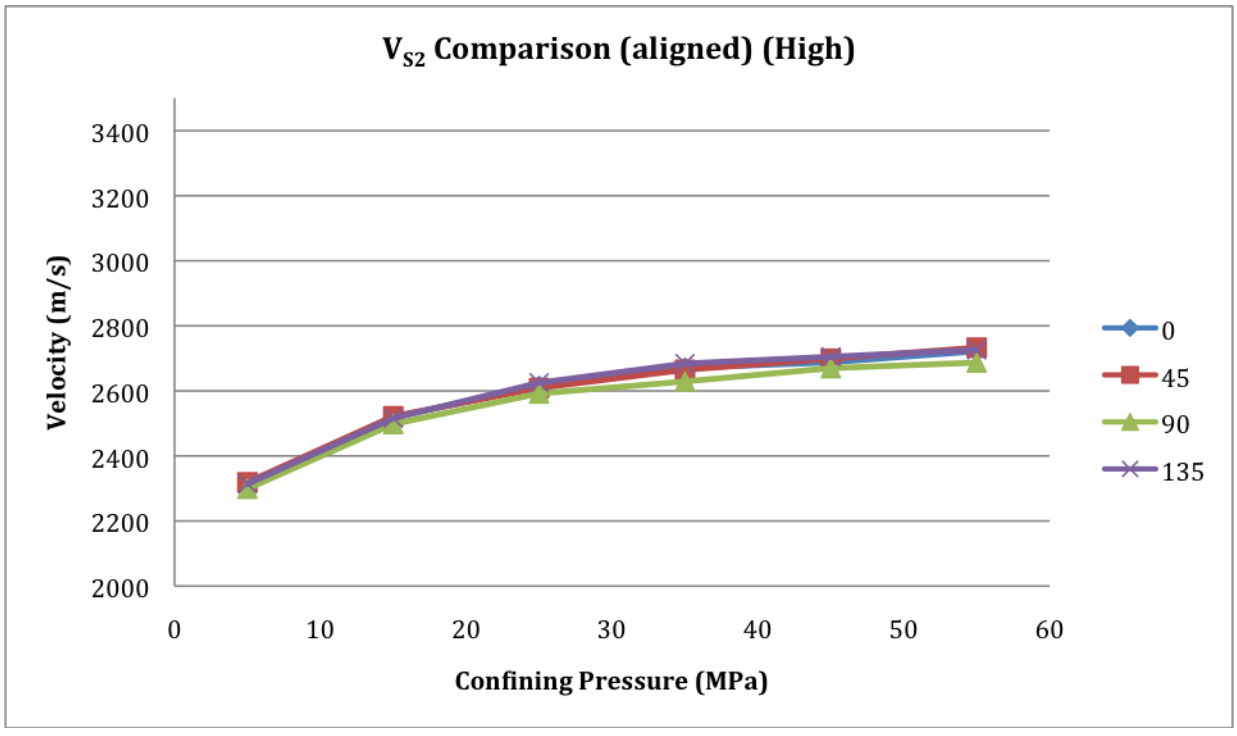

Figure 35 V_{S2} Anisotropy Comparison (High), Velocity vs. Confining Pressure

Next, we plotted V_P, V_{S1} and V_{S2} vs. Angle for each pressure step. This is to better highlight any velocity differences that occur with rotation at different pressures. First, we examine the low porosity core. V_P shows a slight amount of anisotropy, on the order of ~100 m/s difference depending on the core orientation, with 45° and 135° showing higher velocities than 0° and 90° (Figure 36).

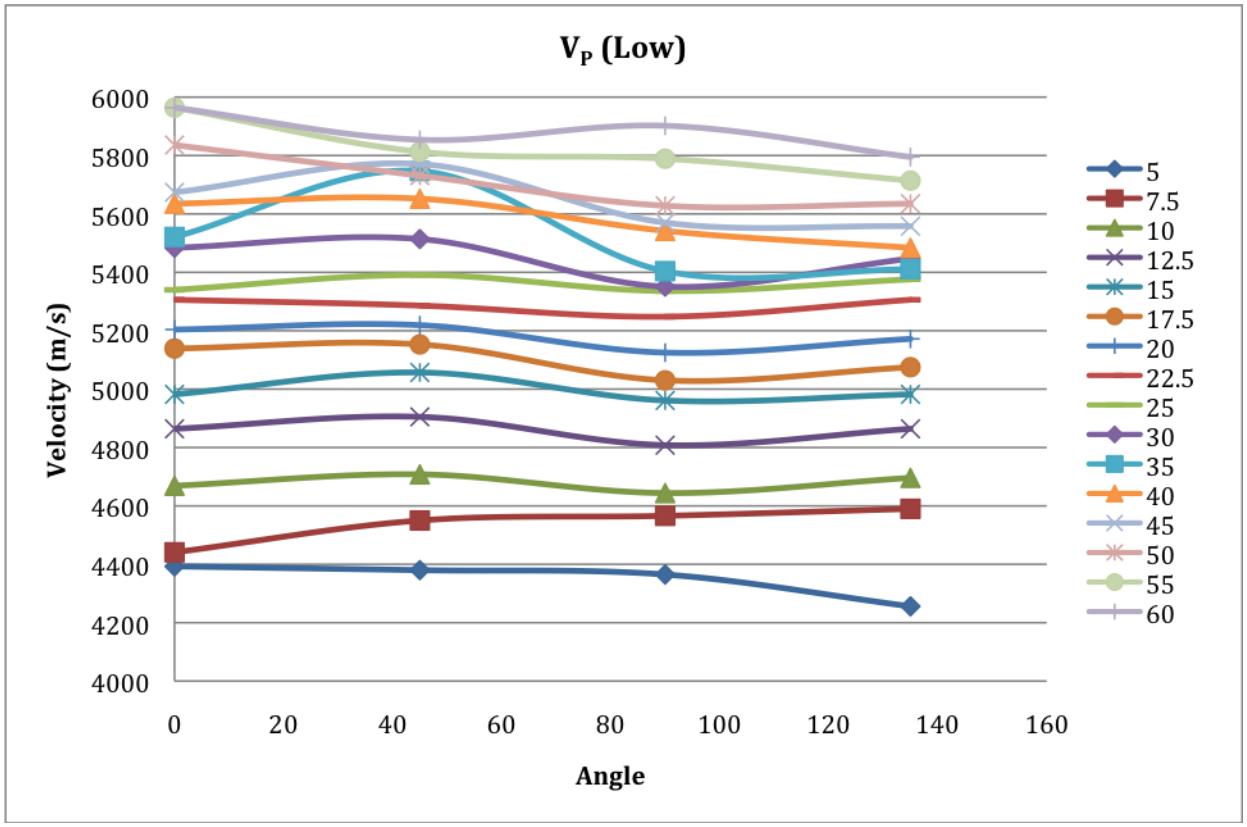

Figure 36 Pressure Anisotropy Comparison V_P (Low), Velocity vs. Angle

For V_{S1}, we see anisotropic differences of 50-100 m/s. At pressures of 17.5 MPa and below, the lowest velocities occur at 0° degrees, and the highest occur at 90°, with 45° and 135° having intermediate velocities. From 20-25 MPa, we see little anisotropy. For pressures above 30 MPa,

the anisotropic velocity differences increase to ~100 m/s, and with 45° and 135° having the highest velocities (Figure 37).

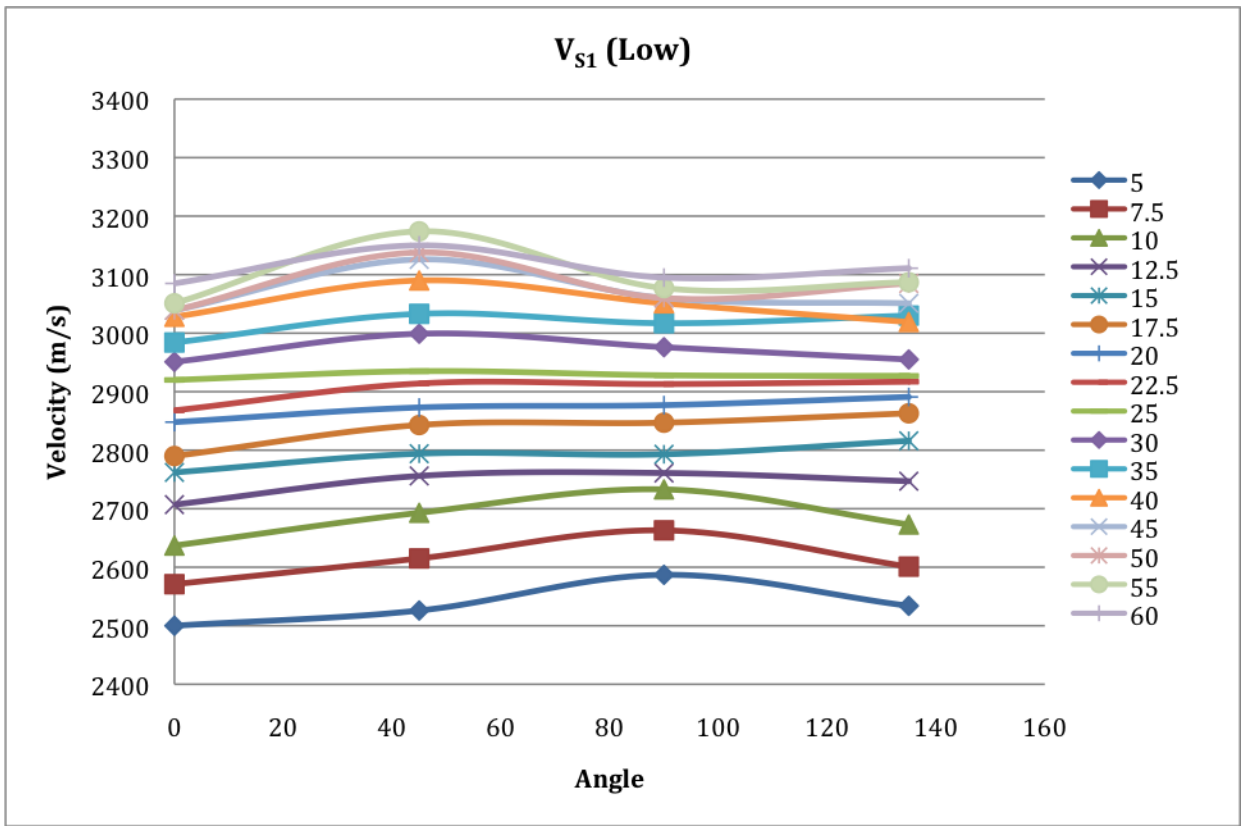

Figure 37 Pressure Anisotropy Comparison V_{S1} (Low), Velocity vs. Angle

For V_{S2}, we see large velocity differences over the whole range of pressures. They are strongly directionally dependant, with most of the highest values occurring at 45°, and the lowest velocities at 90°, 0°, and 135° are intermediate values. The anisotropic variation of V_{S2} is much larger than that of V_{S1}, although it is not clear why this is the case (Figure 38).

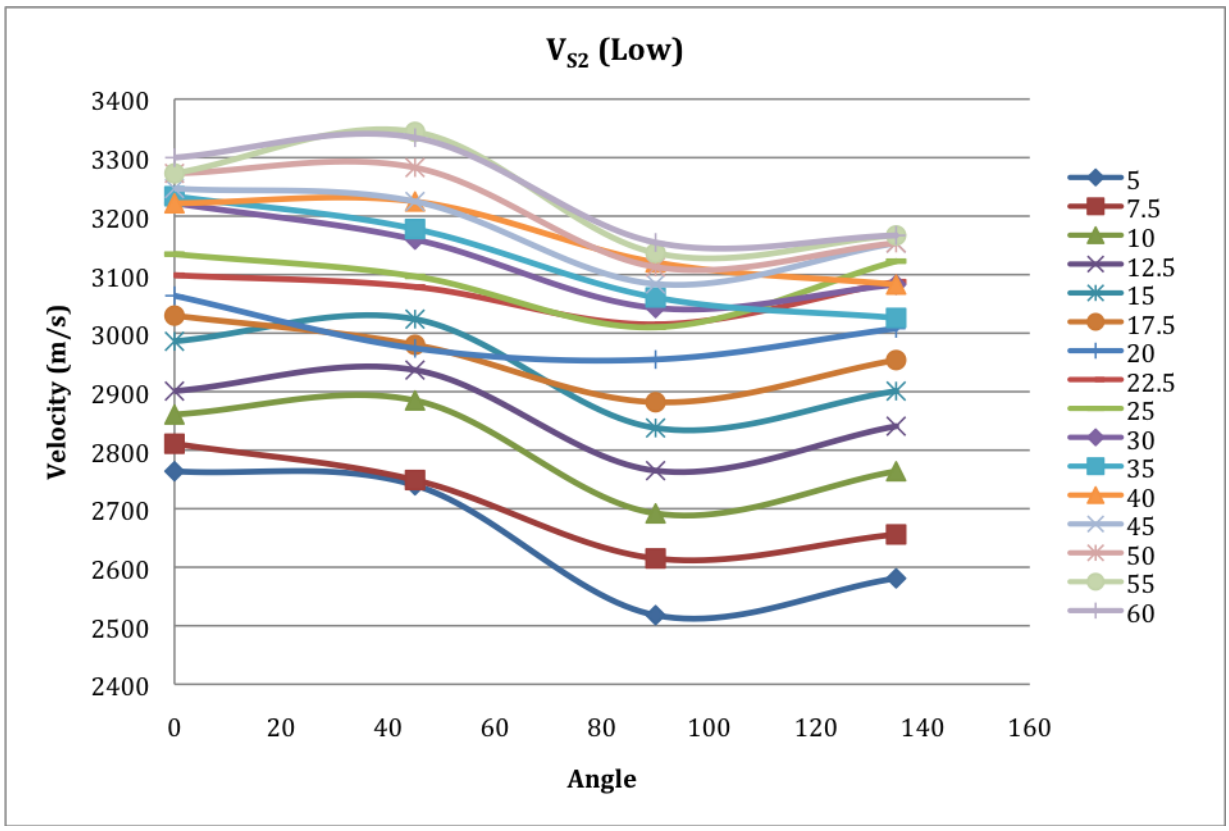

Figure 38 Pressure Anisotropy Comparison V_{S2} (Low), Velocity vs. Angle

When the V_P velocities are plotted for each pressure compared to angle for the high porosity core, variations of ~50-100 m/s are seen, with 90° having the highest velocities, and 0° having the lowest for most pressures (Figure 39).

For V_{S1} in the high porosity core, we see a see a consistent variation of velocities, with the highest values at 90° and the lowest at 0°. The sample is anisotropic over all pressure ranges (Figure 40).

For V_{S2} in the high porosity core, we also see a variation of velocities with an increase in the variation for pressures above 25 MPa. The lowest values are seen at 90°, and the highest values occur at 45° and 135° (Figure 41).

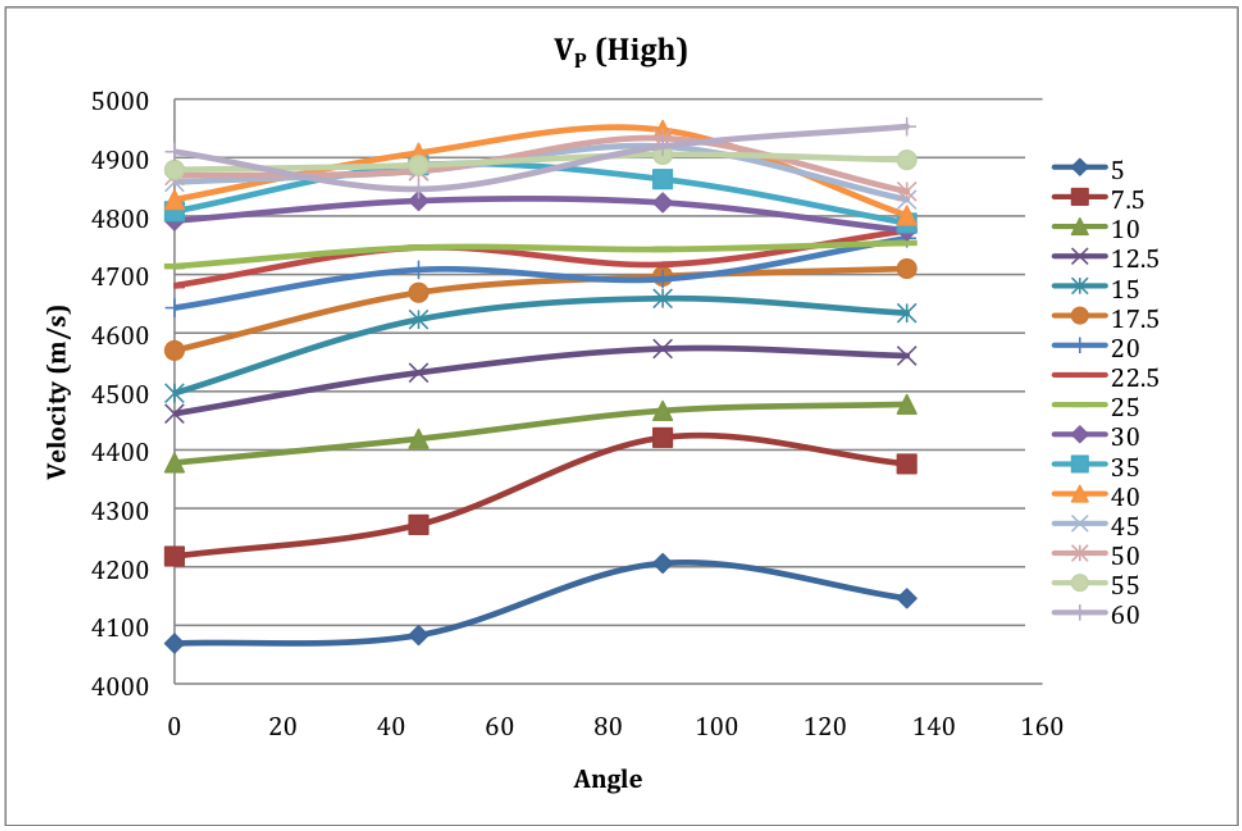

Figure 39 Pressure Anisotropy Comparison V_P (High), Velocity vs. Angle

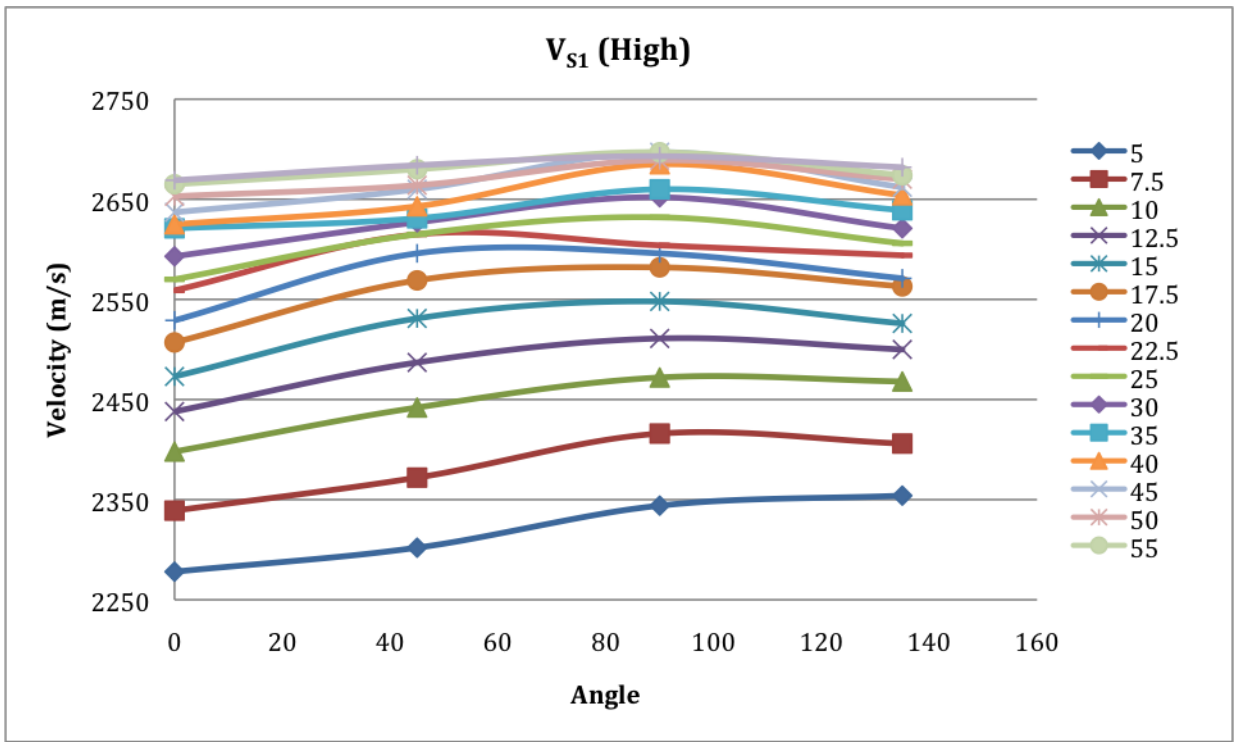

Figure 40 Pressure Anisotropy Comparison V_{S1} (High), Velocity vs. Angle

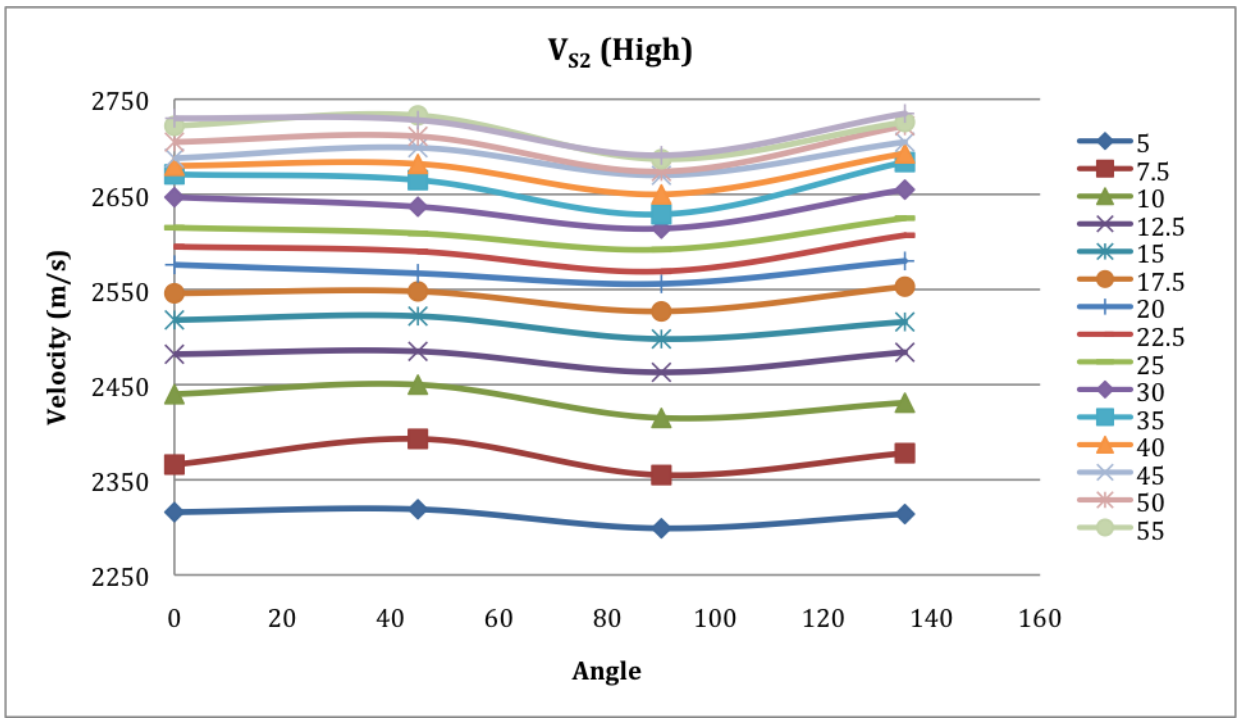

Figure 41 Pressure Anisotropy Comparison V_{S2} (High), Velocity vs. Angle

In order to examine the variation in velocities further, graphs of the % difference between the lowest velocity and the 0°, 45°, 90°, and 135° runs were made. Each velocity at a given pressure had the lowest velocity at that pressure subtracted from it, and was then converted into a percent difference. These were then made into % difference vs. confining pressure plots.

Looking at the low porosity core first, for V_P, we can see that the 90° and 135° runs are the lowest velocities for most pressures. There is a ~3% increase in velocity at 5 MPa for the 0°, 45°, and 90° runs, which becomes smaller as the pressure increases, reaching less and 1% variation at 25 MPa. Beyond 25 MPa, the 0° velocity increases by 2%, and the 45° run reaches its highest variation of 6.4%. Larger variations are seen for 0° and 45° at higher pressures (Figure 42).

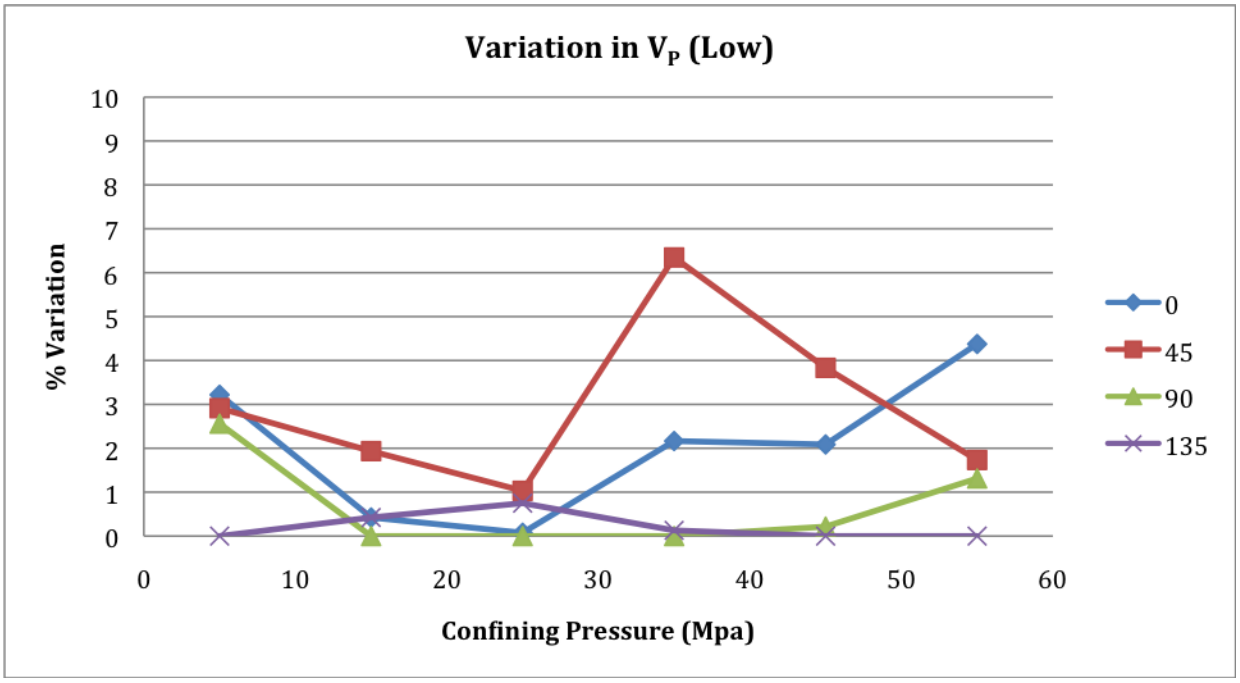

Figure 42 % Variation in V_P (Low), % vs. Confining Pressure

For V_{S1} in the low porosity core, the 90° run shows ~3.5% variation at 5 MPa, which then drops to ~1% for all other pressures. The 0° run has the lowest velocity at all pressures, and the 135°

run velocities vary between 0 and 2% over the whole pressure range. For the 45° run, the variation is ~1% at low pressures, but ramps up from 25 MPa onwards, reaching a 4% variation by 55 MPa (Figure 43).

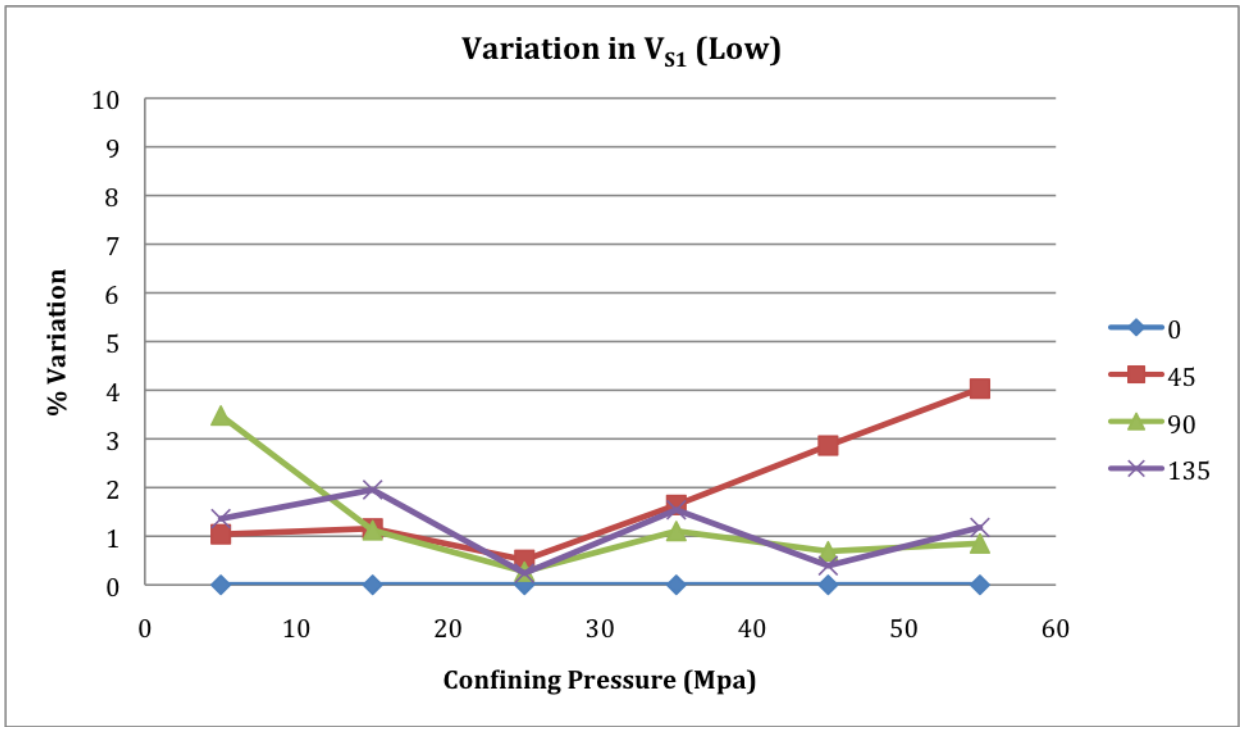

Figure 43 % Variation in V_{S1} (Low), % vs. Confining Pressure

The V_{S2} variations in the low porosity core show the greatest variation of all the experiments run on both cores. The 90° run is the lowest for all pressures except 35 MPa, where the velocity is slightly higher than that of the 135° run. The 135° run has a 1-3% variation over the whole pressure range. For the 0° and 45° runs, the variation at 5 MPa is ~9%, the largest variation seen in these experiments. This then decreases to 3-4% at 25 Mpa, and then varies between 5 and 7% for the rest of the pressures (Figure 44).

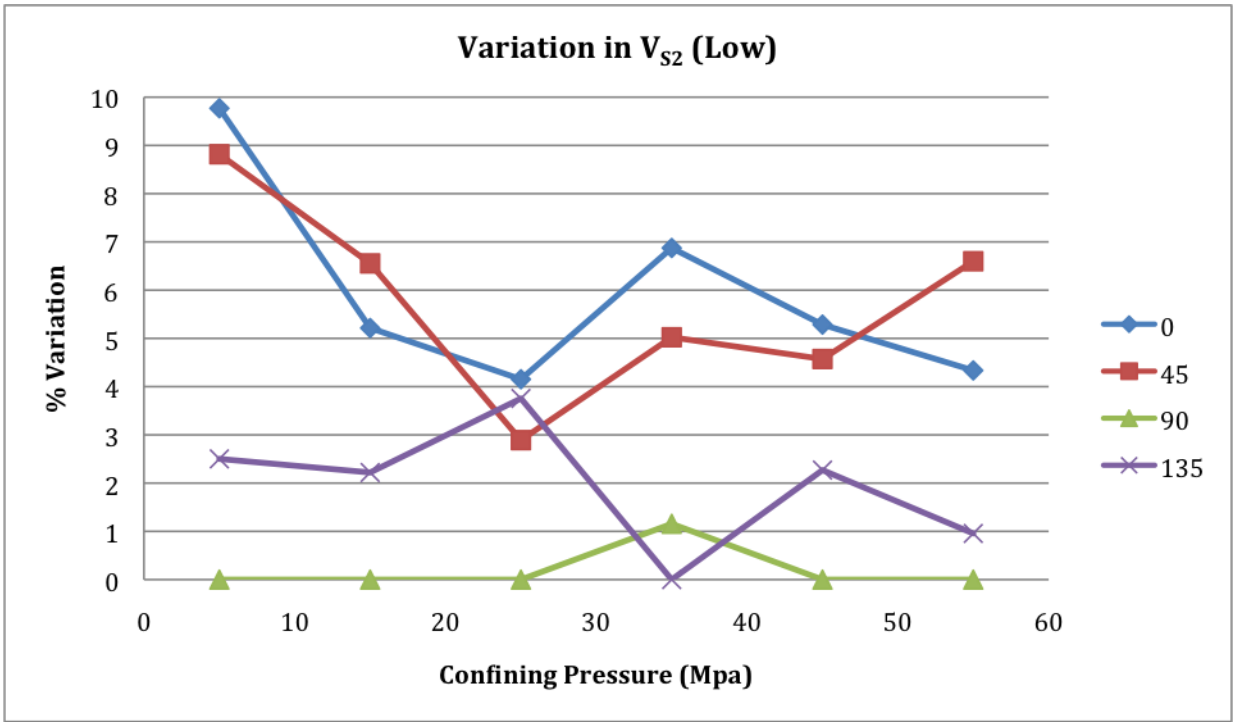

Figure 44 % Variation in V_{S2} (Low), % vs. Confining Pressure

The V_P variations in the high porosity core show that the 0 degree run is the lowest over most of the pressure range. The 45° run shows the most variation at 15 MPa, and then decreases as the pressure increases. There is very little variation seen among all 4 experiments at 25 MPa and 55 MPa. The 90° and 135° degree runs show ~3% variation at low pressures, which decreases at 25MPa, and then is ~2% at higher pressures (Figure 45).

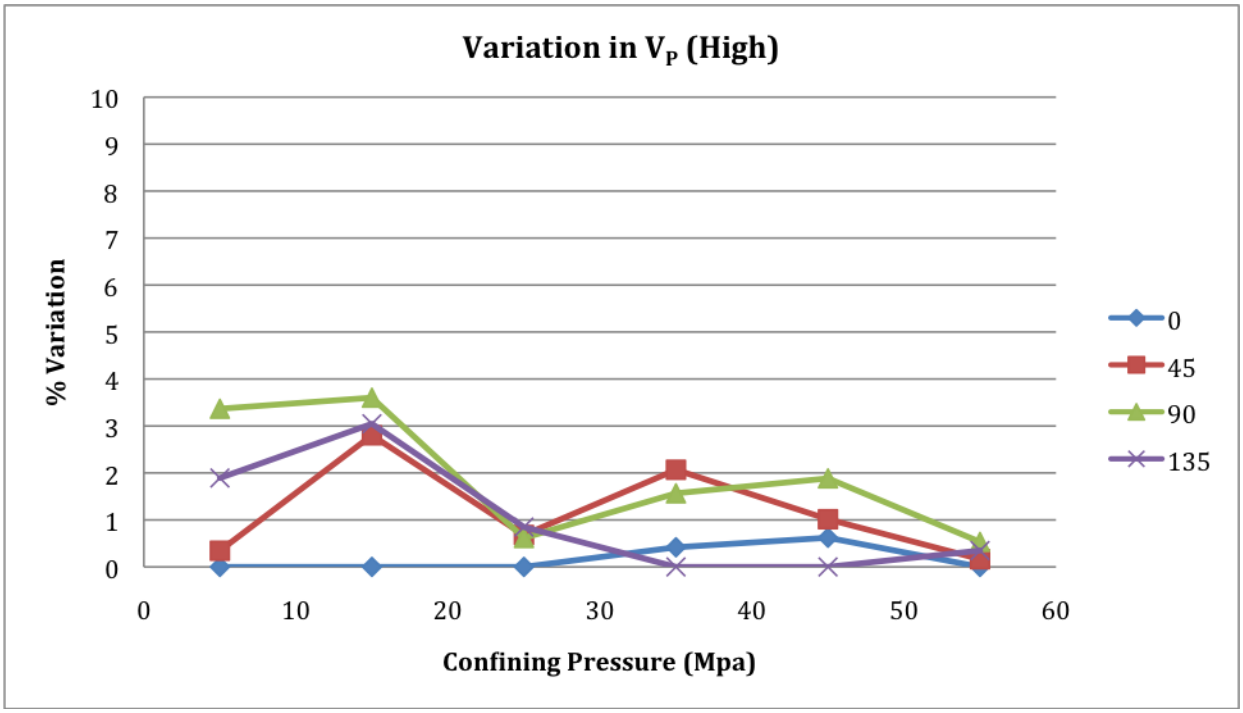

Figure 45 % Variation in V_P (High), % vs. Confining Pressure

The V_{S1} variations in the high porosity core show that the 0° run is the lowest velocity over the entire pressure range, with 90° having the highest variation at all pressures except 5 MPa. The character of the variation in the 45°, 90°, and 135° runs is similar over the whole pressure range, with a slight decrease in variation at 35 MPa and 55 MPa (Figure 46).

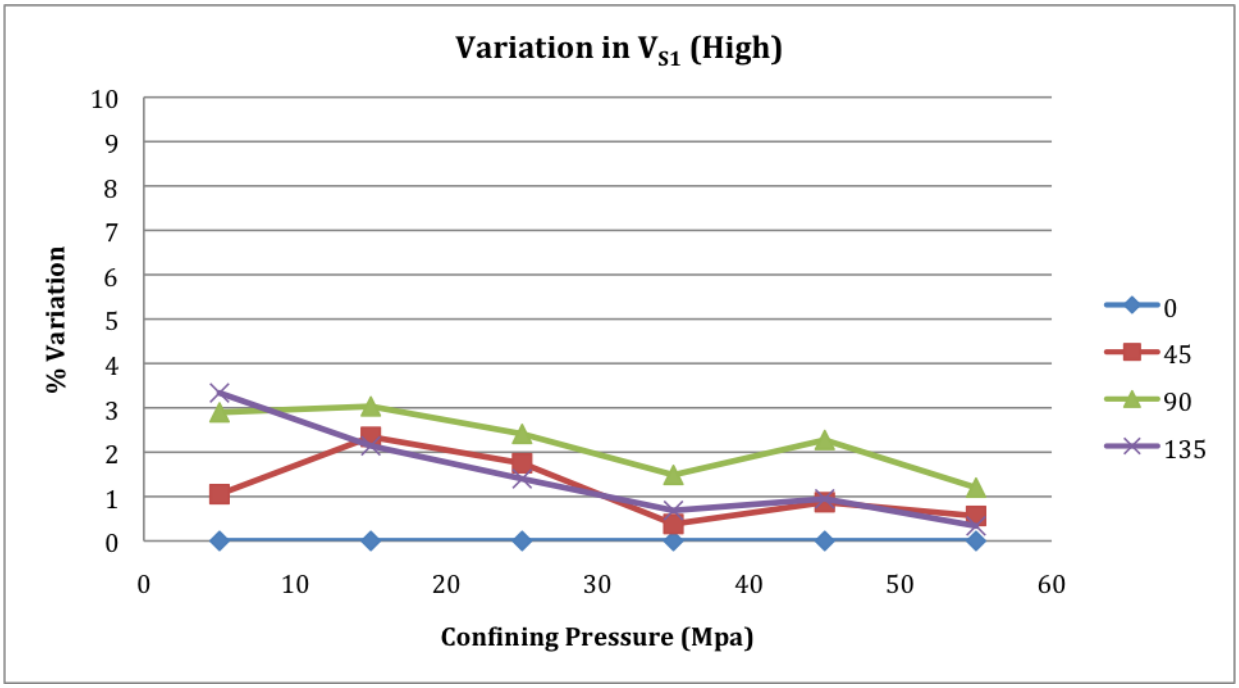

Figure 46 % Variation in V_{S1} (High), % vs. Confining Pressure

The V_{S2} variations for the high porosity core show that the 90° run has the lowest velocities for all pressures. The 0°, 45° and 135° runs show a consistent spread in variation of between 1 and 2% over the whole pressure range (Figure 47).

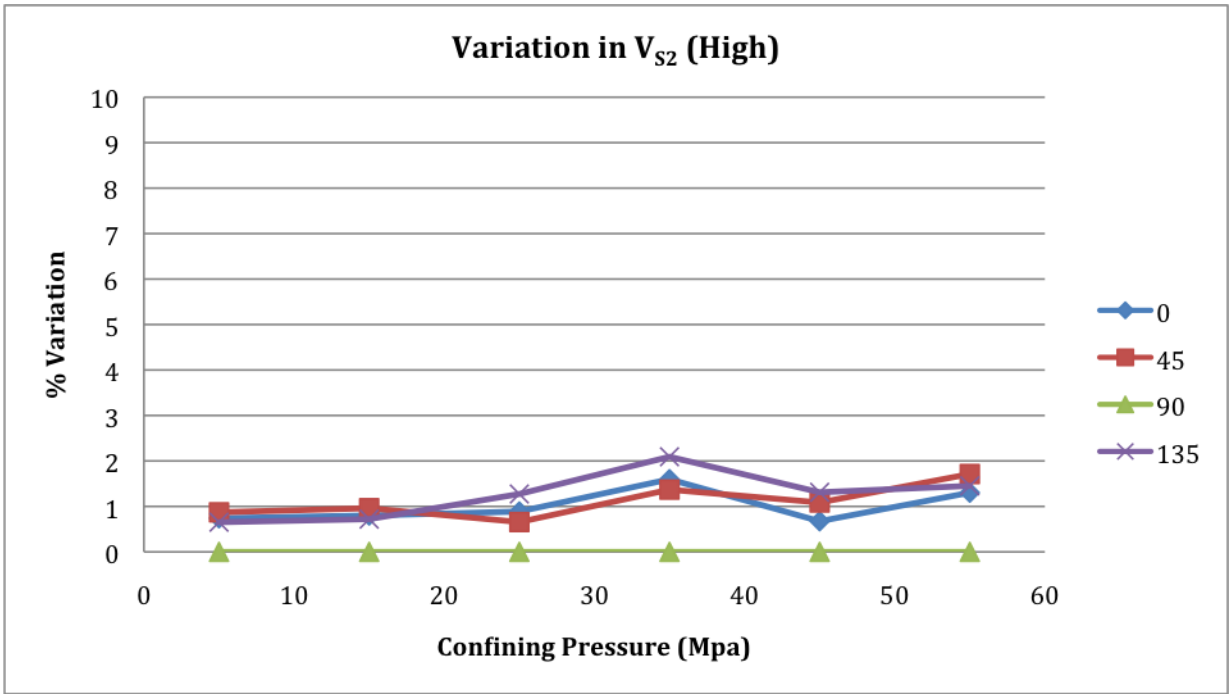

Figure 47 % Variation in V_{S2} (High), % vs. Confining Pressure

The variation in the high porosity core has a different character than that of the low porosity core. Over all, there is less pressure dependent variation than was seen in the low porosity core. The high porosity core shows a lowest velocity for the same orientation in V_P, V_{S1}, and V_{S2} (The lowest velocity in V_{S2} is rotated 90° from V_{S1}). The Low porosity core also shows a shared low velocity orientation for V_{S1} and V_{S2}, but this does not agree with the low velocities for V_P. The variations between both the low and high porosity cores are large enough that these effects should be resolvable seismically, and are an important concern when doing ultrasonic velocity experiments in the lab. It is for this reason that all experiments done after this had the core aligned the same way in the core holder.

1.2.6 New Rock Physics Measurements

After these initial experiments into the properties of our reservoir limestone and how CO_2 affects the velocity, a more thorough set of experiments were performed using both our high porosity core and our low porosity core in order to better characterize the response of our reservoir to changes in pore-filling phases, pressure, and temperature changes. All of these experiments were performed with a finer resolution over the pressure ranges investigated. A list of measurements performed is shown below in Table 2.

Experiment	Core	Porosity	Pore Fluids	Temp
1328199323	LIMESTONE #1 w/oil	13.9	Oil	50
1328114959	LIMESTONE #1 w/oil	13.9	Oil	25
1327595157	LIMESTONE #2	6.39	Dry	25
1327508058	LIMESTONE #2	6.39	Dry	50
1326822698	LIMESTONE #2	6.39	Deionized Water	50
1326813915	LIMESTONE #2	6.39	Deionized water	25
1326468617	LIMESTONE #1	18.53	Deionized Water	50
1326398607	LIMESTONE #1	18.53	Deionized Water	25
1325778014	LIMESTONE #2	6.39	CO_2	50
1322579001	LIMESTONE #1	18.53	CO_2	50
1321544044	LIMESTONE #1	18.53	Dry	50
1320693557	LIMESTONE #2	6.39	Dry	50
1328296045	LIMESTONE #1 w/oil	13.9	Oil/CO_2	50

Table 2: List of new Limestone experiments

Two Limestone cores were used for these experiments, with the following parameters: Limestone Core #1 had a length of 69.7mm, a diameter of 50.12mm, a mass of 303.73g, a density of 2.2087g/cc and a porosity of 18.53%. Limestone Core #2 had a length of 68.27mm, a diameter of 50.34mm, a mass of 346.28g, a density of 2.5484g/cc, and a porosity of 6.386%. The porosities of the samples were determined by using a Temco Helium Porosimeter, taking porosity measurements 3 times, and averaging the results.

These two samples, although from the same formation, show the large variation in potential rock properties in the reservoir, with a large range of porosities and densities over a distance of only a few hundred feet.

1.2.6.1 Hysteresis Experiments

After these samples were placed in a dessicator and brought down to 10% humidity, ultrasonic velocity measurements were taken at pressures ranging up to 50 MPa. These experiments were performed at 50°C, with ~3 minutes between each measurement to allow for equilibration. The initial step size was 0.5 MPa, from 0.5 to 20 MPa, with a step size of 1 MPa from 20 to 50 MPa. The increased step size over the low confining pressure range was chosen to investigate the closure of compliant porosity in this pressure range. Once 50 MPa was reached, the sample was allowed to equilibrate for 30 minutes, and then the pressure was decreased in 1 MPa increments to investigate any hysteresis effects on our samples.

For Core #1, a large increase in V_P of ~600 m/s can be seen until ~20 MPa, at which point the increase levels off, slowly increasing to ~4700 m/s at 50 MPa. A lot of variability was observed

in the fine scale measurements taken from 0-20 MPa, most likely due to difficulty in picking arrival times, as coupling of the sample to the transducers is poor at low effective pressures.

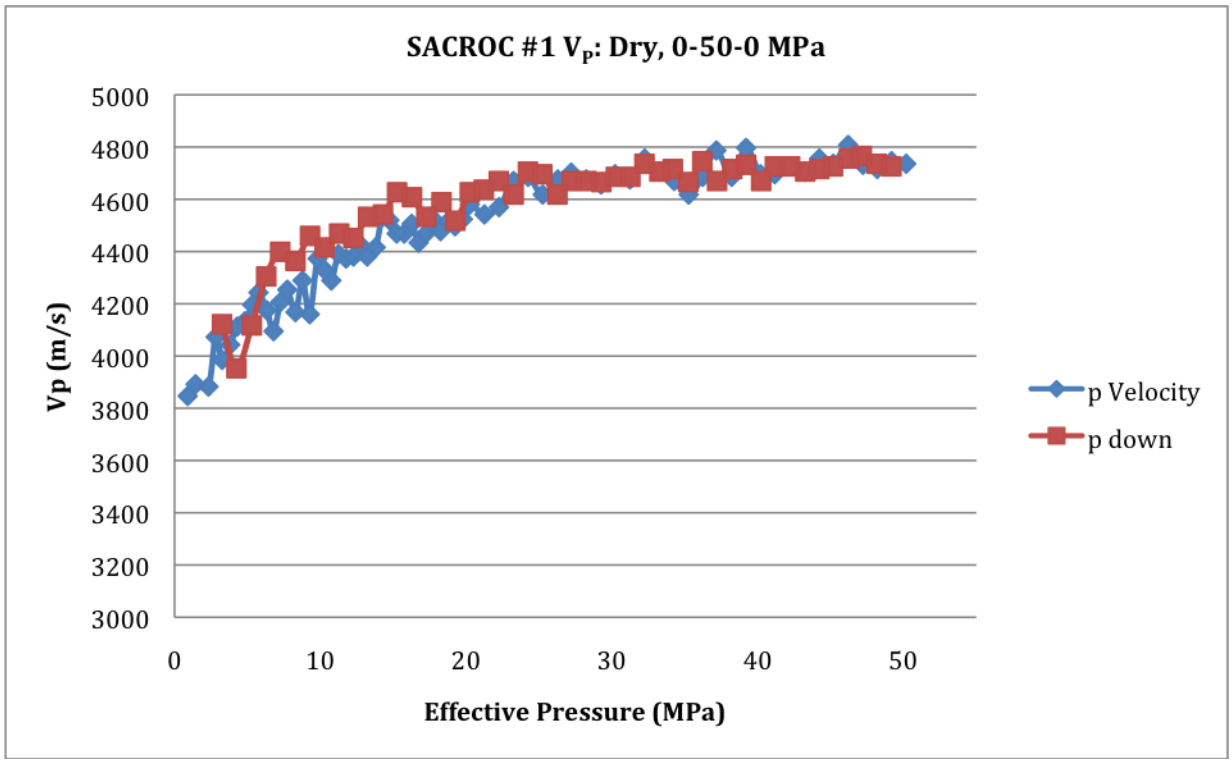

Figure 48:Hysteresis Experiment, Limestone Core #1, V_P

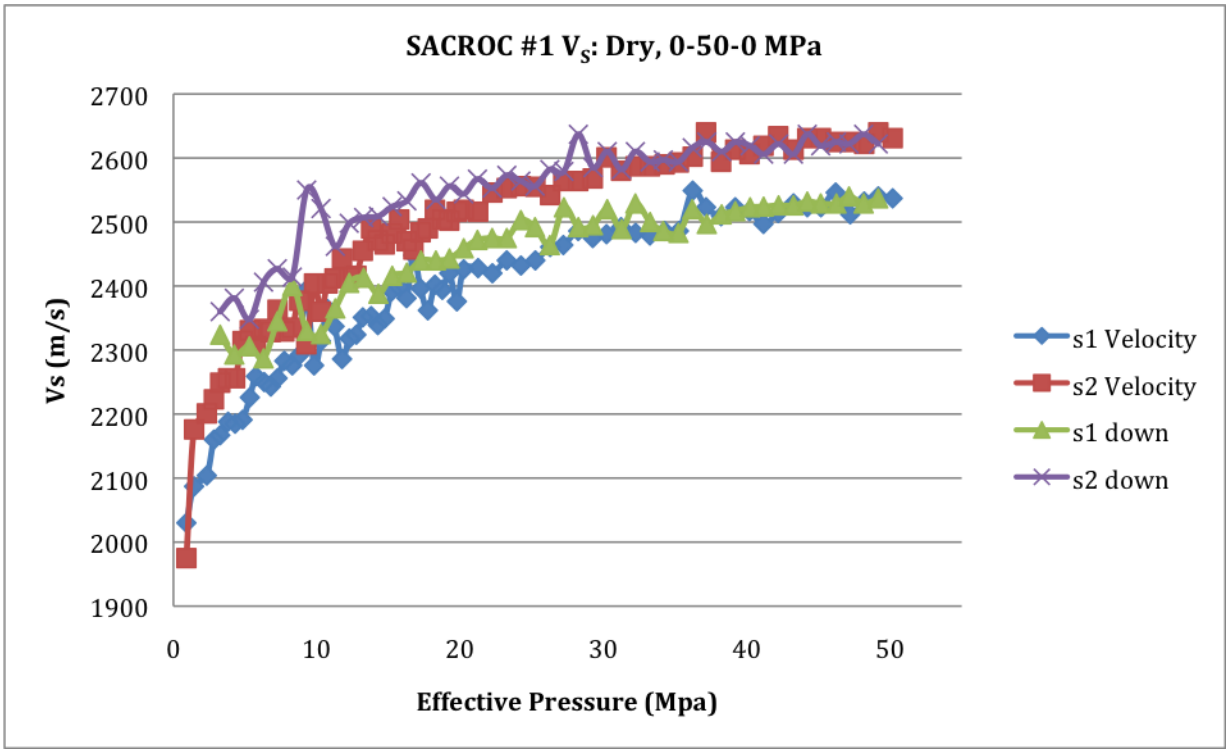

Figure 49: Hysteresis Experiment, Limestone Core #1, V_{S1} and V_{S2}

For V_P, V_{S1} and V_{S2}, it is observed that the unloading velocities were higher than the loading velocities, showing the effects of hysteresis. In order to quantify the hysteresis better, the loading velocities were subtracted from the unloading velocities, giving the hysteresis difference, shown in Figure 50. A general trend of increasing hysteresis with decreasing effective pressure is seen. In order to compare the relative differences between V_P, V_{S1} and V_{S2}, the initial velocities were standardized and then compared to one another. In order to obtain normalized values, the mean and standard deviation were found for the V_P, V_{S1} and V_{S2} datasets. Then by applying the formula:

$$Z = \frac{x-\mu}{\sigma}$$

Equation 17: Standardized Velocity

where Z is the Standardized value, X is the initial value, μ is the mean, and σ is the standard deviation. This returns V_P, V_{S1} and V_{S2} data that can be directly compared to one another. The data was plotted, and then a 10 point moving average was fitted to each trend, as shown in Figure 51.

The moving averages allow the general trend of the hysteresis to be more clearly seen. A general decrease in hysteresis occurs with increasing effective pressure. The relative amount of hysteresis difference is similar for V_P, V_{S1} and V_{S2}. However, the trends are not identical. V_P exhibits a sharper drop off, reaching 0 (no hysteresis) at ~25 MPa, whereas V_{S1} and V_{S2} decay slower, with hysteresis disappearing at ~35 Mpa.

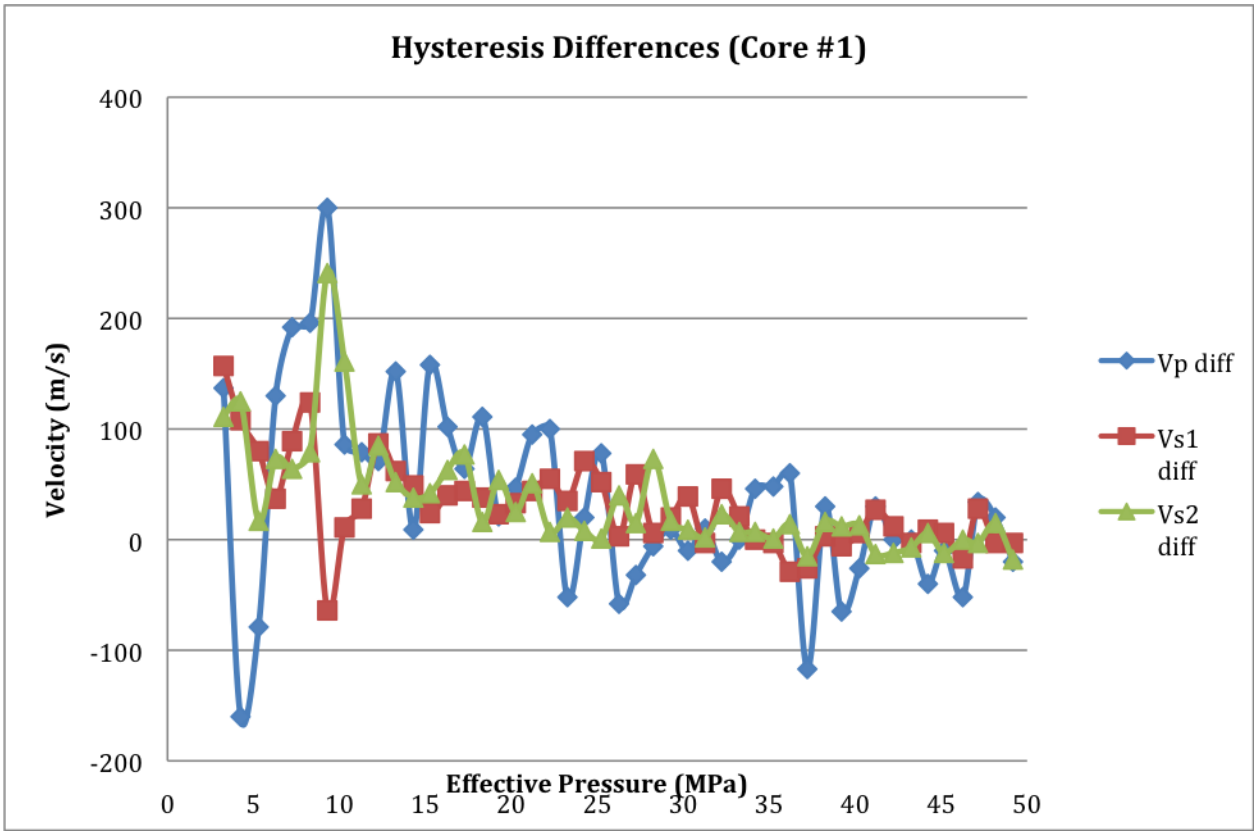

Figure 50: Hysteresis Differences (Core #1)

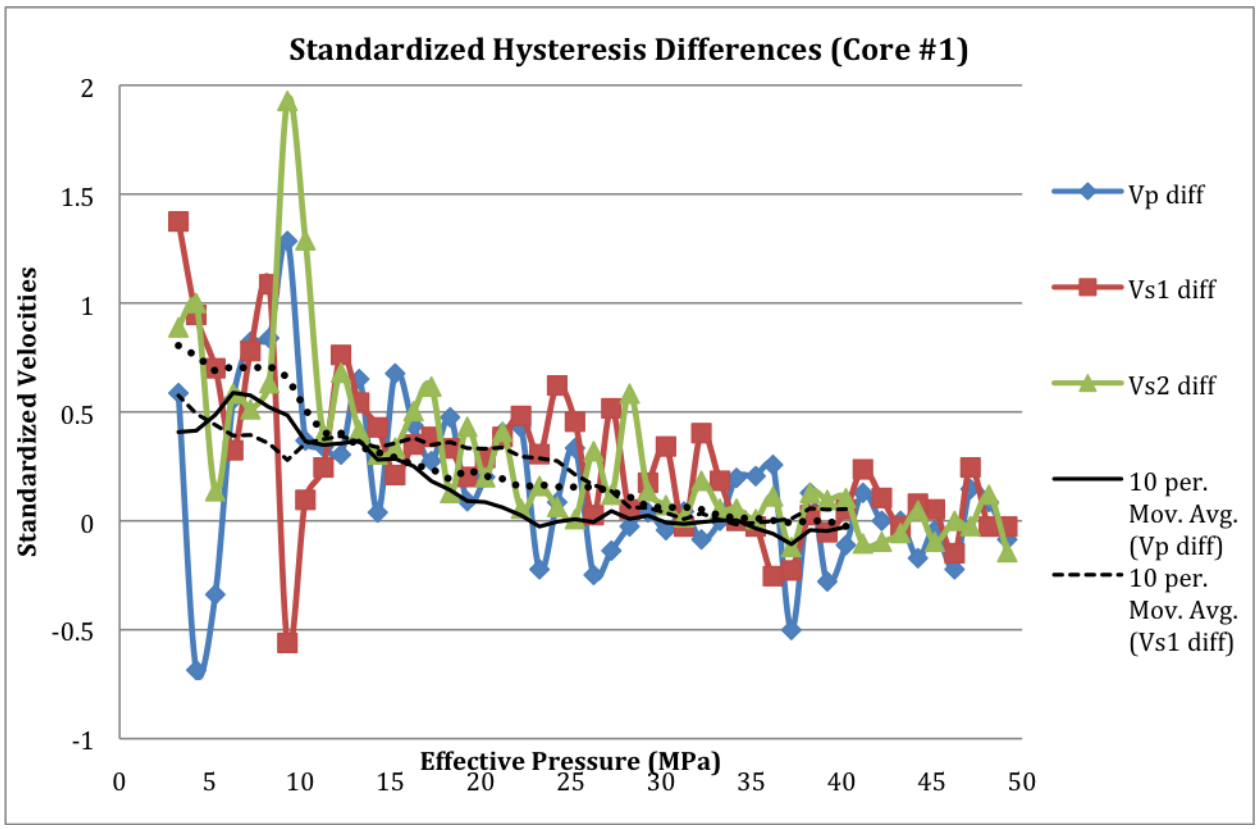

Figure 51: Standardized Hysteresis Differences (Core #1)

For Core #2, the character of the Hysteresis was much different than for Core #1. The velocity increase with Effective Pressure is much larger for Core #2 than it is for Core #1 (~1400 m/s vs. ~1000 m/s). A slightly larger increase in V_S is also observed (~700 m/s vs. ~600 m/s). The velocities of Limestone Core #2 are higher than those of Core #1, due to the lower porosity and higher density (Figure 52 and Figure 53). It can also be seen that the Hysteresis does not follow the same pattern as it does for Core #1.

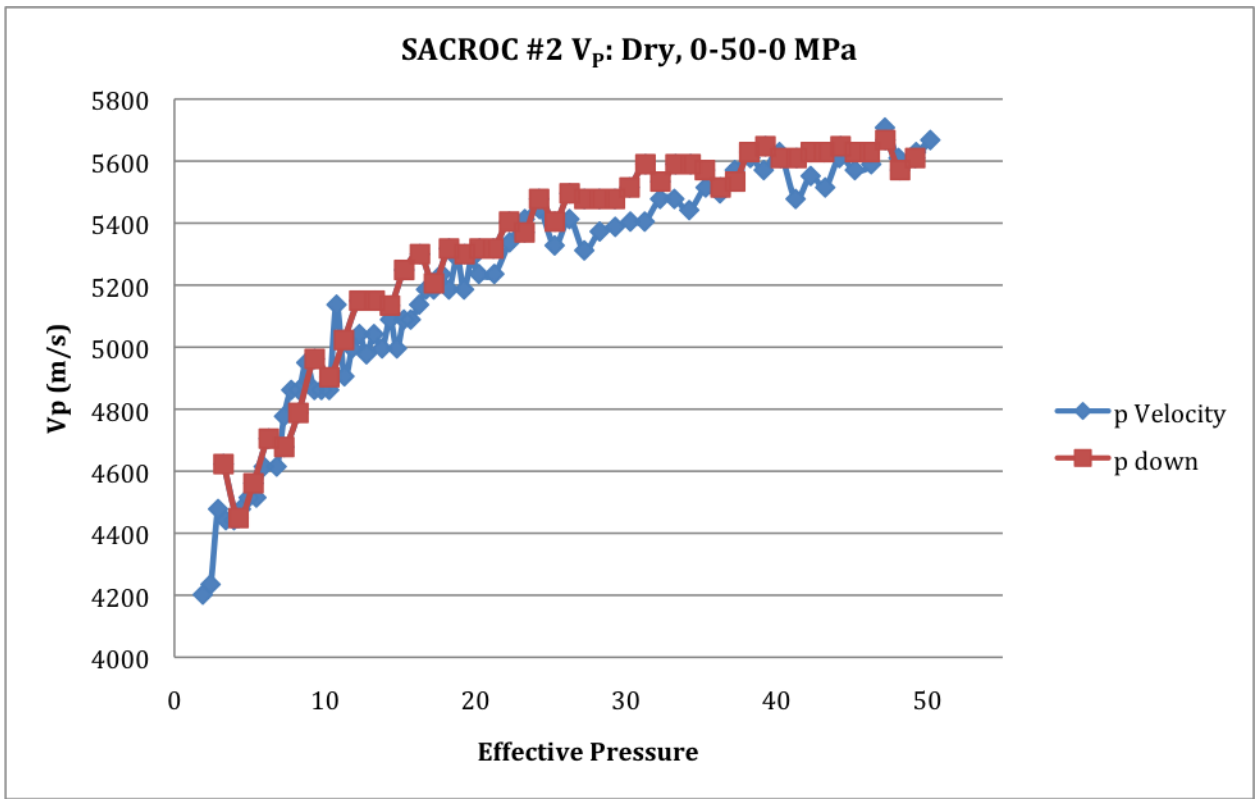

Figure 52: Hysteresis Experiment, Limestone Core #2, V_P

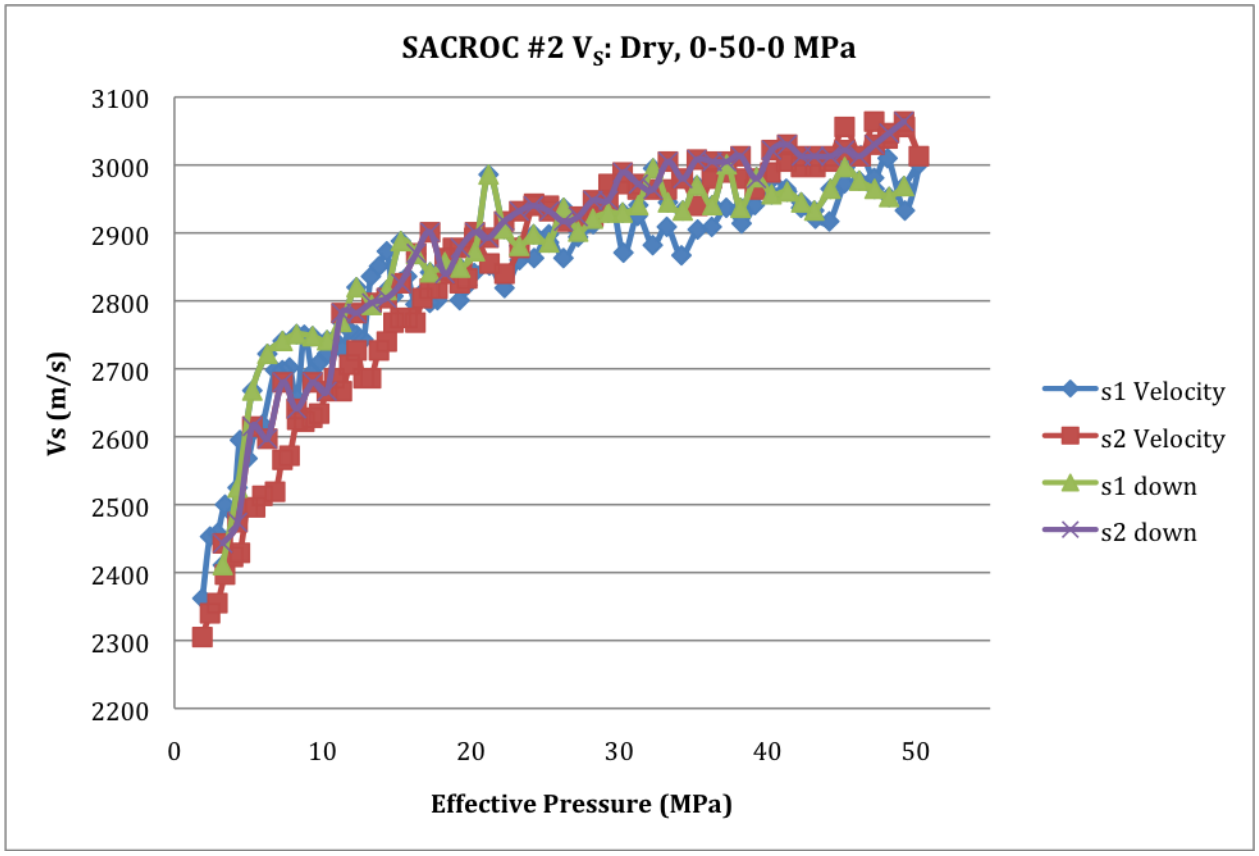

Figure 53: Hysteresis Experiment, Limestone Core #2, V_S

When the differences between the pressurization and depressurization curves are plotted, although the differences are positive on average, there is only a slight decreasing trend, and this trend has a very poor fit to the data (Figure 54). This means that Hysteresis is present even at the highest effective pressures measured in this study (50 MPa), which can be explained by examining the loading curves for both cores with more detail. Looking at V_P velocity for Core #1 (Figure 48), we can see a leveling off of velocity increase around 40 MPa, at which point the velocity increase becomes very small. However, when the V_P curve of Core #2 is examined, a very different character can be seen (Figure 52); although the same rapid increase with effective pressure is found, the velocity is still increasing from 40-50 MPa. This is likely do the large porosity and density differences between the samples. In Core #1, the large pore space makes the

sample as a whole more compliant, and the increasing pressure closes off all of these compliant pores quickly. In Core #2, the much lower pore space equates to an overall stiffer sample, and the compliant pores resist closure, even at higher pressures. This would then lead to an essentially constant Hysteresis effect in Core #2.

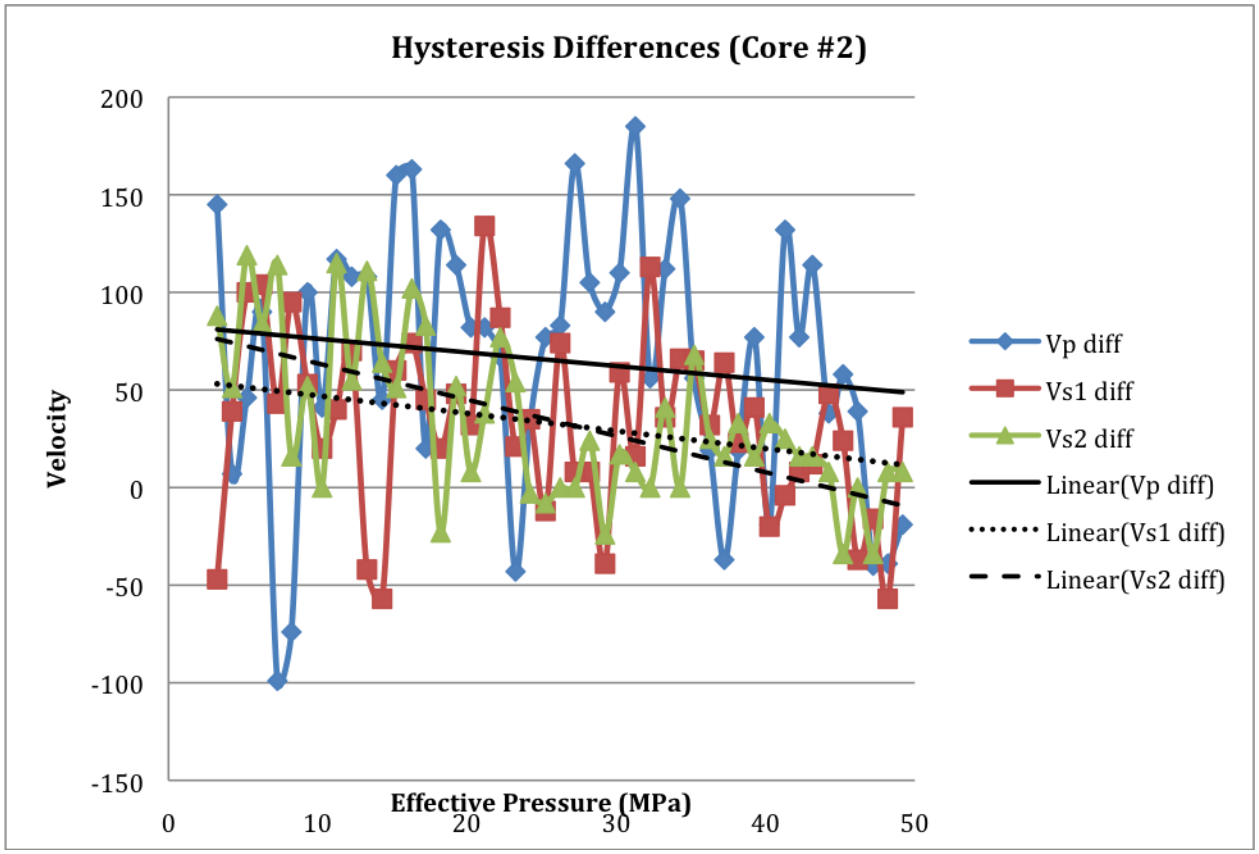

Figure 54: Hysteresis Differences (Core #2)

A clear hysteresis effect was seen in both core samples, especially at lower effective pressures. This type of effect of velocity should be considered when analyzing any post injection velocities around an injector well, as large pressure changes might mask the effects of fluid changes in the reservoir.

1.2.6.2 CO_2 Saturated Limestone Experiments

The next phase of the experiments was to see the effect that supercritical CO_2 would have on the core velocities. Both cores were jacketed, placed in the AutoLab, and allowed to equilibrate at 50°C in order to approximate in situ conditions. The confining pressure was then increased to 40 MPa, and CO_2 was introduced. The pressure of the CO_2 was then increased, up to a maximum of 37 MPa. The step size used was smaller as the Pore Filling Phase Pressure increased closer to the Confining Pressure. The Effective Pressure is then the Confining Pressure minus the pressure of the pore-filling phase.

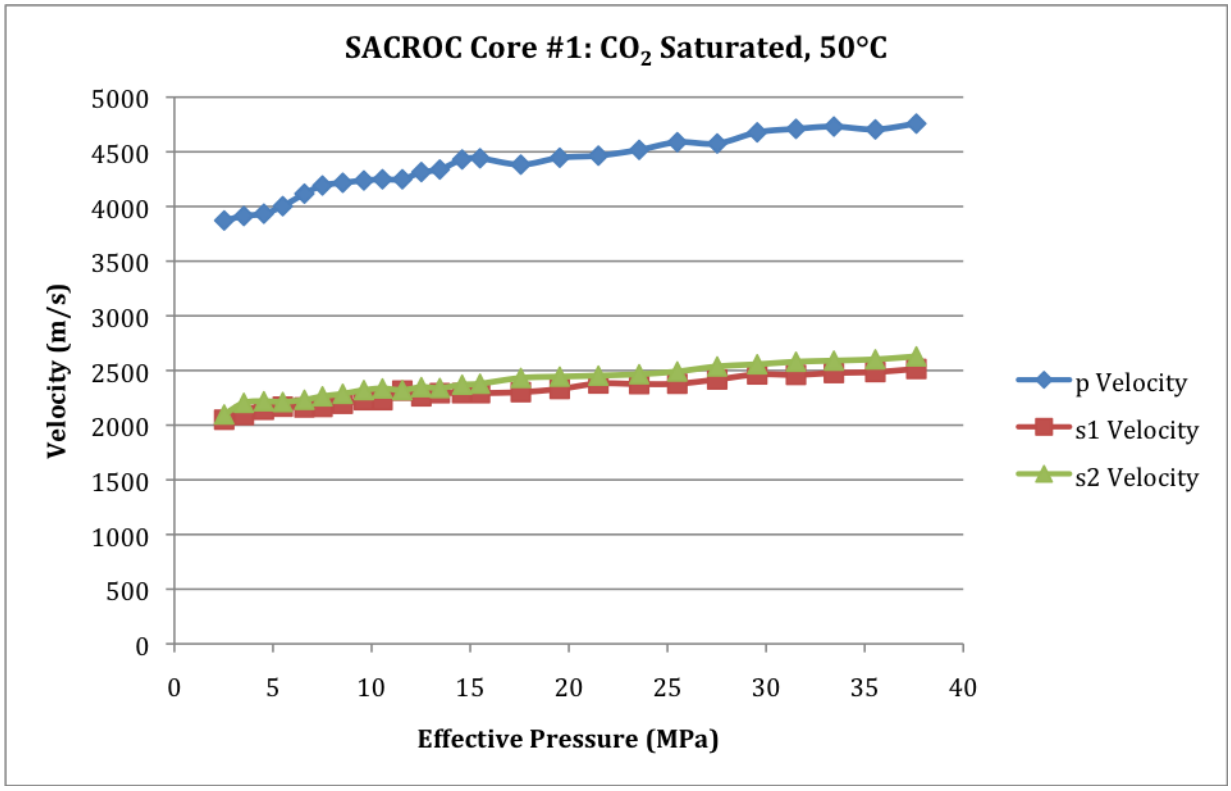

Figure 55: CO_2 Saturated Velocities, Core #1

For Core #1, we can see a steady increase in V_P and V_S velocity with increasing Effective Pressure. This is as expected, as the density and velocity of CO_2 increases with pressure. For V_P velocities, a large change of ~900 m/s was observed over the entire pressure range. This is a ~25% change due to pressure alone, a very large effect.

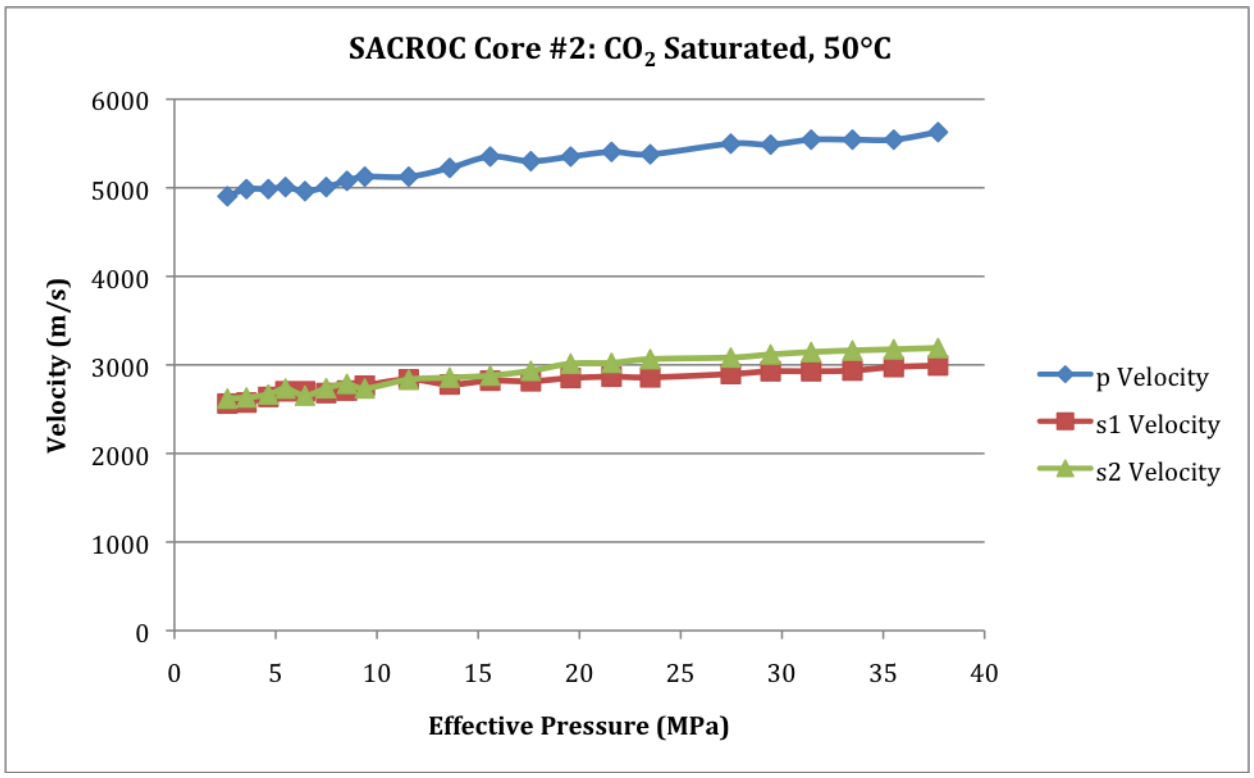

Figure 56: CO_2 Saturated Velocities, Core #2

For Core #2, a similar steady increase is seen over the pressure range. A change of ~700 m/s was seen across the entire pressure range, which represents a ~15% change in V_P velocity. The effect of CO_2 saturation is larger on Core #1 than on #2 due to the much larger pore space in Core #1, which allows the CO_2 to have a much larger effect on the overall velocity.

If the CO_2 saturated velocities are then compared to the previous dry measurements, some interesting observations can be made. For Core #1, V_P velocities are lower when CO_2 is introduced into the core, generally ~100 m/s slower (Figure 57). Similarly, for both V_{S1} and V_{S2}, the velocities are ~100 m/s slower over below ~30 MPa (Figure 59).

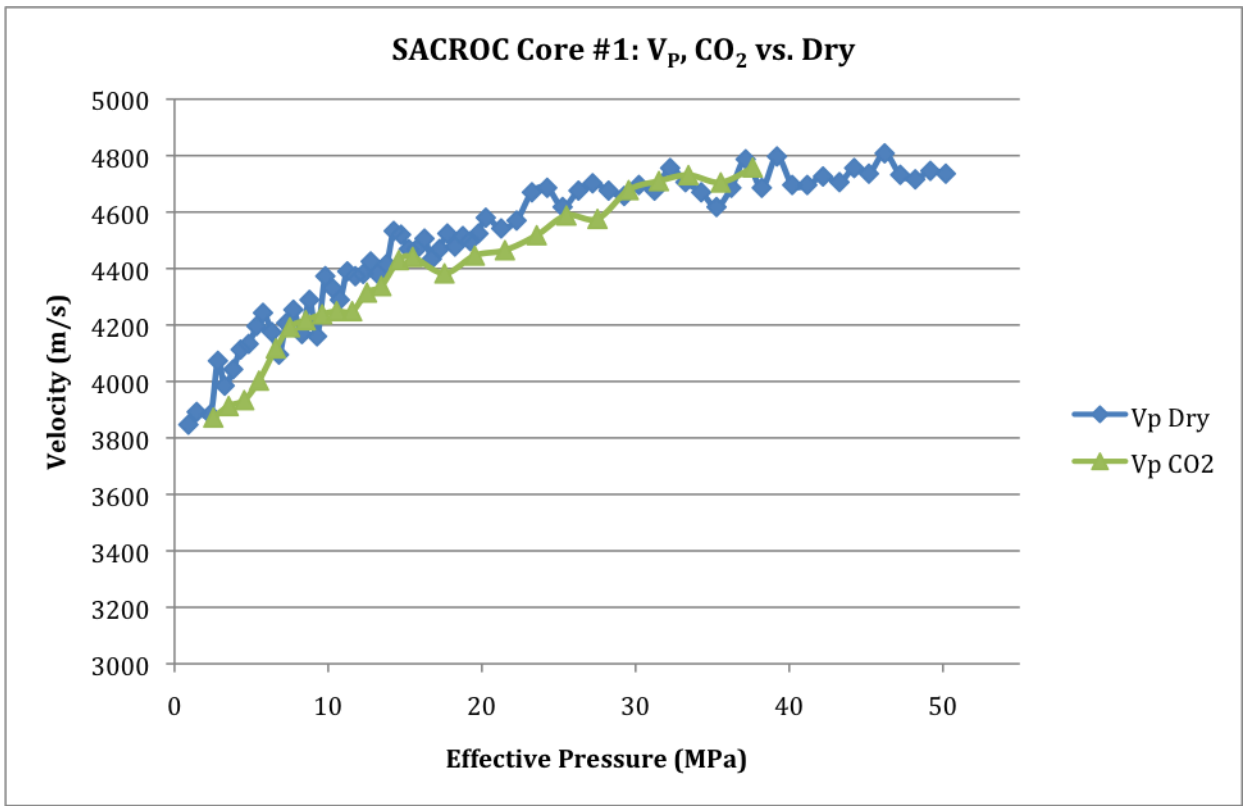

Figure 57: CO_2 V_P vs. Dry V_P, Core #1

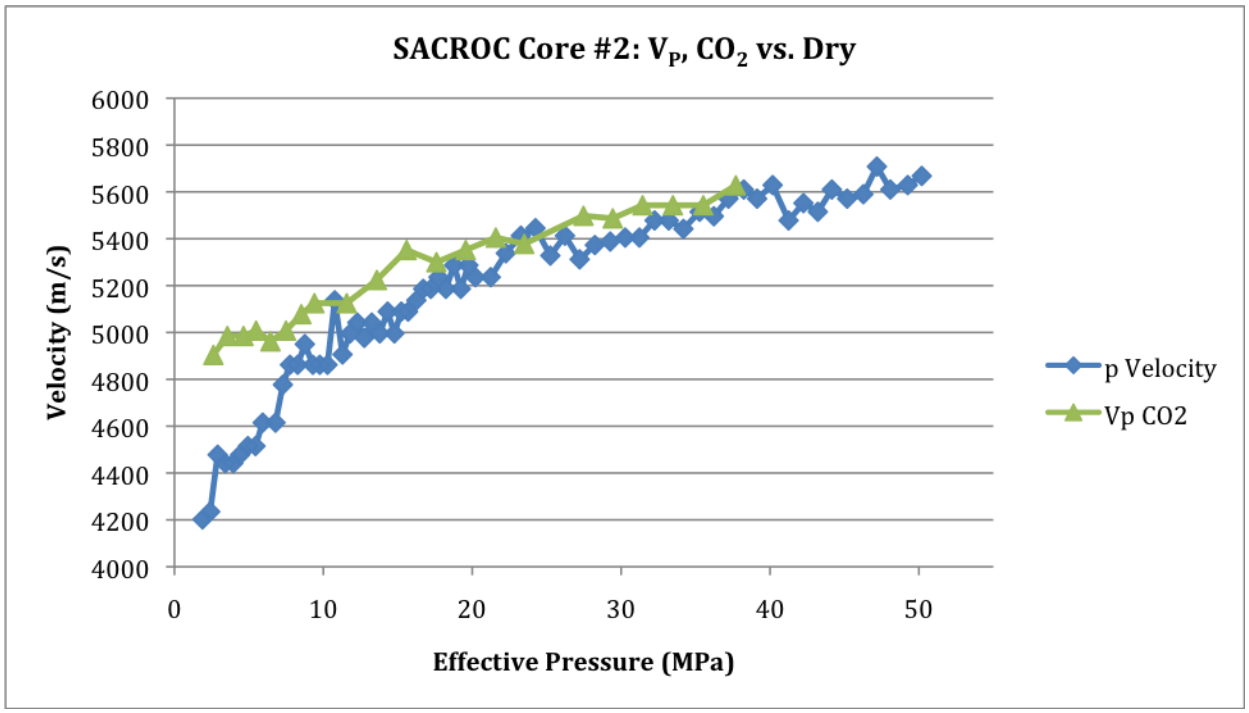

Figure 58: CO_2 V_P vs. Dry V_P, Core #2

For Core #2, a different effect is observed: for V_P velocities, the CO_2 saturated experiments were found to have higher velocities over the whole range, with anomalously high values at Effective Pressures below ~10 MPa (Figure 58). V_P at low Effective pressures was found to be up to ~500 m/s faster for the CO_2 saturated sample, an increase of ~10%.

When the Shear waves were compared, the differences are less clear (Figure 60). The variation between V_{S1} and V_{S2} is smaller for Core #2 than it is for Core #1, and the results overlap. For clarity, V_{S1} velocities and V_{S2} velocities were plotted in separate graphs (Figure 61 and Figure 62). When the V_{S1} velocities are examined, it can be seen that the differences between Dry and CO_2 saturated is very small, only becoming significant at low effective pressures, where the CO_2 velocities become larger (Figure 61).

The V_{S2} velocities show a much different behavior than either the V_{S1} or V_P velocities (Figure 62). The velocities for CO_2 are again higher at low effective pressures, but a large increase is also seen for high effective pressures, up to ~200 m/s. A possible explanation for this lies in Core #2's low porosity.

At high confining pressures, much of the compliant porosity is closed off, although not as fully as in Core #1, as postulated above. Since Core #2 is stiffer, it has higher velocities than Core #1. As CO_2 is introduced into a sample, the overall density goes up, which increases the bulk velocity. This increase in velocity is offset by the reduction in velocity due to the opening of compliant porosity. In Core #1, the CO_2 velocities are slower because the CO_2 easily props open micropores and cracks, and can evenly spread throughout the sample. This overall increase in

porosity causes a corresponding drop in velocities, due to dispersion across the large amount of supercritical CO_2 in the sample. For Core #2, the velocities are higher than Dry velocities because the CO_2 pressure is unable to prop open enough compliant porosity to offset the increase in velocity due to the increased density the CO_2 provides. The fact that this effect is much stronger in V_{S2} than in V_{S1} suggests that the V_{S2} orientation has a much smaller amount of compliant porosity that is aligned with it.

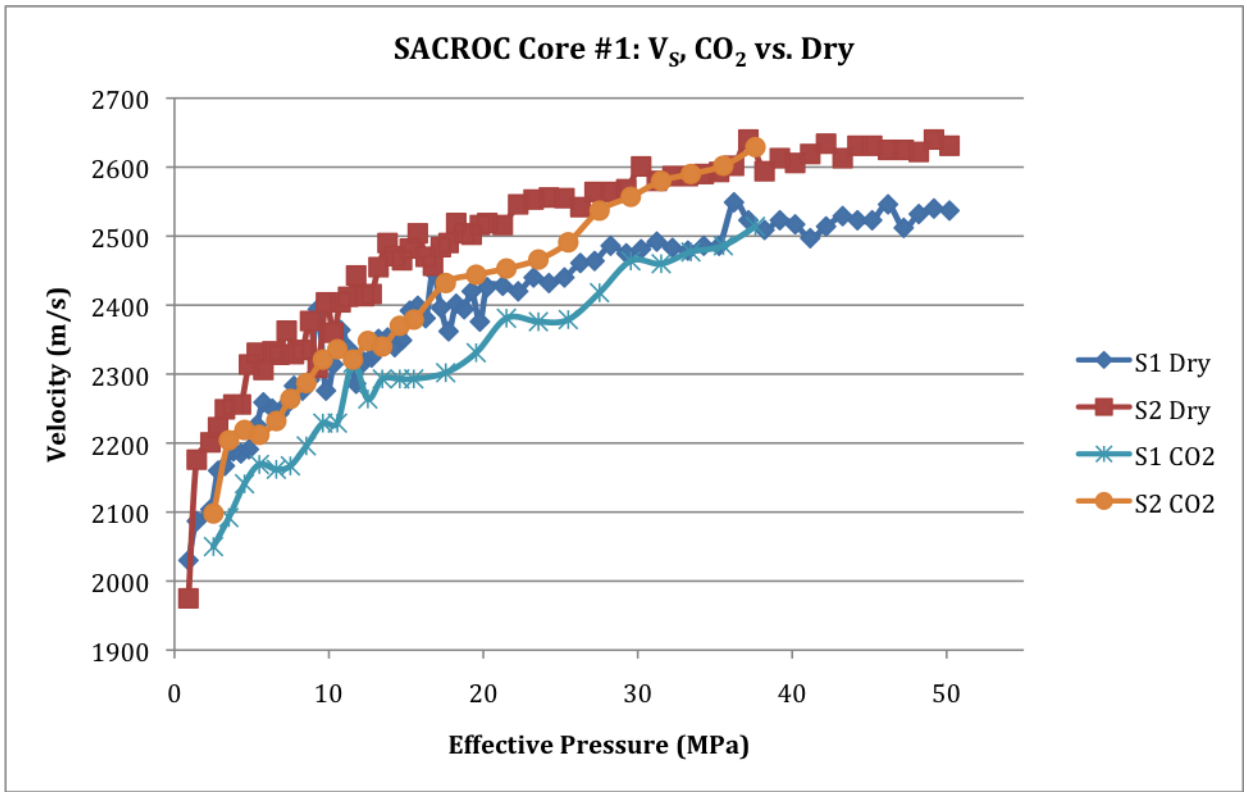

Figure 59: CO_2 V_S vs. Dry V_S, Core #1

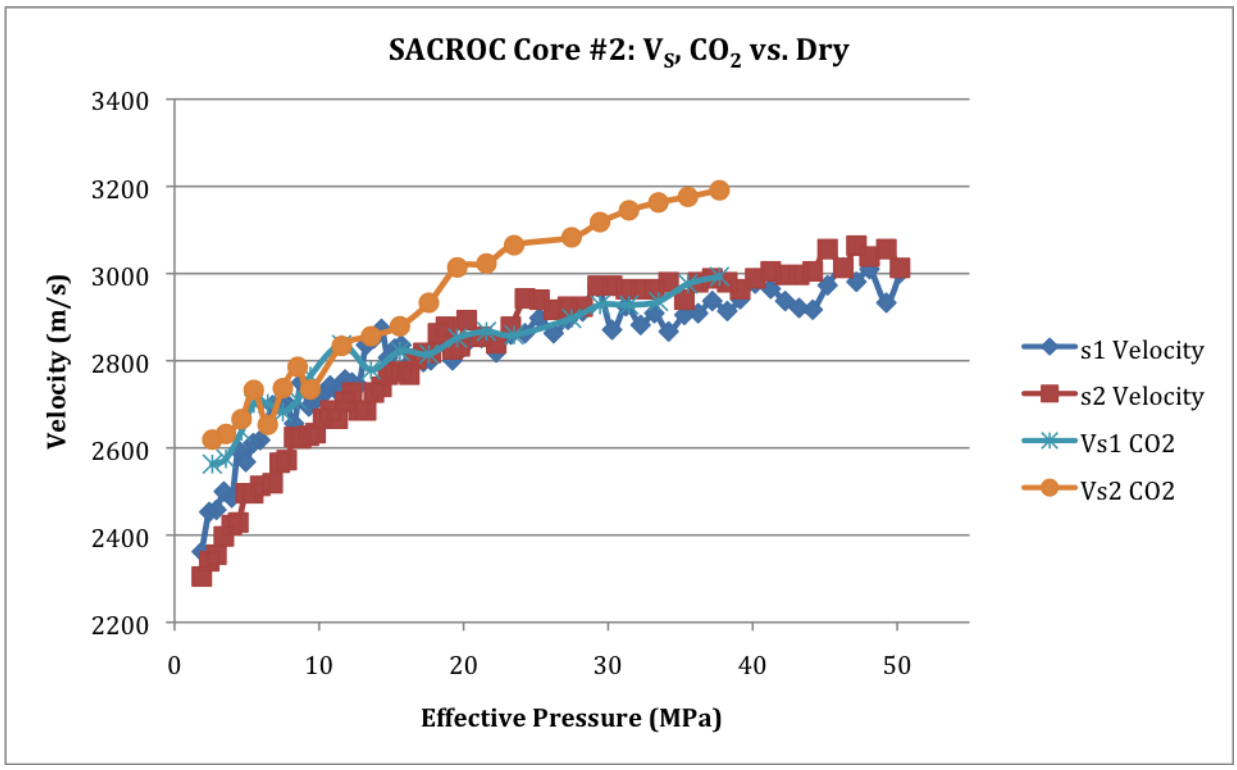

Figure 60: CO_2 V_S vs. Dry V_S, Core #2

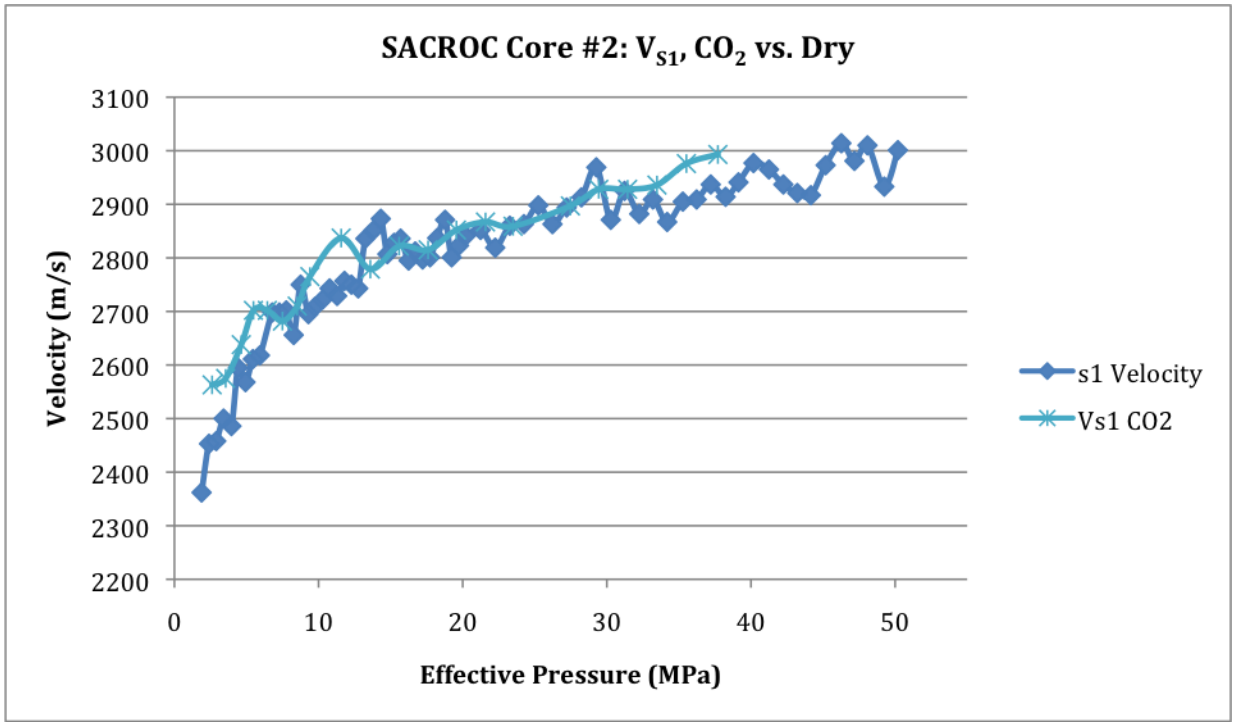

Figure 61: CO_2 V_{S1} vs. Dry V_{S1}, Core #2

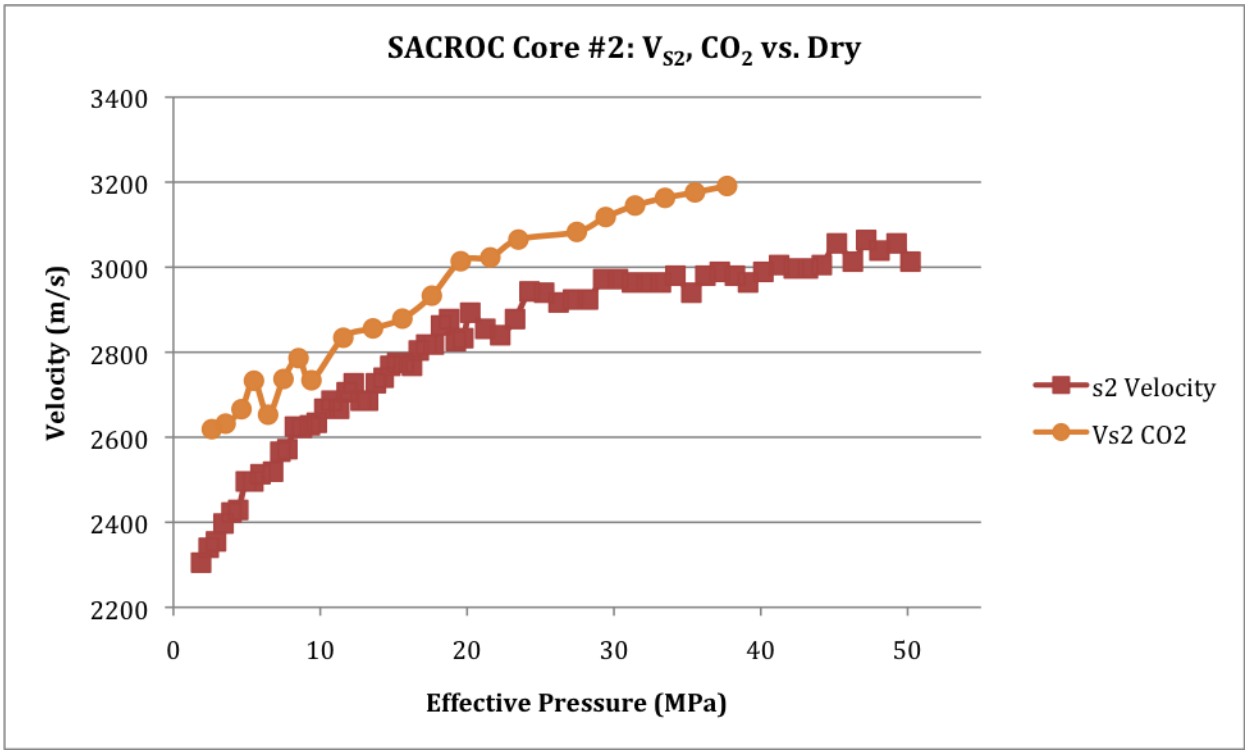

Figure 62: CO_2 V_{S2} vs. Dry V_{S2}, Core #2

This set of experiments shows that although adding supercritical carbon dioxide to a sample of rock significantly changes the velocities, it does not do so in the same way for each sample. Comparison with water saturated cores was therefore needed.

1.2.6.3 Water saturated measurements.

The next set of experiments performed where water saturated velocity experiments. The samples were first allowed to dry to 10% humidity in a dessicator, and where then placed in a vacuum overnight, balanced on top of a beaker of distilled water. The samples were then dislodged under vacuum and allowed to fall into the water. They were then left in the water for another day in

order to become fully saturated. These samples were then placed in a rubber jacket and attached to the core heads, and a small amount of water was added to keep the sample fully saturated. They were then placed into the AutoLab 1500, heated to 50°C, and pressurized to a confining pressure of 40 MPa. The pore pressure plumbing on the AutoLab was filled with distilled water, and all air was bled from the system. This allows the pore pressure of the distilled water to be increased incrementally, lowering the effective pressure.

For Core #1, as the pressure of the water increases (reducing the effective pressure), the V_P velocity drops from ~4800 m/s to ~4300 m/s, a reduction of ~10% (Figure 63). For shear velocities, a similar reduction in velocity is seen, dropping from ~2500 m/s to ~2100 m/s, a change of ~16% (Figure 64).

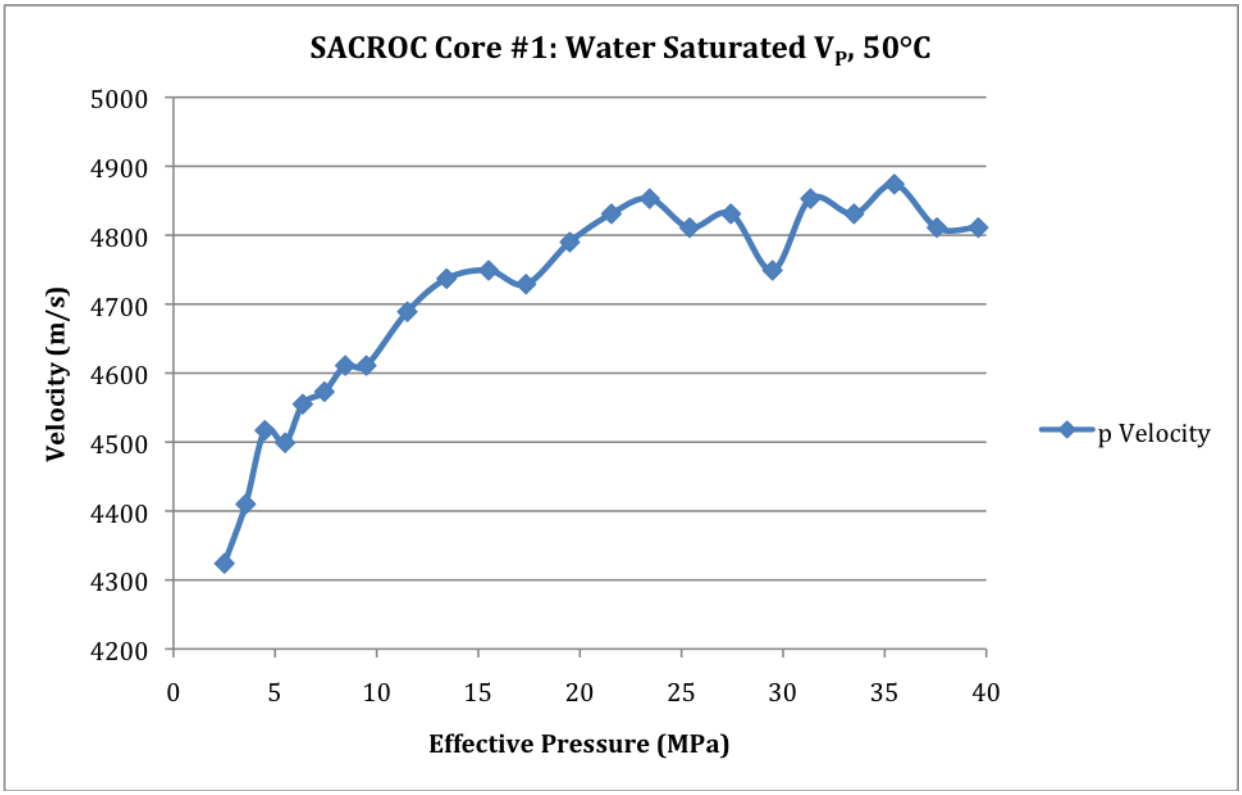

Figure 63: Water saturated V_P, Core #1

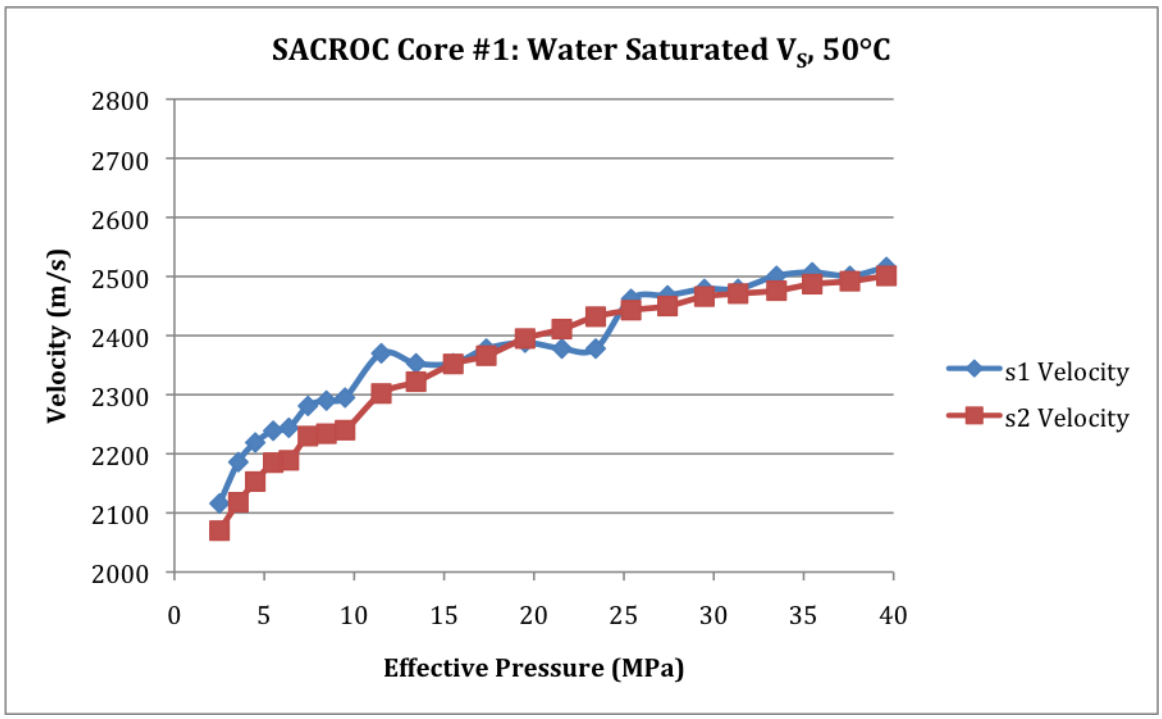

Figure 64: Water Saturated V_S, Core #1

For Core #2, a similar drop in velocities was seen. For V_P velocities, there was a drop of ~400 m/s, corresponding to a velocity change of ~6% (Figure 65). For shear waves, both V_{S1} and V_{S2} dropped with decreasing effective pressure, as in Core #1 (Figure 66). V_{S1} experiences a drop of ~150 m/s, a reduction of ~5%. For V_{S2}, a reduction of ~350 m/s was found, a drop of ~12%.

This shear wave anisotropy in Core #2 was also seen in earlier experiments. In the anisotropy experiments, a large variation was seen in V_{S2} measurements on this same core (Figure 38). Additionally, when saturated with CO_2, we can also see anomalously high V_{S2} velocities (Figure 62). As stated earlier, this effect is much stronger in V_{S2} suggests that this orientation has a much smaller amount of compliant porosity that is aligned with it.

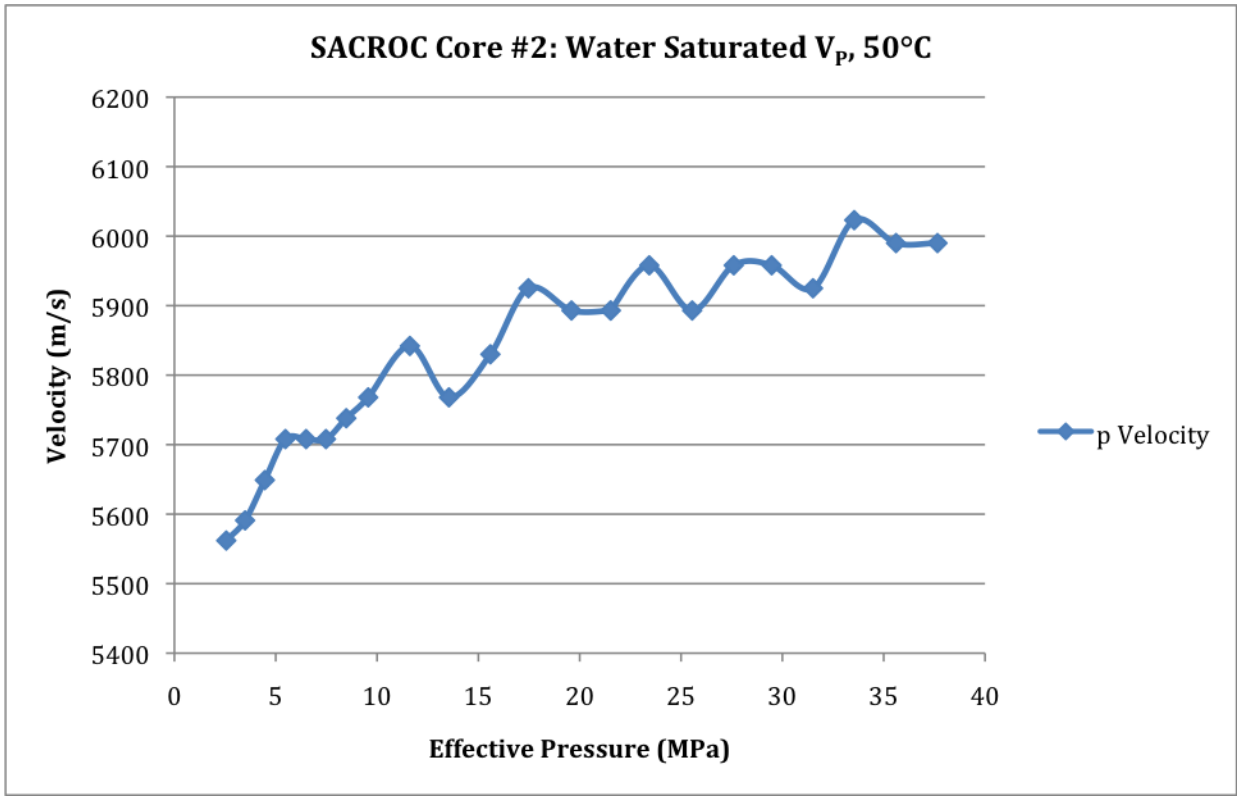

Figure 65: Water Saturated V_P, Core #2

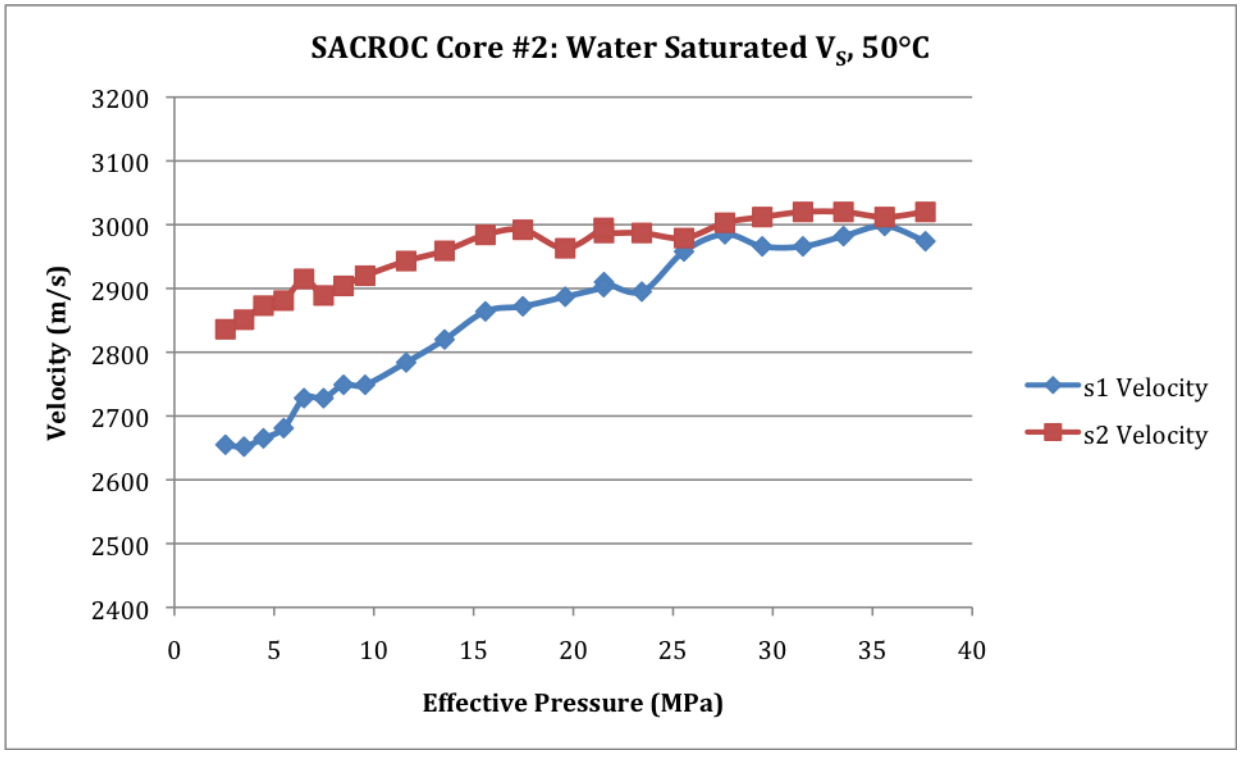

Figure 66: Water Saturated V_S, Core #2

We can then compare these water-saturated measurements to previous measurements in order to quantify velocity differences due to saturation changes. Water-saturated measurements were compared to dry and CO_2 saturated experiments over the same effective pressure range, and at the same temperature. For Core #1, a large increase in compressional velocity can be seen for the water-saturated rock (Figure 67). An increase in velocities of ~10% can be seen.

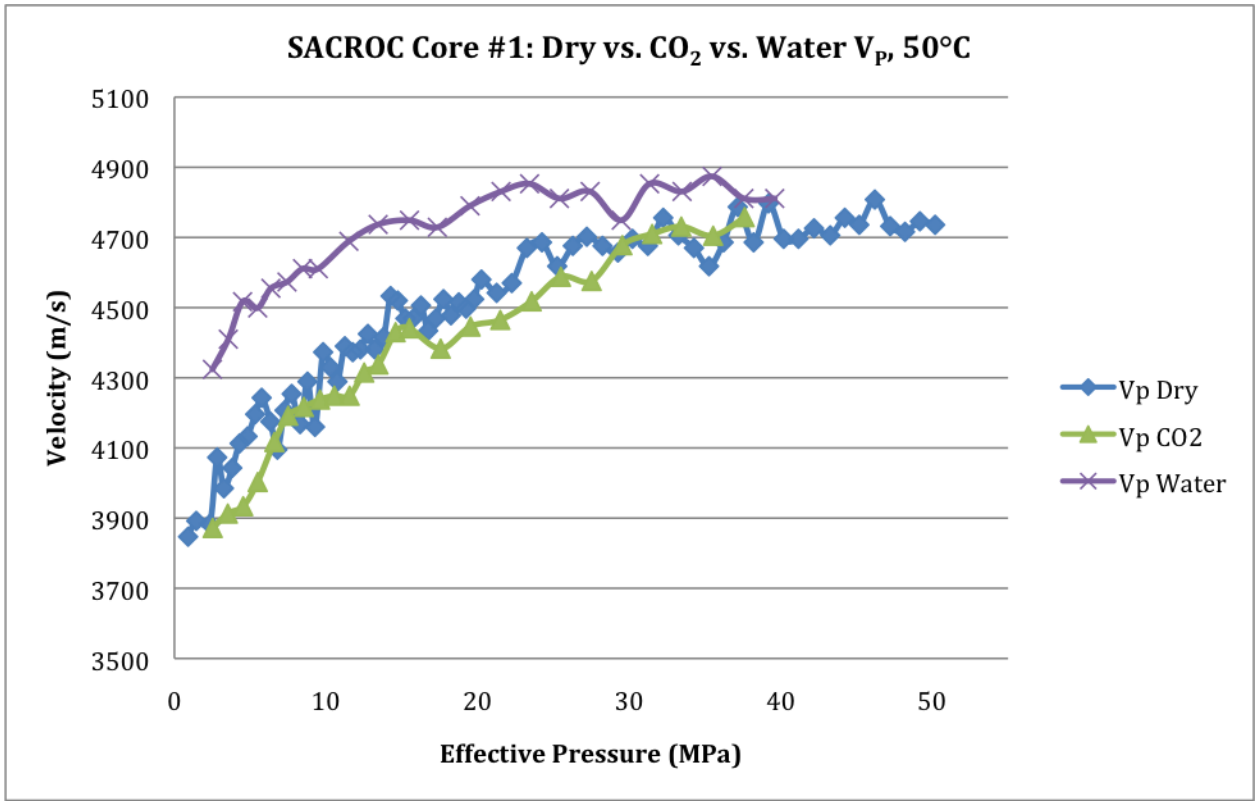

Figure 67: Dry, CO_2 and Water saturated V_P, Core #1

For V_{S1}, very little difference between Dry and Water saturated velocities can be seen (Figure 68). However, CO_2 velocities still show a marked decrease over both dry and water-saturated experiments.

For V_{S2}, the water-saturated velocities are lower than either the dry or the CO_2 saturated experiments (Figure 69). A possible mechanism for this is compliant porosity: whereas supercritical CO_2 opens some of this compliant porosity as the pore pressure is increased (decreasing effective pressure), the denser liquid water would force a much larger portion of this compliant porosity open, even at low pore pressures, since the supercritical CO_2 is able to equilibrate pressure across the pore space very easily compared to the water. This creates zones of higher pressure when water saturated, forcing microcracks to open up at higher effective pressures. It can be seen that CO_2 and Water saturated velocities approach each other as the effective pressure approaches zero (Figure 69).

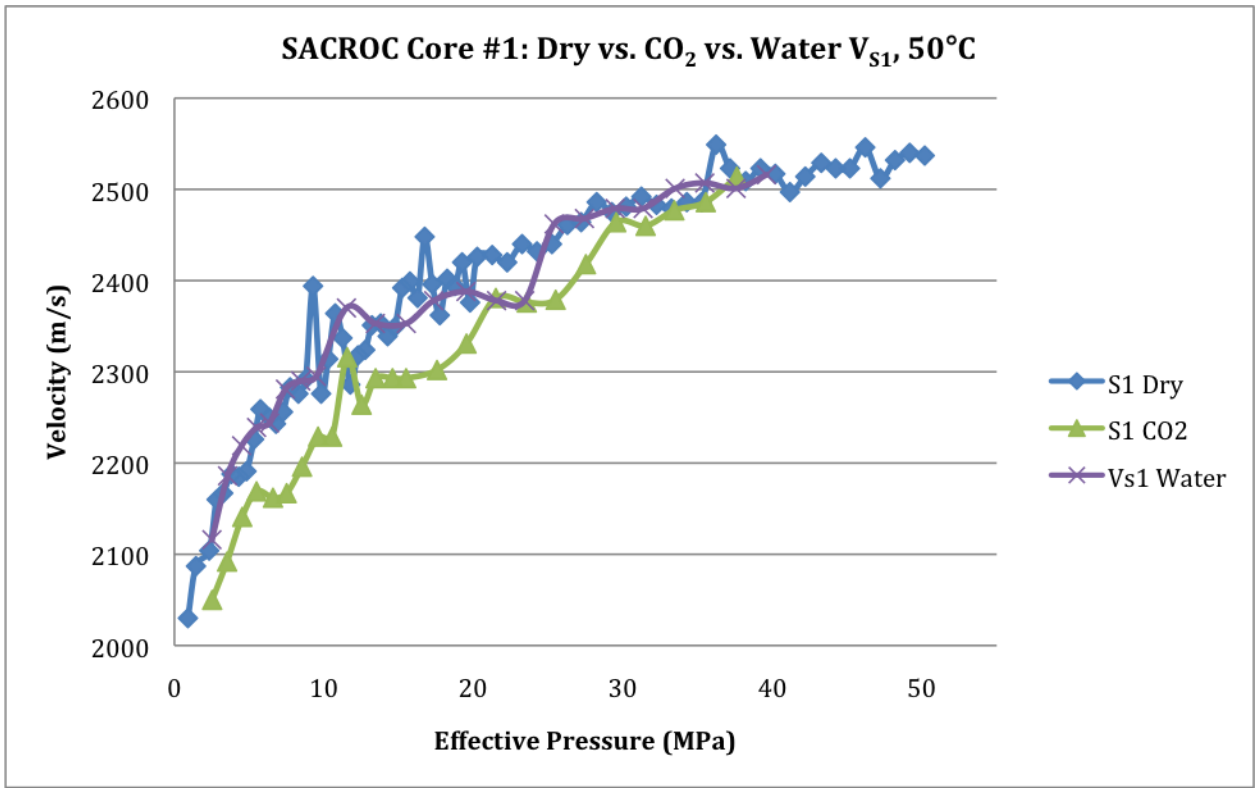

Figure 68: Dry, CO_2 and Water saturated V_{S1}, Core #1

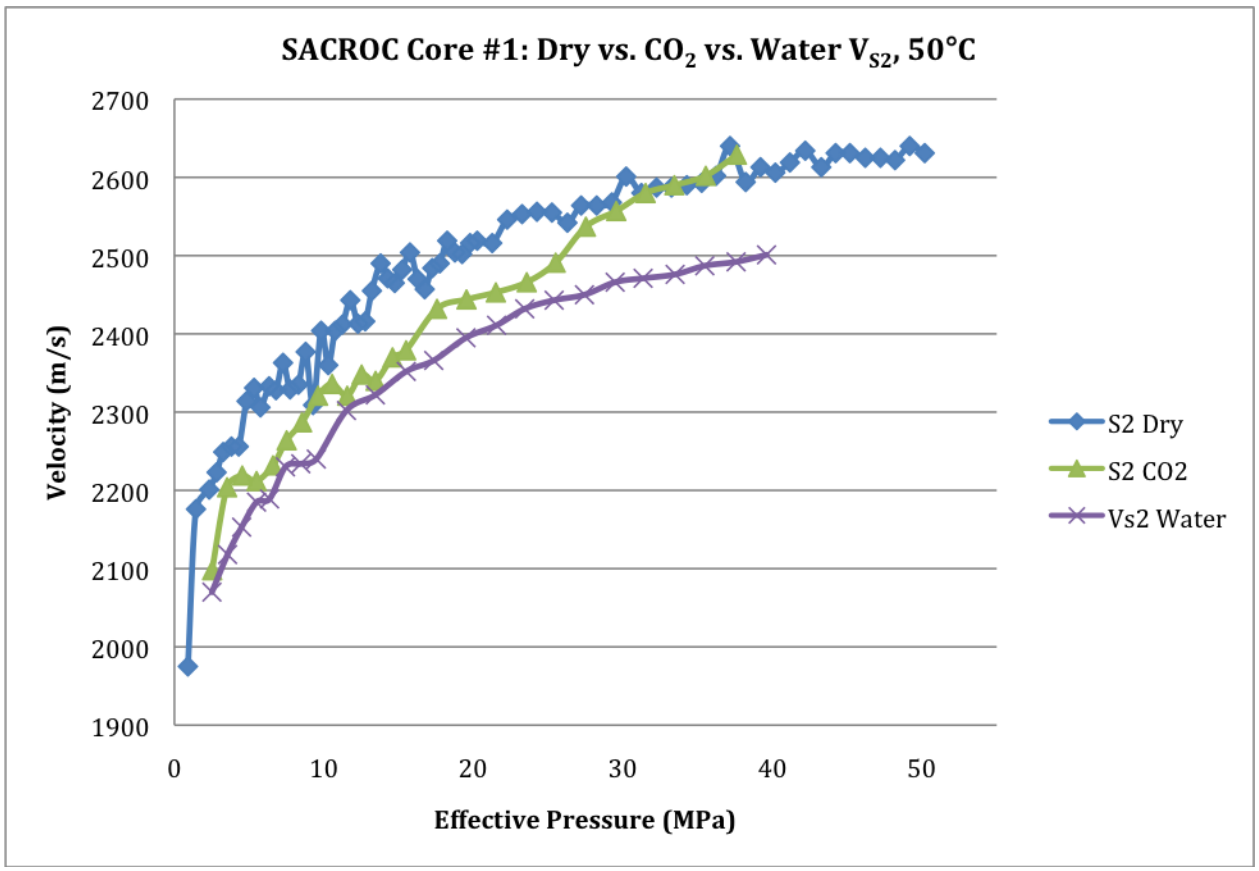

Figure 69: Dry, CO_2 and Water saturated Vs2, Core #1

The comparison of Dry, CO_2 and Water saturated experiments are very similar for Core #2. The Compressional Velocities are ~15% higher for water saturated velocities than for dry velocities, and are ~10% higher than CO_2 saturated velocities (Figure 70). V_{S1} velocities again show very little in the way of fluid effects (Figure 71).

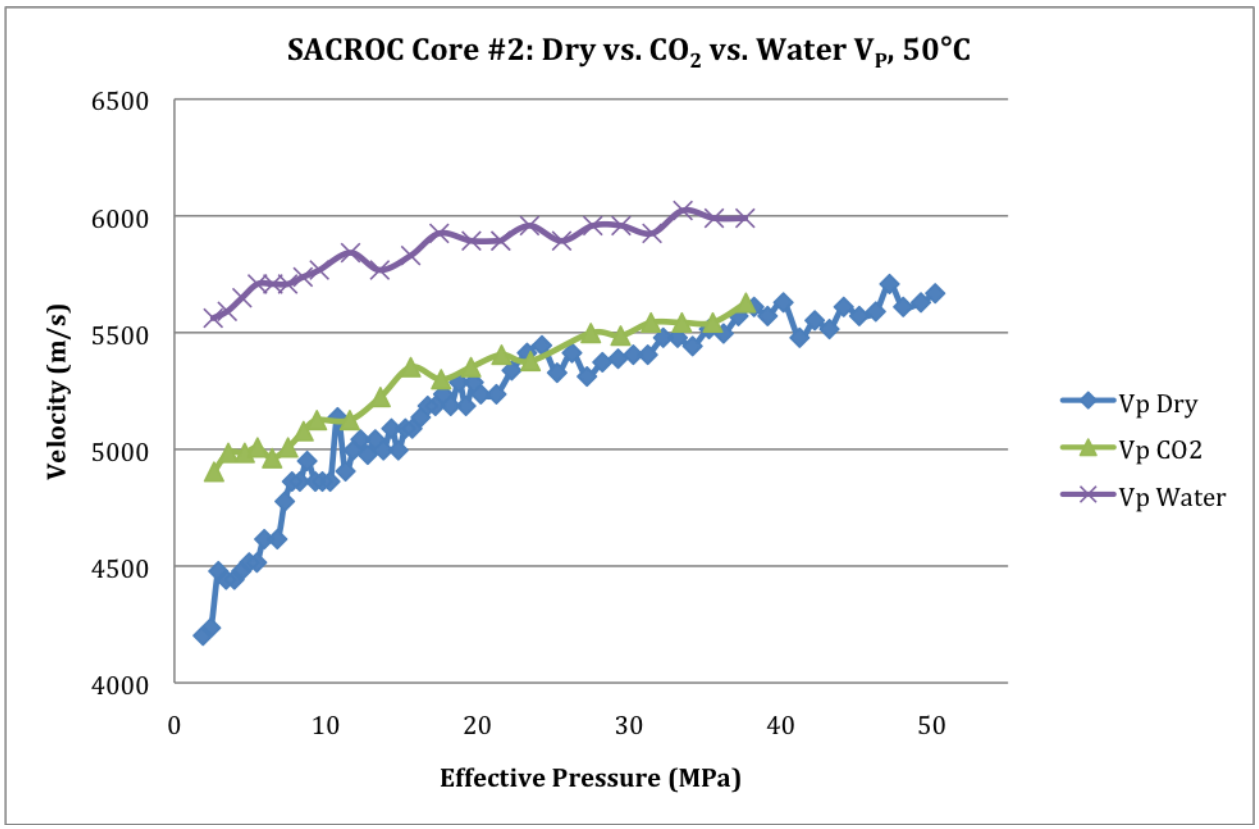

Figure 70: Dry, CO_2 and Water saturated V_P, Core #2

For V_{S2} velocities, the picture becomes more complicated. At high effective pressures, the water-saturated velocities are much lower than the CO_2 saturated velocities, falling very close to the Dry measurements. At lower effective pressures, the water-saturated velocities don't drop as fast as the CO_2 velocities, leading to the water saturated velocities being higher than the CO_2 saturated velocities (Figure 72). A possible mechanism to explain this is the compliant porosity opening as explained above, in addition to an increase of the Shear Modulus at low effective pressures due to a frame stiffening effect of the highly pressurized pore-filling water.

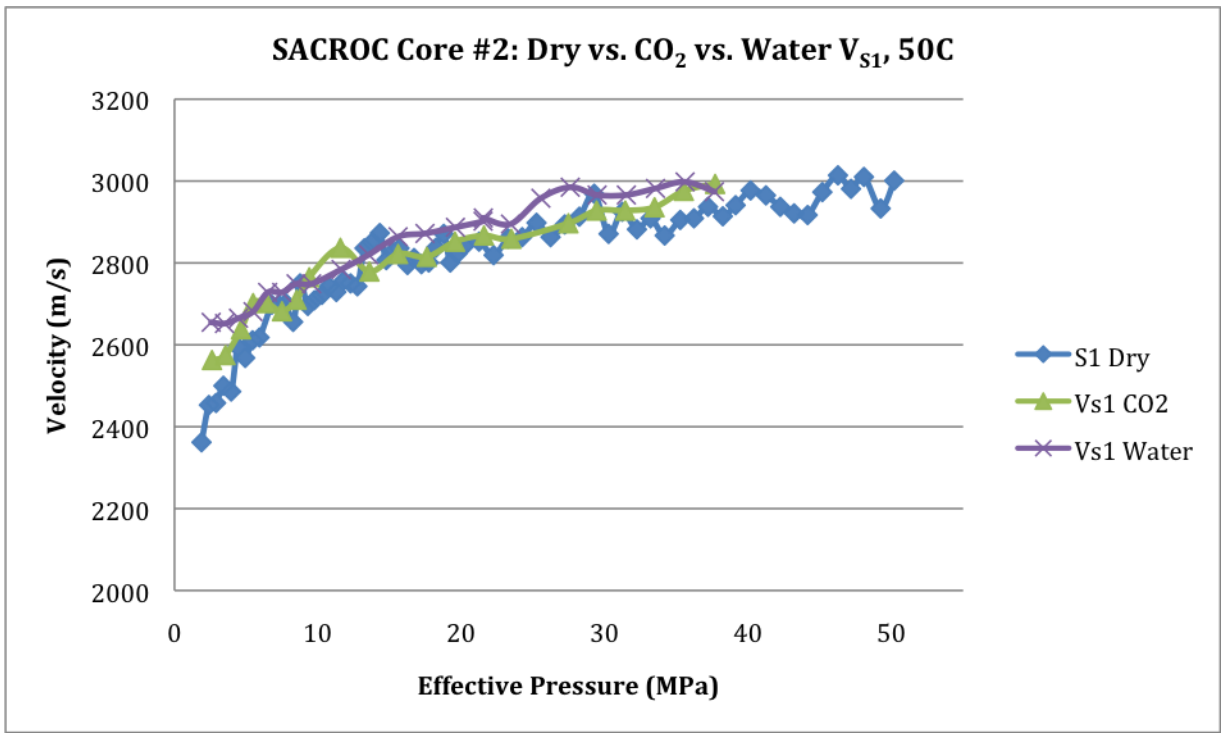

Figure 71: Dry, CO_2 and Water saturated V_{S1}, Core #2

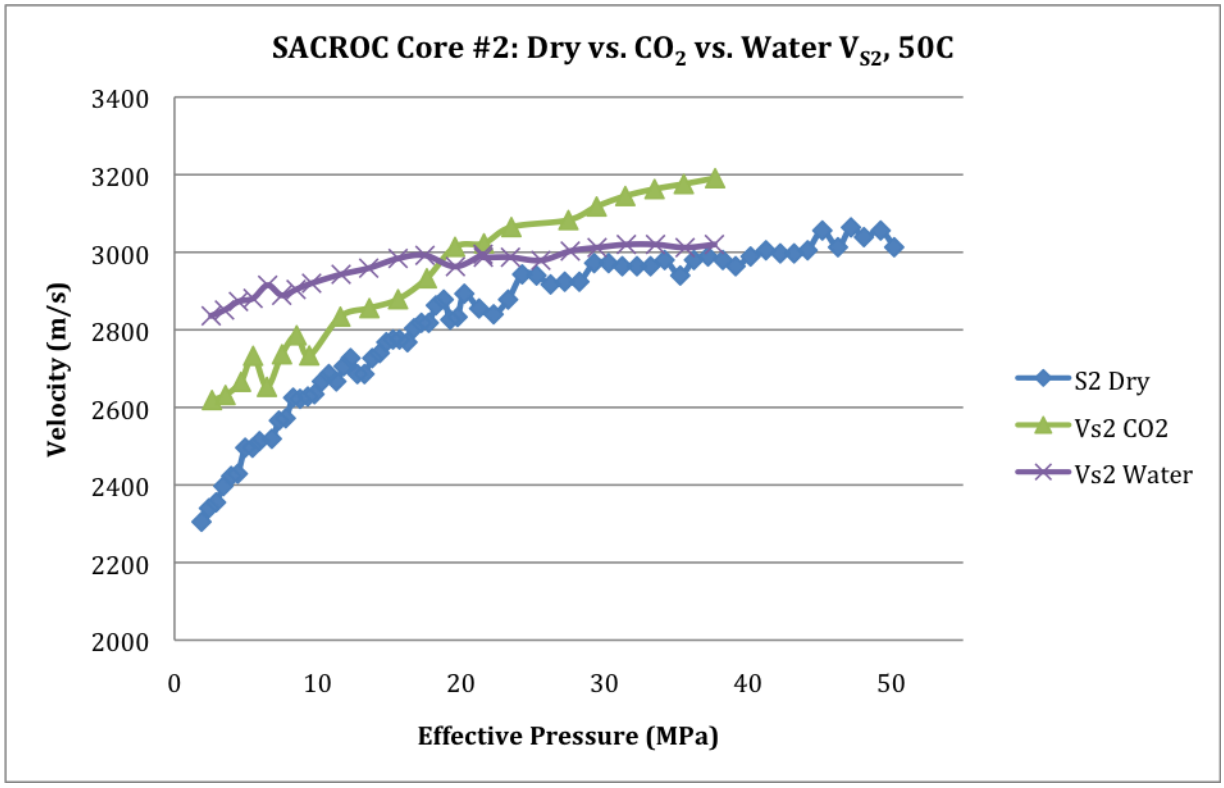

Figure 72: Dry, CO_2 and Water saturated V_{S2}, Core #2

This set of experiments was able to show that the differences between water and CO_2 saturated velocities in our limestone cores were not only detectable, but consistent across the entire pressure range studied. Our limestone reservoir rock, when saturated with CO_2, exhibits lower velocities than when saturated with water. Post injection, as the CO_2 pushes the water out of the pore space, this drop in velocities should be detectable in well logs or seismic imaging. The next step in our velocity experiments is to measure what effect, if any, oil will have on these results.

1.2.6.4 Oil Saturated Experiments

In the study site, CO_2 is being used as tertiary enhanced oil recovery (EOR). The CO_2 flood is used to sweep out any residual oil saturation in the subsurface. The subsurface is unlikely to be under purely water or CO_2 saturated conditions. Ideally, a mixture of pore-filling phases would be studied. Although we do not have the capability to study a mixture of pore-filling phases, a fortuitous accident allowed us to glimpse the effects that oil saturation would have on subsurface velocities.

After the above experiments were completed, an error in the loading of the sample caused Core #1 to become flooded with mineral oil. After a thorough cleaning with alcohol to remove as much oil as possible, the sample was weighed and compared to previous measurements. We assume this state to be the residual oil saturation, as all efforts were made to remove as much oil as possible. It was found that the weight of the sample increased from 303.73g to 306.90g, an increase of 3.17g. The density of the mineral oil used in our system is 0.88 g/cc. This corresponds to the sample retaining 3.60 cc of oil.

The reduction of connected porosity was then investigated using the helium porosimeter. The porosity of the sample was found to be 13.91%, a loss of 4.59% from the original 18.5% porosity. This porosity loss corresponds to a loss of 6.31 cc of pore space, much larger than the amount of oil in the sample based on mass measurements. Since the helium porosimeter cannot measure absolute porosity (here used to mean all pore space contained in the sample), but only interconnected porosity (that is, pore space that the helium is able to reach), we then have a direct measure of the loss of interconnected porosity due to a known amount of oil saturation. Only 57% of the lost interconnected porosity is actually saturated with oil, leading to the conclusion that the oil effectively blocks off pore throats, thereby creating 2.71 cc of isolated pore space.

Since this accident allowed us to investigate the effects of residual oil saturation on one of our samples, a set of experiments was performed to investigate the effects the oil would have on the velocity. First, a set of dry experiments was performed. The confining pressure was increased to 50 MPa, and then slowly lowered in order to investigate any possible hysteresis effects. As the pressure was lowered in increments of 5 MPa, a measurement was taken as soon as the pressure was lowered, and then again after waiting 5 minutes. This procedure was first performed at a temperature of 25°C, and then repeated at 50°C.

For the 25°C measurements, the character of the velocities vs. pressure is unchanged (Figure 73, Figure 74). The difference in the initial and delayed hysteresis curves appears to be minimal. In order to investigate these hysteresis effects, the difference between them was calculated and plotted. It can be seen the character of the hysteresis effects is much different for the oil-

saturated sample than it is for the original dry sample (Figure 75). A large hysteresis effect can be seen at low effective pressures, and this effect effectively becomes zero by 15 MPa, and although some slight variation is still seen above this pressure, it is not consistent. The obvious explanation for this effect is due to the residual oil saturation. Whereas the hysteresis effects decay slowly with increasing effective pressure in the original dry rock (Figure 50), the only significant hysteresis effects seen here are at relatively low effective pressures (Figure 75). This is due to the oil filling up part of the pore space. The oil has a stiffening effect on the pore space, increasing the bulk modulus, and after pressurization, it moves out of the smallest pores. This shifting of the small amount of fluid inside the pore space is likely to account for hysteresis effects, and is likely not reversible.

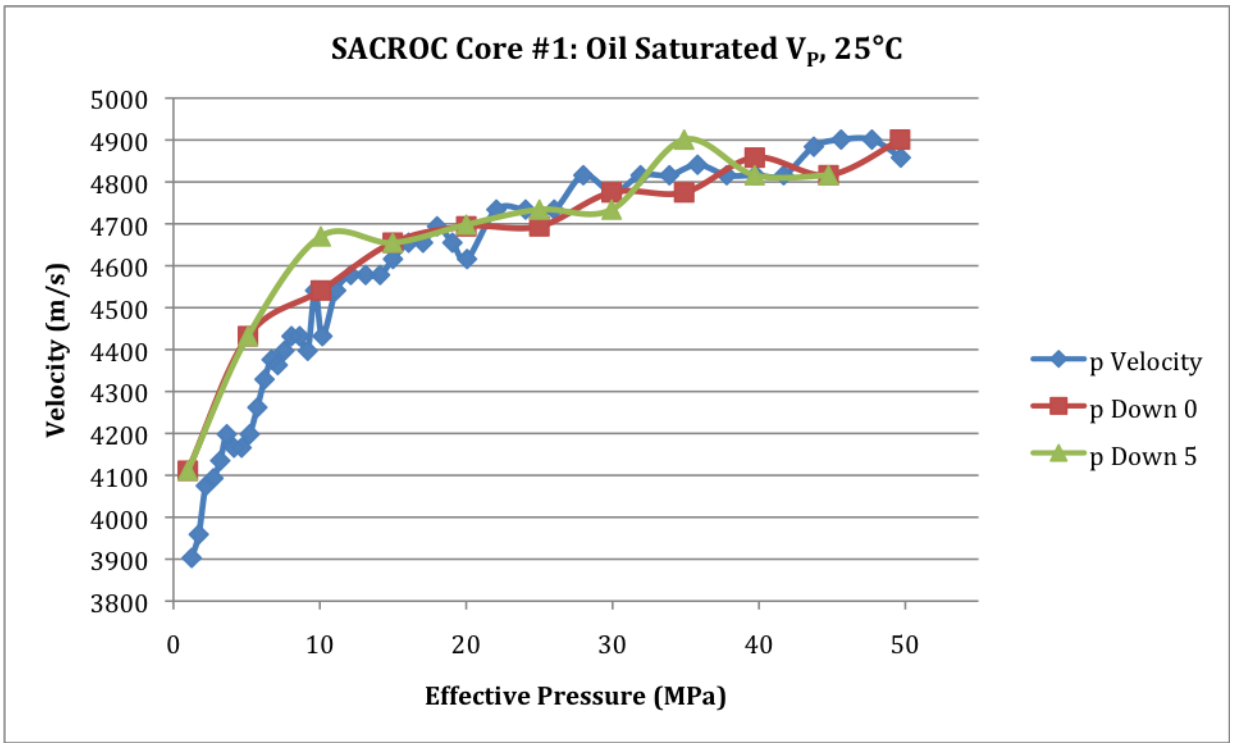

Figure 73: Oil Saturated Core #1 V_P, 25°C

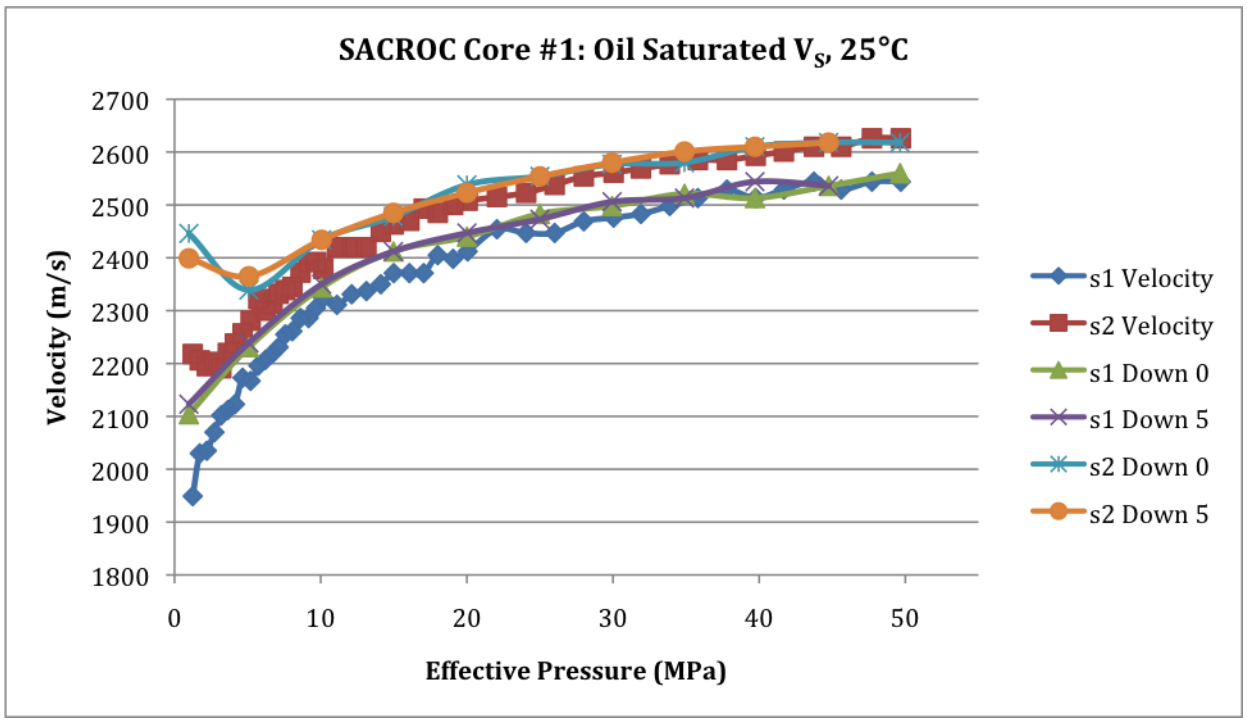

Figure 74: Oil Saturated Core #1 V_S, 25°C

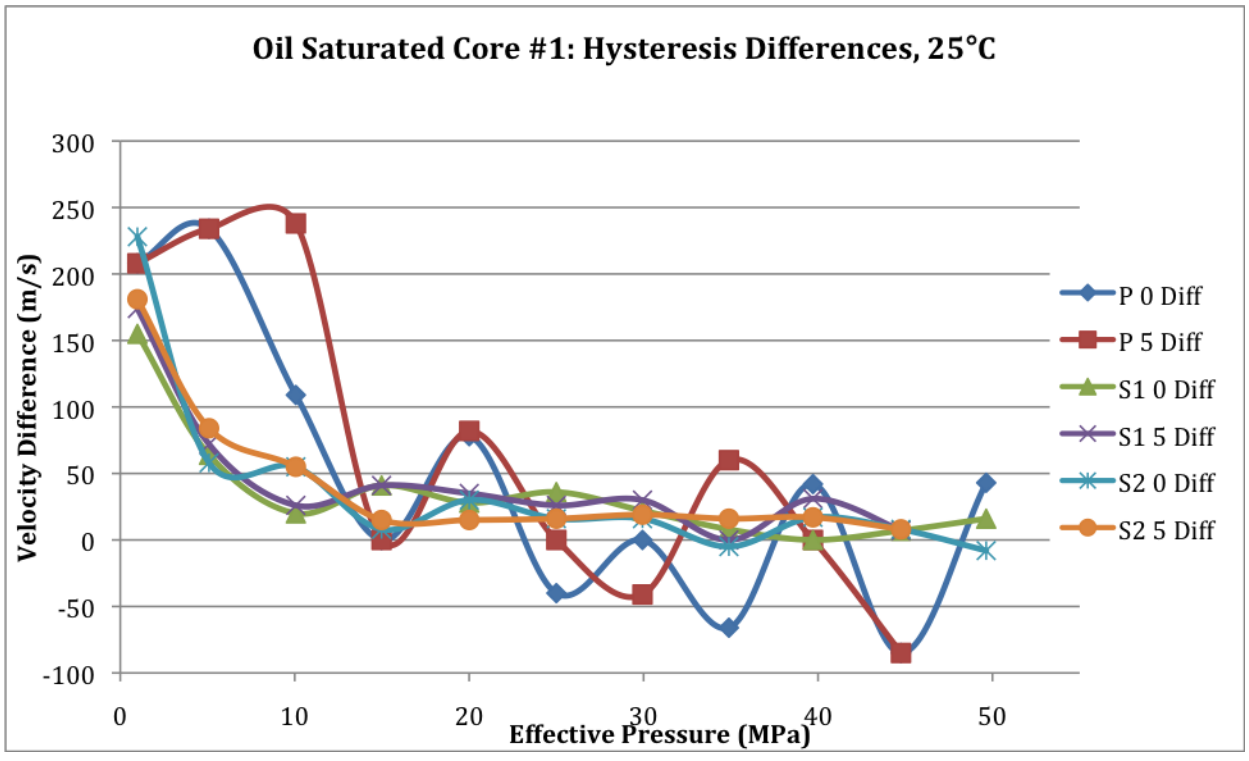

Figure 75: Oil Saturated Core #1, Hysteresis Differences, 25°C

For the measurements taken at 50°C, the response of the velocities to pressure is unchanged (Figure 76, Figure 77). The difference in the initial and delayed hysteresis curves appears to be minimal. In order to investigate these hysteresis effects, the difference between the pressurization and depressurization curves were calculated. The hysteresis effects at 50°C show a very different character than the 25°C measurements (Figure 78). V_P shows variation, but no clear trend with pressure, whereas V_{S1} shows an increased hysteresis effect at low pressures. V_{S2} velocities show a negative hysteresis effect at the lowest effective pressure, then a positive hysteresis effect that decreases with increasing pressure. The reason for these discrepancies is not clear, though it could be related to a decrease in the mineral oil's viscosity at higher temperatures, decreasing any pressure differentials found in the pore space at the lower temperatures.

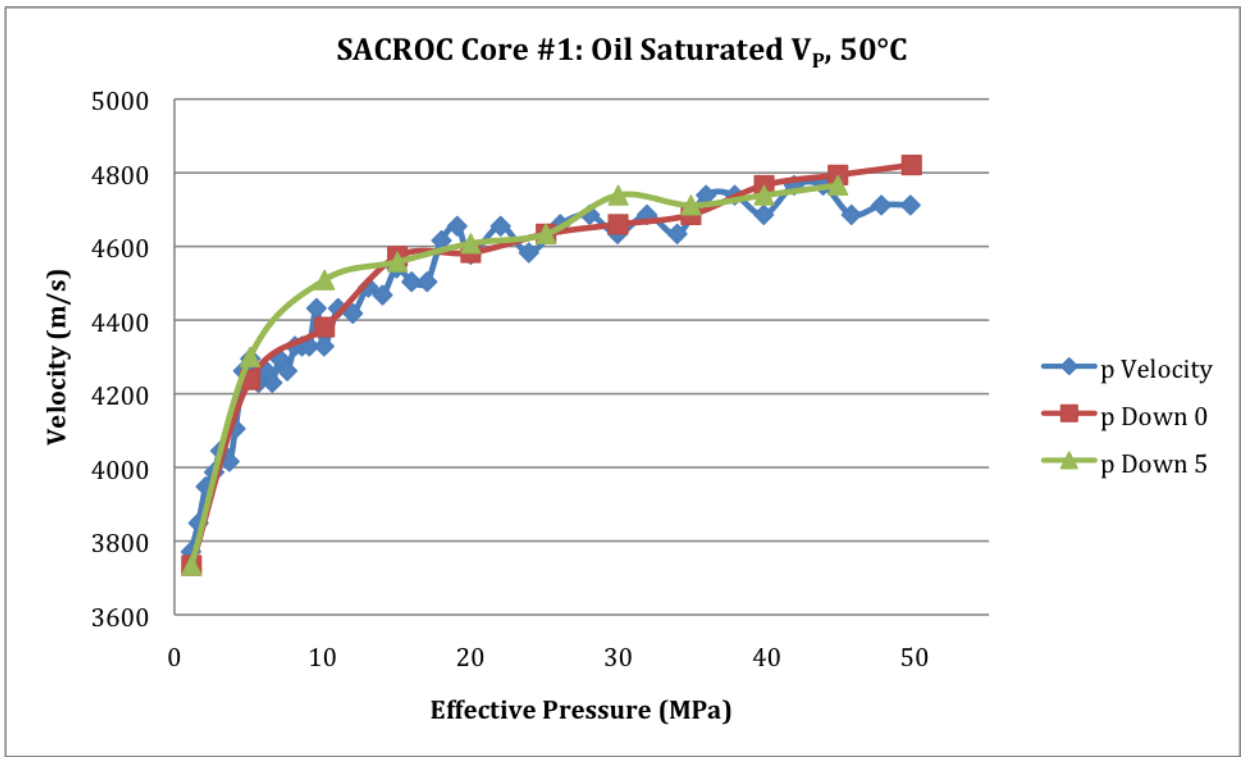

Figure 76:Oil Saturated Core #1 V_P, 50°C

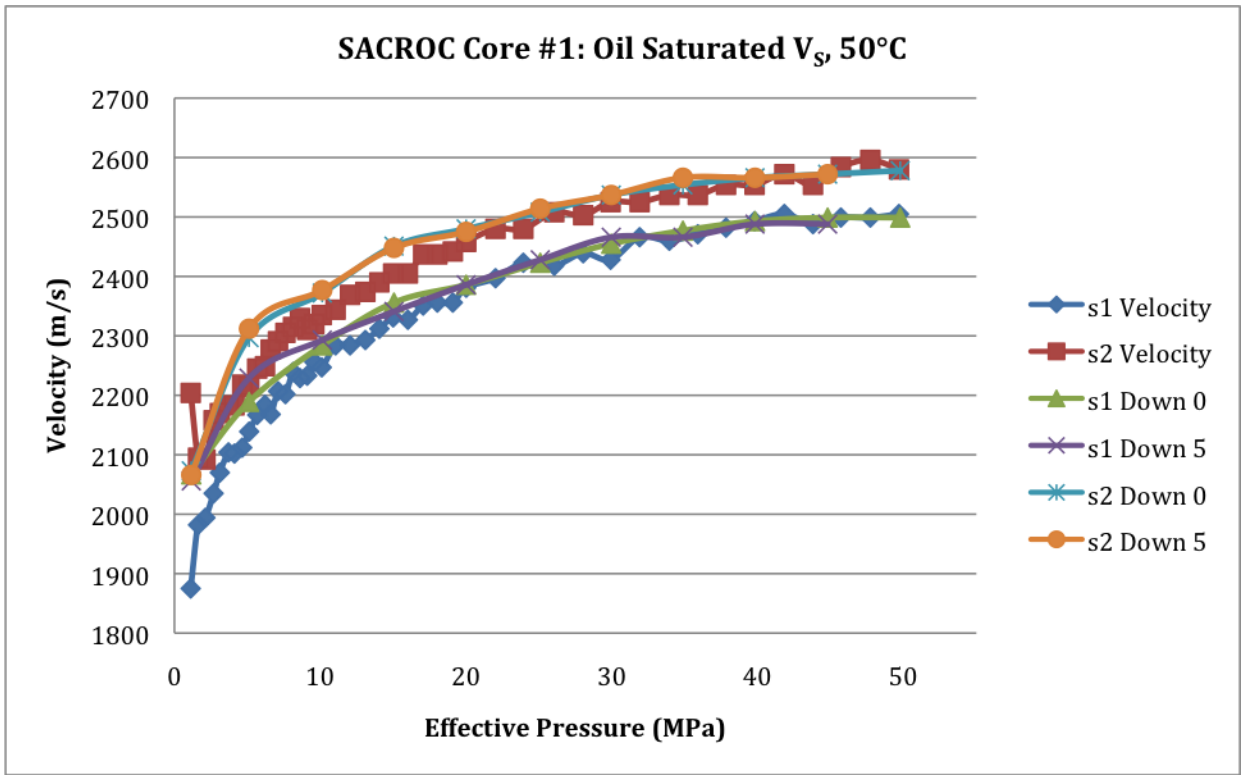

Figure 77: Oil Saturated Core #1 V_S, 50°C

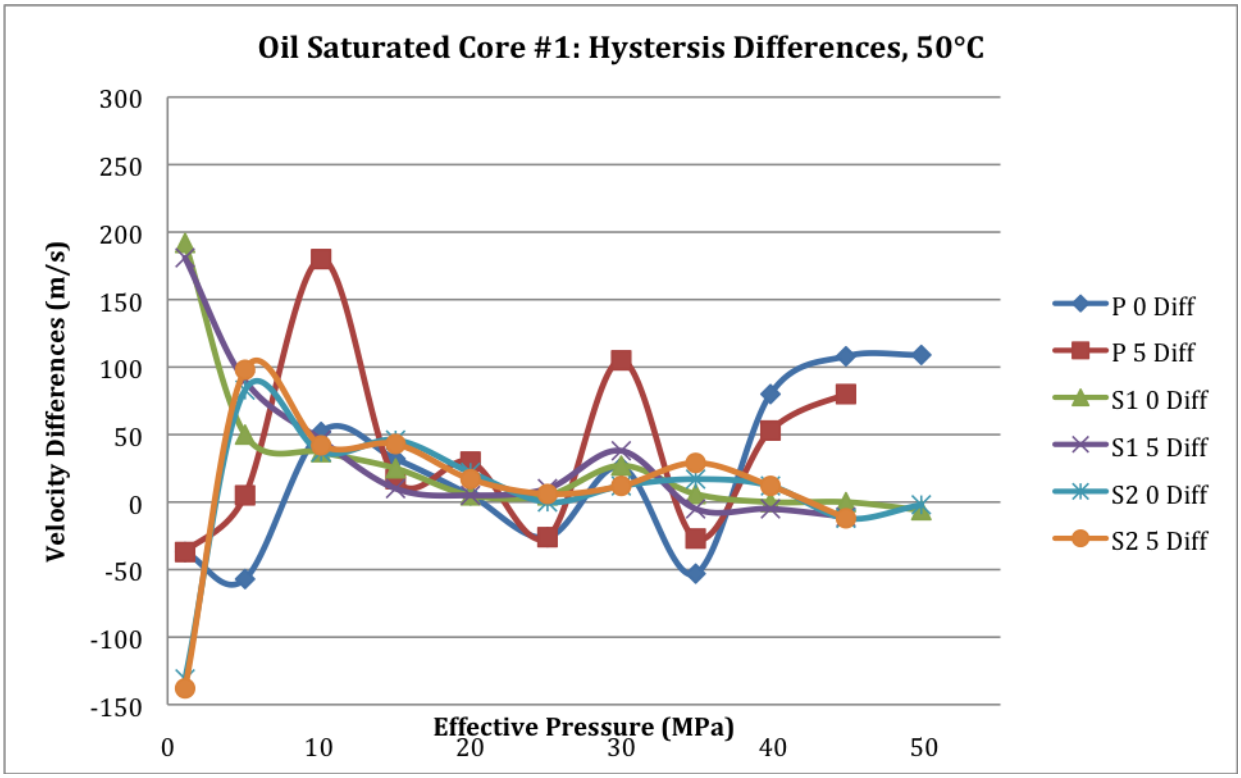

Figure 78: Oil Saturated Core #1, Hysteresis Differences, 50°C

The next logical step is to compare the oil saturated measurements to those of the initial dry rock. When we examine the V_P velocities, a few things can be noticed: at low effective pressures, the differences are small, less than ~100 m/s, but as the effective pressure increases, the spread in velocities increases; in addition, although both oil saturated measurements have a higher velocity than the dry sample, the 25°C measurement has a consistently higher velocity than the 50°C measurement does (Figure 79).

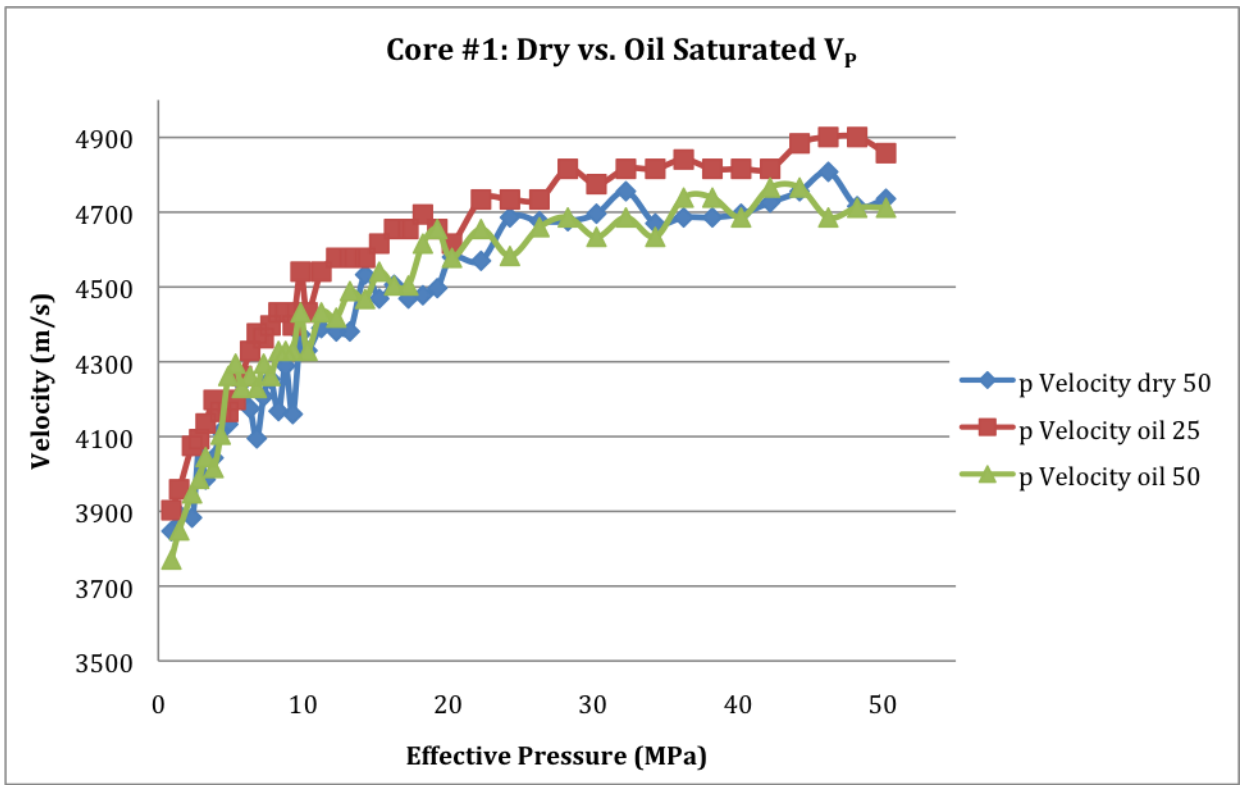

Figure 79: Core #1 Dry vs. Oil Saturated V_P

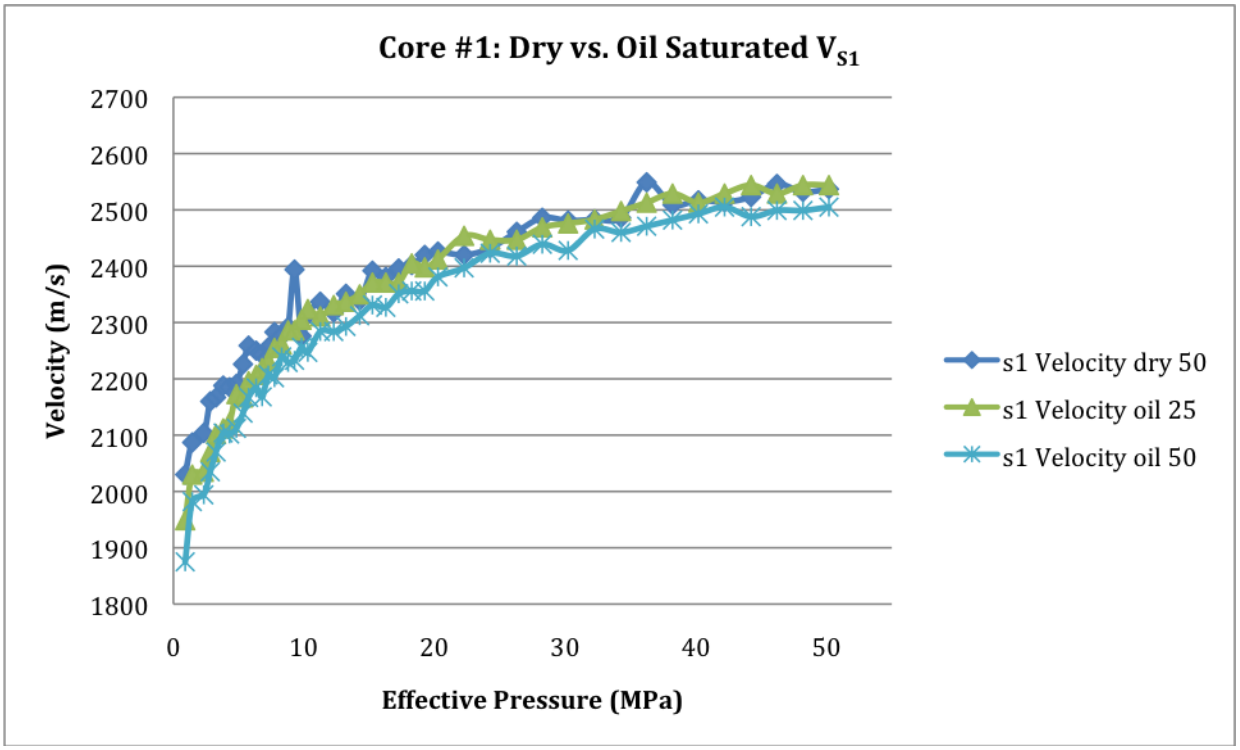

Figure 80: Core #1 Dry vs. Oil Saturated V_{S1}

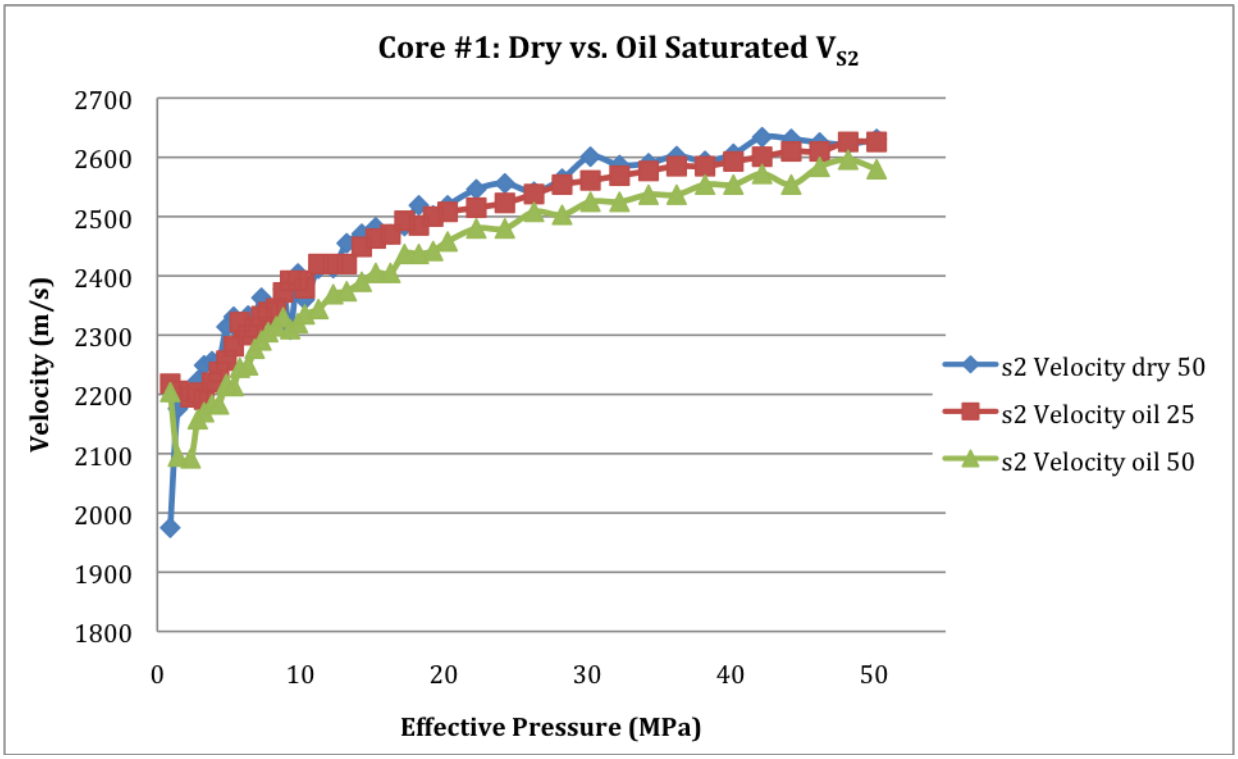

Figure 81: Core #1 Dry vs. Oil Saturated V_{S2}

For V_{S1}, the velocities all show a similar spread of values over the entire pressure range, but the Oil saturated 50°C measurements appear to be slower than the dry velocities across the entire pressure range (Figure 80). As with V_P, the 50°C measurements are slower than the measurements for 25°C.

For the V_{S2} experiments, the trends are similar to those of V_{S1} (Figure 81). The Oil-saturated measurements have a slower shear velocity than the dry samples, and the 50°C measurements are slower than the 25°C measurements.

Since we wanted to investigate the velocity differences between the dry and oil-saturated experiments, the difference between 50°C oil-saturated and dry measurements was calculated for V_P, V_{S1} and V_{S2} (Figure 82). This was calculated by subtracting the Dry velocities from the Oil-Saturated velocities. The most obvious thing is the positive V_P response vs. the negative V_{S1} and V_{S2} response. The increase in V_P is due to the added density provided by the oil, and the increasing bulk modulus due to saturation changes. For isotropic rocks, the Shear Modulus stays fixed with differing states of saturation, and only density effects are important. However, the Brown and Koringa relations predict that for certain anisotropic conditions, fractured rocks can show shear wave sensitivity to saturation (Cardona 2001). Certain fracture symmetries can lead to a decrease in Shear Modulus when more compressible pore-filling phases are present (Cardona 2001). Although only a small amount of oil is present in the sample, it is distributed across the entire sample. In some locations, oil in the pore throats could trap air in the pore space, creating zones of unequal pressure, and increasing the compressibility of the pore-filling phase, even under only confining pressure.

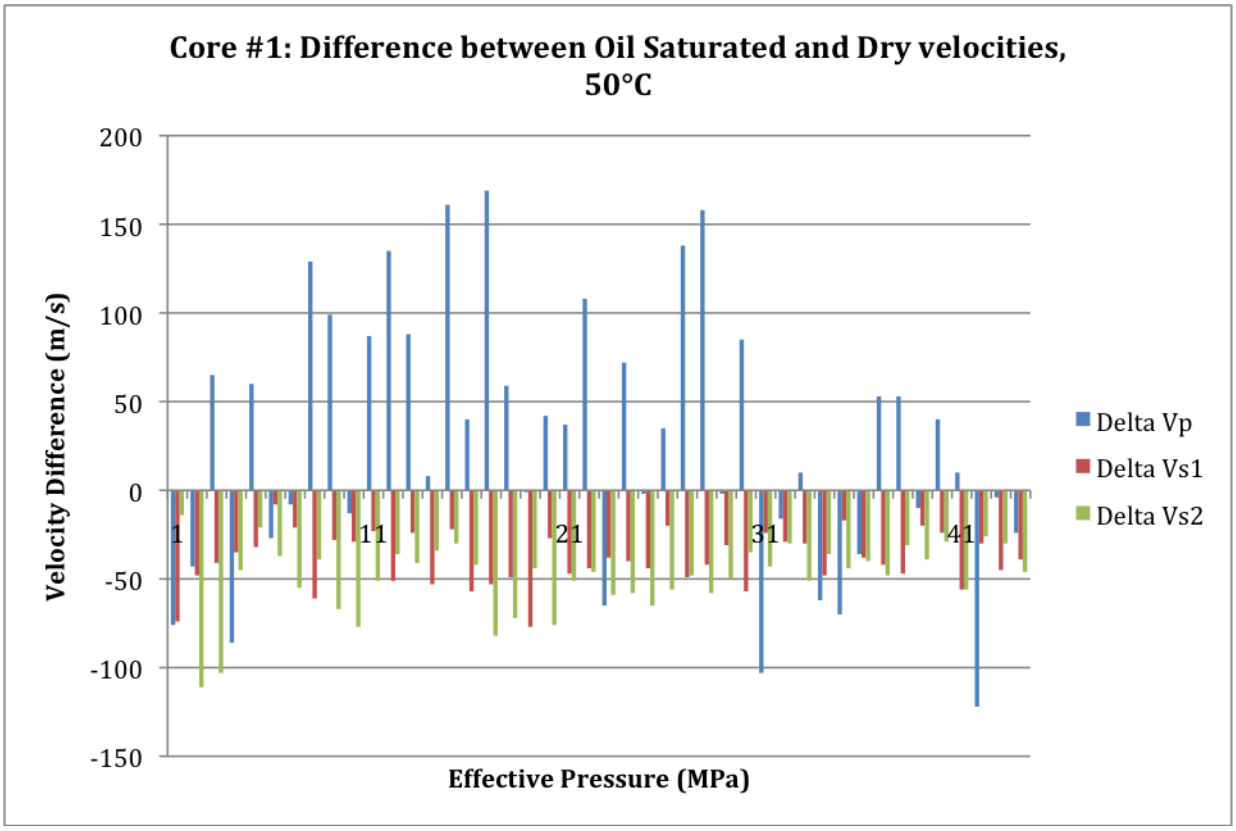

Figure 82: Velocity Differences, Dry vs. Oil, Core #1, 50°C

In order to better quantify these velocity differences, histograms were made to see the distribution of positive and negative velocity changes. The differences were binned and plotted in a histogram, and then a curve was fit to the data in order to attempt to find the peak of the distribution. When the V_P difference histogram is examined, it becomes clear that the overall trend is a positive velocity response to oil saturation of Core #1. Although negative responses were recorded at certain pressures (due to possible picking errors and pressure effects), the overall distribution shows an average velocity increase in the 50-100 m/s bin. This velocity increase is logical due to the increasing bulk modulus and density provided by the oil in the pore space.

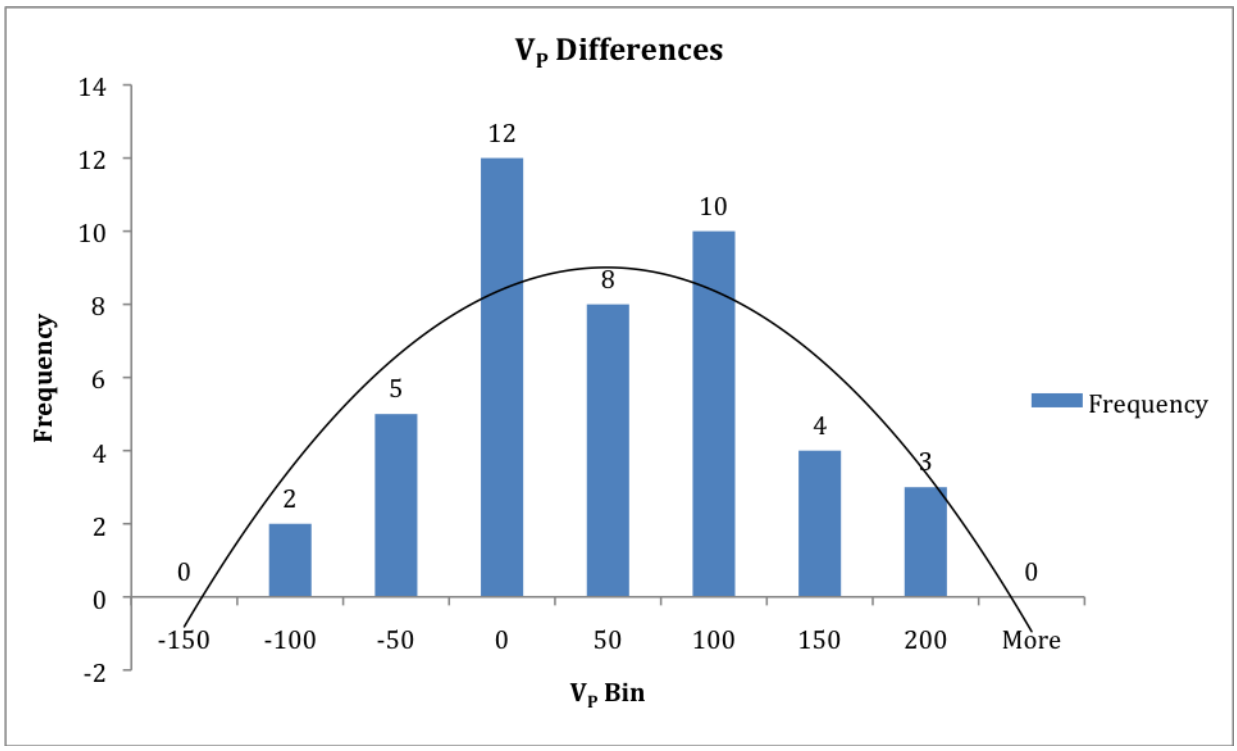

Figure 83: Histogram of V_P Differences, Dry vs. Oil, Core #1, 50°C

When the V_{S1} difference histogram is examined, we see that at no pressures was a velocity increase recorded with the addition of oil. The average velocity response to the oil saturation falls in the -40 to -60 m/s bin. If we examine V_{S2}, a very similar story is seen: only negative responses were recorded, with the average velocity response falling in the -40 to -60 m/s bin. The spread of velocity differences was larger than for V_{S1}, although this is likely due to anisotropic effects observed in earlier experiments. This velocity decrease is interesting, because Gassmann's theory stipulates that shear modulus (and hence shear wave velocity) should not be effected by fluid effects. Since the density of the oil-saturated sample is higher than the dry sample due to the introduction of oil, the velocity should correspondingly increase, not decrease. However, this assumes an isotropic rock, which is an unrealistic assumption for our sample, a complex limestone (Mur, Purcell et al. 2010). This shear wave anisotropy was outlined earlier.

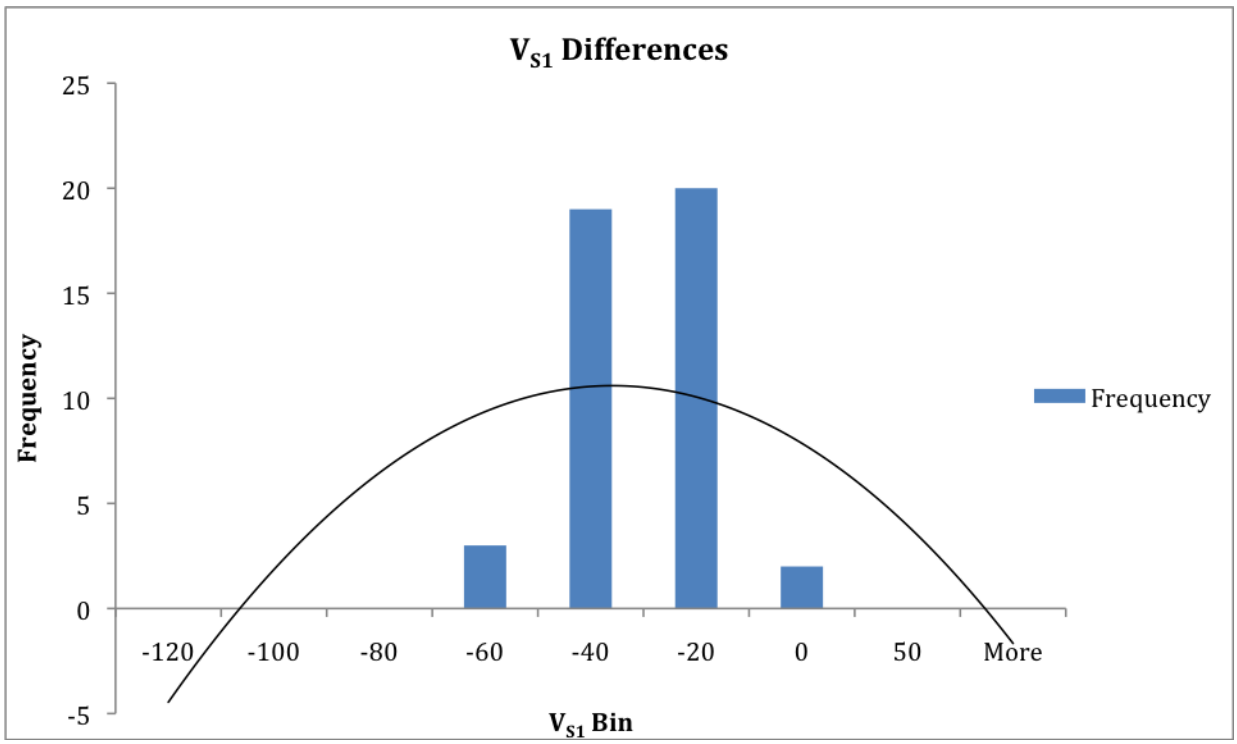

Figure 84: Histogram of V_{S1} Differences, Dry vs. Oil, Core #1, 50°C

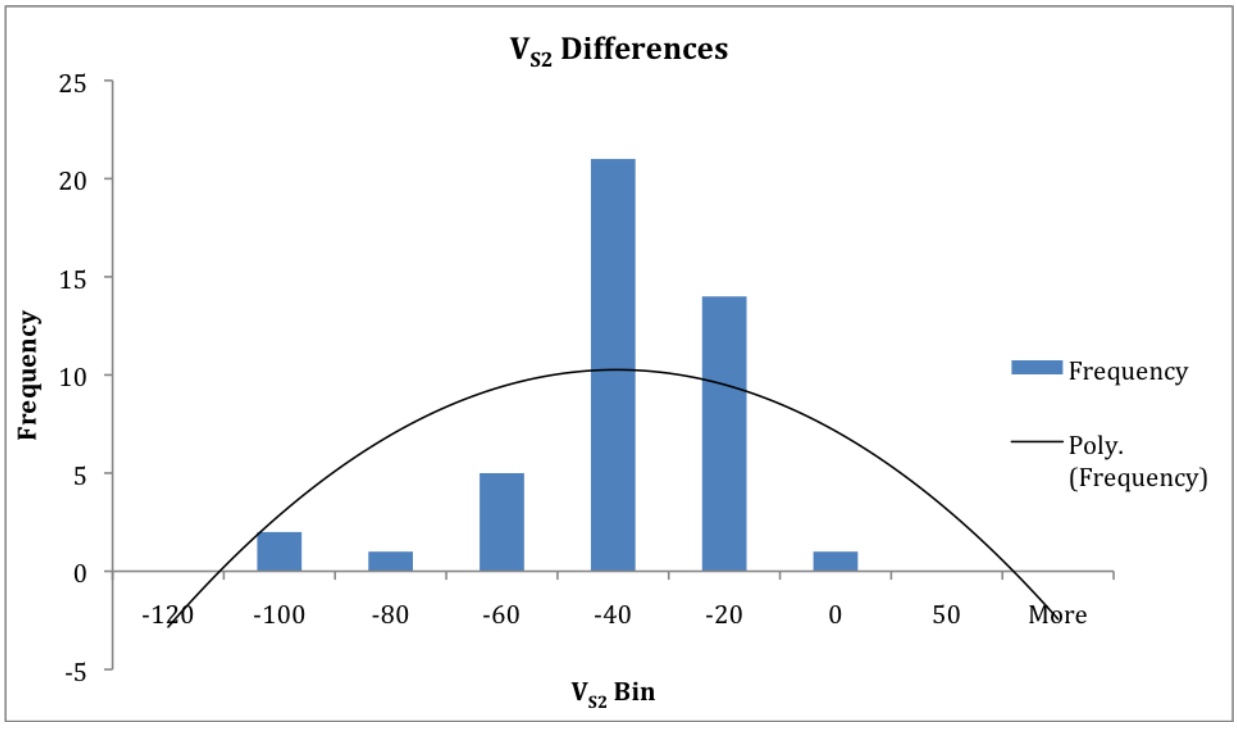

Figure 85: Histogram of V_{S2} Differences, Dry vs. Oil, Core #1, 50°C

It has been shown that for a sample under conditions of equilibrated pore pressure, that for fractured rocks with symmetry lower than or equal to monoclinic, the Brown and Koringa relations predict a saturation induced shear wave velocity change (Brown 1975; Cardona 2001). When the compressibility of the pore fluid increases, a decrease in shear velocities can occur. Additionally, other studies have found changes in V_{S1} and V_{S2} velocities in time-lapse seismic surveys over a CO_2 sequestration site (Duranti 1999). As stated earlier, it is possible that oil in the pore throats could trap air in the pore space, creating zones of unequal pressure, and increasing the compressibility of the pore-filling fluid.

Since this opportunity to study the effects of residual oil saturation on our reservoir rock presented itself, the next experiment performed was to saturate the rock with supercritical CO_2 under reservoir conditions to see the effect this oil would have on the velocity response due to CO_2 saturation. These experiments represent the closest analogue to in situ conditions in the reservoir that could be carried out in our lab.

When we compare these CO_2 saturated velocities with the CO_2 saturated velocities taken before oil saturation, we see some small, but detectable differences. For V_P, at low effective pressures, the velocities with and without oil are very close to one another (Figure 86). At higher effective pressures, the oil-saturated velocities are lower than the velocities without oil. For V_{S1}, the oil-saturated velocities are lower across the entire pressure range (Figure 87). For V_{S2}, the oil-saturated velocities are lower, with the difference increasing with effective pressure (Figure 88).

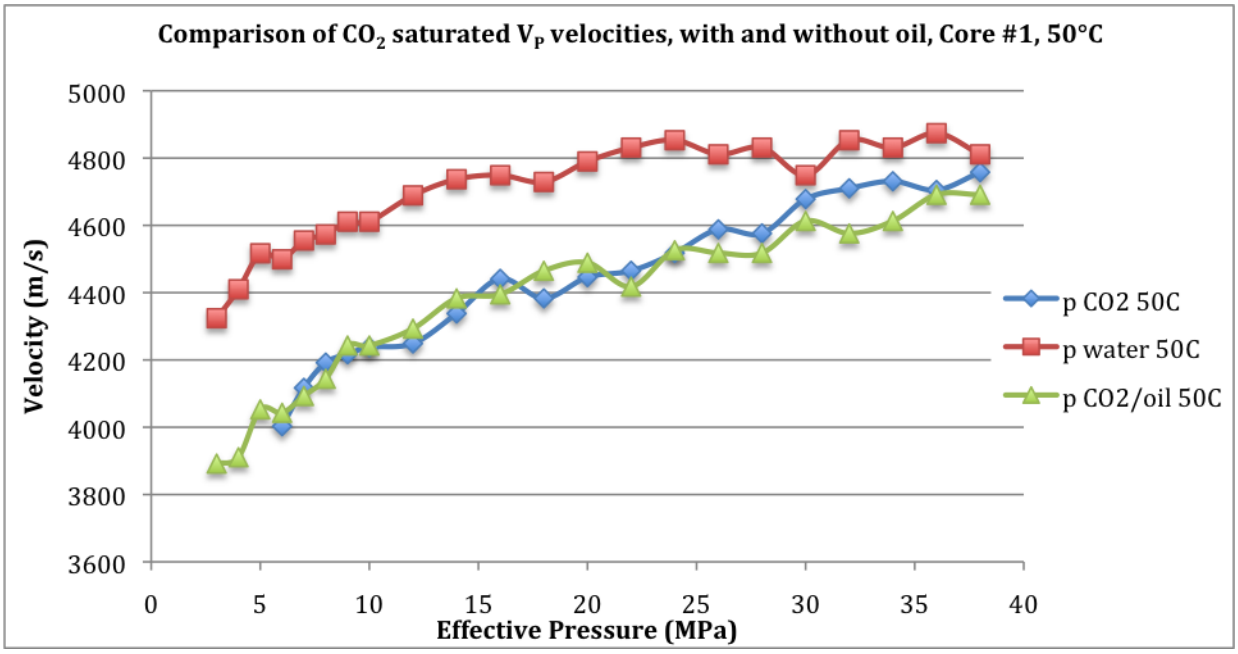

Figure 86: Comparison of CO_2 saturated V_P, before and after oil saturation.

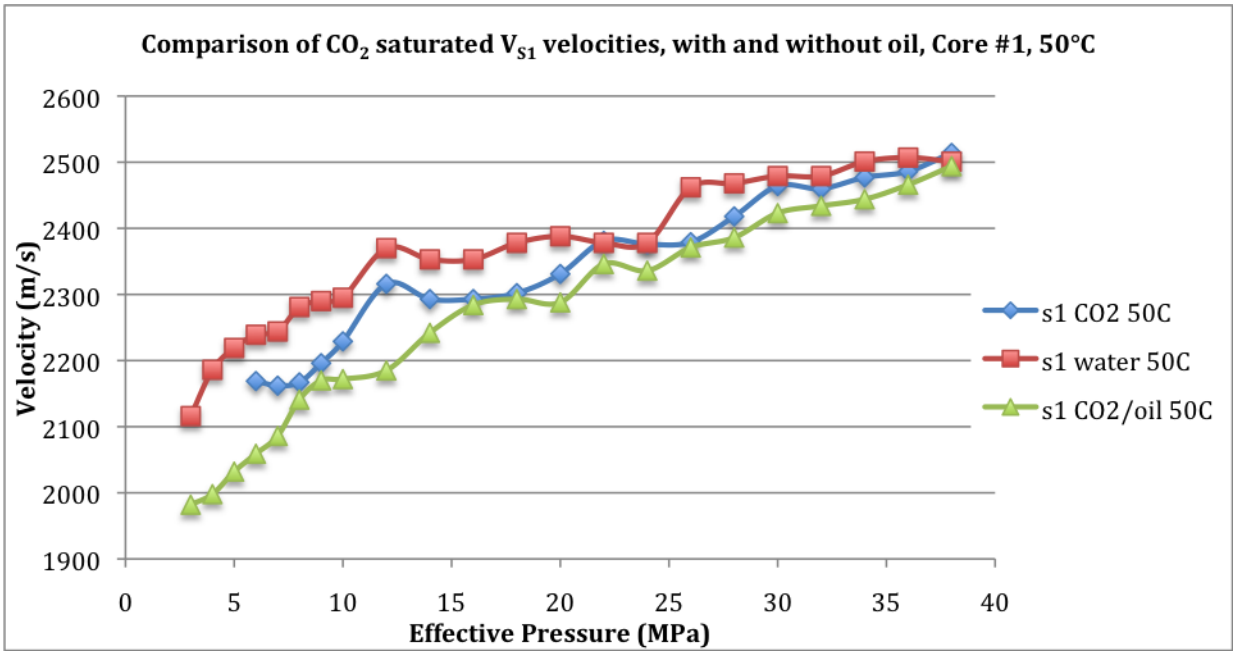

Figure 87: Comparison of CO_2 saturated V_{S1}, before and after oil saturation.

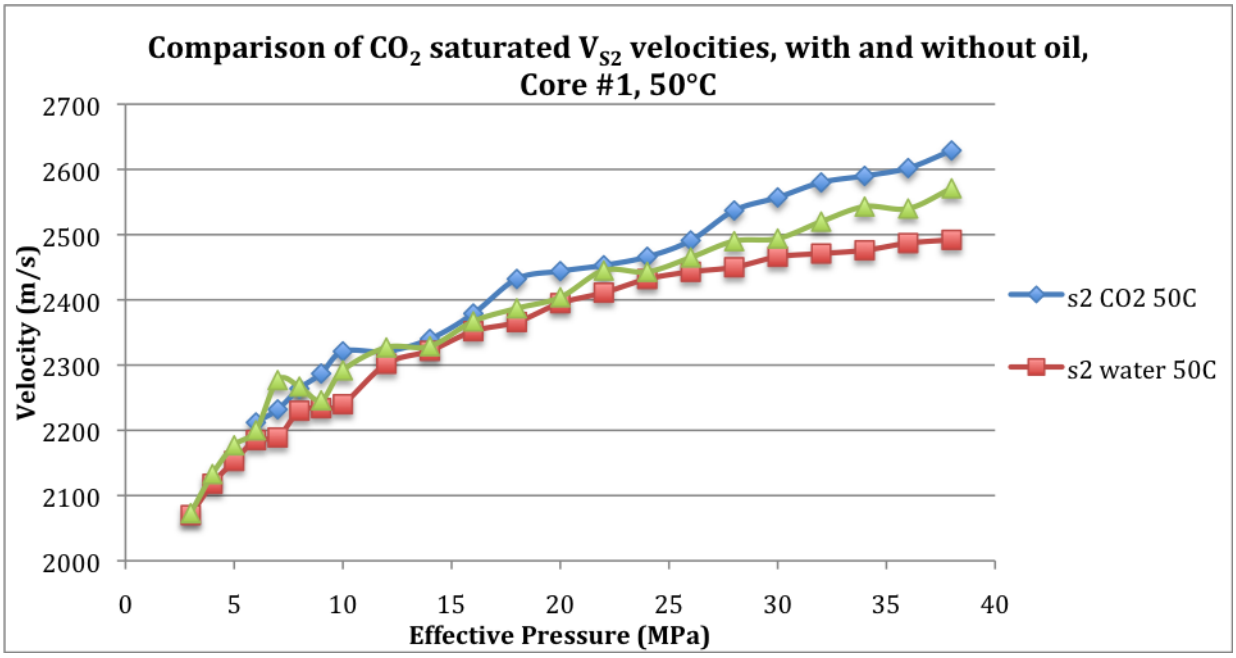

Figure 88: Comparison of CO_2 saturated V_{S2}, before and after oil saturation.

If we take the difference between the CO_2 saturated velocities before and after oil saturation, we can more easily quantify any trends in the data. When we plot the differences, we can see that V_P, V_{S1} and V_{S2} each have a different response to oil saturation (Figure 89). For this plot, a positive response indicates a slower oil-saturated velocity, and a negative response indicates a faster oil-saturated velocity. A linear trend was fit to each dataset and examined. For V_P, the response is negative for low effective pressures (~0-20 MPa), and positive for higher effective pressures (~20-40 MPa), with the largest difference around 35 MPa. This effect can be explained via two mechanisms: the increased density from the added oil gives faster velocities at low effective pressures, and the more incompressible oil in the pore space is able to keep the compliant porosity open at higher effective pressures, resulting in slower velocities for oil-saturated samples.

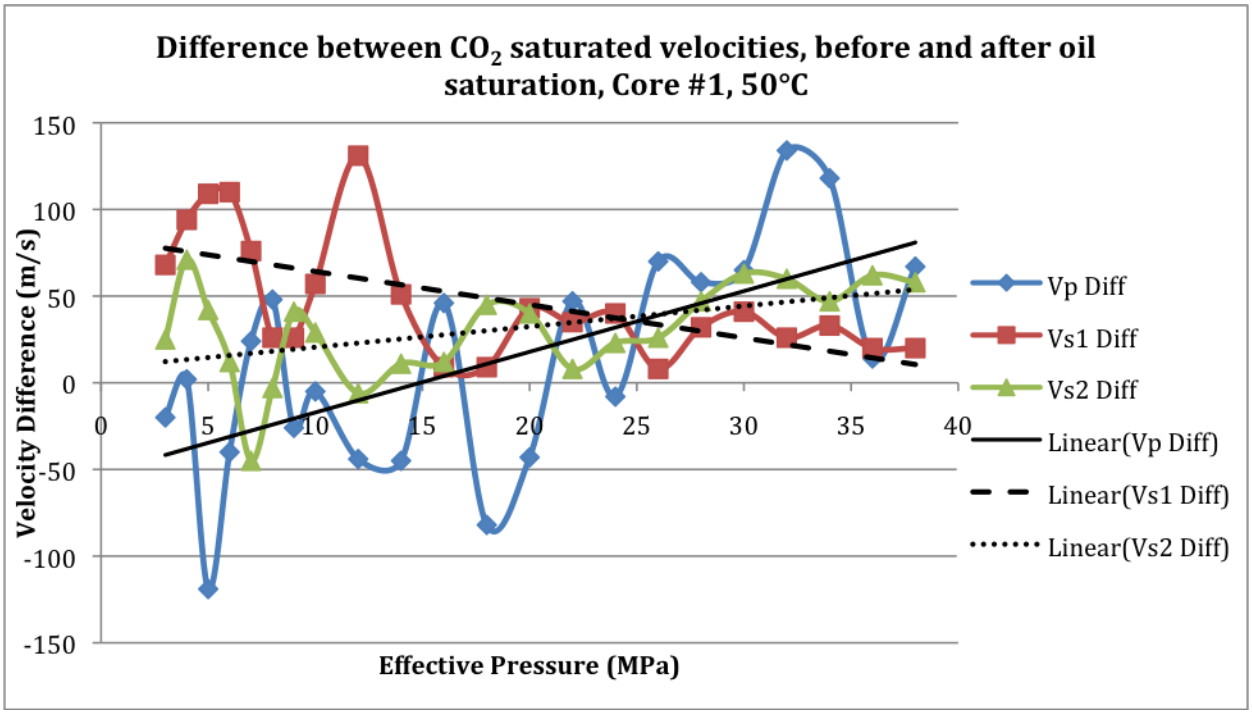

Figure 89: Difference between CO_2 saturated velocities, before and after oil saturation.

For V_{S1} and V_{S2}, the overall response is positive across the entire pressure range (Figure 89). For V_{S1}, the difference is larger at lower effective pressures, while for V_{S2}, the response is larger at higher effective pressures. These differences in response are very small, and the linear fit is quite poor. This response is likely due to measurement error in the data.

As outlined at the beginning of this section, the addition of oil to the sample blocked off a significant amount of the available porosity due to becoming trapped in small pore throats. Although only 3.6 cc's of oil are in the sample, the pore space measured by the helium porosimeter decreased by 6.3 cc's. This sample was then exposed to supercritical CO_2 in the above experiments. The sample was again weighed and the porosity measured after this exposure to CO_2. We found a mass loss of 0.4g, and a porosity increase of 0.54%, or 0.74 cc's. This increase in porosity is due to the supercritical CO_2 mobilizing some of the oil inside the sample

and carrying it out. When the sample was removed from its rubber jacket, oil could be seen on the outside of the sample. This is consistent with the goals of the enhanced oil recovery program at this site, which is to produce more oil via tertiary recovery using CO_2. The CO_2 is able to move the oil through the reservoir from the injector wells to the producer wells via a large pressure front.

These experiments show that in addition to velocity changes caused by the presence of oil in the rock samples, that CO_2 is able to move oil through the pore space of the rock, validating the approach of using CO_2 for Enhanced Oil Recovery in this reservoir.

These experiments proved useful in the characterization of our reservoir because they showed the character of velocity changes in our reservoir rock for a large variety of conditions that would be found in the subsurface. The effect of pressure on the core samples was analyzed, and the effect of differing pore fluids was examined. In addition, they showed that anisotropy plays an important role when analyzing a material as complex as this limestone. These results were then used to help interpret well log and seismic data, and as a basis for AVO calculations.

2.0 AVO ANALYSIS OF SEISMIC DATA

We have currently obtained and analyzed the 2001 3D reflection seismic survey taken before the 2008 injection. The field has had CO_2 previously injected for enhanced oil recovery. We can use this fact to anticipate the type of signature we expect for our CO_2-saturated areas. Our data from the initial survey was processed by a third party and provided to us in prestack format. We then analyzed the 3D survey and completed an AVO analysis over our study area. The use of AVO analysis can help in determining the type of pore-filling phase present in our reservoir.

2.1 AVO THEORY AND CALCULATION

AVO (Amplitude Variation with Offset) is the variation of seismic reflection amplitude with source-receiver offset. When a seismic wave reflects off of an interface in the subsurface, a portion of it is reflected, and a portion of it is refracted. The portion of the incoming wave that is reflected depends on the elastic properties of the two layers forming the interface. Changes in the elastic properties of either layer will have an effect on the variation of the reflected amplitude as a function of the incidence angle. The way in which this occurs can be visualized via Snell's Law of Reflection.

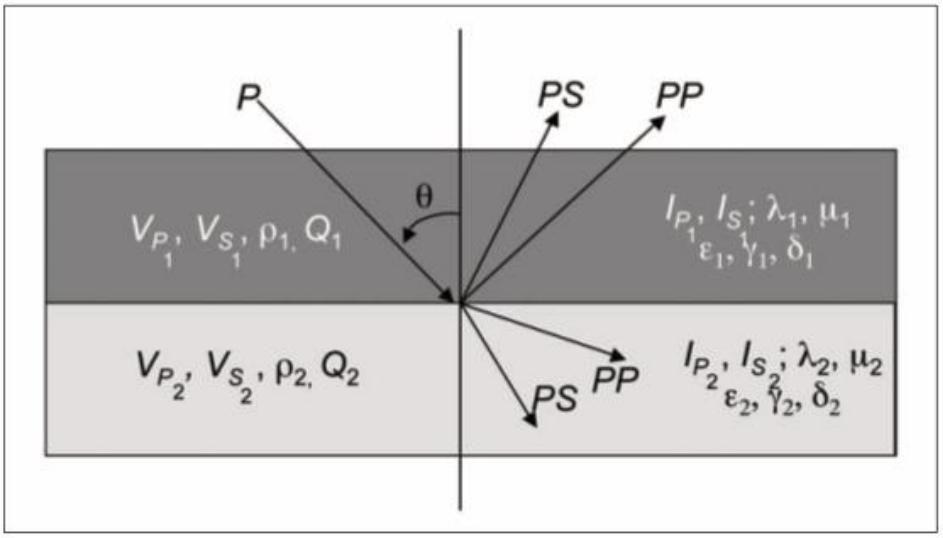

Figure 90: Reflections and transmissions at an interface.

For an incident P-Wave, there is a reflected P-Wave, a reflected S-Wave, a transmitted P-Wave, and a transmitted S-Wave. These can be denoted as PP_R, PS_R, PP_T and PS_T respectively. The amplitude of these waves can be expressed as a coefficient ranging from 0 to 1, representing 0-100% reflection or transmission at the interface. The coefficients of reflection and transmission are determined via the Zoeppritz equations and are represented as R_{PP}, R_{PS}, T_{PP}, and T_{PS} (Sheriff 1995).

$$A_1 \cos\theta_1 - B_1 \sin\lambda_1 + A_2 \cos\theta_2 + B_2 \sin\lambda_2 = A_0 \cos\theta_1$$

Equation 18: Zoeppritz Equations

$$A_1 \sin\theta_1 + B_1 \cos\lambda_1 - A_2 \sin\theta_2 + B_2 \cos\lambda_2 = -A_0 \sin\theta_1$$

Equation 19: Zoeppritz Equations

$$A_1 Z_1 \cos 2\lambda_1 - B_1 W_1 \sin 2\lambda_1 - A_2 Z_2 \cos 2\lambda_2 - B_2 W_2 \sin 2\lambda_2 = -A_0 Z_1 \cos 2\lambda_1$$

Equation 20: Zoeppritz Equations

$$A_1 \frac{\beta_1}{\alpha_1} W_1 + B_1 W_1 \cos 2\lambda_1 + A_2 \frac{\beta_2}{\alpha_2} W_2 \cos 2\lambda_1 = A_0 \frac{\beta_1}{\alpha_1} W_1 \sin 2\theta_1$$

Equation 21: Zoeppritz Equations

These equations are prohibitively complex, so many approximations have been formulated, such as the Shuey 2 and 3 term approximations, the Aki Richards approximation, and the Verm-Hilterman approximation (Aki 1980; Shuey 1985; Sheriff 1995; Avseth 2007). The Shuey 3 term approximation was chosen for our work, and was used for all work using real data. The Shuey 3 term approximation solves for Intercept, Gradient, and Curvature.

$$R(\theta) = R(0) + G \sin^2 \theta + F(\tan^2 \theta - \sin^2 \theta);$$

Equation 22: Shuey Three-Term approximation

$$R(0) = \frac{1}{2}\left(\frac{\Delta V_P}{V_P} + \frac{\Delta \rho}{\rho}\right);$$

Equation 23: Normal Reflection Coefficient

$$G = \frac{1}{2}\frac{\Delta V_P}{V_P} - 2\frac{V_S^2}{V_P^2}\left(\frac{\Delta\rho}{\rho} + 2\frac{\Delta V_S}{V_S}\right);$$

Equation 24: Gradient

$$F = \frac{1}{2}\frac{\Delta V_P}{V_P}$$

Equation 25: Curvature

where R = reflection coefficient, G = Gradient, F = describes the behavior at angles greater than ~30°, θ =angle of incidence; V_P = P-wave velocity in medium; ΔV_P = P-wave velocity contrast across interface; V_S = S-wave velocity in medium; ΔV_S= S-wave velocity contrast across interface; ρ= density in medium; and Δρ = density contrast across interface (Shuey 1985; Sheriff 1995).

The key to AVO analysis is studying how these coefficients change with offset, such as positive or negative intercept, increasing or decreasing amplitude, phase change, and the critical angle. Cross plotting these coefficients for each common midpoint at a certain interface can give the large scale character of an AVO anomaly (Castagna 1998).

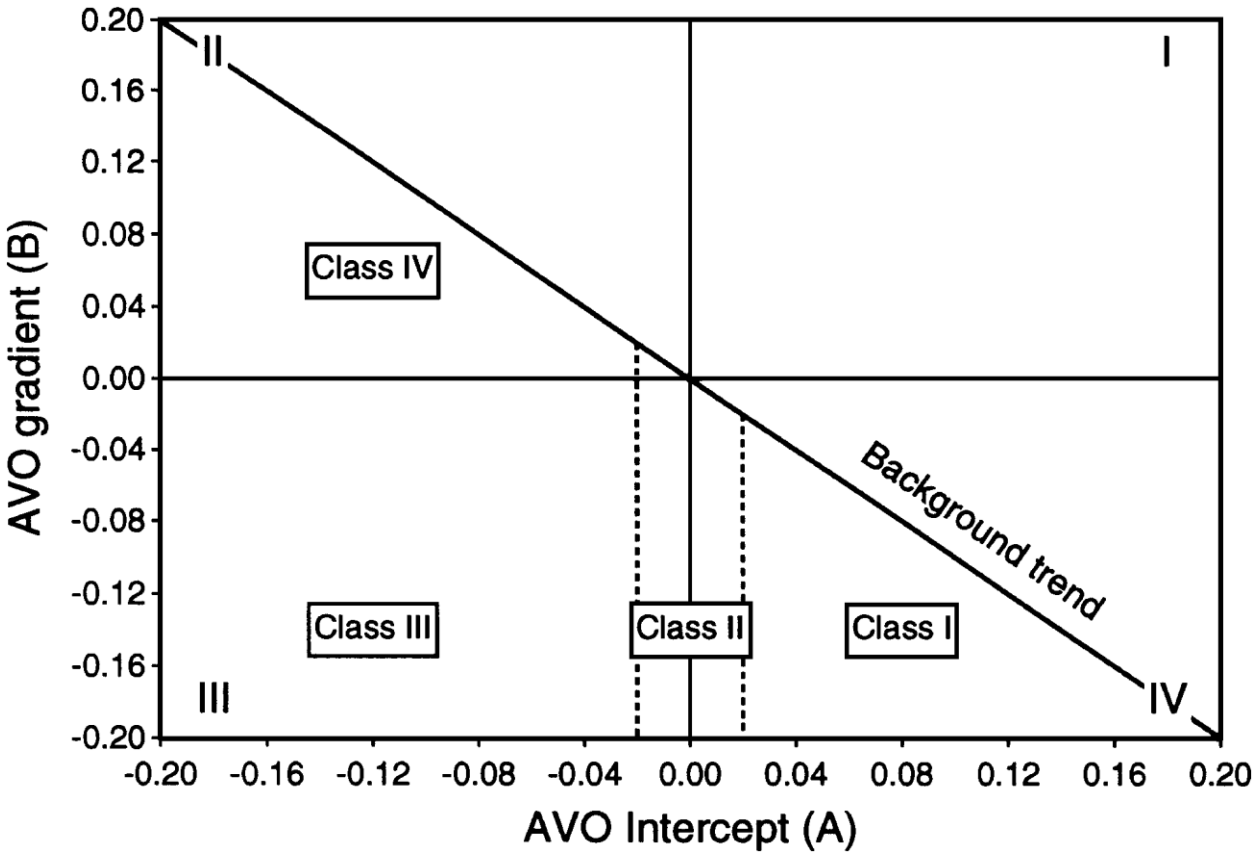

Figure 91: AVO intercept vs. gradient crossplot showing classification system developed by Rutherford and Williams (Rutherford 1989). From (Castagna 1998).

There are also many ways to classify AVO anomalies, using curves plotted vs. offset, or by cross plotting. A common classification system originally developed by Rutherford and Williams, and presented by Castagna et al, is shown in Figure 91 and Figure 92 and breaks down these anomalies into Class I, Class II, Class III and Class IV, each with differing properties (Rutherford 1989; Castagna 1998). By utilizing this classification system, we can gain insights into any AVO anomalies present in the reservoir.

Class	Relative Impedance	Quadrant	A	B	Amplitude vs. Offset
I	Higher than overlying unit	IV	+	-	Decreases
II	About the same as the overlying unit	II, III, or IV	+ or -	-	Increase or decrease; may change sign
III	Lower than overlying unit	III	-	-	Increases
IV	Lower than overlying unit	II	-	+	Decreases

Figure 92: Table of classification system for Figure 94, from (Castagna 1998).

Before undertaking our AVO analysis, we wanted to model how CO_2 replacing brine would change the AVO response of our reservoir. For this we used the CREWES Zoeppritz Explorer, which solves for the exact solution of the Zoeppritz equations (CREWES 2001-2005). The Zoeppritz equations model the reflection and transmission coefficients as a function of offset angle at an interface that can be used to infer properties of the pore-filling phase. We used our laboratory measurements as the input values for the lower layer and values taken from our reference shale for the top layer. We first calculated the response of the dry Limestone material, and calculated all four coefficients. Focusing on R_{PP}, as this is the measured amplitude by the receiver, we see an intercept of 0, an increase in R_{PP} at angles past ~10° offset, eventually reaching large positive values at the critical angle of 60.18° (Figure 93).

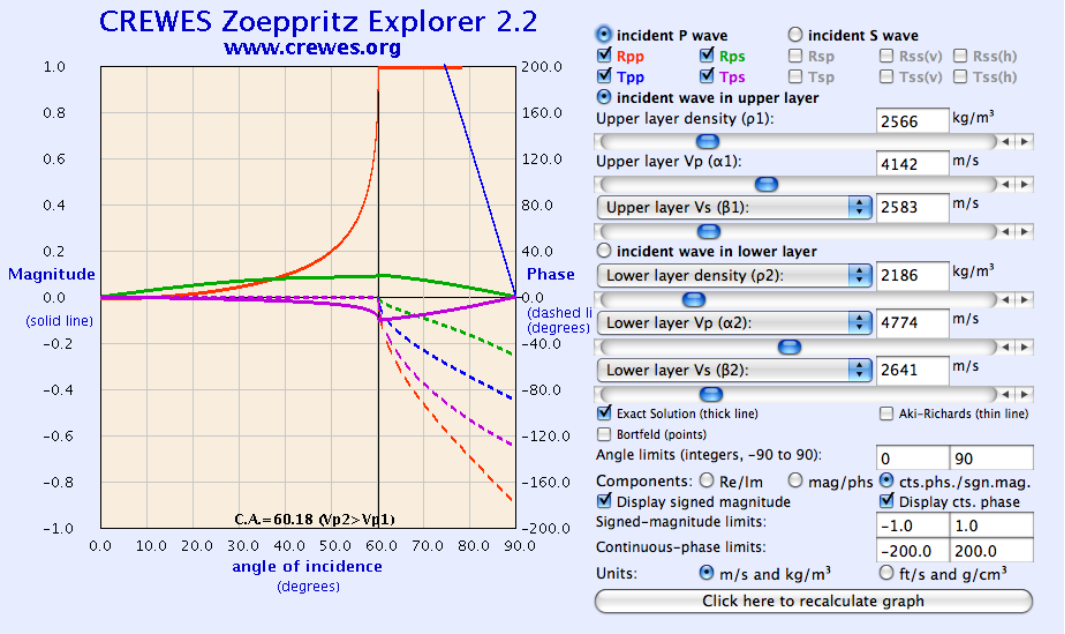

Figure 93: Exact Zoeppritz solution of an interface of shale and dry limestone (CREWES 2001-2005).

The AVO response of brine filled limestone was then calculated, again using measurements obtained in the laboratory. For this case, the intercept is positive, and increases until it reaches the critical angle of 55.77° (Figure 94).

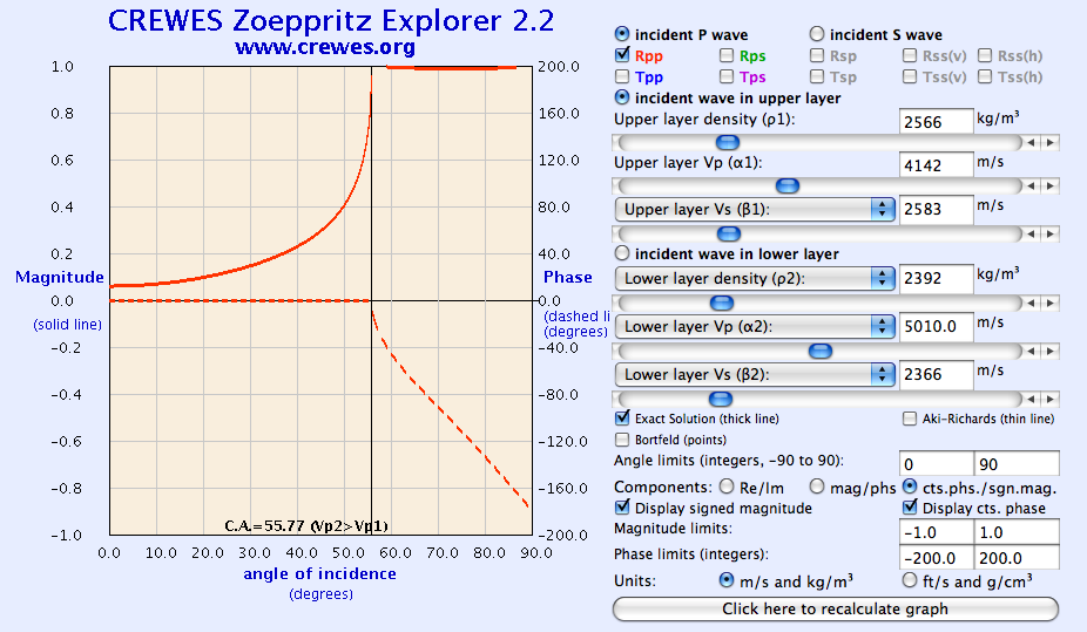

Figure 94: Exact Zoeppritz solution of an interface of shale and brine filled limestone (CREWES 2001-2005).

We then substituted in 100% CO_2 saturation to see the maximum effect of pore fluid substitution on the AVO response. We can see that the intercept is negative, becoming positive again around 15°, then increasing sharply up to the critical angle of 72.67° (Figure 95).

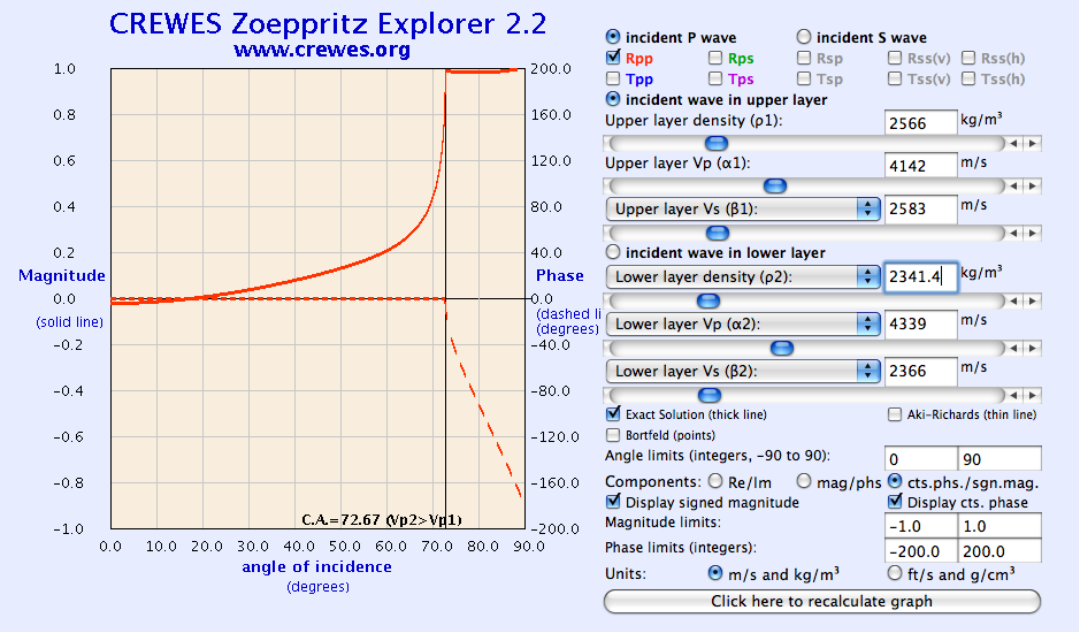

Figure 95: Exact Zoeppritz solution of an interface of shale and CO_2 saturated limestone (CREWES 2001-2005).

When we plot these two graphs against one another, the difference between brine-filled and CO_2-filled phases is noticeable: The intercept for the brine-filled example is positive, whereas when CO_2 is substituted in it becomes slightly negative, and the critical angle for the CO_2-saturated example is at a larger angle than it is for brine (Figure 96).

Modeling the AVO response to changing fluid saturations gave us insight into how large of a difference is expected in reflection coefficients in different areas of the reservoir. Brine-filled and CO_2-filled AVO responses are quite different, and should be detectable via seismic surveys.

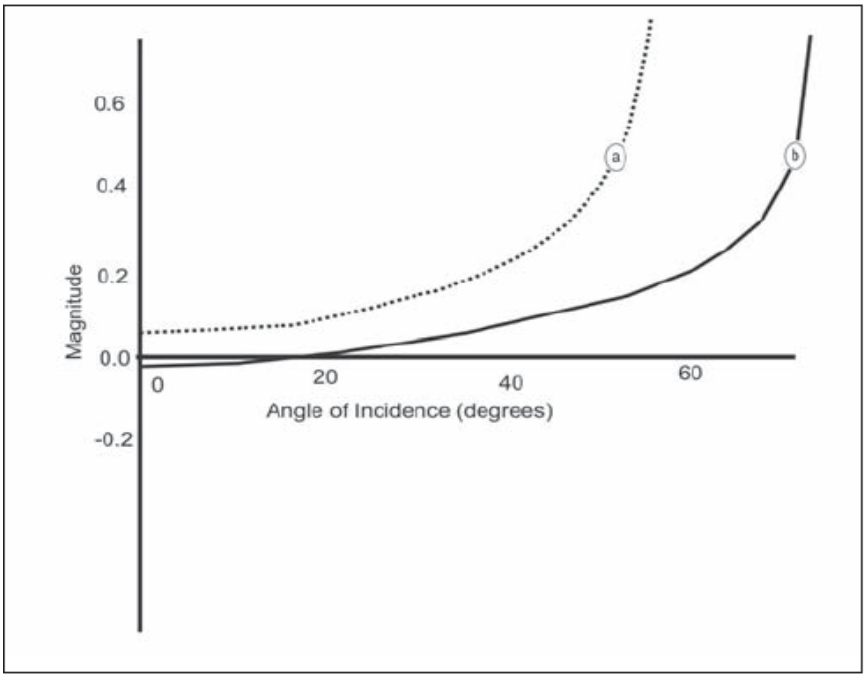

Figure 96: Plot of Rpp vs. angle comparing Brine (Dashed line) and CO_2 saturated (Solid line) interfaces.

2.2 AVO ANALYSIS OF SEISMIC DATA

We then computed the AVO response immediately around our survey region using approximately 3500 separate points on a picked horizon of our reef surface. This work was completed using SMT Kingdom AVOPAK software. This plotted prestack gathers vs. angle at each common mid point in the survey area. The data was then fit to a Shuey 3 term approximation to get Intercept, Gradient, and Curvature values (Shuey 1985).

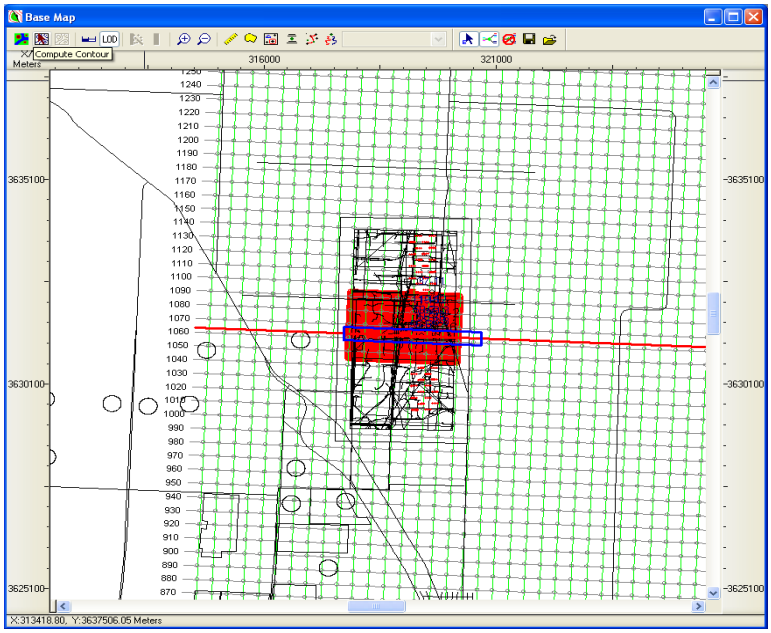

Figure 97: Basemap of seismic survey, red area represents area around injection well chosen for AVO analysis.

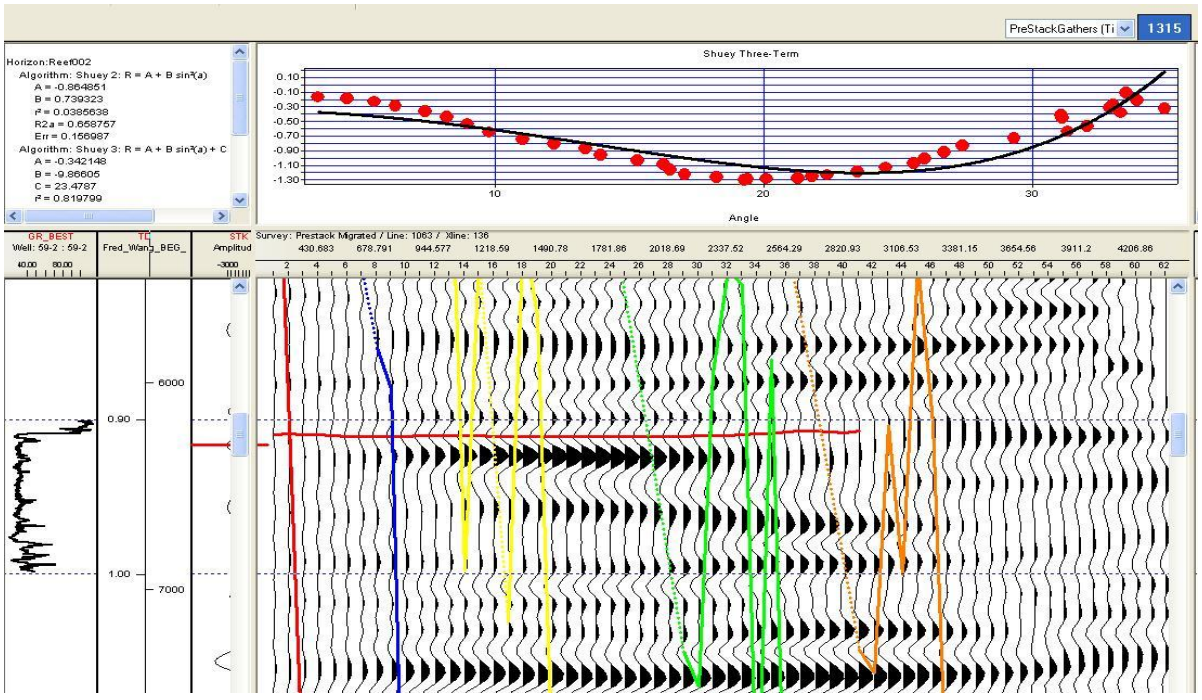

Figure 98: Example of Shuey Three Term fit (black line) to offset data (red dots).

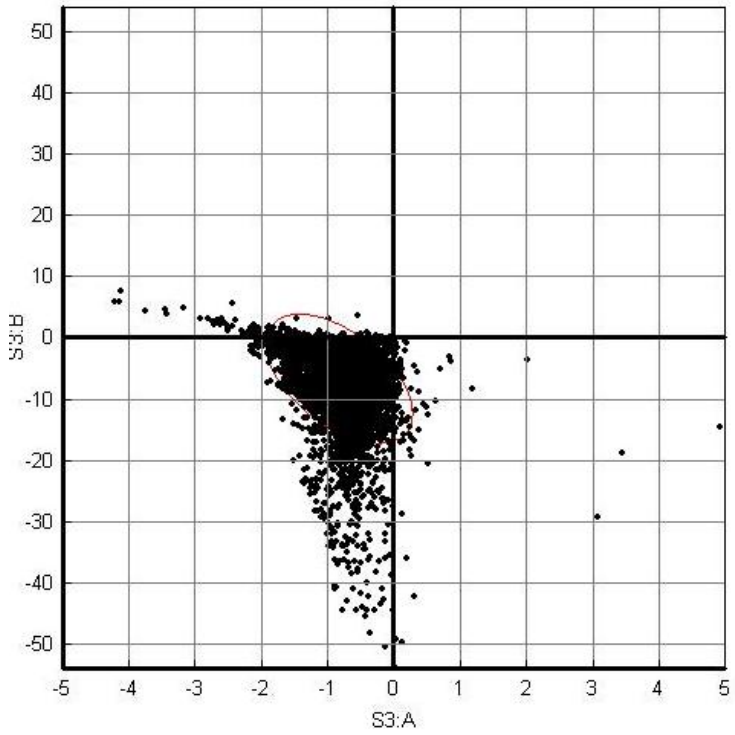

Figure 99: Crossplot of A vs. B, showing a large Class III anomaly.

When these points are cross plotted, the overall AVO response of our area on the A vs. B plot is that of a Type III anomaly (Figure 99)(Rutherford 1989; Castagna 1998). When we analyze these AVO coefficients further, we can use them to determine where CO_2 is located in the reservoir. If we look at the AVO response in the area and depth of the injector well, we see that the intercept is negative, and it becomes positive far away from the anomolous region. This agrees well with Zoeppritz calculations for CO_2-saturated rock.

After examining different combinations of coefficients for different approximations, it was determined that for our limestone reservoir, a high value for ½(A+B) using the Shuey three-term approximation appears to be an excellent indicator for CO_2, as large positive values were found around the well at the injector depth (Figure 100). For the Shuey three-term approximation, the

attribute ½(A+B) is an estimate of R_P-R_S (P Reflectivity-S Reflectivity) (Castagna 1994; Ross 2000; Roden 2008).

This is a powerful indicator of injected CO_2 in the subsurface. Using AVO attributes, an anomaly was found at the location and depth of a CO_2 injection in our reservoir. This method of using detailed AVO attribute analysis holds great promise for the monitoring of any enhanced oil recovery or carbon sequestration sites.

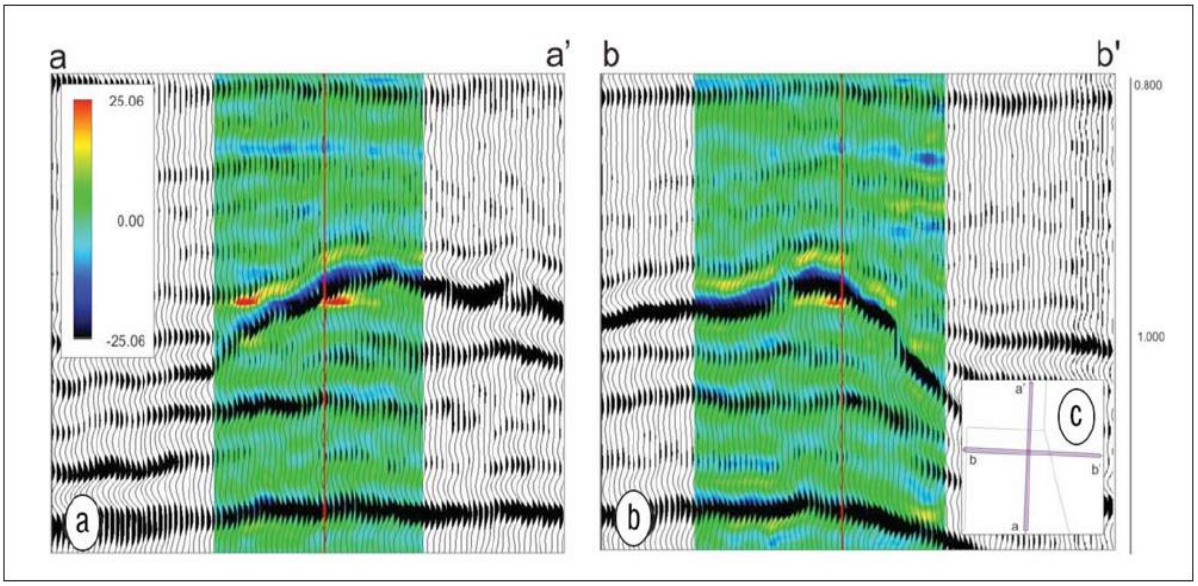

Figure 100:Plot of 1/2(A+B) for two cross sections passing through the injector well, indicated by the red line. Areas of high values can be seen around the injector well at the depth of injection.

Although this is likely to be different for each reservoir, as the AVO response depends on many factors, including lithology and the preexisting pore fluids in the rock, analyzing the response around the well using AVO approximations and linear combinations of these coefficients could prove to be a powerful tool when conducting 4D seismic monitoring of a field, as these changes

may prove to be easier to detect than velocity changes alone, especially in less porous rocks, or very deep reservoirs.

2.3 AVO ANALYSIS OF WELL LOGS AND SIMULATED FLUID SUBSTITUTION

In addition to seismic data, well logs at two injection sites were shared with us, containing fluid saturation data. This was used to better quantify the AVO response across the entire thickness of the reservoir, something that could not be done using Zoeppritz modeling at a single interface. Changes in lithology, porosity and saturation all have an effect on the AVO response within our limestone unit.

Two wells are discussed below, 59-02 and 56-6, both of which are injector wells within the our study field. A full suite of well logs was provided for both wells, including saturation data. For well 56-6, saturation data was provided at two different times, although it is unclear how far apart these logs were collected.

The Ikon Rokdoc software package was used to analyze and interpret these logs. The top of the limestone was chosen for both wells using a combination of Gamma Ray and lithology logs.

Fluid substitution was then done using Gassmann dry rock modeling over the entire reservoir interval. The dry rock properties of the reservoir were determined using velocity, density, lithology and saturation logs, and then differing fluids were substituted in to produce new V_P, V_S, and density log sets.

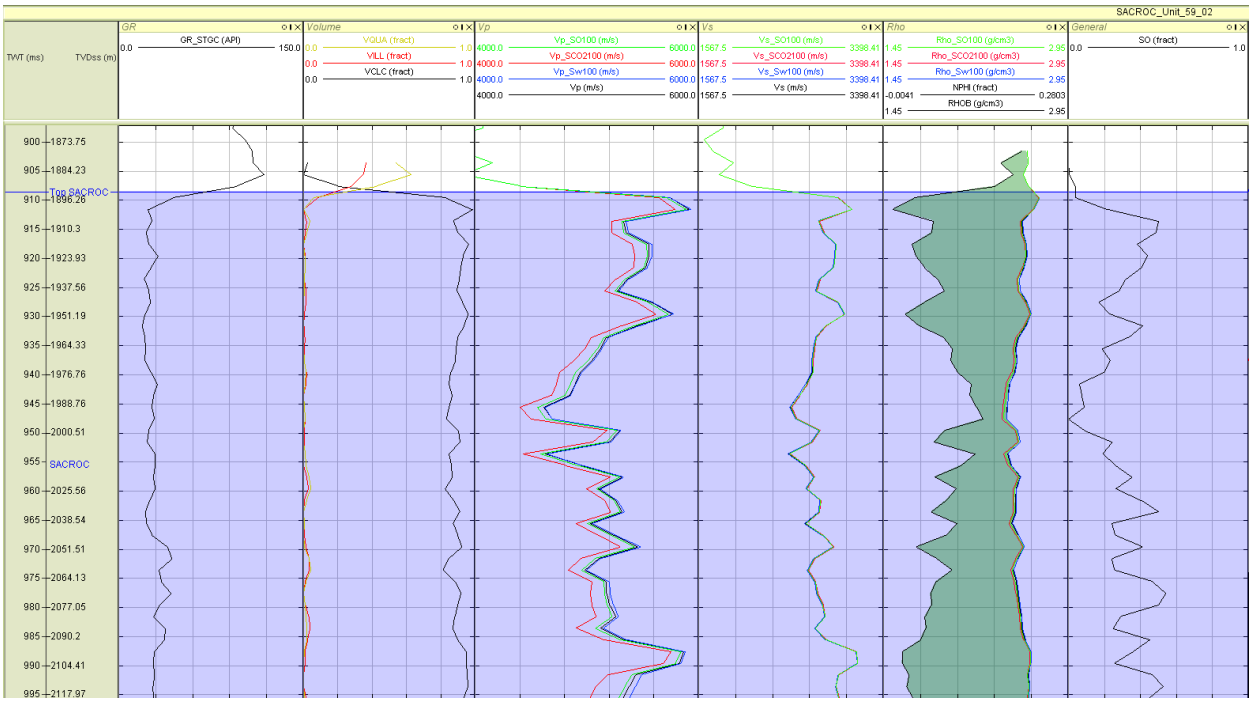

Figure 101:Close up of well logs for well 59-02. From left to right: Gamma, Lithology, V_P, V_S, and Density for various saturations, initial Oil saturation.

For well 59-02, initial fluid saturations were replaced with 3 saturation scenarios: fully brine saturated, fully oil saturated, and fully CO_2 saturated. V_P-V_S-Rho log sets were created for each

scenario using Gassmann Dry Rock modeling (Figure 101). These logs were then used to create synthetic gathers using the Zoeppritz equations.

In order to create synthetic gathers using Rokdoc, a wavelet was required. A statistical wavelet was used, which was created using our seismic survey over the field, in order to gain the most accurate response with offset. The wavelet was extracted from around well 59-02, and contained 494 traces, using times of 0-2.9980s.

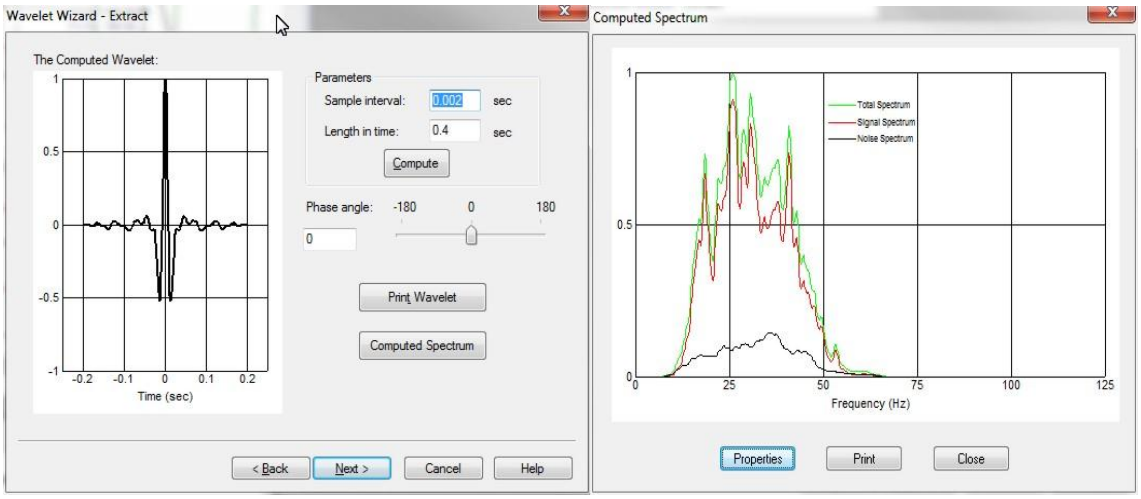

Figure 102: Statistical wavelet used for Zoeppritz modeling. Left: Computed wavelet. Right: Computed spectrum.

The Zoeppritz equations were used to model the offset from 0-50° over the whole depth of our well logs. This includes the major reflector found at the bottom of the shale unit capping the reservoir and the top of our limestone unit. Additionally, near angle stack, far angle stack, and full angle stack values were calculated. These gathers are shown in Figure 103, and show the different gathers for original saturation, brine saturation, oil saturation, and CO_2 saturation.

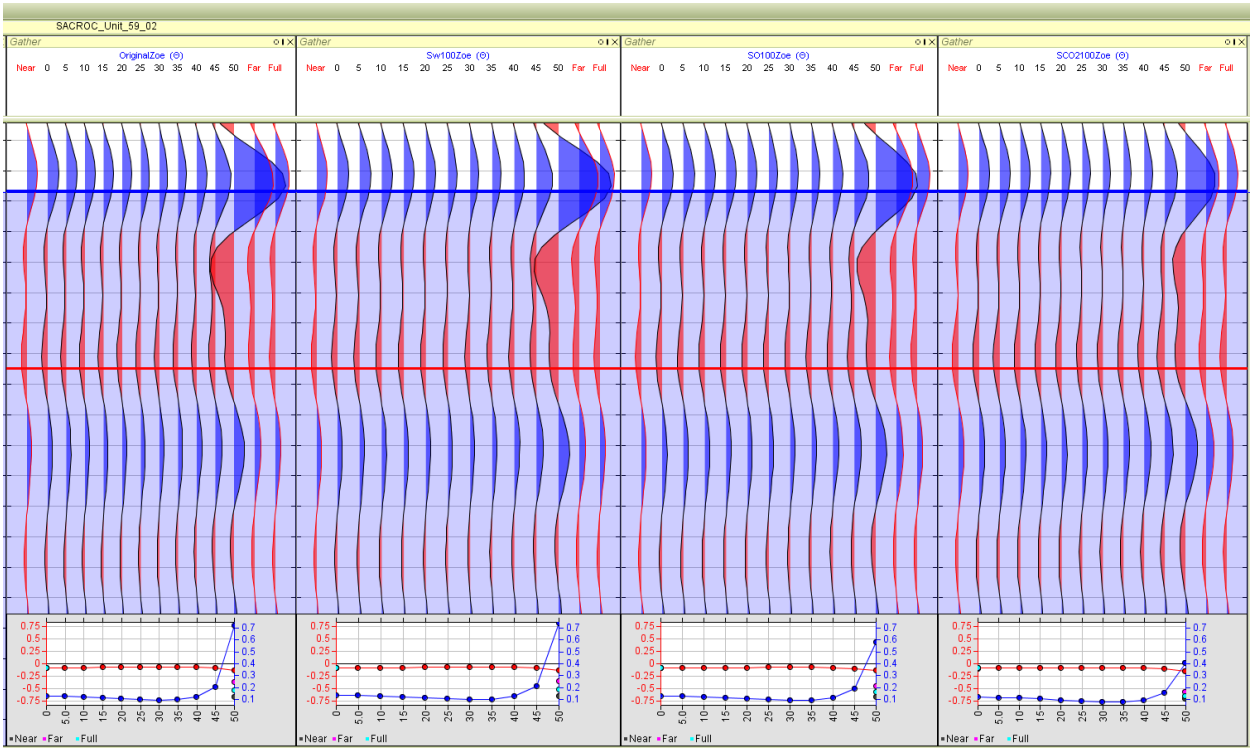

Figure 103: Synthetic gathers for well 59-02. From left to right: Original saturation, fully brine saturated, fully oil saturated, and fully CO_2 saturated. Graphs show amplitudes at red and blue lines.

This same procedure was done for well 56-6, and fully brine saturated, fully oil saturated, and fully CO_2 saturated synthetic log sets were created (Figure 104, Figure 105). For well 56-6, we had, in addition to initial saturation logs, a set of saturation logs collected at a later date. This quantified saturation changes over time post CO_2 injection, which helps to show the variations in saturation changes at different depths in the reservoir. A set of synthetic logs was also created using this second set of saturation data.

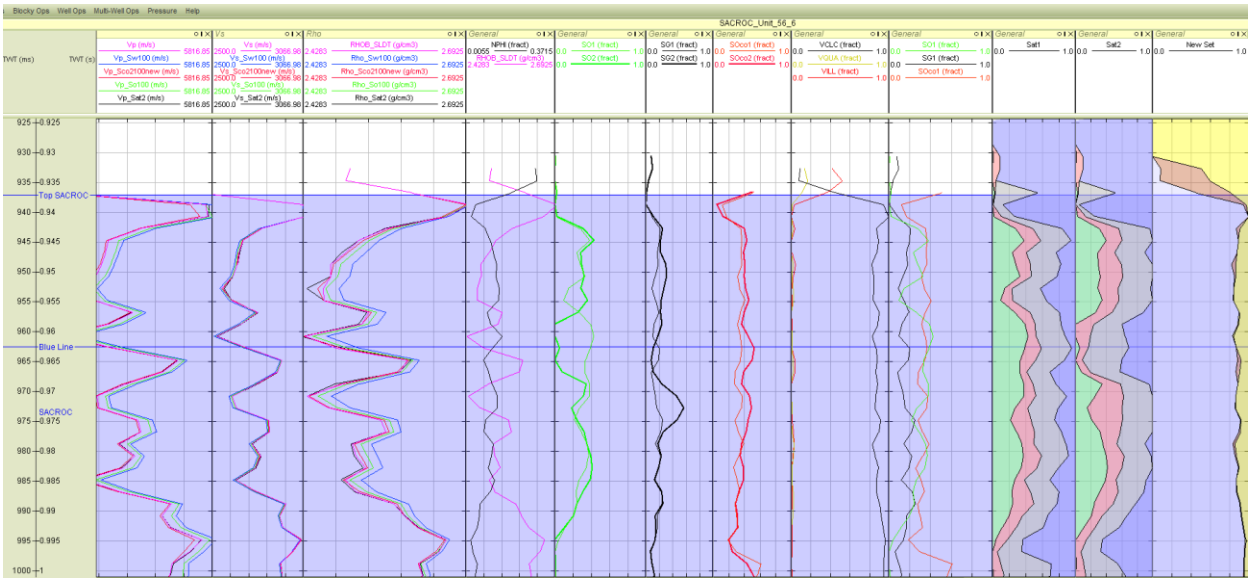

Figure 104: Well logs for well 56-6. From left to right: Vp, Vs, density logs for various saturations, Porosity, Oil saturations, Gas saturations, CO_2 saturations, Lithology logs, Initial sat. logs, Saturation set 1, saturation set 2, mineralogy set.

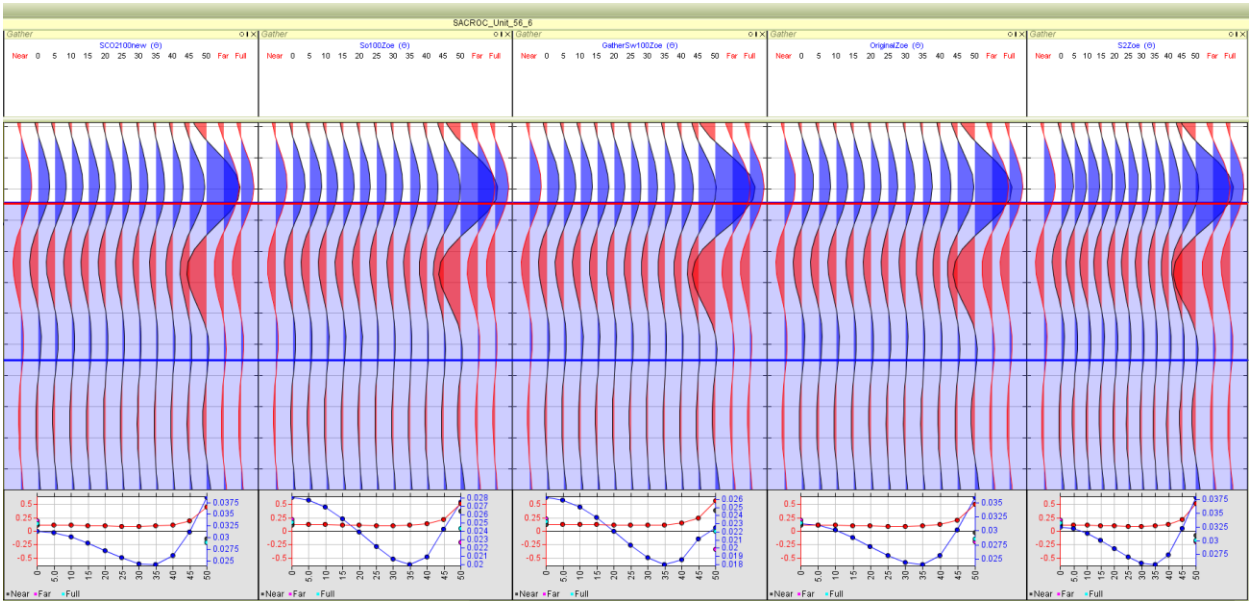

Figure 105: Gathers for well 56-6. From left to right: fully CO_2 saturated, fully oil saturated, fully water saturated, original saturation, saturation 2.

For well 59-02, the AVO response was then examined in detail for the top limestone interface. Amplitude data were exported for each of the saturation scenarios and then compared (Figure 106). For all saturation scenarios at this well, a positive intercept was calculated, with an initial reduction in amplitude with offset, with steeply increasing amplitude at very far offsets. Angles past 45° are not graphed here, for clarity. Near stack, Far stack, and Full stack amplitudes are graphed as well. It can be seen that the initial saturation response falls in between the water and oil curves, as expected from the initial saturation containing no CO_2 or gas. The highest intercept is for water saturation, with the oil saturation intercept being slightly lower. The intercept for CO_2 saturation is markedly lower than either the water or oil saturation. The same is true for the response with angle, with CO_2 saturated amplitudes being the smallest.

The response of fluid saturation becomes larger with offset, as seen in the Far Angle stack amplitudes (Figure 106). A decrease in the far stack amplitudes could be a good indicator of CO_2 saturation in any seismic monitoring studies, and shows the importance of collecting good offset data in any monitoring study, as the far offsets are more sensitive to fluid saturation.

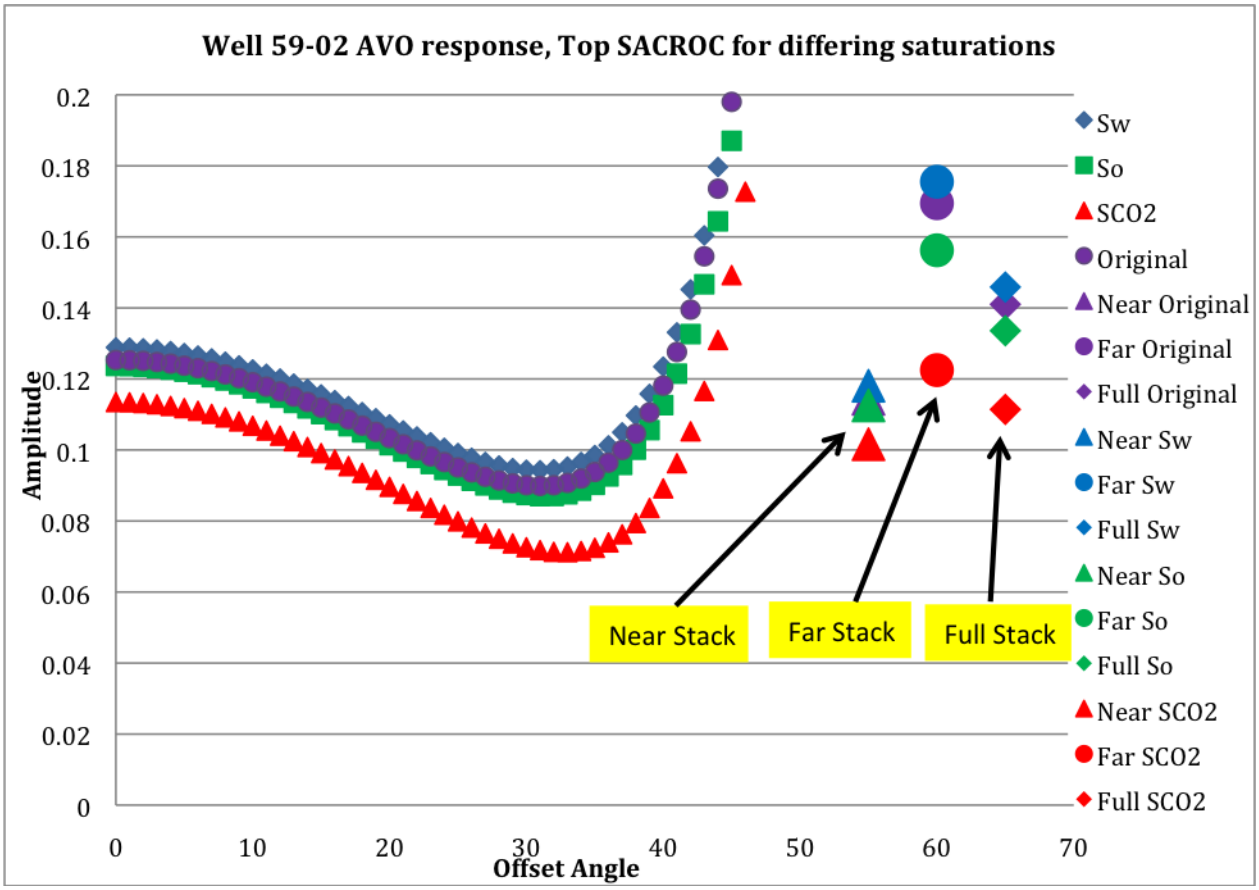

Figure 106: Well 59-02 AVO response, Top Limestone.

Well 56-6 was then examined as a way to look at two differing saturations in the same well. These two saturation sets can be seen in Figure 104, near the right hand side. The portion of the box filled with blue represents water, CO_2 is represented by grey, gas is represented by red, and oil corresponds to green. As we move from Saturation 1 to Saturation 2, we can see that there is a decrease in the oil content, and an increase in CO_2 and water content, although this occurs in large patches, not uniformly across the reservoir. A depth of 2003.5 meters was chosen for study,

in addition to the Top Limestone, as there was a large amount of oil lost in this area (represented by the blue line in Figure 104).

When we examine the response at the Top Limestone interface, we find similarity with well 59-02. Water saturated amplitudes are the highest, with CO_2 saturated amplitudes being the lowest (Figure 107). At far offsets, this difference becomes more pronounced. We also plotted the Original saturation, and the saturation at time 2. Both of these saturations plot close to the CO_2 line, as they both saturations have 15-20% CO_2 content. At far offsets, both of these saturations plot in between the oil line and the CO_2 line, with saturation 2 being slightly higher (Figure 107). This is due to the nature of injections, which are water alternating with CO_2. This additional water overwhelmed the response of the small amount of additional CO_2 found in saturation 2.

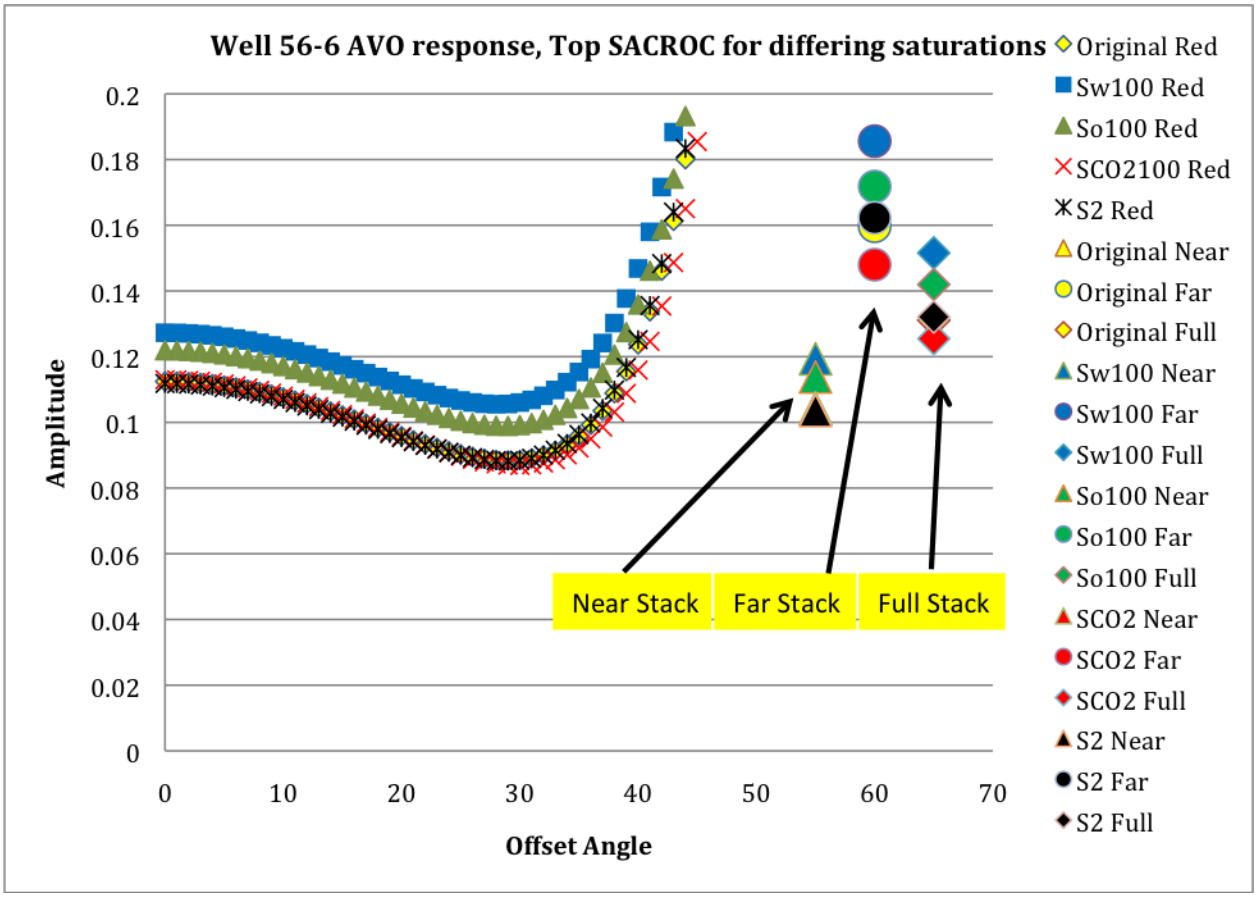

Figure 107: AVO response for well 56-6, Top Limestone.

We also wanted to look at any possible AVO response within the reservoir unit itself, to see if subtle variations could be found. A depth of 2003.5m was chosen as a depth with a large reduction in oil saturation. When we examine the AVO response at this depth, it can be seen that the amplitudes are much smaller than at the Top Limestone interface (Figure 108, Figure 107). Additionally, in this case the response to fluid saturation is inverted, with the smallest amplitudes being the water saturated ones, and CO_2 saturated having the highest amplitudes.

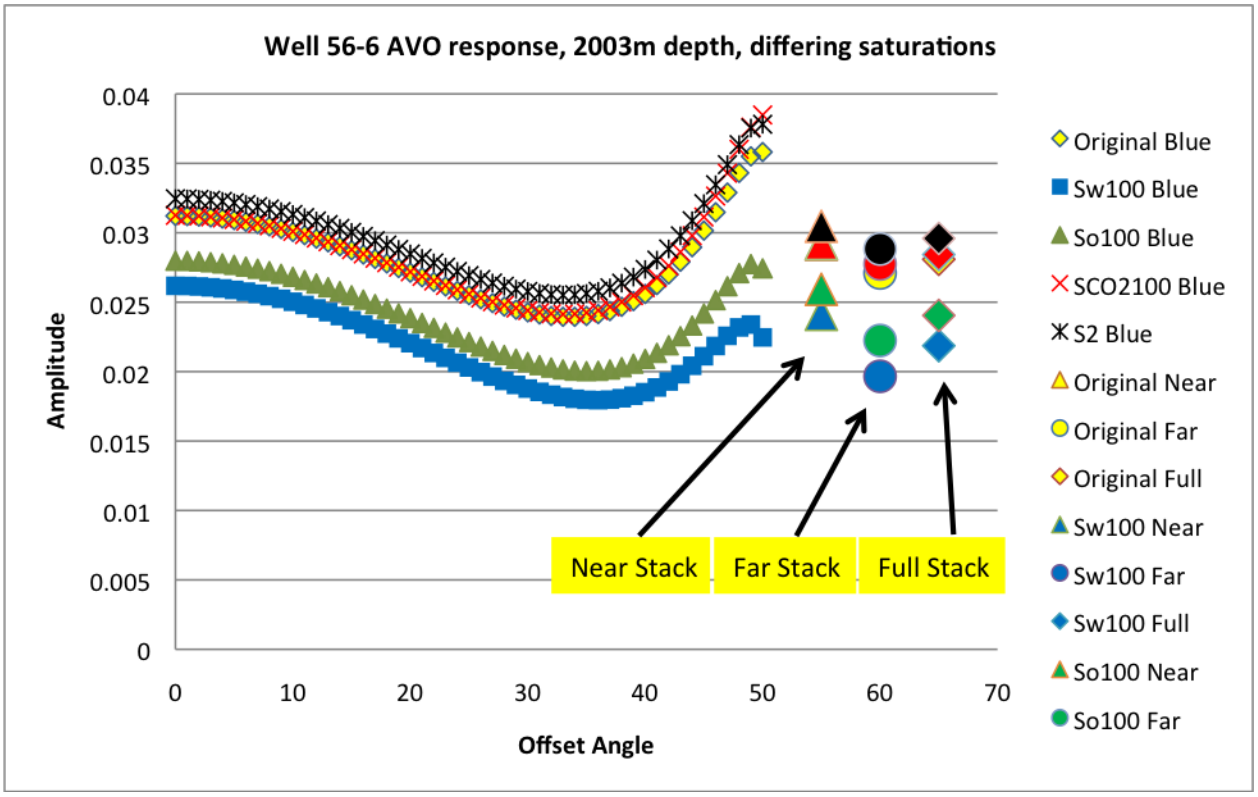

Figure 108: AVO response for well 56-6, 2003.5m depth.

The original saturation and the final saturation again plot near the CO_2 saturated line, but in this case saturation 2 has higher amplitudes than the fully CO_2 saturated amplitudes. When the saturation sets are examined (Figure 104), we see that for saturation 2, there is a large amount of gas present, with some water and almost no oil left compared to the original saturation. Thus, AVO response may not provide an accurate indicator of small CO_2 saturation changes, especially in areas charged with gas.

By using well logs to create gathers, changes in AVO response can be quantified for various fluid saturations. Using fluid substitution, the effect of CO_2 on well logs and synthetic gathers was investigated. Our experiments show that if a significant portion of water is replaced with

CO_2, that it can have a large effect on velocities and on the AVO response, which we expect from our earlier rock physics experiments. By using well logs in addition to seismic, any expected AVO response can be used to help estimate the amount of CO_2 present in any area of the reservoir.

This study has shown that by using a multifaceted approach utilizing core samples, seismic data and well logs, monitoring of a CO_2 injection can be successfully carried out. Using seismic data alone may not provide enough insight into the velocity response of the reservoir after injection, as any effects are likely to be reservoir dependent. Utilizing core samples and performing ultrasonic velocity experiments aids in quantifying the velocity response to CO_2 saturation over a broad pressure range. Additionally, well logs can be integrated into a monitoring study by utilizing fluid substitution and synthetic gathers. An injection can be modeled beforehand in order to determine if the response is large enough to be detectible.

By utilizing core samples, seismic data and well logs, a CO_2 injection was detected in a 3D seismic survey via AVO attribute analysis. We believe this can be a powerful tool in any Carbon Sequestration or Enhanced Oil Recovery operation. However, a full analysis should be completed for each reservoir, as different lithologies will react differently to CO_2 injection. Variations in rock type, porosity, permeability, and density can all influence any change in velocity an injection will have. By utilizing a pre injection study of this type, the expected AVO response to CO_2 can be determined and then used to analyze subsequent seismic surveys. By carrying out these post injection surveys, the plume of CO_2 can be monitored and tracked in the subsurface. This method offers advantages over any surface monitoring strategies, as the plume

of CO_2 can be tracked before it reaches the surface, so any potential seal leaks or migration along faults can be seen before they become a hazard.

APPENDIX A

PROPERTIES OF CARBON DIOXIDE

In order to fully investigate the effects of CO_2 on our core samples, its properties had to be studied carefully at the pressures and temperatures associated with geologic injection. Temperatures of 25°-50°C were used in this study, although the temperature could be higher under some geologic conditions. We specifically look at four properties: Density, Velocity, Viscosity, and Bulk Modulus. The way these properties change with temperature and pressure have an effect on our observed velocities, and can help to explain some of the different effects seen in the data. This data was collected from the NIST online database (Lemmon 2005) and plotted over a temperature and pressure range applicable to geological storage applications.

When the density isotherms for Carbon Dioxide are examined (Figure 109), a few obvious things are seen. Isotherms ranging from 0° to 300°C were plotted over a range of 1 to 100 MPa, (Log scale used for clarity) representing the range of temperatures and pressures associated with enhanced oil recovery operations. We can see that below pressures of ~3 MPa, the density values at all temperatures are very low, due to its gaseous phase state at these pressures. As the pressure increases, isotherms at low temperatures begin to make the sudden transition from a gaseous

state to a liquid state, associated with a large increase in density. Once the temperature reaches 31°C, there is no rapid jump in density, but a smooth density transition from a gaseous state to a supercritical fluid state. As the temperature is increased further, this transition to a supercritical fluid exhibits a more gradual increase in density.

Our CO_2 saturated experiments were performed at two temperatures, 25°C and 50°C. At 25°C, CO_2 is in a gaseous state below 6.43 MPa, and is liquid for pressures above this. A large jump in densities occurs at this pressure (Figure 109). The density increases from 0.24 g/cc to 0.71 g/cc at 6.43 MPa. This transition could be seen in the lab as a large transducer displacement required to keep the pressure above this value, indicating a large decrease in the volume of CO_2. The supercritical phase is not seen at this temperature. It must be stated that this temperature is unrealistically low for our reservoir, and is unlikely to be found at the depths associated with CO_2 injection studies.

The other temperature studied, 50°C, was chosen to represent the in situ temperature of our reservoir. At this temperature, a large jump in density was not seen, as the transition in density is continuous. The phase transition from gas to supercritical fluid occurs at 7.4 MPa. There is no jump in density at this pressure, but the densities increase faster as the pressure is increased beyond this point. Beyond ~16 MPa, the density begins to increase linearly (Figure 109).

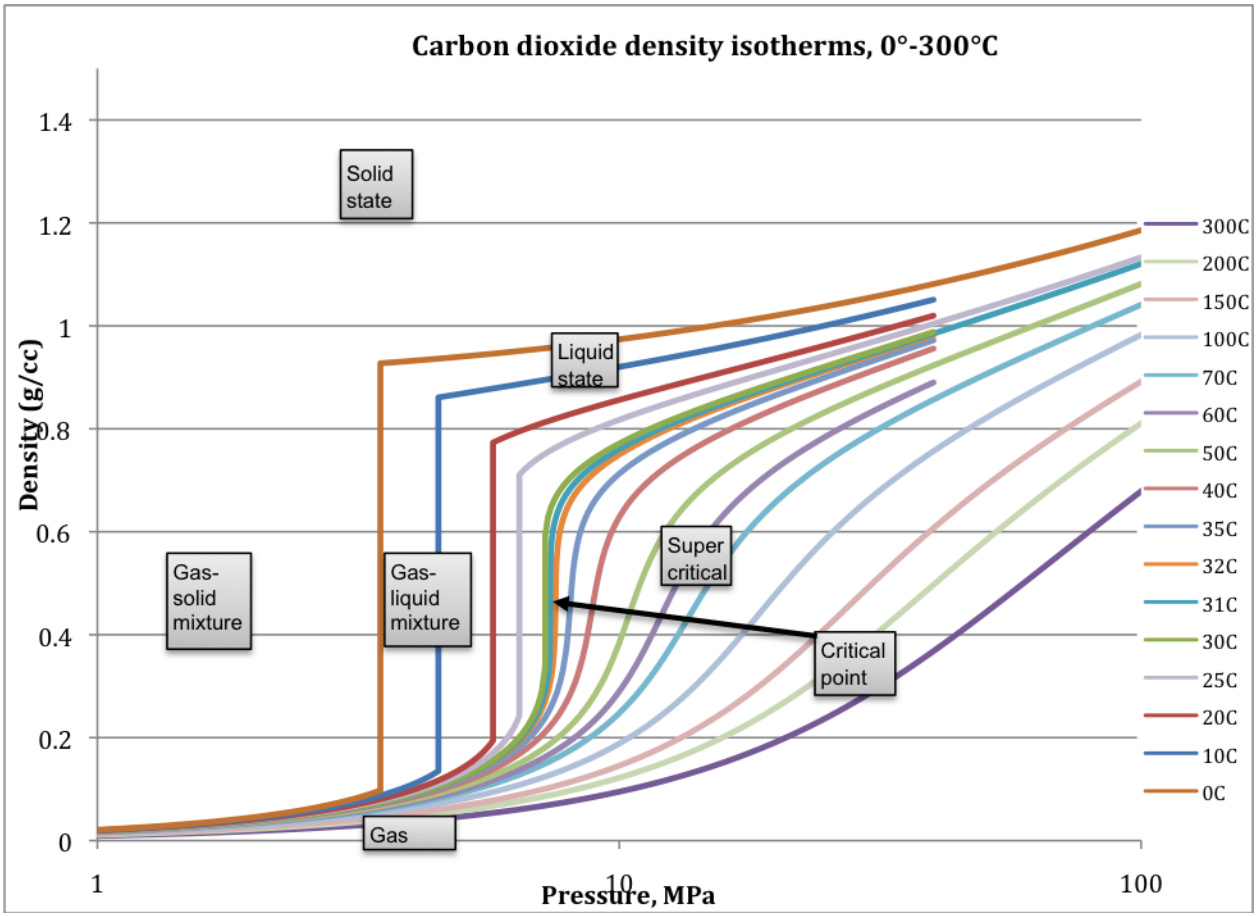

Figure 109: Density Isotherms, 0°-300°C (Lemmon 2005)

Velocity isotherms were plotted over the same pressure and temperature range. Large velocity increases are seen for temperatures below the critical temperature (31°C) at the point of the phase transition between gas and liquid occurs. Above 31°C, the velocity changes are continuous. We note that for pressures below the critical pressure (7.4 MPa), the velocity gradually decreases with increasing pressure, up to and past the critical point, and then quickly increases at a certain distance past the critical point (Figure 110). This is due to the supercritical fluid behaving in a more gas-like manner near the critical point, and more like a fluid at higher pressures [16].

At 25°C, the velocity slowly decreases unit it reaches the transition pressure of 6.43 MPa, and then quickly increases (189 m/s to 274 m/s). For 50°C, the velocity gradually decreases until it reaches the critical pressure of 7.4 MPa. Above this pressure, the CO_2 is in a supercritical state. However, the velocity continues to increase up to 9.7 MPa, above which it increases quickly. This is due to the supercritical fluid behaving more like a liquid than a gas past this point (Sun 2009).

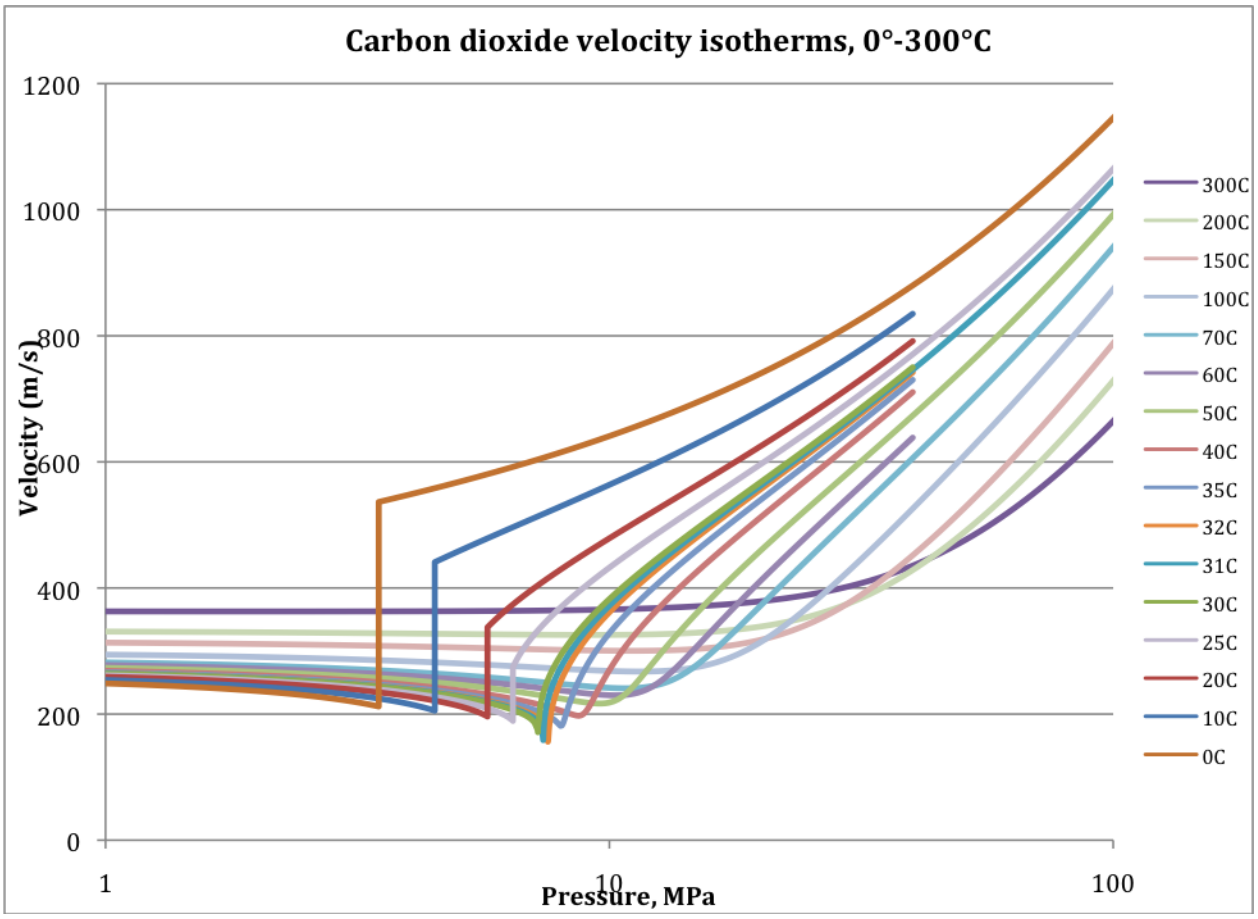

Figure 110: Velocity isotherms, 0°-300°C (Lemmon 2005)

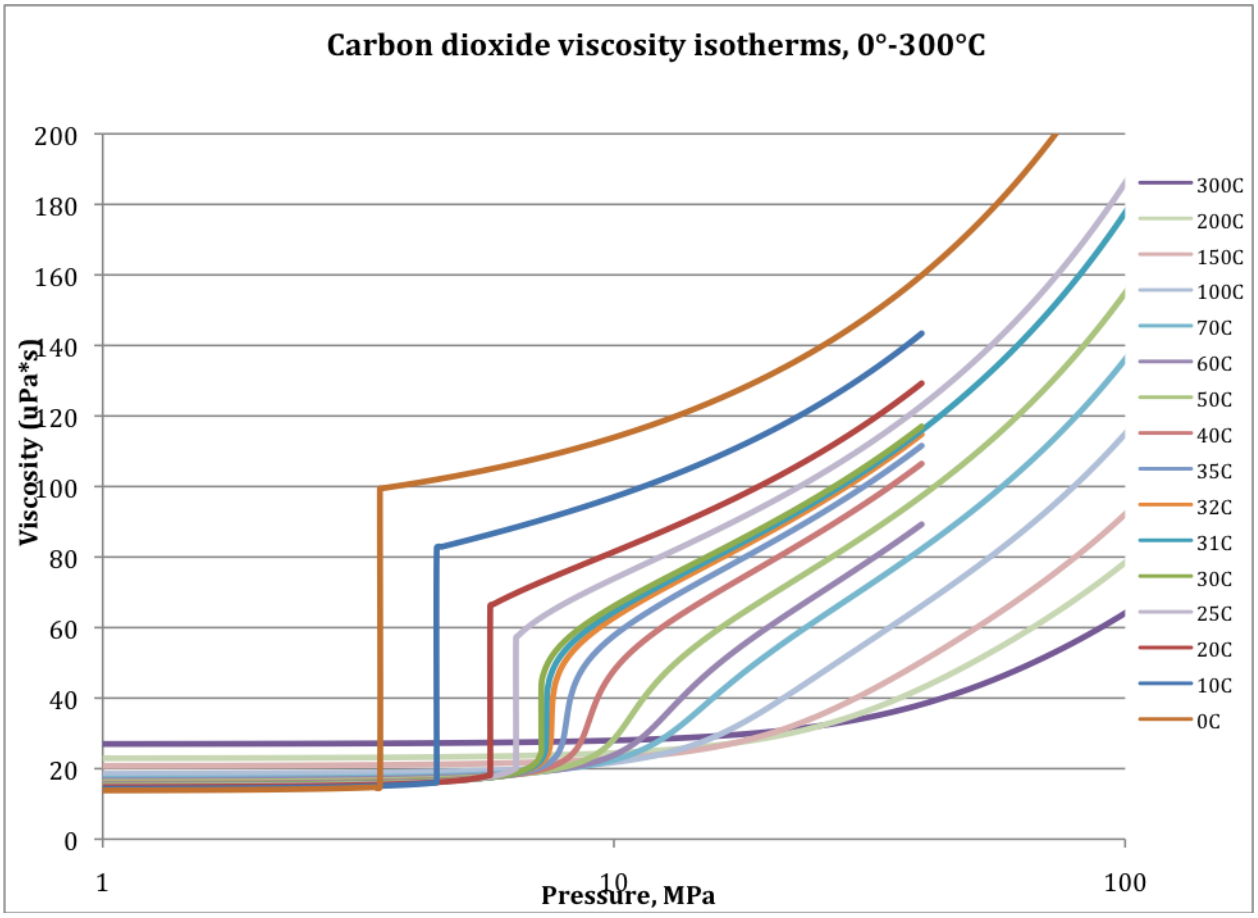

Figure 111:Viscosity isotherms, 0°-300°C (Lemmon 2005)

When the viscosity isotherms are examined, we notice that for the 25°C isotherm, the viscosity makes a sharp jump at the transition point from a gaseous state to a liquid state (6.34 MPa). For 50°C , the viscosity begins to increase after the transition pressure of 7.4 MPa, but makes its largest jump around 10.5 MPa, and then continues to rise with increasing pressure (Figure 111).

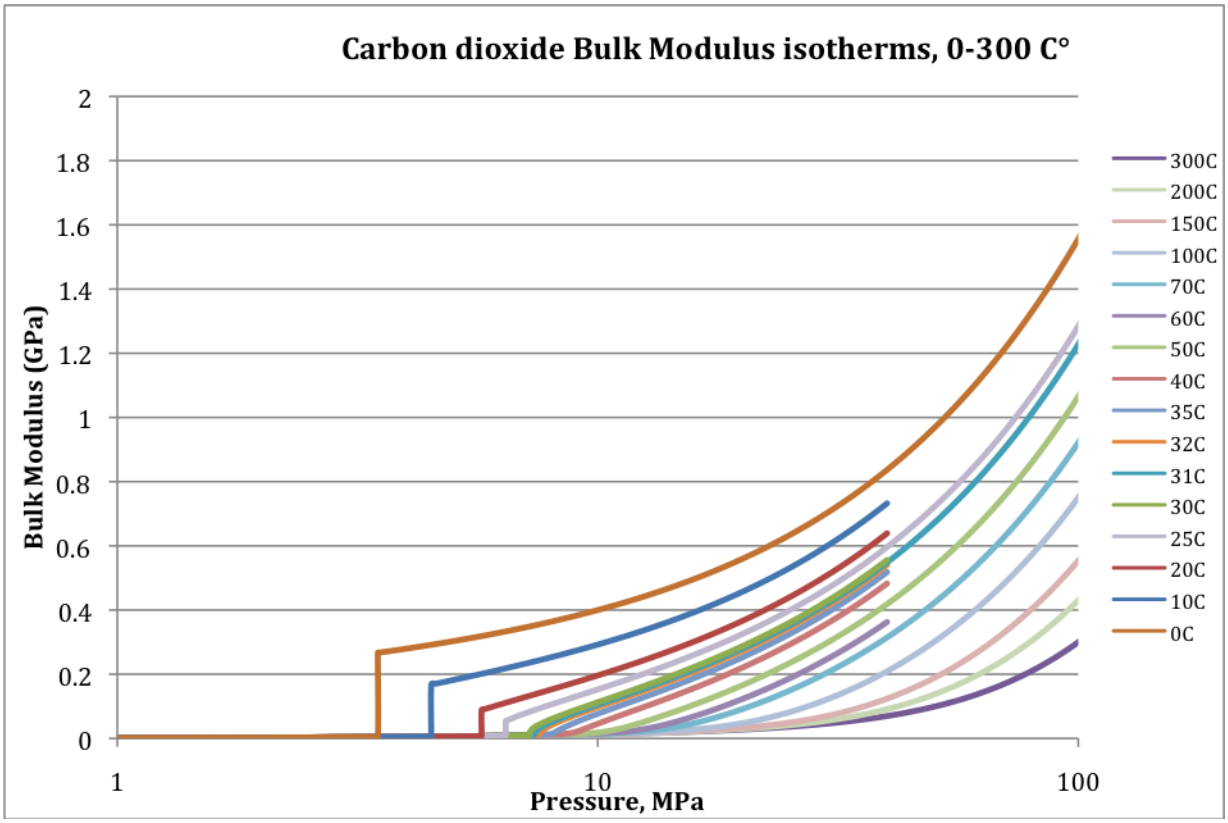

Figure 112: Bulk Modulus Isotherms, 0°-300°C (Lemmon 2005)

When the Bulk Modulus Isotherms are examined, it can be seen that for 25°C, there is a small jump in bulk modulus, and then an increase with increasing pressure. For 50°C, no jump is seen, but Bulk Modulus increases sharply after 10 MPa (Figure 112). The changes in bulk modulus from 10-100 MPa are quite large, increasing from less than 0.1 GPa to over 1 GPa at 100 MPa of pressure.

Comparison of CO_2 and Water properties

In addition to studying the properties of CO_2 over a wide pressure and temperature range, a comparison of CO_2 and water properties was undertaken for the pressure and temperature range

used in our experiments. Water properties were also obtained from the NIST online database (Lemmon 2005), and we chose to focus on the 25°C and 50°C isotherms, as these were the temperatures used in our laboratory experiments. Distilled water was used in the experiments, and the properties of distilled water were obtained from the online database. Of course, the properties of water in situ will vary, as brine is found in the reservoir, not distilled water. Although the total dissolved solids content will vary from reservoir to reservoir, the comparison to distilled water is still useful, as the properties of brine will behave similarly across the pressure and temperature ranges studied.

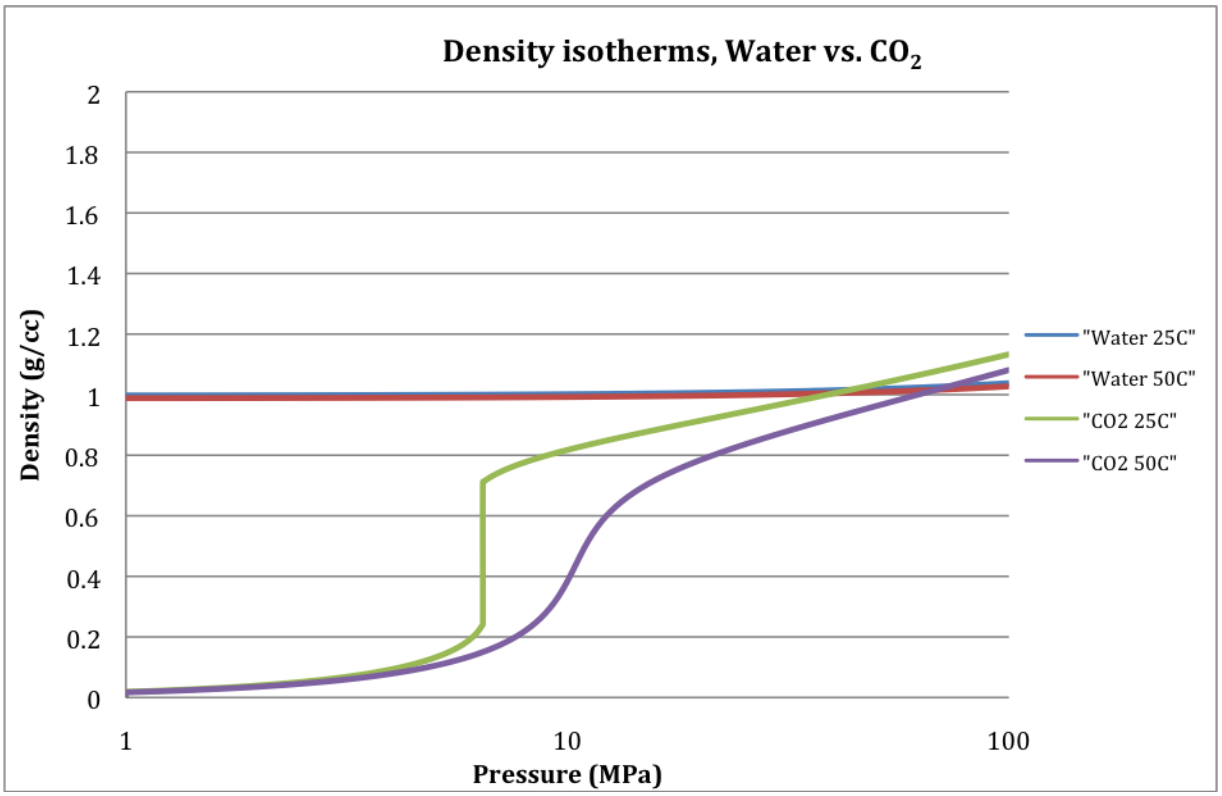

Figure 113: Water and CO_2 Density Isotherms (Lemmon 2005)

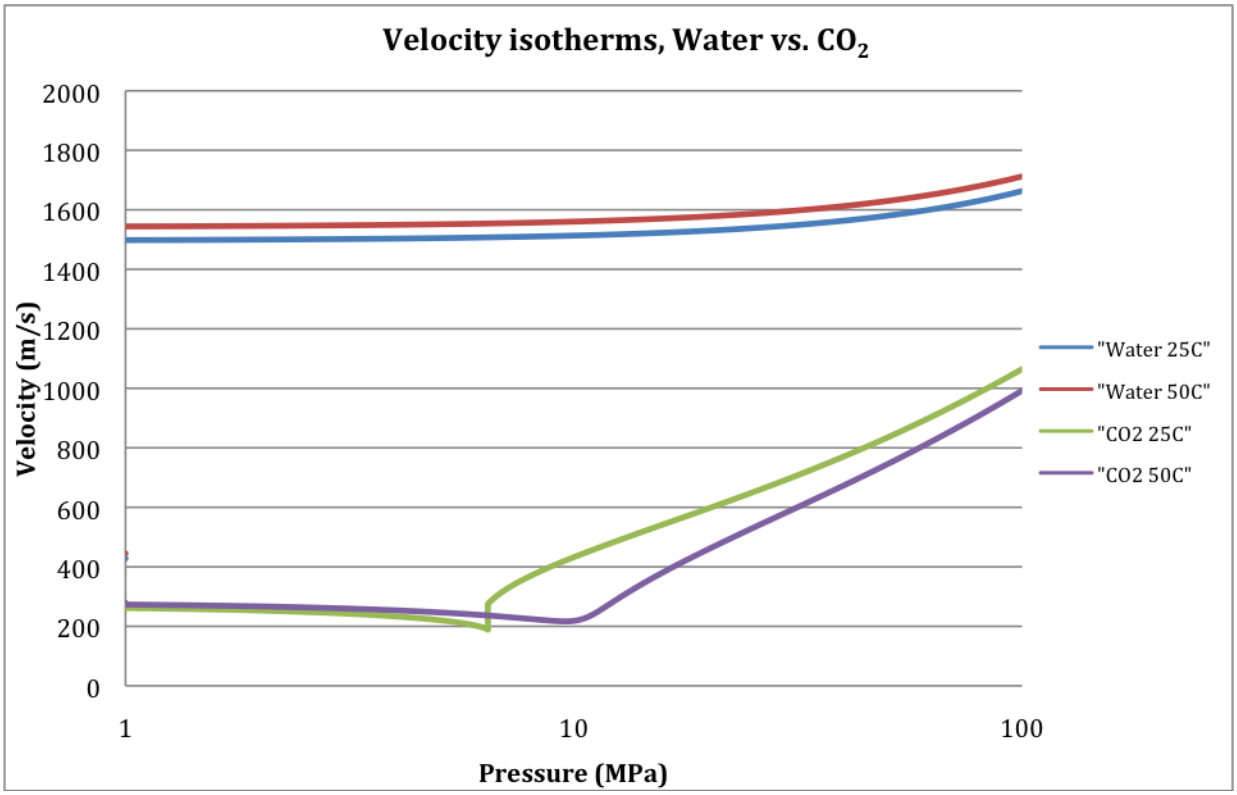

Figure 114: Water and CO_2 Velocity Isotherms (Lemmon 2005)

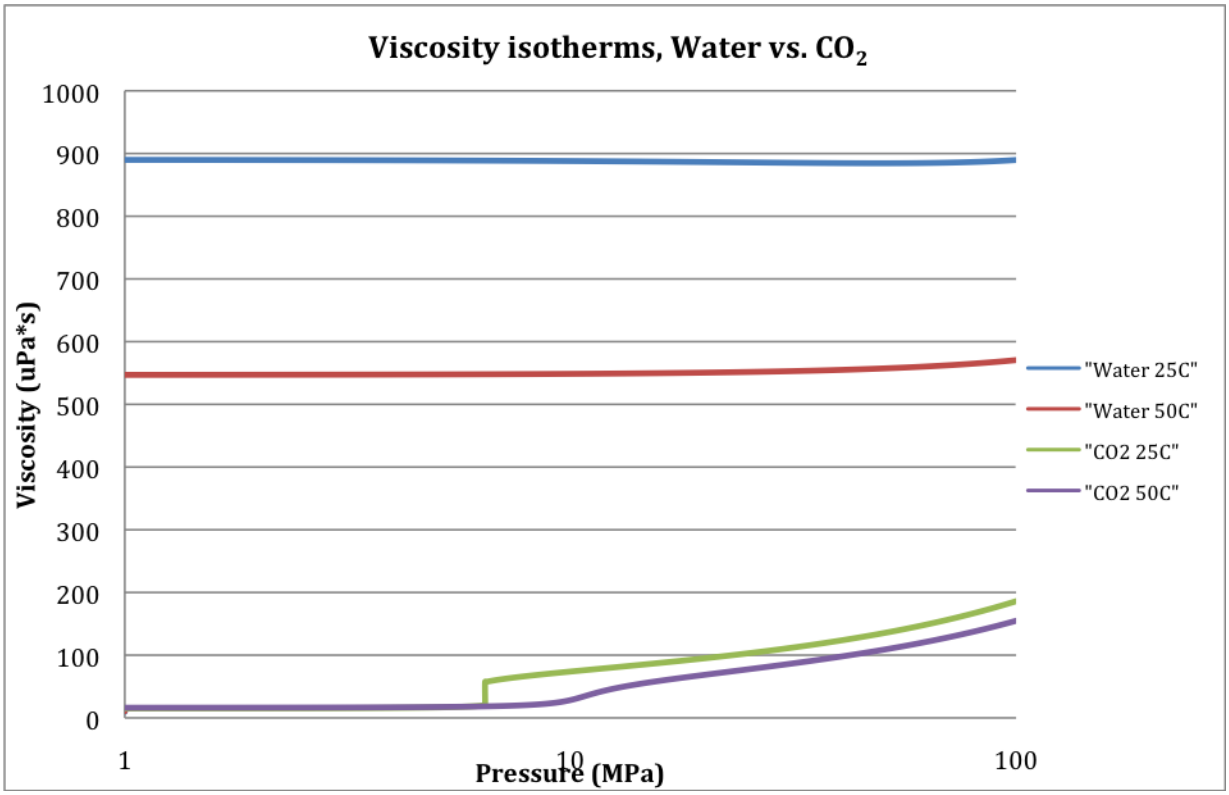

Figure 115: Water and CO_2 Viscosity Isotherms (Lemmon 2005)

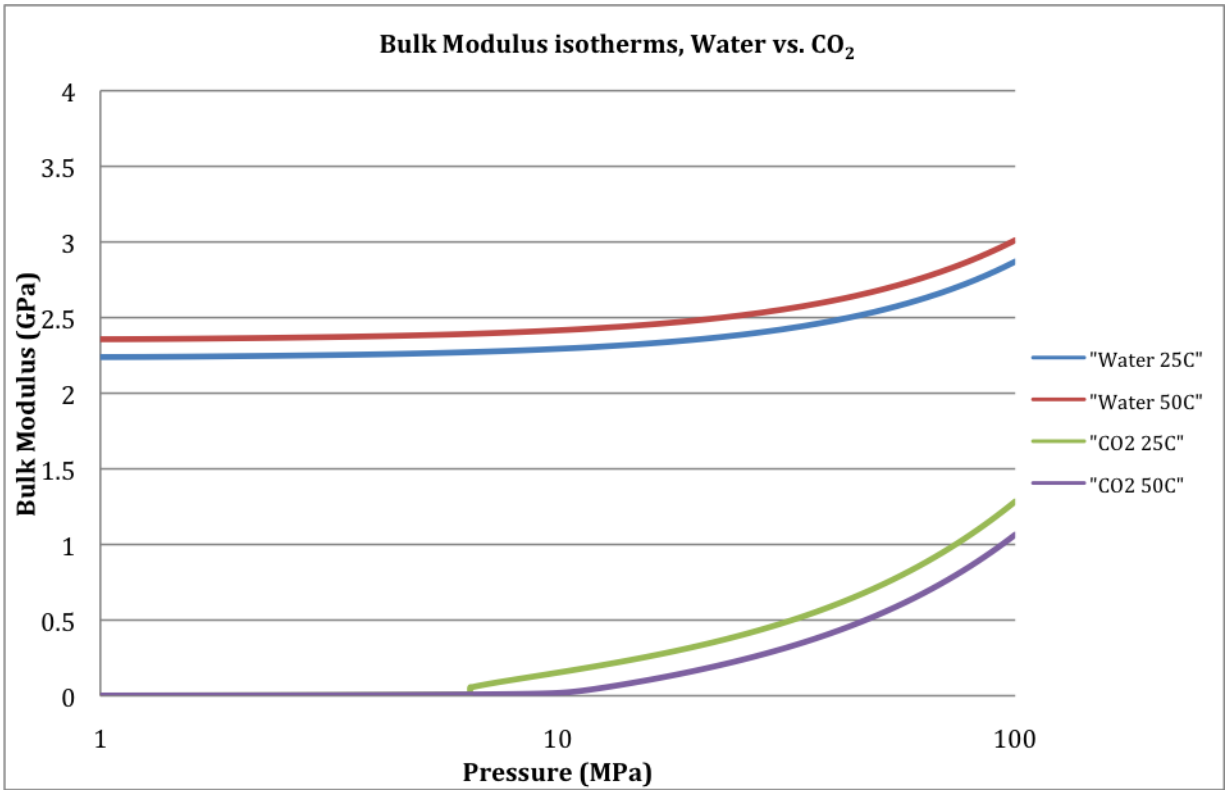

Figure 116: Water and CO_2 Bulk Modulus Isotherms (Lemmon 2005)

3.0 BIBLIOGRAPHY

Aki, K., Richards, P. G. (1980). Quantitative seismology: Theory and methods, v.1, W.H. Freeman and Co.

Avseth, P., Mukerji, T., Mavko, G. (2007). Quantitative Seismic Interpretation, Cambridge University Press.

Biot, M. A. (1956). "Theory of Propagation of Elastic Waves in a Fluid-Saturated Porous Soild. II. Higher Frequency Range." The Journal of the Acoustical Society of America: 179-191.

Brown, R., Korringa, J. (1975). "On the dependence of the elastic properties of a porous rock on the compressibility of the pore fluid." Geophysics **40**: 608-616.

Cardona, R., Batzle, M., Davis, T. (2001). Shear wave velocity dependance on saturation. SEG Annual Meeting. San Antonio, TX.

Castagna, J., Swan, H., Foster, D. (1998). "Framework for AVO gradient and intercept interpretation." Geophysics **63**(3): 948-956.

Castagna, J. P., Smith, S. W. (1994). "Comparison of AVO indicators: A modeling study." Geophysics **59**(12): 1849-1855.

CREWES (2001-2005). "CREWES Zoeppritz Explorer." from www.crewes.org.

Duranti, L., Davis, T., Benson, R. (1999). Time-lapse analysis and detection of fluid changes at Vacuum field, New Mexico. 69th Ann. Internat. Mtg., Soc. Expl. Geophys.**:** 1528-1531.

Gassmann, F. (1951). "Elastic Waves Through a Packing of Spheres." Geophysics.

Gurevich, B., D. Makarynska, et al. (2010). "A simple model for squirt-flow dispersion and attenuation in fluid-saturated granular rocks." Geophysics.

Kaselow, A. and S. A. Shapiro (2004). "Stress sensitivity of elastic moduli and electrical resistivity in porous rocks." Journal of Geophysics and Engineering **1**(1): 1-11.

Lemmon, E. W., McLinden, M. O., Friend, D. G. (2005). "Thermophysical Properties of Fluid Systems, in NIST Chemistry WebBook, NIST Standard Reference Database Number 69." from http://webbook.nist.gov.

Mavko, G., Jizba, D. (1991). "Estimating grain-scale fluid effects on velocity dispersion in rocks." Geophysics: 1940-1949.

McKenna, J. J., Gurevich, B., Urosevic, M., Evans, B.J. (2003). "Rock Physics-Application to geological storage of CO2." Appea Journal.

Mur, A., C. Purcell, et al. (2010). "CO2 Sequestration at SACROC: Integration of core sample velocity measurements into a 4D seismic survey and analysis of SEM and CT images to obtain pore scale properties." Energy Procedia **00**.

Purcell, C., Mur, Alan, Soong, Yee, McLendon, T. Robert, Haljasmaa, Igor V.,Harbert, William (2010). "Integrating velocity measurements in a reservoir rock sample from

the SACROC unit with an AVO proxy for subsurface supercritical CO2." The Leading Edge.

Roden, R. (2008). "Examples of Gas Pay on AVO Crossplots."

Ross, C. P. (2000). "Effective AVO crossplot modeling: A tutorial." Geophysics **65**(3): 700-711.

Rutherford, S. R., Williams, R. H. (1989). "Amplitude-versus-offset variations in gas sands." Geophysics **54**: 680-688.

Sheriff, R. E., Geldart, L.P. (1995). Exploration Seismology, Cambridge University Press.

Shuey, R. T. (1985). "A simplification of the Zoeppritz equations." Geophysics **50**((9)): 609-614.

Sun, M., Han, D., Batzle, M. (2009). CO2 Velocity Measurements and Models for Temperatures down to -10 °C and up to 200 °C and Pressures up to 100 MPa. SEG Houston 2009 International Exposition and Annual Meeting.

Wang, Z., Nur, Amos M. (1989). "Effects of CO2 Flooding on Wave Velocities in Rocks With Hydrocarbons." SPE Reservoir Engineering **4**(4): 429-436.